Terahertz spectroscopy applied to food model systems

Møller, Uffe

Publication date:
2009

Document Version
Publisher's PDF, also known as Version of record

Terahertz spectroscopy applied to food model systems

Uffe Møller

Terahertz spectroscopy applied to food model systems

by

Uffe Møller

August 2009

Submitted in accordance with the requirements for the degree of Doctor of Philosophy.

Technical University of Denmark
DTU Fotonik - Department of Photonics Engineering

Supervisors: Professor Peter Uhd Jepsen, DTU Fotonik
Dr. Jacob Riis Folkenberg, FOSS Analytical A/S

Abstract

This thesis describes terahertz time-domain spectroscopy applied on aqueous food model systems, with particular focus on ethanol-water mixtures and confined water pools in inverse micelles.

A detailed analysis of general realizations of transmission, reflection and attenuated total reflection terahertz time-domain spectroscopy is given. These different geometries are compared for analysis of a low-absorbing and a high-absorbing material, respectively, and pros and cons are discussed. It is found that transmission THz spectroscopy are superior for measurements on low-absorbing materials, while attenuated total reflection THz spectroscopy are well suited for measurements on high-absorbing materials.

The dielectric properties of ethanol-water mixtures measured by reflection and attenuated total reflection terahertz time-domain spectroscopy is discussed. The reflection technique is applied for the determination of alcohol and sugar concentration of commercial alcoholic beverages and liquors. The attenuated total reflection measurements of the dielectric function of ethanol-water mixtures are combined with previously published low frequency data, which covers the wide frequency range 100 MHz - 2.5 THz. It is shown that the dielectric properties of ethanol-water mixtures are closely linked to their thermodynamic properties.

Reflection terahertz time-domain spectroscopy is also used for remote detection and classification of liquids, and in particular alcohol solutions, inside closed containers. It is demonstrated that it is possible to determine the alcohol content of an aqueous solution, and that liquids can be classified as either harmless or inflammable. The method operates in reflection mode with the result that liquids opaque to THz radiation can be characterized with little influence of the bottle shape. The method works with plastic bottles as well as glass bottles, with absorption of THz radiation by the plastic or the glass being the limiting factor. The reflection mode allows for automatic control of the validity of the measurement. The method will be useful in liquid scanning systems at security checkpoints.

Finally, the dielectric properties nanometer-sized water pools inside inverse micelles in water-AOT-heptane systems are investigated with transmission terahertz time-domain spectroscopy. The dielectric properties of different vegetable oils, lard as well as water in butter are also discussed.

Resumé

Denne afhandling omhandler terahertz tidsdomæne spektroskopi anvendt på modelsystemer af fødevarer med særlig fokus på ethanol-vand blandinger og indelukkede vanddråber i inverse miceller.

Der gives en detaljeret analyse af transmissions-, reflektions- samt dæmpet totalreflektionssystemer baseret på terahertz tidsdomæne spektroskopi. Disse forskellige systemer sammenlignes for målinger på henholdsvis lavabsorberende samt højabsorberende materialer. Det demonstreres, at terahertz transmissionsspektroskopi er bedst til at måle på lavabsorberende materialer, mens terahertz dæmpet totalreflektionsspektroskopi er bedst egnet til målinger på højabsorberende materialer.

De dielektriske egenskaber af ethanol-vand blandinger målt med terahertz reflektions- og dæmpet totalreflektionsspektroskopi diskuteres. Teknikken er anvendt til at bestemme alkohol- og sukker-koncentrationer i kommercielle alkoholiske drikkevarer. Målingerne af den dielektriske funktion af ethanol-vand blandinger er kombineret med tidligere publicerede lavfrekvente målinger, der gør det muligt at dække frekvensområdet 100 MHz - 2,5 THz. Det demonstreres, at de dielektriske egenskaber af ethanol-vand blandingerne hænger nøje sammen med deres termodynamiske egenskaber.

Terahertz reflektionsspektroskopi bruges til at detektere og klassificere væsker, i særdeleshed alkoholblandinger, i lukkede beholdere. Det demonstreres, at det er muligt at bestemme indholdet af alkohol i en blanding, og at væsken kan klassificeres som enten uskadelig eller brandfarlig. Metoden sikrer, at væsker, der er uigennemsigtige for terahertzstråling, kan karakteriseres med minimal indflydelse af flaskeformen. Metoden virker både på plastik- og glasflasker, og flaskematerialets absorption af terahertzstrålingen er den begrænsende faktor. Metoden vil være brugbar i væskescannere ved sikkerheds checkpunkter.

Slutteligt undersøges de dielektriske egenskaber af vånddråber i nanometerstørrelsen indesluttede i inverse miceller i vand-AOT-heptan blandinger målt med terahertz transmissionsspektroskopi. De dielektriske egenskaber af forskellige vegetabilske olier, svinefedt samt vand i smør diskuteres også.

Preface

Most of the results presented in this thesis were obtained at DTU Fotonik - Department of Photonics Engineering, Technical University of Denmark in the group of Professor Peter Uhd Jepsen.

The attenuated total reflection measurements presented in Chapter 7 were performed in the group of Professor Koichiro Tanaka at the Department of Physics, Graduate School of Science and the Institute for Integrated Cell-Material Sciences both located at Kyoto University, Japan.

This Ph.D. project was part of the Photonics Academy Denmark research programme and financed by the Department of Photonics Engineering, Technical University of Denmark (1/3), FOSS Analytical A/S (1/3) and the Ministry of Science, Technology and Innovation (1/3).

About this thesis

The thesis is divided into two parts: (I) a theoretical part containing 4 chapters (2-5) and (II) an experimental part also containing 4 chapters (6-9).

Chapter 2 gives an introduction to electromagnetic waves and the Fresnel equations. Furthermore, the relation between the optical properties and the dielectric function of a sample is discussed. Chapter 3 describes how to generate and detect terahertz radiation. In Chapter 4 the concepts of terahertz time-domain spectroscopy are described including transmission-, reflection- and attenuated total reflection- measurement techniques. Chapter 5 deals with the dynamics of liquids in the terahertz region and introduces the concepts of molecular vibration and dielectric relaxation. In the same Chapter spectroscopy of heterogenous samples are also discussed.

Measurements on ethanol and sucrose in water are treated in Chapter 6 where it is demonstrated how an unknown concentration of ethanol or sucrose in water can be determined. The dielectric properties of ethanol-water mixtures are discussed in Chapter 7. Chapter 8 discusses the measurements on micelles of water in heptane and compares these with measurements on butter. Finally, it is demonstrated how one can inspect liquids inside bottles in Chapter 9. Fitting parameters for the dielectric properties of ethanol-water

mixtures can be found in Appendices A and B while published and submitted journal papers can be found in Appendix D.

Kongens Lyngby,
August 14th, 2009

UFFE MØLLER

Contents

Chapter 1

Introduction

When Sir Isaac Newton (1643-1727) in the 17th century showed that the white light from the sun could be dispersed into a continuous series of colors he founded the science of spectroscopy. During the following centuries it was realized that the sun's radiation had components outside the visible part of the spectrum, and it became clear that by studying the spectrum of an unknown sample, valuable information about it could be gained.

A portion of the electromagnetic spectrum is depicted in Fig. 1.1. Terahertz (THz) radiation is electromagnetic radiation whose frequency lies between the microwave region and the infrared region and is sometimes referred to as far-infrared radiation.

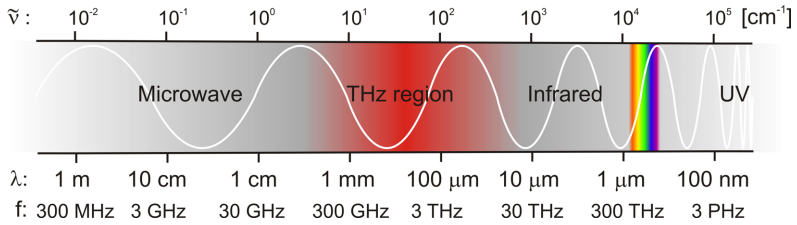

Figure 1.1: *The electromagnetic spectrum. The "THz-region" spans the gap between the microwave and the infrared region. The visible part of the spectrum is shown with rainbow colors between the infrared and ultraviolet (UV) region.*

Different units are used to describe electromagnetic radiation dependent on the scientific community. The frequency of 1 THz corresponds to

$$1 \text{ THz} = 1 \cdot 10^{12} \text{ Hz} = 300 \ \mu\text{m} = 33.3 \text{ cm}^{-1} = 4.14 \text{ meV} = 47.6 \text{ K}.$$

The THz region (the red region in Fig. 1.1) is loosely defined as the spectral region between 0.1-10 THz. This part of the electromagnetic spectrum is for the time being the least explored, mainly due to the technical difficulties involved in making detectors and sources. Because of this fact, it is often

referred to as the "THz-gap". However, with the introduction of *terahertz time-domain spectroscopy* (THz-TDS) in the late 1980s [1, 2] and the technical advances since then, this gap has been more or less eliminated.

Radiation from different regions of the electromagnetic spectrum that interacts with a sample can contribute to valuable information about it. Electronic transitions is often observed in the ultraviolet (UV) region, vibrations of bonds in molecules in the infrared region and rotations of molecules in the microwave region, respectively, while terahertz radiation interacts strongly with intermolecular bonds.

The optical properties of bulk water have been investigated virtually at all wavelengths normally associated with electromagnetic radiation. In Fig. 1.2 the absorption coefficient (on a logarithmic scale) and the index of refraction (on a linear scale) are shown as function of frequency (lower, horizontal axis) or wavenumber (upper, horizontal axis) [3].

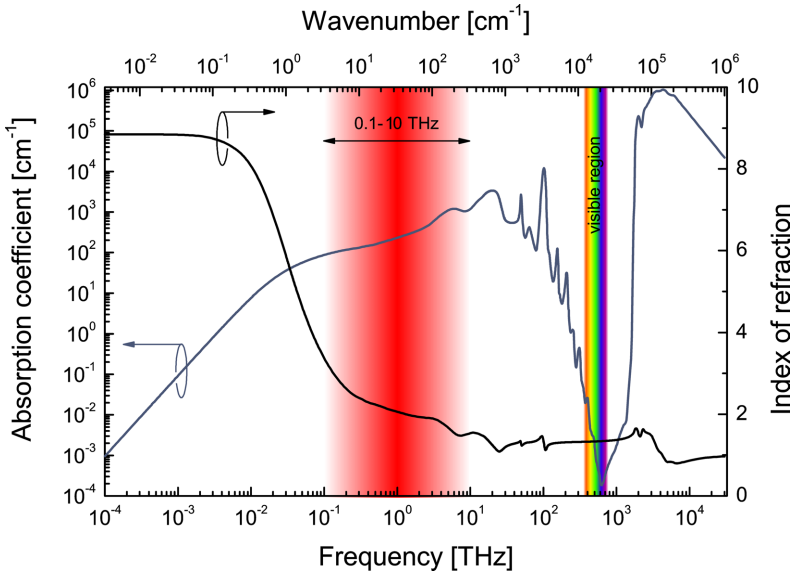

Figure 1.2: *Absorption spectrum (blue curve, logarithmic scale) and index of refraction (black curve, linear scale) as function of frequency (lower horizontal scale) and wavenumber (upper, horizontal scale). The red area indicates the 0.1-10 THz region, and the rainbow colored area indicates the visible part of the spectrum.*

The red area indicates the THz region of the spectrum, and the visible region of the spectrum is indicated by the rainbow colored bar. The figure shows that the THz region gives access to the part of the optical properties of water which lies below the vibrational bands in the infrared.

The large dipole moment of the water molecule together with the dynamic intermolecular network of hydrogen bonds forms a highly complex many-body system. This system interacts collectively in a strong and characteristic manner with electromagnetic radiation at THz frequencies. This is due to the fact

that the typical time scales involved in relaxation dynamics of water molecules displaced or rotated from their equilibrium positions falls in the picosecond to sub-picosecond range. Thus THz spectroscopy is a unique tool for the study of the collective properties of water in particular, and of hydrogen-bonded liquids in general.

Water plays a crucial role in the quality of food. Apart from the natural water content of a food product, the state of that water is very important. Knowledge about the state of water can give valuable information about the food product, e.g. shelf life, taste and consistency.

In spite of the promising and exciting potential of THz spectroscopy to investigate water in different environments, this potential has so far not been applied to products from the food industry. In this thesis we will discuss THz spectroscopy applied to food model systems.

Part I

Theory

Chapter 2

Electromagnetic waves in matter

Starting from Maxwell's equations basic concepts such as propagation, reflection and transmission of electromagnetic waves in matter will described in this Chapter. Furthermore, the relation between the optical properties and the dielectric function of a sample will be discussed.

2.1 Maxwell's equations

As it is the case for any other spectral region, Maxwell's equations can be used to describe THz waves which propagate in and interact with macroscopically uniform media. The macroscopic representation of Maxwell's equations has the form

$$\nabla \cdot \mathbf{D} = \rho_f, \tag{2.1}$$

$$\nabla \cdot \mathbf{B} = 0, \tag{2.2}$$

$$\nabla \times \mathbf{E} = -\frac{\partial \mathbf{B}}{\partial t}, \tag{2.3}$$

$$\nabla \times \mathbf{H} = \mathbf{J}_f + \frac{\partial \mathbf{D}}{\partial t}, \tag{2.4}$$

where $\mathbf{E}$, $\mathbf{B}$, $\mathbf{D}$, and $\mathbf{H}$ are the electric field, the magnetic field, the electric displacement field and the magnetizing field, respectively, ρ_f is the free charge density and $\mathbf{J}_f$ is the free current density. The macroscopic electromagnetic properties of the matter can be described by the polarization $\mathbf{P}$ and the mag-

netization $\mathbf{M}$ which are related to the fields in the following way,

$$\mathbf{D} \equiv \varepsilon_0 \mathbf{E} + \mathbf{P} = \varepsilon \mathbf{E}, \tag{2.5}$$

$$\mathbf{H} \equiv \frac{1}{\mu_0}\mathbf{B} - \mathbf{M} = \frac{1}{\mu}\mathbf{B}, \tag{2.6}$$

where ε_0 and μ_0 are the permittivity and the permeability of free space, respectively, and ε and μ are the permittivity and the permeability of the matter, respectively. From the coupled electric and magnetic fields one can find the wave equation. In the case of an uncharged and nonconducting medium the wave equation will have the form

$$\nabla^2 \mathbf{E} = \varepsilon\mu \frac{\partial^2 \mathbf{E}}{\partial t^2}. \tag{2.7}$$

One of the solutions of the wave equation is a linearly polarized monochromatic plane wave. Such a wave with angular frequency ω propagating in the z-direction through a dielectric medium with absorption coefficient α and refractive index n has the form

$$\mathbf{E}(z,t) = \mathbf{E}_0 \cdot e^{-\frac{\alpha}{2}z} \cdot e^{-i\omega\left[\frac{n}{c}z - t\right]}, \tag{2.8}$$

where the term $\mathbf{E}_0$ represents the wave before propagating through the dielectric medium. If the wave propagates through a dielectric medium of thickness d it will undergo a phase shift as well as an attenuation due to absorption. In the frequency domain the plane wave consisting of a continuous spectral distribution can then be expressed as

$$E(\omega) = E_0(\omega) \cdot e^{-\frac{\alpha(\omega)d}{2}} \cdot e^{-i\frac{n(\omega)d}{c}\omega}. \tag{2.9}$$

2.2 The Fresnel equations

When an electromagnetic wave meets an interface of two media it will be reflected from and transmitted through the interface. Fig. 2.1 shows such a plane wave in the vicinity of an interface between two homogenous, isotropic, dielectric media of frequency dependent complex refractive indices $\hat{n}_1$ and $\hat{n}_2$ in the cases where the incoming electric field, $E_i(\omega)$, is perpendicular ($\perp$) and parallel ($\parallel$) to the plane of incidence, respectively.

Assuming that the magnetic permeabilities of the media differ from unity by a negligible amount, using the law of reflection, $\theta_i = \theta_r$, and applying boundary conditions that the tangential components of the electric and magnetic fields to the sample interface are continuous across the interface, one can now find the reflection coefficients $\hat{r}_{12}$ and the transmission coefficients $\hat{t}_{12}$ for

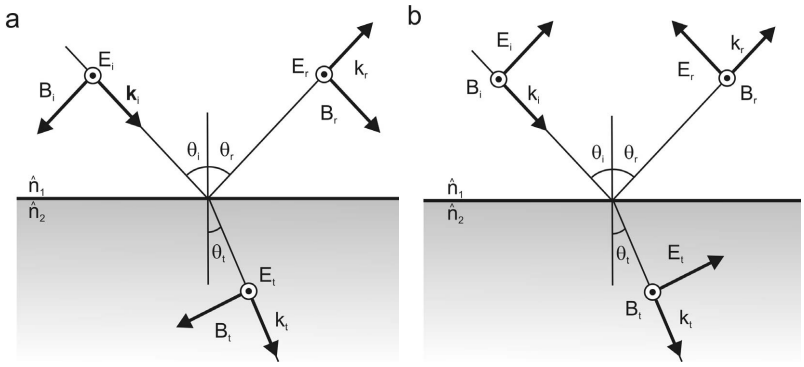

FIGURE 2.1: *A plane incoming wave whose electric field is (a) perpendicular and (b) parallel to the plane of incidence.*

parallel ($\parallel$) and perpendicular ($\perp$) polarized fields propagating from medium 1 to medium 2 to [4, 5]

$$\hat{r}_{12}^{\perp} = \frac{\hat{n}_1 \cos\theta_i - \hat{n}_2 \cos\theta_t}{\hat{n}_1 \cos\theta_i + \hat{n}_2 \cos\theta_t}, \tag{2.10}$$

$$\hat{t}_{12}^{\perp} = \frac{2\hat{n}_1 \cos\theta_i}{\hat{n}_1 \cos\theta_i + \hat{n}_2 \cos\theta_t}, \tag{2.11}$$

$$\hat{r}_{12}^{\parallel} = \frac{\hat{n}_2 \cos\theta_i - \hat{n}_1 \cos\theta_t}{\hat{n}_2 \cos\theta_i + \hat{n}_1 \cos\theta_t}, \tag{2.12}$$

$$\hat{t}_{12}^{\parallel} = \frac{2\hat{n}_1 \cos\theta_i}{\hat{n}_2 \cos\theta_i + \hat{n}_1 \cos\theta_t}. \tag{2.13}$$

Equations 2.10-2.13 are also known as the *Fresnel equations*. Since $\hat{n}$ is frequency dependent and complex, the reflection and transmission coefficients are that as well. By use of Snell's law, $\hat{n}_1 \sin\theta_i = \hat{n}_2 \sin\theta_t$, the Fresnel equations can be reformulated to

$$\hat{r}_{12}^{\perp} = \frac{\hat{n}_1 \cos\theta_i - \hat{n}_2\sqrt{1-(\hat{n}_1/\hat{n}_2)^2\sin^2\theta_i}}{\hat{n}_1 \cos\theta_i + \hat{n}_2\sqrt{1-(\hat{n}_1/\hat{n}_2)^2\sin^2\theta_i}}, \tag{2.14}$$

$$\hat{t}_{12}^{\perp} = \frac{2\hat{n}_1 \cos\theta_i}{\hat{n}_1 \cos\theta_i + \hat{n}_2\sqrt{1-(\hat{n}_1/\hat{n}_2)^2\sin^2\theta_i}}, \tag{2.15}$$

$$\hat{r}_{12}^{\parallel} = \frac{\hat{n}_2 \cos\theta_i - \hat{n}_1\sqrt{1-(\hat{n}_1/\hat{n}_2)^2\sin^2\theta_i}}{\hat{n}_2 \cos\theta_i + \hat{n}_1\sqrt{1-(\hat{n}_1/\hat{n}_2)^2\sin^2\theta_i}}, \tag{2.16}$$

$$\hat{t}_{12}^{\parallel} = \frac{2\hat{n}_1 \cos\theta_i}{\hat{n}_2 \cos\theta_i + \hat{n}_1\sqrt{1-(\hat{n}_1/\hat{n}_2)^2\sin^2\theta_i}}. \tag{2.17}$$

If the polarization of the incoming wave and its incident angle are known together with the refractive index of medium 1 (typically air, $\hat{n}_1 = 1$) the Fresnel equations will then be a function of the refractive index of medium 2. Later, in Chapter 4, it will be shown that the Fresnel equations are essential in THz time-domain spectroscopy in order to extract the optical properties of a sample from the measurements of the electric field.

2.3 The complex refractive index and the dielectric function

In the previous section the complex refractive index of a medium $\hat{n}$ was mentioned. This is simply a compressed form to describe the optical properties of the medium, i.e. the absorption coefficient α and the refractive index n. The frequency dependent complex refractive index of a medium $\hat{n}$ can be expressed as

$$\hat{n}(\omega) = n(\omega) - i\kappa(\omega) = n(\omega) - i\frac{\alpha(\omega)c}{2\omega}, \tag{2.18}$$

where $n(\omega)$ is the refractive index, $\kappa(\omega)$ is the extinction coefficient, $\alpha(\omega)$ is the absorption coefficient and c is the speed of light in vacuum ($c = 3.0 \cdot 10^8 m/s$). Alternatively, one can also describe the dielectric function of the medium $\hat{\epsilon}(\omega)$ which contains a real part, $\epsilon'(\omega)$, and an imaginary part, $\epsilon''(\omega)$

$$\hat{\varepsilon}(\omega) = \varepsilon'(\omega) - i\varepsilon''(\omega) \tag{2.19}$$

It is solely a matter of preference as to whether one refers to the dielectric function or the complex refractive index since they are related by $\hat{\varepsilon}(\omega) = [\hat{n}(\omega)]^2$. The connections between real and imaginary parts of the complex refractive index and the dielectric function, respectively, are summarized in Tab. 2.1.

TABLE 2.1: *Relationships between the complex refractive index $\hat{n}$ and the dielectric function $\hat{\varepsilon}$.*

	Complex refractive index	Dielectric Function
$\hat{n}$	$\hat{n} = n - i\kappa$	$n^2 = \frac{1}{2}(\varepsilon'^2 + \varepsilon''^2)^{\frac{1}{2}} + \frac{\varepsilon'}{2}$ $\kappa^2 = \frac{1}{2}(\varepsilon'^2 + \varepsilon''^2)^{\frac{1}{2}} - \frac{\varepsilon'}{2}$
$\hat{\varepsilon}$	$\varepsilon' = n^2 - \kappa^2$ $\varepsilon'' = 2n\kappa$	$\hat{\varepsilon} = \varepsilon' - i\varepsilon''$

Chapter 3

Terahertz pulses

As mentioned in the introduction the so-called THz-gap is placed in between the longer electronic wavelengths and the shorter optical wavelengths. This gap has historically not been easily accessible and it was not explored until the middle of the last century [6–8]. These far infrared techniques required helium cooled detectors in order to cope with the ambient black body radiation and were in general not easy to work with. A radical change happened in the late 1980s when free space propagation of THz pulses generated and detected by photoconductive switching was reported [1, 2].

An alternative method to generate and detect THz pulses is by use of nonlinear optical effects in crystals. In 1893, Friedrich Pockels (1865-1913) discovered the linear electrooptic effect which was experimentally demonstrated by Harris and coworkers in 1962 [9]. The same year optical rectification was experimentally demonstrated for the first time by Bass *et al.* [10] and twenty years later Valdmanis *et al.* build the first electrooptic sampling system with picosecond resolution [11]. In 1992, the group of X.-C. Zhang demonstrated that optical rectification in a nonlinear crystal could generate THz radiation [12–14]. A few years later, the same group [15], Jepsen *et al.* [16] and the group of Nahata [17] demonstrated THz detection by electrooptic sampling in nonlinear crystals.

In this Chapter it will be described how THz pulses are generated and detected with a near infrared pulsed laser focussed on photoconductive antennas. It will also briefly be discussed how THz pulses can be generated by optical rectification and detected by free space electrooptic sampling in a nonlinear crystal. It should however be pointed out that a lot of other techniques can be used to generate and detect terahertz radiation, i.e. continuous wave THz based on difference frequency generation and photomixing detection [18], quantum cascade lasers (QCL's) [19], synchrotron radiation [20], high power THz generation and detection [21], ultra broadband THz radiation [22] and THz radiation based on Schottky diode frequency multipliers [23]. These

methods are beyond the scope of this thesis and the reader is referred to the given Refs. for additional information.

3.1 Photoconductive antennas

Photoconductive generation and detection of THz pulses arise from the transient flow of charges and thus it can be described theoretically by Maxwell's equations. The geometry of a typical photoconductive generation antenna is shown in Fig. 3.1.

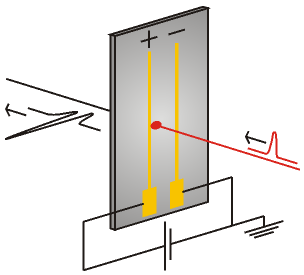

Figure 3.1: *Schematic of a photoconductive emitter. Two biased metallic striplines are placed on a semiconductor substrate. Laser pulses are focussed in between the striplines and THz radiation is generated.*

Two metallic striplines are placed on a semiconductor substrate with a high mobility μ. The striplines are DC-biased, typically with $10 - 50\ VDC$, to produce an electric field between them. The first step is to photoexcite the region of the electric field between the striplines by pulsed light with higher energy than the bandgap of the semiconductor in order to form a electron-hole plasma on a femtosecond time scale. These electron-hole pairs are accelerated by the applied field and give rise to a transient current $\mathbf{J}(t)$ and the polarization will create a time dependent opposing field that screens the electric DC field. This transient field will then give rise to electromagnetic radiation. In other words, the transient current serves as a source term in Maxwell's equations and will therefore give rise to electromagnetic radiation [24]

$$\nabla \times \mathbf{E}_{THz}(t) = -\mu \frac{\partial \mathbf{H}_{THz}(t)}{\partial t}, \tag{3.1}$$

$$\nabla \times \mathbf{H}_{THz}(t) = \mathbf{J}(t) + \frac{\partial \varepsilon(t) \mathbf{E}_{THz}(t)}{\partial t}, \tag{3.2}$$

where $\mathbf{E}_{THz}$ and $\mathbf{H}_{THz}$ are the radiated electric field and the magnetic field intensity, respectively. The radiated electric field will have a nearly single-cycle form in the time-domain and thus it will be broadbanded in the frequency domain [25]. Immediately after the radiation of the THz pulse and in the

absence of an incoming optical pulse the semiconductor recovers, typically on a picosecond time scale determined by the recombination time of the semiconductor.

Typically, a Ti:Sapphire laser with a wavelength of $\lambda \sim 800$ nm, a pulse duration of ~ 100 fs, a repetition rate of ~ 100 MHz and an average power level of $P_{av} \sim 100$ mW or similar is used. Ti:Sapphire lasers are very stable with low noise levels, require only little maintenance, are low-cost compared to other systems and they are available as a turn-key systems and thus easy to use. A high mobility material is preferable in order to rapidly accelerate carriers. Because of this, the favorite choice of semiconductor material is low-temperature grown gallium arsenide (LT-GaAs) [26–28] but also other materials, such as silicon on sapphire (SOS) [29], are used.

The dimensions of the striplines, i.e. their separation, will influence the maximum field strength and bandwidth of the radiated pulse. A typical emitter chip will have metallic striplines of ~ 10 μm width with a separation of ~ 50 μm and a length much larger than the separation. The optical excitation spot should be focused near the anode as illustrated in Fig. 3.1 in order to get maximum radiation. This is due to the fact that the field distribution between the striplines is nonuniform with the high fields concentrated near the anode [30]. The THz emitter can be regarded as a point source since the size of the optical excitation spot is smaller than the generated terahertz wavelength.

Photoconductive detection of THz pulses relies on the same physical principles as photoconductive generation. The geometry of a typical photoconductive detection antenna is shown in Fig. 3.2.

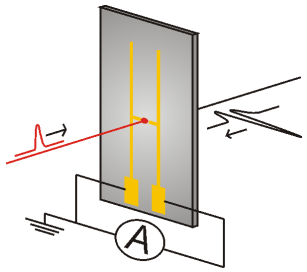

FIGURE 3.2: *Schematic of a photoconductive detector. Two metallic striplines making up a capital "h" are placed on a semiconductor substrate. Laser pulses are focussed in the center of the h-structure and THz radiation is detected by measuring the photocurrent.*

The only fundamental difference is that the striplines are not biased. Instead it is the incoming THz field that work as a (time dependent) bias field. If a field is present at the same time as the incoming optical pulse a current can be measured due to the charge movement. The recorded current will be

a convolution of the incoming field E_{THz} and the detector response σ,

$$J(\tau) = \frac{1}{T}\int_0^{\tau} E_{THz}(t)\sigma(t-\tau)dt, \tag{3.3}$$

with τ as the arrival time of the optical pulse. In theory if the detector response is a delta function the detected current will proportional to the time dependent electric field E(t). However, in practice the the response will be finite because of the duration of the incoming laser pulse and the carrier lifetime of the semiconductor substrate. The exact detector response is however not needed to be known in the sense of spectroscopy applications since such an analysis imply the ratio between two Fourier transformed electric fields. A convolution in the time domain is a product in the Fourier domain and thus the detector response form will not influence the spectroscopic analysis given that the detector response is the same for both electric field measurements. The time dependent electric field can then simply be mapped by means of optoelectronic sampling where the arrival time of the incoming laser pulse is determined with a controllable delay line.

Again, as in the case for photoconductive generation, the dimensions of the striplines are of importance. Grischkowsky *et al.* showed that by using an $h-$structured antenna the bandwidth and power were increased [31] (the name "h-structured" originates from the design of the striplines which formes a capital "H" as seen in Fig. 3.2). The typical dimensions of a detector chip will be metallic striplines of $\sim$ 10 μm width with a separation of $\sim$ 25 μm, a separation of $\sim$ 5 μm in the gap of the $h-$structure (comparable to the spot size) and a length much longer than the separation. As for the photoconductive emitters, LT-GaAs is the favorite choice of material because of its high mobility and low recombination time.

A hyper-hemispherical silicon lens is placed on the backside of the emitter chip in order to collimate the radiated THz field as illustrated in Fig. 3.3.

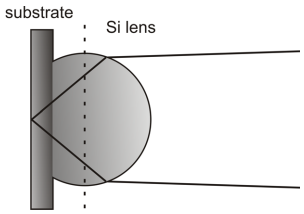

Figure 3.3: *Ray tracing diagram. A hyper-hemispherical lens placed on a substrate with similar refractive index.*

High resistivity silicon is non-dispersive in the THz range [32] and LT-GaAs and Si have similar refractive indices which reduces the interfacial reflection losses. The lens is designed in such a way that the beam is focussed on the front side of the semiconductor substrate. A similar Si lens on the backside

of the detector chip can be used to collect and focus the THz field onto the detector.

3.2 Optical rectification

An alternative way to generate THz pulses is to utilize optical rectification in nonlinear crystals. Optical rectification is a second order nonlinear effect that occurs when the induced electric polarization $\mathbf{P}$ is a nonlinear function of the applied field. The induced polarization is in the frequency domain a function of the wavenumber k and the angular frequency ω and may be expressed as a series expansion [33]

$$\begin{aligned}\mathbf{P}(k,\omega) &= \mathbf{P}^{(0)}(k,\omega)+\mathbf{P}^{(1)}(k,\omega)+\mathbf{P}^{(2)}(k,\omega)+\cdots \\ &= \mathbf{P}^{(0)}(k,\omega) \\ &\quad +\varepsilon_0(\chi^{(1)}_{ij}\mathbf{E}_i(k_i,\omega_i)+\chi^{(2)}_{ijk}\mathbf{E}_i(k_i,\omega_i)\mathbf{E}_j(k_j,\omega_j)+\cdots), \quad (3.4)\end{aligned}$$

where $\chi^{(n)}$ is the susceptibility tensor of rank $n+1$, $\mathbf{P}^{(0)}$ is the static polarization, i.e. independent of the electric field, $\mathbf{P}^{(1)}$ is the linear polarization, i.e. linear in the electric field, $\mathbf{P}^{(2)}$ is the quadratic polarization, i.e. quadratic in the electric field and so on. It is seen from Eq. 3.4 that the higher order nonlinear susceptibilities provide mixing of the frequencies of the different waves.

Let us assume that we have two plane electromagnetic waves $E_1 = \frac{1}{2}[A_j(t)exp(-i\omega_1 t)+c.c.]$ and $E_2 = \frac{1}{2}[A_k(t)exp(-i\omega_2 t)+c.c.]$ where $A_{k,l}$ are the envelopes, $\omega_{1,2}$ are the carrier frequencies and *c.c.* are the complex conjugate, then the second order induced polarization can be expressed as

$$\begin{aligned}P^{(2)}(\omega=\omega_1+\omega_2) &= \varepsilon_0\chi^{(2)}_{ijk}\frac{1}{2}[A_j(t)exp(-i\omega_1 t)+c.c.] \\ &\quad \cdot\frac{1}{2}[A_k(t)exp(-i\omega_2 t)+c.c.] \\ &= \frac{1}{4}\varepsilon_0\chi^{(2)}_{ijk}\{[A_jA_kexp[-i(\omega_1-\omega_2)t]+c.c.] \\ &\quad +[A_jA_kexp[-i(\omega_1+\omega_2)t]+c.c.]\} \\ &= P^{(2)}_{\Delta}(\omega)+P^{(2)}_{\Sigma}(\omega). \quad (3.5)\end{aligned}$$

Thus, the second order polarization consists of a sum of two terms $P^{(2)}_{\Delta}$ and $P^{(2)}_{\Sigma}$ containing the difference and sum frequencies. If we now let the two waves be identical, i.e. $A = A_j = A_k$ and $\omega = \omega_1 = \omega_2$, we get

$$\begin{aligned}P^{(2)} &= \frac{1}{2}\varepsilon_0\chi^{(2)}_{ijk}A^2(t)\Big[1+\frac{1}{2}exp(-i2\omega_1 t)+c.c.\Big] \\ &= P^{(2)}_{\Delta}(0)+P^{(2)}_{\Sigma}(2\omega). \quad (3.6)\end{aligned}$$

We now have two terms which both depend on the electric field. $P_{\Delta}^{(2)}(0)$ is independent of the carrier frequency and describes the effect called *optical rectification*. The term $P_{\Sigma}^{(2)}(2\omega)$ is oscillating with the double of the carrier frequency and describes the effect *second harmonic generation (SHG)*.

If the electromagnetic wave is time-dependent, e.g. light from a pulsed laser, the term $P_{\Delta}^{(2)}(0)$ will also be time dependent. As previously described a time-varying polarization will lead to electromagnetic radiation and this property is used to generate THz radiation in crystals.

$\langle 110 \rangle$-oriented ZnTe is often used as the nonlinear medium. This kind of crystal has a cubic structure with point group $\bar{4}3m$ and has only one independent non-vanishing second-order nonlinear optical coefficient [33, 34]. At 800 nm it has a large nonlinear coefficient and there is a good phase matching between the optical pulse and the THz pulse [35].

3.3 Electrooptic detection

The electrooptic effect, or Pockels effect, is like optical rectification a second order nonlinear optical process. A low frequency or dc electric field applied to the crystal will induce a birefringence in crystal. Propagating electromagnetic waves polarized along and perpendicular to the applied external field will then experience different refractive indices in the crystal depending on their polarization.

In THz spectroscopy the THz wave is used as the low frequency external field and the near infrared laser pulse is used as the probe beam. $\langle 110 \rangle$-oriented ZnTe, which is sketched in Fig. 3.4, is the most popular detection crystal since it has a high nonlinear coefficient, high transparency at optical and THz frequencies and the phase velocity of the THz field almost matches the group velocity of the optical probe pulse [17]. This means that the optical pulse will feel a constant electric field as it propagates in the crystal.

Figure 3.5 illustrates a typical setup of free space electrooptic sampling to measure field induced birefringence.

In the lower part of Fig. 3.5, the probe pulse polarization are shown as it propagates through the setup, with and without a THz field. Without a THz field there will not be induced any birefringence in the crystal. Thus, the optical field will still be linearly polarized after the crystal. A $\lambda/4$-plate transforms the linear polarized light to circular polarized light. The Wollaston prism will then split the two orthogonal polarization components which are measured by a balanced photo detector. If, on the other hand, a THz field is co-propagating with the optical pulse there will be induced a birefringence in the crystal. The linearly polarized light will now be slightly elliptically polarized. After the $\lambda/4$-plate the polarization evolves into almost circular, but still elliptical polarization, which will lead to unequal signals measured by the detectors.

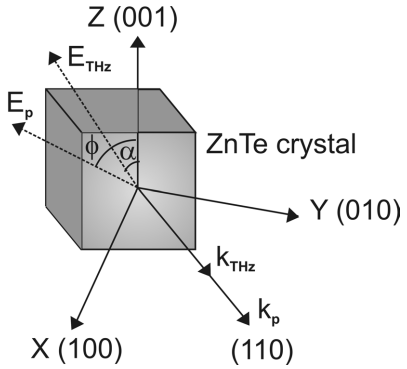

FIGURE 3.4: *The crystal axis of a ZnTe crystal and the angles of the THz and probe beam polarizations with respect to the crystal z axis. The propagation directions of the THz beam and the probe beam are denoted k_{THz} and k_p, respectively.*

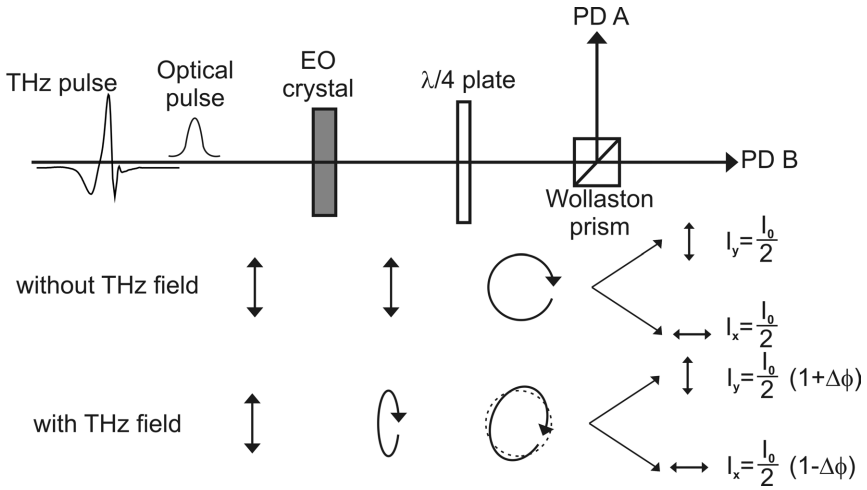

FIGURE 3.5: *Schematic diagram of a typical setup for electrooptic sampling. Probe polarizations with and without a THz field are shown in between the polarization optics. A Wollaston prism works as a polarizing beam splitter and two balanced photodiodes (PD A and PD B) detect the signal.*

The special case where the THz beam is polarized parallel to the crystal z-axis ($\alpha = 0°$ in Fig. 3.4) and optical beam is polarized at 45° with respect to the crystal z-axis is widely used as a detection scheme. In this case the differential phase retardation $\Delta\phi$ experienced by the optical probe beam will be [35, 36]

$$\Delta\phi = \frac{1}{2}\frac{\omega n_o^3 d_{14} L}{c} E_{THz},$$

where n_o is the refractive index at the optical frequency, d_{14} is the electrooptic coefficient (∼4pm/V for ZnTe), L is the thickness of the crystal and E_{THz} is

the electric field amplitude of the THz field. Thus, the measured difference signals of the balanced photodiodes will be proportional to the THz field amplitude. By controlling the arrival time of the THz pulse with respect to the probe pulse one can sample the temporal profile of the THz pulse.

The polarization angles can of course have arbitrary angles. For a more general discussion the reader is referred to Refs. [24, 36–38].

Chapter 4

Terahertz time-domain spectroscopy

Terahertz time-domain spectroscopy (THz-TDS) is a method to determine the optical properties, i.e. absorption coefficient and refractive index, of a sample. Since the breakthrough of this technique around 20 years ago where research groups led by Auston and Nuss at Bell Labs and Grischkowsky at IBM Watson Research Center demonstrated free space propagation of THz pulses [1, 2], the field has been growing rapidly resulting in more than 1,000 peer-reviewed journal publications in 2008 [39].

In this Chapter the basic concepts of THz-TDS will be discussed including how to obtain optical properties of a sample in different spectrometer configurations, such as transmission, reflection and attenuated total reflection measurements. Furthermore, a comparison between the different techniques will be carried out.

4.1 Basic concepts of THz time-domain spectroscopy

In Chapter 3 it was described how THz pulses can be generated and detected. Here we will discuss the basic principles of THz-TDS based on photoconductive generation and detection of THz pulses. In Fig. 4.1 a typical THz-TDS setup is shown and the principle is as follows: A pulse train consisting of femtosecond optical laser pulses with a typical duration of 100 fs and a wavelength of 800 nm is split into two parts by a beamsplitter. Each part is focussed on a photoconductive switch which generates and detects the THz pulse, respectively. One of the parts is led through a variable delay line in order to secure that the optical pulse at the detector arrives at the same time as the THz pulse and gates the detector. Changes in the delay line allows

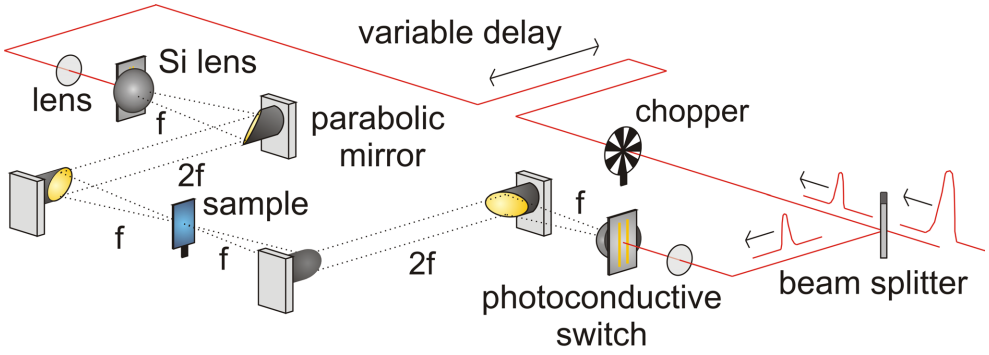

Figure 4.1: *Typical THz-TDS setup - here shown in a transmission configuration with photoconductive antennas. A detailed description is given in the text.*

the THz pulse to be mapped as a function of time. The photocurrent in the detector is measured with a lock-in amplifier to ensure a good signal-to-noise ratio. For this purpose, either the optical beam (as shown in Fig. 4.1) or the THz beam is modulated with a known frequency. The emitted THz beam is collimated with a high resistivity hyper-hemispherical Si lens, guided via four off-axial paraboloidal mirrors with focal length f through the sample in a $f-2f-2f-2f-f$ configuration and focussed onto the detector with another Si lens. This geometry ensures a 1:1 image of the emitter on the sample and again a 1:1 image of the sample on the detector. Even though the Si lens collimates the beam, it will diverge since the beam spot size is comparable to the wavelength. The first (and last) mirror will therefore collimate the beam whereas the second mirror will focus the beam onto the sample. The modulation of the beam and the gating of the detector both lead to effective reduction of the noise which makes this method immune to the ambient black body radiation which are quite dominant in the THz regime [24].

An example on the detected time dependent electric field $E(t)$ propagating in lab air and nitrogen purged environment, respectively, is shown in Fig. 4.2.

The oscillations on the trailing edge of the measurement of the temporal pulse of lab air are actually not noise but free induction decay of pure rotational transitions in H_2O molecules of the water vapor in atmospheric air [40]. The THz beam path is therefore usually kept in a N_2 or dry air atmosphere.

The obtained time dependent electric field $E(t)$ can now be *Fourier transformed* according to

$$E(\omega) = \frac{1}{2\pi}\int_{-\infty}^{\infty} E(t)e^{-i\omega t}d\tau, \tag{4.1}$$

where $E(\omega)$ is the frequency dependent electric field. The amplitude of the Fourier transformation of the time dependent electric field $E(t)$ shown in Fig.

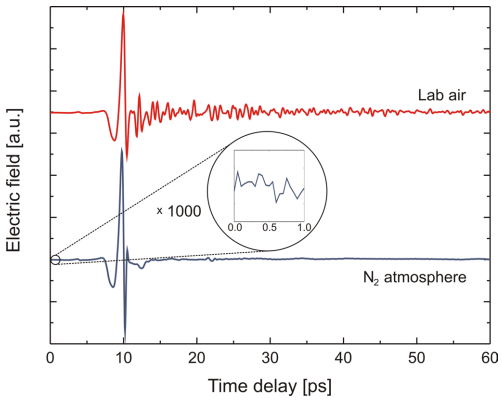

FIGURE 4.2: *Temporal shape of THz pulses propagating in lab air (red) and in nitrogen purged atmosphere (blue), respectively (horizontally offset for clarity). Each pulse is an average of 10 scans recorded with 50 fs steps and an integration time of 50 ms. The inset shows a × 1000 magnification of the noise level.*

4.2 are shown in Fig. 4.3. The water vapor absorption is now clearly seen as distinct lines in the spectrum.

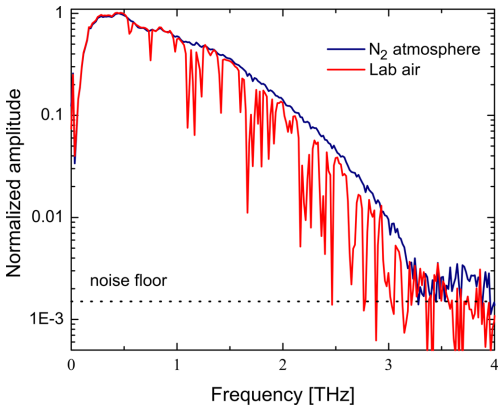

FIGURE 4.3: *Spectra of the THz pulses in Fig. 4.2. The absorption lines from water vapor is clearly seen as dips in the spectrum of. The maximum dynamic range is ∼800 and the maximum detectable frequency is ∼3.2 THz.*

The fact, that it is the electric field and not the intensity that is measured, is one of the greatest advantages of THz-TDS compared to other optical spectroscopic techniques. In this way the amplitude and phase of the field is provided directly without the need of the *Kramers-Kronig* relation which describes the mathematical relation between the real and imaginary part of a complex function [33].

One should keep in mind that even though the measurements are made in the time domain, THz-TDS does not provide any *time-resolved* dynamical in-

formation. However, THz time-resolved spectroscopy (TRTS), which is closely related to THz-TDS, deals with this issue (see for example Refs. [41, 42]).

4.2 Transmission THz spectroscopy

The most common use of THz time-domain spectroscopy is to measure the transmitted field through a sample of known thickness as illustrated in Fig. 4.4.

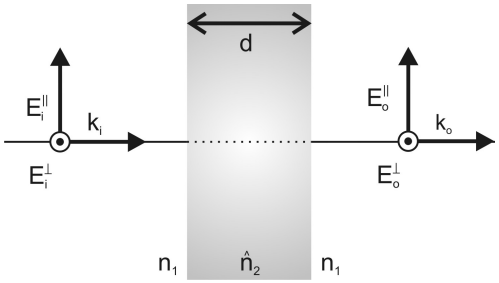

Figure 4.4: *Transmission through a sample with thickness d and complex refractive index $\hat{n}_2$.*

To extract the complex refractive index of this sample a reference measurement without sample is conducted first. The measured frequency dependent reference pulse $E_{ref}(\omega)$ can then be expressed as

$$\begin{aligned}\begin{pmatrix} E^{\parallel}_{ref}(\omega) \\ E^{\perp}_{ref}(\omega) \end{pmatrix} &= \begin{pmatrix} E^{\parallel}_{i}(\omega) \\ E^{\perp}_{i}(\omega) \end{pmatrix} \cdot e^{-\alpha_{air} d/2} \cdot e^{-i\omega n_{air} d/c} \\ &= \begin{pmatrix} E^{\parallel}_{i}(\omega) \\ E^{\perp}_{i}(\omega) \end{pmatrix} \cdot e^{-i\omega d/c}, \end{aligned} \tag{4.2}$$

where $E_i(\omega)$ is the incident THz pulse generated by the source, n_{air} is the refractive index of air which is assumed to be unity and α_{air} is the absorption coefficient of air which is assumed to be zero.

After the sample is placed into the spectrometer, the measured transmitted pulse $E_{sam}(\omega)$ is then

$$\begin{pmatrix} E^{\parallel}_{sam}(\omega) \\ E^{\perp}_{sam}(\omega) \end{pmatrix} = \begin{pmatrix} E^{\parallel}_{i}(\omega) \cdot t^{\parallel}_{12} \cdot t^{\parallel}_{21} \\ E^{\perp}_{i}(\omega) \cdot t^{\perp}_{12} \cdot t^{\perp}_{21} \end{pmatrix} \cdot e^{-\alpha_{sam}(\omega) d/2} \cdot e^{-i\omega n_{sam}(\omega) d/c}, \tag{4.3}$$

where $n_{sam}(\omega)$ and $\alpha_{sam}(\omega)$ is the refractive index of the sample and the absorption coefficient, respectively, and multiple reflections are neglected. In the following it is assumed for simplicity reasons that the incoming field is parallel ($\parallel$) polarized. Since the incident electric field E_i is unknown but

present in both Eq. 4.2 and Eq. 4.3 it can be eliminated by taking the ratio (for simplicity $n = n_{sam}$ and $\alpha = \alpha_{sam}$)

$$\begin{aligned} \frac{E_{sam}(\omega)}{E_{ref}(\omega)} &= \frac{E_i(\omega) \cdot t_{12} \cdot t_{21} \cdot e^{-\alpha(\omega)d/2} \cdot e^{-i\omega n(\omega)d/c}}{E_i(\omega) \cdot e^{-i\omega d/c}} \\ &= t_{12} \cdot t_{21} \cdot e^{-\alpha(\omega)d/2} \cdot e^{-i\omega[n(\omega)-1]d/c}. \end{aligned} \tag{4.4}$$

In the case of normal incidence ($\theta_i = 90°$) Eq. 4.4 simplifies to

$$\frac{E_{sam}(\omega)}{E_{ref}(\omega)} = \frac{4\hat{n}(\omega)}{[1+\hat{n}(\omega)]^2} \cdot e^{-\alpha(\omega)d/2} \cdot e^{-i\omega[n(\omega)-1]d/c} \equiv A(\omega) \cdot e^{-i\phi(\omega)}. \tag{4.5}$$

The ratio between $E_{sam}(\omega)$ and $E_{ref}(\omega)$ can be regarded as a complex number with the amplitude $A(\omega)$ and phase $\phi(\omega)$. The refractive index and absorption coefficient can be extracted simply by looking at the real and imaginary part of Eq. 4.5.

When the sample thickness is comparable or larger than the wavelength (1 THz = 300 μm), the refractive index of the sample can be extracted simply by looking at the phase difference between the reference and the sample pulse. In this case the phase shift originating from the Fresnel coefficients is much smaller than the phase shift originating from the sample propagation,

$$n(\omega) \simeq 1 + \frac{c}{\omega d}\phi(\omega). \tag{4.6}$$

Once the refractive index is known the absorption coefficient of the sample can be found from the amplitude of Eq. 4.5

$$\alpha(\omega) \simeq -\frac{2}{d} \cdot \ln\left\{A(\omega)\frac{[1+n(\omega)]^2}{4n(\omega)}\right\}. \tag{4.7}$$

In the case that the sample is a gas or a liquid it is necessary to use a sample cell to confine the sample which implies that sample windows are introduced in the beam path. This will complicate the analysis of the sample since two more interfaces are introduced as depicted in Fig. 4.5.

The measured reference and sample pulse will now be

$$E_{ref}(\omega) = E_i(\omega)(t_{13}t_{31})^2 \cdot e^{-\alpha_{win}(\omega)D} \cdot e^{-i\omega 2Dn_{win}(\omega)/c} \cdot e^{-i\omega d/c}, \tag{4.8}$$

$$\begin{aligned} E_{sam}(\omega) &= E_i(\omega)t_{13}t_{32}t_{23}t_{31} \cdot e^{-\alpha_{win}(\omega)D} \cdot e^{-\alpha(\omega)d/2} \\ &\quad \cdot e^{-i\omega 2Dn_{win}(\omega)/c} \cdot e^{-i\omega n(\omega)d/c}, \end{aligned} \tag{4.9}$$

where $\alpha_{win}(\omega)$ and $n_{win}(\omega)$ are the absorption coefficient and the refractive index of the sample cell windows, respectively and $2D$ is the total window

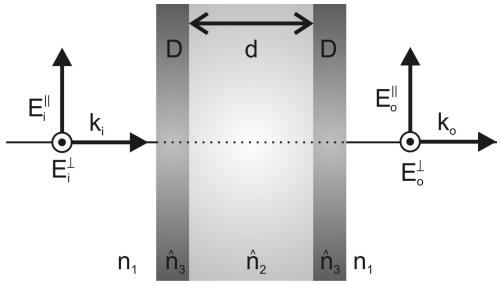

Figure 4.5: *Transmission through a sample in a cell with sample thickness d and complex refractive index $\hat{n}_2$ and sample cell thickness $2D$ and complex refractive index $\hat{n}_3$.*

thickness. Again, the ratio between the reference and sample pulse at normal incidence can be found to

$$\frac{E_{sam}(\omega)}{E_{ref}(\omega)} = \frac{\hat{n}(\omega)[1+\hat{n}_{win}(\omega)]^2}{[\hat{n}(\omega)+\hat{n}_{win}(\omega)]^2} \cdot e^{-\alpha(\omega)d/2} \cdot e^{-i\omega[n(\omega)-1]d/c}. \tag{4.10}$$

It can be seen from Eq. 4.10 that to find the optical properties of the sample the optical properties of the cell windows have to be known. The step from here is again to look at the amplitude and phase of the ratio between the two pulses to obtain the optical properties of the sample. By inspection of Eq. 4.10 it can be seen that if $\hat{n}_{win}(\omega) = 1$ Eq. 4.10 equals Eq. 4.5 as expected. It should also be noted that results of Eq. 4.10 and Eq. 4.5 also are realized with perpendicular polarized fields at normal incidence.

The most common used window materials are materials which are dispersionless and negligible absorbing in the spectral range under investigation. Therefore, crystalline high-resistivity silicon [32] and high density polyethylene [43] are often used.

Variable cell length measurements

A commonly used variant of standard transmission THz-TDS is so-called *variable cell length measurements* which is illustrated in Fig. 4.6.

The principle here is simply that instead of taking a reference measurement one measures two sample measurements with different sample thicknesses and analyzes the ratio between them:

$$\frac{E_{sam,1}(\omega)}{E_{sam,2}(\omega)} = e^{-\alpha(\omega)[d_1-d_2]/2} \cdot e^{-i\omega[n(\omega)-1][d_1-d_2]/c}, \tag{4.11}$$

where $E_{sam,1}(\omega)$ and $E_{sam,2}(\omega)$ are the measured electric fields at normal incidence with sample thickness d_1 and d_2, respectively. The advantage of this setup is that the ratio of the measured electric fields is independent of the window material.

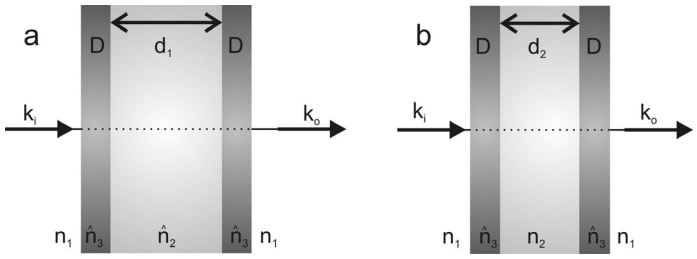

FIGURE 4.6: *Variable cell length measurement. Transmission through a sample with thickness (a) d_1 and (b) d_2.*

A special case of the variable cell measurement will be to put the windows together in one of the measurements ($d_2 = 0$). In this case Eq. 4.11 is not valid since all the transmissions coefficients do not cancel out. Instead the ratio $E_{sam,1}(\omega)/E_{sam,2}(\omega)$ can in the case of normal incidence be found to

$$\left.\frac{E_{sam,1}(\omega)}{E_{sam,2}(\omega)}\right|_{d_2=0} = \frac{4\hat{n}(\omega)\hat{n}_{win}(\omega)}{[\hat{n}_{win}(\omega)+\hat{n}(\omega)]^2} \cdot e^{-\alpha(\omega)d_1/2} \cdot e^{-i\omega[n(\omega)-1]d_1/c}. \quad (4.12)$$

Here the refractive index of the window material has to be known but on the other hand this measurement only has uncertainty on one sample length.

An example of a variable cell transmission measurement with $d_2 = 0$ and the belonging data analysis on 5 mm heptane ($CH_3(CH_2)_5CH_3$, anhydrous, 99%, Sigma Aldrich) is shown in Fig. 4.7.

The time shift of the sample pulse is due to the fact that heptane is a more dense medium than air. The higher refractive index of the sample, the more will the pulse be delayed with respect to the reference pulse. The attenuation of the sample pulse is due to two factors: Reflection losses from the two additional interfaces, in this case $\sim 20\%$, and losses because of absorption in the sample.

Secondary peaks originating from multiple reflections will be measured at multiples of times of t after the main pulse at time t_0 if the given conditions are fulfilled

$$\frac{2nd}{c} < (t - t_0) \quad \text{and} \quad \alpha d < DR, \quad (4.13)$$

where DR is the dynamic range of the spectrometer.

If the chosen time window used in the analysis is less than t, secondary peaks due to multiple reflections will disrupt the analysis since they will show up as oscillations in the frequency spectrum. One way to get rid of these oscillations is simply to truncate the time signal before the secondary pulses. This will however give the possibility of losing information about the sample

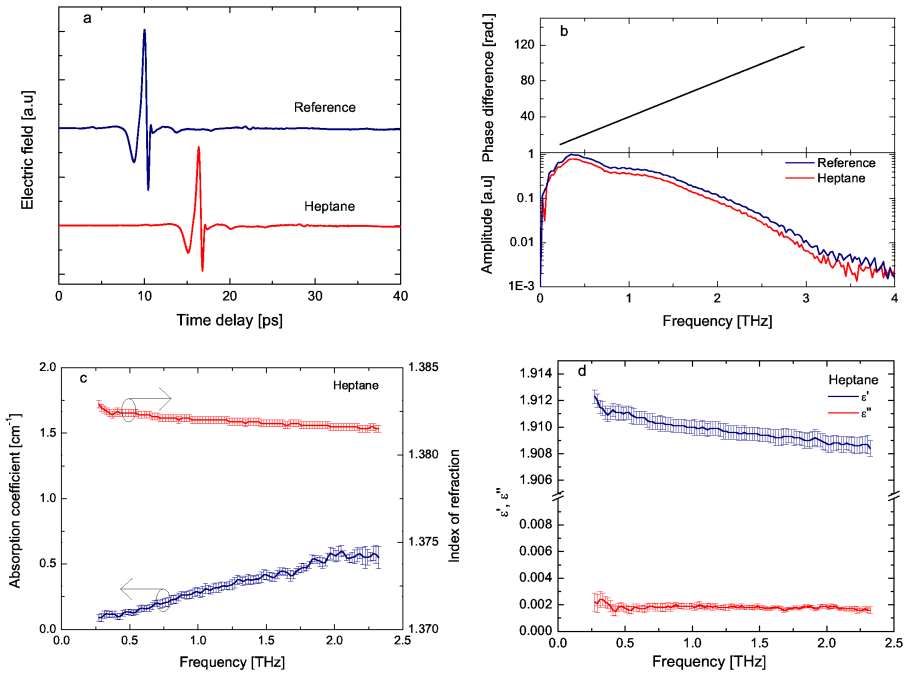

Figure 4.7: *Transmission THz-TDS on heptane. (a) Temporal pulses of reference scan (blue) and scan through 5 mm of heptane (red) (horizontally offset for clarity), (b) phase difference and frequency spectrum and the calculated (c) complex refractive index and (d) dielectric function. The error bars indicate the standard deviation of 5 consecutive scans.*

and also decrease the frequency resolution. Another way is to numerically remove the secondary reflection peaks either in the time domain or in the frequency domain [44–48].

4.3 Reflection THz spectroscopy

Since the calculation of the optical properties relies on the Fresnel equations which are given in Eq. 2.10-2.13 an analysis based on the reflection coefficients will yield the equivalent information about the optical properties of the sample. Transmission THz-TDS is undoubtedly easiest to implement but in cases of e.g. high absorptive samples where the sample thickness limits the dynamic range, reflection THz-TDS is useful. This method has previously been used to investigate the temperature dependency of the dielectric properties of liquid water [49, 50]. In fact, water is an excellent example on a sample where reflection THz-TDS is preferred over transmission THz-TDS since water is highly absorptive in the THz range, $\alpha_{H_2O}(1\text{ THz}) = 225\text{ cm}^{-1}$ at 19°C [49]. The reflection geometry can be realized in several ways [49, 51, 52]. This section will give a detailed description of the THz reflection spectroscopy setup

depicted in Fig. 4.8.

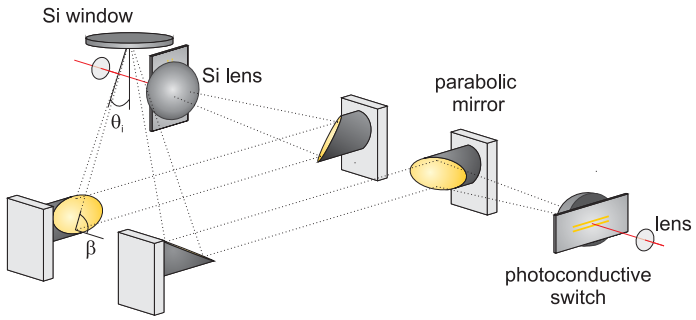

FIGURE 4.8: *Reflection THz-TDS setup based on photoconductive antennas. The sample window (Si window) is elevated from the main plane of the spectrometer by rotation of the mirrors before and after the sample.*

As seen in Fig. 4.8 the THz beam is reflected out of the main plain of the spectrometer by an angle of β to the sample window with an angle of incidence of θ. Because of these out-of-plane reflections the polarization will be rotated. The polarization change is easiest calculated by use of the Jones formalism in which the reflected electric field can be expressed in terms of the Fresnel reflection coefficients as

$$\begin{pmatrix} E_r^{\parallel} \\ E_r^{\perp} \end{pmatrix} = \begin{pmatrix} -r^{\parallel} & 0 \\ 0 & r^{\perp} \end{pmatrix} \cdot \begin{pmatrix} E_i^{\parallel} \\ E_i^{\perp} \end{pmatrix}, \tag{4.14}$$

where the sign difference of the reflection coefficients describes the difference in the geometrical mirroring of the electric fields illustrated in Fig. 2.1. Most metals are good mirrors in the THz range and thus are the reflections coefficients $r^{\parallel} \simeq 1$ and $r^{\perp} \simeq 1$. An out-of-plane reflection will also change the plane of incidence. The transformation to a new coordinate system from the previous incidence plane is described by the rotation matrix

$$M(\beta) = \begin{pmatrix} \cos\beta & \sin\beta \\ -\sin\beta & \cos\beta \end{pmatrix}, \tag{4.15}$$

where β is the rotation angle between the two planes. Based on Eq. 4.14-4.15 it is possible to calculate the evolution of the polarization through the spectrometer which is illustated in Fig. 4.9.

Thus by knowing the polarization angle α (with respect to the x-axis) and the polarization of the incident THz field in the incidence plane of the sample window, the polarization state at the THz detector can be determined.

A detailed view of the reflection geometry at the sample window is shown in Fig. 4.10.

The general idea is that some of the electric field is reflected from the lower interface and used as a reference. The transmitted part from the lower

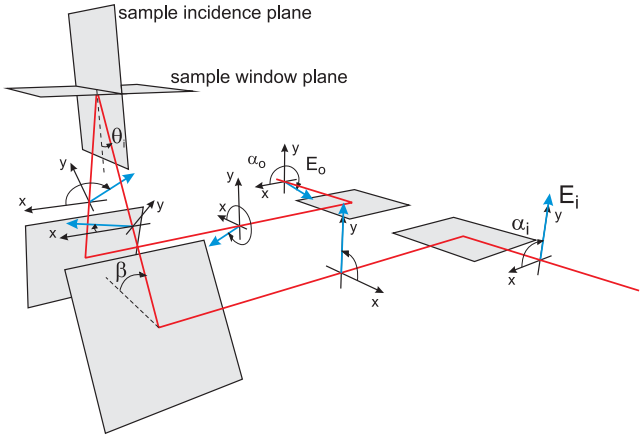

Figure 4.9: *Beam path of the reflection spectrometer. The gray rectangles indicate the incidence planes of the four off-axis paraboloidal mirrors. The vectors shown in blue color illustrate the polarization of an initially vertically polarized THz field through the spectrometer.*

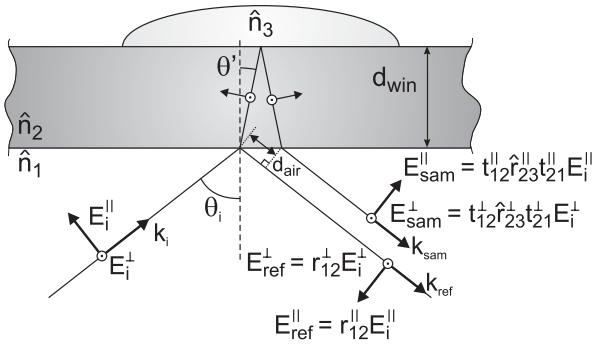

Figure 4.10: *Detailed view of the reflection geometry at the window which splits the input THz signal into a reference part and a sample part. The sample is placed on top of the window.*

interface will then propagate to the upper interface where some of it is reflected. This reflected portion propagates back to the lower interface and the transmitted part will hereafter propagate to the detector. In order to perform the analysis, the optical properties of the ambient environment ($\hat{n}_1$) and the window ($\hat{n}_2$), respectively, along with the thickness of the window have to be known. As in transmission THz-TDS, the ambient environment is typically dry air or nitrogen for which $\hat{n}_1 = n_1 = 1$. Most of the reflection experiments presented in this thesis have been performed on high-resistivity silicon which has a refractive index of 3.4175 and negligible absorption at room temperature in the spectral range relevant here [53]. In the analysis, the knowledge of the optical properties of the window is not only used to extract the Fresnel

coefficients, but also applied to compensate for the spatial walk-off of the sample pulse with respect to the reference pulse as illustrated in Fig. 4.10. This sample pulse walk-off will result in a different coupling to the detector antenna. To numerically compensate for this, a calibration amplitude A_{cal} and phase ϕ_{cal} is introduced in the expression for the electric field of the sample pulse. The electric fields at the detector originating from the reflection from the lower interface E_{ref} and from the upper interface E_{sam}, respectively, can be expressed as

$$\begin{pmatrix} E^x_{ref}(\omega) \\ E^y_{ref}(\omega) \end{pmatrix} = \frac{1}{2}\begin{pmatrix} E^x_i \\ E^y_i \end{pmatrix}\begin{pmatrix} (\hat{r}^{\parallel}_{12} - \hat{r}^{\perp}_{12})\cos\alpha - (\hat{r}^{\parallel}_{12} + \hat{r}^{\perp}_{12})\cos(\alpha - 2\beta) \\ (\hat{r}^{\parallel}_{12} - \hat{r}^{\perp}_{12})\sin\alpha + (\hat{r}^{\parallel}_{12} + \hat{r}^{\perp}_{12})\sin(\alpha - 2\beta) \end{pmatrix}, \quad (4.16)$$

$$\begin{pmatrix} E^x_{sam}(\omega) \\ E^y_{sam}(\omega) \end{pmatrix} = \frac{1}{2}\begin{pmatrix} E^x_i \\ E^y_i \end{pmatrix} A_{cal}\cdot e^{-i\phi_{cal}}\cdot e^{-\alpha_2(\omega)d_2}\cdot e^{-2in_2(\omega)\omega d_{eff}/c}$$
$$\cdot\begin{pmatrix} (\hat{r}^{\parallel}_{23}\hat{t}^{\parallel}_{12}\hat{t}^{\parallel}_{21} - \hat{r}^{\perp}_{23}\hat{t}^{\perp}_{12}\hat{t}^{\perp}_{21})\cos\alpha - (\hat{r}^{\parallel}_{23}\hat{t}^{\parallel}_{12}\hat{t}^{\parallel}_{21} + \hat{r}^{\perp}_{23}\hat{t}^{\perp}_{12}\hat{t}^{\perp}_{21})\cos(\alpha - 2\beta) \\ (\hat{r}^{\parallel}_{23}\hat{t}^{\parallel}_{12}\hat{t}^{\parallel}_{21} - \hat{r}^{\perp}_{23}\hat{t}^{\perp}_{12}\hat{t}^{\perp}_{21})\sin\alpha + (\hat{r}^{\parallel}_{23}\hat{t}^{\parallel}_{12}\hat{t}^{\parallel}_{21} + \hat{r}^{\perp}_{23}\hat{t}^{\perp}_{12}\hat{t}^{\perp}_{21})\sin(\alpha - 2\beta) \end{pmatrix}, \quad (4.17)$$

where d_2 is the path length in the window material. The effective propagation thickness d_{eff} through the window can be found by considering the optical path difference between the reference beam and the sample beam

$$\begin{aligned} OP = \frac{2n_2 d_{win}}{\cos\theta'} - d_{air} &= \frac{2n_2 d_{win}}{\cos\theta'} - 2d_{win}\sin\theta\tan\theta' \\ &= 2n_2 d_{win}\left(1 - \frac{\sin^2\theta}{n_2^2}\right)^{1/2}. \end{aligned} \quad (4.18)$$

Hence we can define

$$d_{eff} \equiv d_{win}\left(1 - \frac{\sin^2\phi}{n_2^2}\right)^{1/2}. \quad (4.19)$$

Assuming that the polarization angle $\alpha = 90°$ (horizontal striplines on emitter), the out-of-plane angle $\beta = 60°$, the angle of incidence $\theta_i = 30°$, the ambient environment is dry air or nitrogen and the window material is silicon, the ratio of the x-components of the electric fields at the detector (vertical striplines on detector) can be expressed as:

$$\frac{E^x_{sam}(\omega)}{E^x_{ref}(\omega)} = A_{cal}\cdot e^{-i\phi_{cal}}\cdot e^{-2in_2(\omega)\omega d_{eff}/c}\cdot\frac{\hat{r}^{\parallel}_{23}t^{\parallel}_{12}t^{\parallel}_{21} + \hat{r}^{\perp}_{23}t^{\perp}_{12}t^{\perp}_{21}}{r^{\parallel}_{12} + r^{\perp}_{12}}. \quad (4.20)$$

The only unknown parameters on the right-hand side of Eq. 4.20 prior to any measurements are the calibration amplitude A_{cal}, the calibration phase ϕ_{cal} and the Fresnel reflection coefficients containing information about the sample

($\hat{r}_{23}^{\parallel}$ and $\hat{r}_{23}^{\perp}$). In order to determine the calibration terms a measurement with air as the sample is performed and the calibration terms are then

$$A_{cal} \cdot e^{-i\phi_{cal}} = \frac{E_{sam}^{x}(\omega)}{E_{ref}^{x}(\omega)} e^{2in_2(\omega)\omega d_{eff}/c} \cdot \frac{r_{12}^{\parallel} + r_{12}^{\perp}}{r_{23,air}^{\parallel} t_{12}^{\parallel} t_{21}^{\parallel} + r_{23,air}^{\perp} t_{12}^{\perp} t_{21}^{\perp}}. \quad (4.21)$$

The result of Eq. 4.21 are then reinserted in Eq. 4.20 in order to find the optical properties of the sample. The general expressions of Fresnel reflection coefficients in Eq. 2.14 and Eq. 2.16 can be expressed in terms of the incidence angle of the window

$$\hat{r}_{23}^{\perp} = \frac{n_2\sqrt{1-\sin^2\theta_i/n_2^2} - \hat{n}_3\sqrt{1-\sin^2\theta_i/\hat{n}_3^2}}{n_2\sqrt{1-\sin^2\theta_i/n_2^2} + \hat{n}_3\sqrt{1-\sin^2\theta_i}/\hat{n}_3^2}, \quad (4.22)$$

$$\hat{r}_{23}^{\parallel} = \frac{\hat{n}_3\sqrt{1-\sin^2\theta_i/n_2^2} - n_2\sqrt{1-\sin^2\theta_i/\hat{n}_3^2}}{\hat{n}_3\sqrt{1-\sin^2\theta_i/n_2^2} + n_2\sqrt{1-\sin^2\theta_i/\hat{n}_3^2}}. \quad (4.23)$$

The complex refractive index $\hat{n}_3$ can now be found by solving Eq. 4.20 with respect to $\hat{n}_3$. The complexity of the analysis arises from the presence of both parallel and perpendicular polarized light. For a given rotation angle β, pure parallel or perpendicular polarization at the sample can be obtained by rotating the polarization angle α. If this is done the complex refractive index of the sample can be expressed in a closed form [52]. Some typical reflection measurements of air (calibration) and liquid water at room temperature are shown in Fig. 4.11.

In the case of the calibration measurement, the sample pulse is attenuated due to reflection losses and phase shifted by π because of internal reflection ($n_t < n_i$) whereas the reference reflection is an external reflection ($n_t > n_i$). The first reflection from the air-silicon interface is independent on the sample and thus it can be used as a reference. Once the calibration amplitude and phase have been found the sample measurements are *self-referenced* in the sense that the first part of the scan is used as the reference pulse and the remaining part is used as the sample pulse in the analysis [52]. In the shown example the silicon slab has a thickness of 2.00 mm which implies that the sample pulse is 46 ps delayed with respect to the reference pulse.

In Figs. 4.12a-d the Fourier transformation of the water measurement is shown along with the calculated optical and dielectric properties of liquid water.

By comparing Fig. 4.12 and Fig. 4.7 it is clear that water and heptane are two very different liquids. Water is a more dispersive material than heptane and at 1 THz water absorbs ~ 1000 times more than heptane.

To obtain an accurate sample characterization it is important that the reference and sample pulse are separated enough in time such that the reference

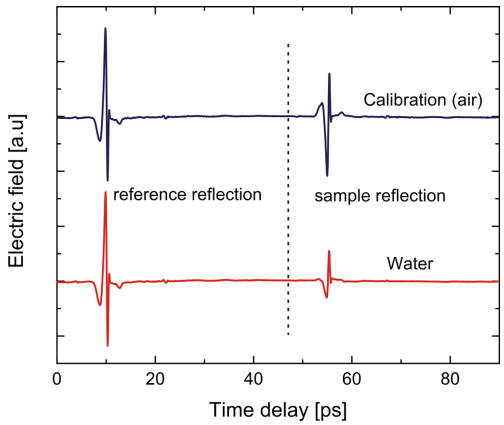

FIGURE 4.11: *Temporal shape of THz pulses in reflection geometry. The first reflections are from the air-silicon interface and the second reflections are from the silicon sample interface, in this case air (blue) and water (red) (horizontally offset for clarity). Each pulse is an average of 10 scans recorded with 50 fs steps and an integration time of 50 ms. The dotted line indicates where the reference and sample pulses are separated.*

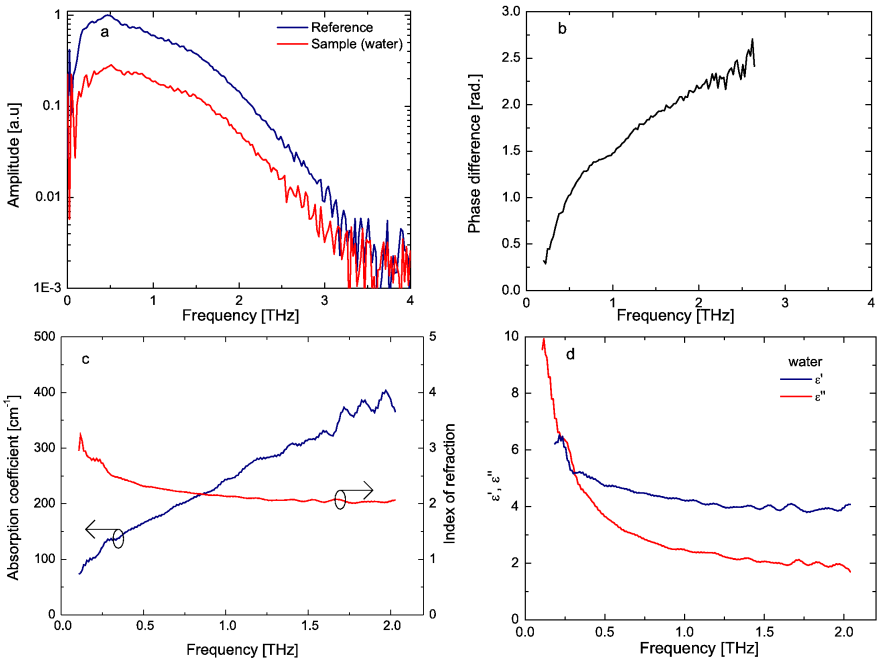

FIGURE 4.12: *(a) Frequency spectrum , (b) phase difference of reflection measurement on water (red curve in Fig. 4.11) and the calculated (c) complex refractive index and (d) dielectric function.*

pulse does not interfere with the sample pulse. However, even if this is not

the case it is possible to extract valuable information about the sample [54]. Huang *et al.* have recently proposed a numerical method to deal with these interferences [55]. Their setup needed to be optically transparent and hence they used a thin quartz slab. They then used measurements on air and quartz as references in a numerical algorithm to compensate for the spectrometer artifacts.

4.4 Attenuated total reflection THz spectroscopy

Yet another way to measure the optical properties of a sample is attenuated total reflection (ATR) THz-TDS which is the most sensitive method to determine the optical properties of a strongly absorbing liquids [56, 57]. Keiding and Grischkowsky conducted some early THz total internal reflection measurements to determine the dispersion of quartz [58], but it took quite a few years before other research groups took up the technique to do spectroscopy. The method has previously been used to investigate surface plasmons in InAs [56], dielectric properties of liquid water [59, 60], hydration states of sucrose in water [61] and aqueous glycine in water [62] to mention a few. In this section it will be treated how to extract the optical properties of a sample placed on top a silicon Dove prism with the dimensions depicted in Fig. 4.13. If the incidence angle of the total internal reflected beam is defined as θ, the apex angle of the prism will be 2θ. Letting the incoming beam enter the center of the side of the prism with an incidence angle of θ and parallel to the top plane of the prism, geometrical considerations and Snell's law then gives $\sin\theta = \hat{n}_2 \sin(2\theta - \pi/2)$.

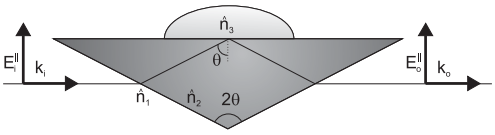

Figure 4.13: *Sketch of Dove prism for ATR THz-TDS with a sample placed on top of it.*

High-resistivity silicon has a refractive index of 3.4175 and negligible absorption at room temperature in the THz range [53]. With silicon as the prism material, the angle θ will be 51.6° [57].

The ATR geometry is simply realized by placing the prism in the focus of THz beam (where the sample is placed in Fig. 4.1). With the dimensions of the prism as described above, the direction of the outgoing beam will be identical to the incoming beam which makes it easy to change between transmission geometry and ATR geometry.

With a parallel polarized incoming beam the ratio between the electric fields originating from the sample and reference measurements, respectively,

gives

$$\frac{E^{\parallel}_{sam}(\omega)}{E^{\parallel}_{ref}(\omega)} = \frac{\hat{r}^{\parallel}_{23}}{r^{\parallel}_{21}}, \tag{4.24}$$

where the reflection coefficients $\hat{r}^{\parallel}_{23}$ and $r^{\parallel}_{21}$ are given by Eq. 2.16. When the refractive index of the sample $\hat{n}_3 \leq 2.68$ *total internal reflection* (TIR) will occur at the prism-sample interface. Since the term $[1-(n_2/\hat{n}_3)^2\sin^2\theta]^{1/2}$ in Eq. 2.16 will be purely imaginary for a non-absorbing sample when the condition of TIR is satisfied it will lead to the absolute value of the Fresnel reflection coefficient $|\hat{r}^{\parallel}_{23}| = 1$. All the energy in the incoming beam will in other words be transferred to the reflected beam and hence it is a perfect mirror. However, the Fresnel transmission coefficient $t \neq 0$ which means that there will be a field in the sample. This electric field carries no energy, propagates along the boundary and varies exponentially with the distance to the interface, i.e. it is an evanescent wave. For an absorbing sample, i.e. a sample with a complex refractive index, the absorption coefficient will contribute to the reflection coefficient. Hence, not all of the energy of the incoming beam will be transferred to the reflected beam since some of it is absorbed [63].

In Figs. 4.14a-d an example of ATR THz-TDS on water at room temperature is shown. The attenuation of the temporal pulse is clearly seen while the phase shift is easiest observed after the Fourier transform.

4.5 Comparison of transmission-, reflection- and ATR-methods

Since the analysis of measurements based on transmission, reflection and ATR relies on the Fresnel coefficients, they all give, in principle, the same information about the sample. However, the best suitable method depends on the sample under investigation. To illustrate this the ratio between the electric fields $E_{sam}(\omega)$ and $E_{ref}(\omega)$, which can be regarded as a complex number with the amplitude $A(\omega)$ and phase $\phi(\omega)$, is examined in a polar plot for different samples in the range $0.1-3$ THz [57]. The samples examined are water, a high absorbing material, and heptane, a low absorbing material. In this spectral range water can be described with a double Debye relaxation mode and a single intermolecular vibration mode (thoroughly described in Chapter 7). The measured optical properties of water can be seen in Fig. 4.14c. The modeled absorption coefficient $\tilde{\alpha}_{heptane}(\omega)$ and refractive index $\tilde{n}_{heptane}(\omega)$ of heptane can, based on linear fits of Fig. 4.7c, be approximated to

$$\tilde{\alpha}_{heptane}(\omega) = 0.2740\omega/2\pi, \tag{4.25}$$

$$\tilde{n}_{heptane}(\omega) = 1.3826 - 5.12\cdot 10^{-4}\omega/2\pi. \tag{4.26}$$

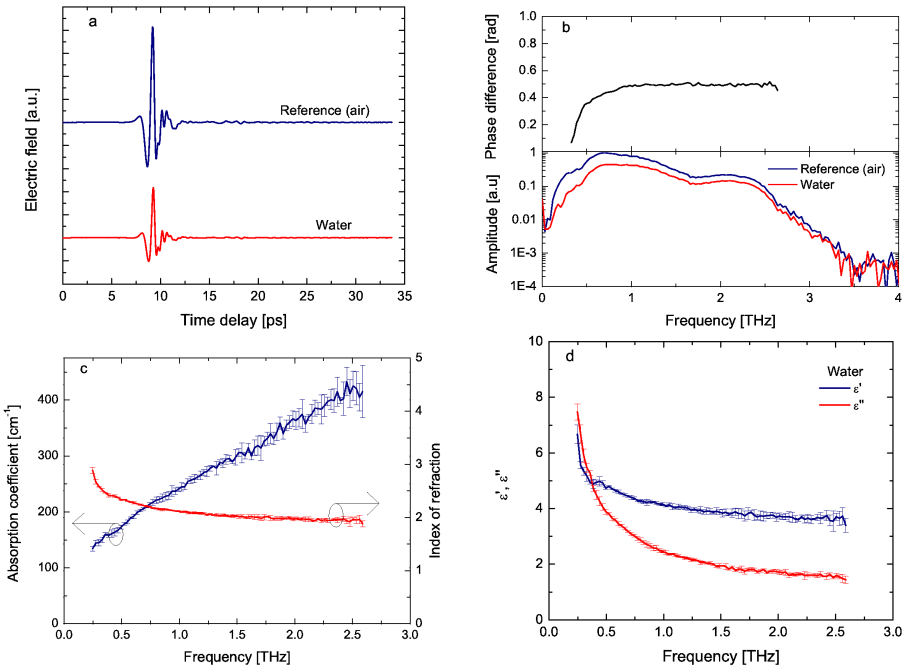

Figure 4.14: *ATR-THz-TDS on water. (a) Temporal pulses of reference scan (blue) and sample scan (red) (horizontally offset for clarity), (b) phase difference and frequency spectrum, and the calculated (c) complex refractive index and (d) dielectric function. The error bars indicate the standard deviation of 5 consecutive scans.*

The different measurement methods are described in Sections 4.2-4.4 and can briefly be outlined as:

- Transmission. Normal incidence on transmission cell with silicon windows (Fig. 4.5, Eq. 4.10).
- Reflection. Incidence angle of 30° on 2 mm silicon slab. The calibration amplitude $A_{cal} = 1$ and the calibration phase $\phi_{cal} = 0$ (Fig. 4.10, Eq. 4.20).
- Attenuated total reflection. Incidence angle of 51.6° on silicon Dove prism (Fig. 4.13, Eq. 4.24).

In transmission there will typically be a large phase difference between the reference field and the sample field because of the different optical path lengths. As seen in Eq. 4.10, $(n(\omega) - 1)d/c$ is the slope of the frequency dependent phase difference between the transmitted reference and sample fields. The refractive index $n(\omega)$ can be expressed in terms of a constant refractive index n_0, the background, and a frequency dependent additional refractive index $\Delta n(\omega)$,

$$n(\omega) - 1 = n_0 + \Delta n(\omega). \tag{4.27}$$

By subtracting n_0 the slope of the phase one now gets

$$\phi'(\omega) = \frac{\Delta n(\omega) d}{c}\omega. \tag{4.28}$$

In reflection, the phase originating from the propagation of the silicon slab in reflection mode can also be subtracted the total phase since it is independent on the sample.

The detector of the spectrometer will, regardless of the geometry used, limit the minimum and maximum detectable frequencies. It is therefore assumed that the $0.1 - 3$ THz frequency range is measurable for all three geometries.

Low absorbing materials

In Fig. 4.15 simulations of the real and imaginary part of the ratio $E_{sam}(\omega)$ $/E_{ref}(\omega)$ for heptane are shown in a polar plot. The thickness of the sample influence the transmitted field and four different thicknesses are therefore used to illustrate the transmission spectroscopy method.

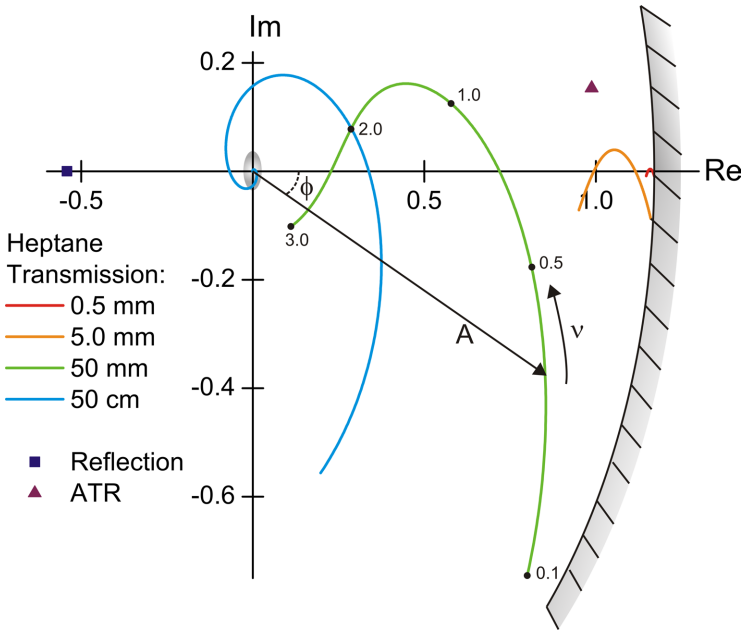

FIGURE 4.15: *Real and imaginary part of the ratio $E_{sam}(\omega)/E_{ref}(\omega)$ simulated for heptane in the 0.1-3 THz range for transmission on 4 different sample thicknesses, reflection and ATR. The vector with length A and angle ϕ illustrates one frequency component. The borderline to the right represents the maximum amplitude obtainable. The boundary of the inner circle represents the minimum measurable values which is dependent of the dynamic range of the spectrometer. The points on the green curve represent different frequency values.*

In order to obtain a good determination of the optical properties of the sample each frequency component, represented by $A \cdot exp[i\phi]$, should result in a new point in the polar coordinate system. In transmission geometry, the refractive index of samples with thicknesses comparable or larger than the wavelength, can be determined sorely from the phase difference between the sample pulse and the reference pulse. Thus, a phase change between two point vectors on a transmission curve in Fig. 4.15 means that there is a change in the refractive index. The amplitude will be dominated of the absorption of the sample. Thus, the more spread out these points are, the more sensitive the method is to measure the given sample. The borderline to the right of Fig. 4.15 represents the maximum amplitude obtainable and the boundary of the inner circle represents the minimum measurable values which is dependent of the dynamic range of the spectrometer, i.e. points within the circle cannot be resolved by the spectrometer. From the simulation of the transmission measurements it can also be seen that the thickness influence the measurement sensitivity. The example with a thin sample of 0.5 mm heptane shows almost no spreading. On the other hand, transmission through a very thick sample of 50 cm heptane leads to too much absorption which results in points in the origin of the polar plot. The optimal sample thickness is therefore to be found in between these two extremes. To put it another way, heptane is almost non-dispersive which means that we need a thick sample to resolve this. On the other hand, if the sample is too thick it will absorb some (in this case the highest) frequency components and the transmitted beam will therefore not contain information about these.

It is seen that ATR and reflection measurements on heptane are each represented by a point in the polar plot. In practice this means that it is impossible to frequency resolve the optical properties of heptane if it is measured ATR or reflection geometry.

High absorbing materials

Water is far more absorptive and dispersive compared to heptane. In Fig. 4.16 simulations of the real and imaginary part of the ratio $E_{sam}(\omega)/E_{ref}(\omega)$ for water are shown in a polar plot.

For both ATR and reflection measurements the frequency components are now spread out making a curve in the complex plane. Since the curve originating from the ATR simulation is longer than the curve origination from the reflection, ATR is in this case a more sensitive technique. In the case of transmission measurements the optimal sample thickness is again to be found in between the two shown extremes. Because of the high absorption of water a much thinner sample compared to that of heptane is now needed in order to use transmission geometry for measurements.

The low frequency components are more spread out than the high frequency components. This has nothing to do with the measurement technique

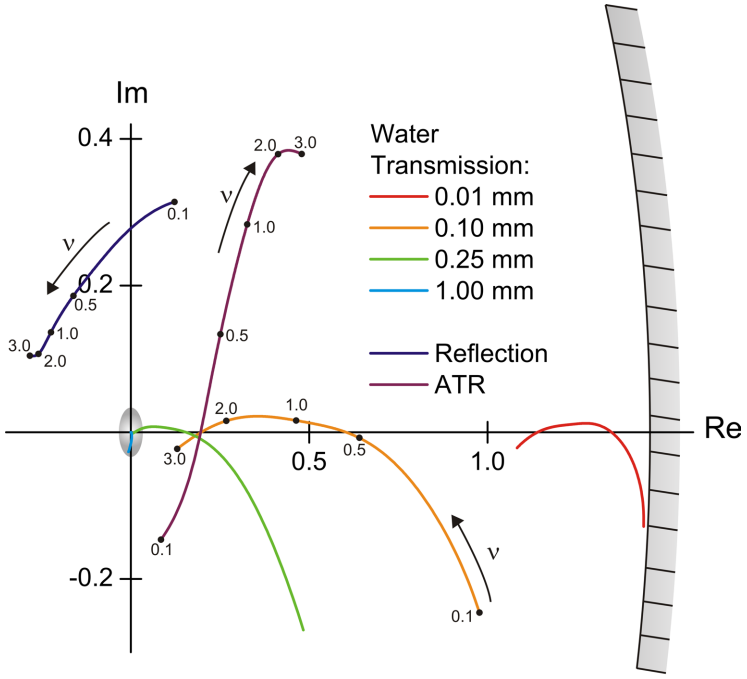

FIGURE 4.16: *Real and imaginary part of the ratio $E_{sam}(\omega)/E_{ref}(\omega)$ simulated for water in the 0.1-3 THz range for transmission on 4 different sample thicknesses, reflection and ATR. The borderline to the right represents the maximum amplitude obtainable. The inner circle represents the minimum measurable values which is dependent of the dynamic range of the spectrometer. The points on the curves represent different frequency values.*

but is simply due to the fact that the optical properties of water are changing more at low frequencies, e.g. see Fig. 4.14.

In the case of transmission, the absorption limits the maximum sample thickness where information about the full spectral range can be obtained. If the sample is thin etalon effects will occur in the recorded time dependent signal which will complicate the analysis and the relative uncertainly on the sample thickness will also increase. In the case of the thick 1 mm water sample it is seen in Fig 4.16 that the curve is within the circle, indicating that these measurements cannot be resolved by the spectrometer due to its dynamic range.

In the special case where a frequency component of the optical properties of the sample material is the same as the prism or slab material, e.g. if one wants to measure on Si, a discontinuity point in the vicinity of this frequency component will occur on the ATR curve or the reflection curve. This is due to the fact that all of the the incoming wave will be transmitted because it will not experience an interface between the sample and window material.

The ATR technique is superior to the reflection technique. However, re-

flection geometry is more suitable than ATR geometry in some applications, i.e. stand-off detection for security applications, inspection hazardous liquids in containers, and imaging.

The dynamic range of the spectrometer

The dynamic range (DR) in transmission and reflection THz-TDS has previously been investigated by Jepsen and Fisher [64]. They showed that in case of transmission THz-TDS, the DR and the sample thickness determine the maximum detectable absorption coefficient $\alpha_{max}(\omega)$ and thus the bandwidth of the system. For a transmission cell the maximum detectable absorption will be,

$$\alpha_{max}(\omega)d = 2\ln\left\{DR\frac{n(\omega)[1+n_{win}(\omega)]^2}{[n_{win}(\omega)+n(\omega)]^2}\right\}. \tag{4.29}$$

Since the sample thickness and the maximum detectable absorption are inversely proportional one can increase the sample thickness in order to be able to detect higher absorption. To do a back-of-the-envelope calculation suppose a THz setup with a dynamic range of $\sim 10^3$. At 2 THz the absorption coefficient of water is ~ 400 cm^{-1} and the refractive index is ~ 2. The maximum sample thickness will then be ~ 0.35 mm which means that etalon effects in the recorded time dependent signal will occur in intervals of ~ 2.3 ps after the main pulse for the reference measurement and in intervals of ~ 4.6 ps for the measurement on water.

In case of reflection and ATR, the largest absorption coefficient is measured in the vicinity of $A = 1$ and $\phi = 0$ the maximum detectable absorption will depend on the phase accuracy and amplitude accuracy. This limit will typically lie well above absorption coefficients that are normally encountered in dielectric and semiconductor materials [64].

Heterogenous samples

The difference between the transmission method, where a volume of a sample is probed, and the ATR/reflection methods, where the interface of a sample is probed, implies that the sample homogeneity is an important factor when determining the optical properties. The ATR and reflection methods will be more sensitive to phase separation in e.g. water-fat emulsions. If such an emulsion with time is separated into water and fat the fat will rise to the surface and thus away from the probed interface. This is illustrated in Fig. 4.17 where reflection measurements of cream (38 %, Arla Karolines Køkken®) are shown.

The same sample was measured again after time intervals of 5 minutes. It is clearly seen that the sample reflection changes with time whereas the

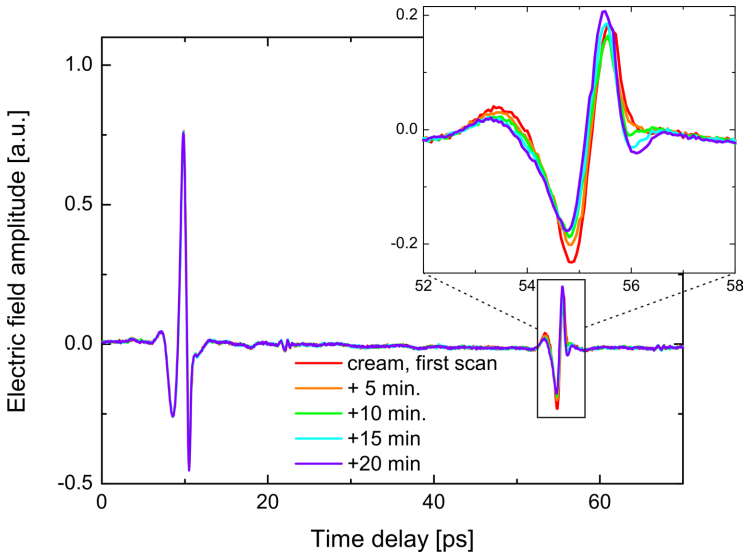

FIGURE 4.17: *Reflection measurements of cream. Each measurement is on the same sample but measured with time intervals of 5 minutes.*

reference reflections are identical. This means that the change can only be due to changes of the sample which is this case is believed to be phase separation.

Chapter 5

Liquid dynamics in the terahertz region

In this Chapter we will outline how one can describe (a) the dielectric relaxation of molecules by means of the *Debye model* and (b) intermolecular vibrations by means of the *Lorentz oscillator model*. We will first make some initial assumptions which are common for both models. After the description of the two models we move on to discuss the dielectric properties of a medium based on the properties and the relative fractions of its components, i.e. effective medium theory.

When an electric field is applied to a dielectric material the the dipoles in the material will align to the direction of the field. If the field is alternating at a given frequency the dipoles will strive to keep themselves aligned. This phenomena can be described by the polarization of a material P which is a measure of the dipole moments per unit volume. The slowest polarization mechanism is often that of dipolar reorientation and as the frequency of the alternating electric field is increased the dipoles will not be able to keep in alignment with the direction of the electric field. This will lead to a reduction of the permittivity, also know as dielectric relaxation. For large hindered macromolecules these dipole reorientations can happen below 1 Hz whereas for small molecules it can be as fast as several THz [65]. Atomic displacements, i.e. vibrations of bonds, can be into two groups: *inter*-molecular and *intra*-molecular vibrations. The latter describes vibrational modes within a molecule, e.g. a C-H-stretch mode, while the first describes vibrations between molecules, e.g. H-bond modes. The intermolecular modes will typically appear at lower resonance frequencies than the intramolecular modes simply because of the bigger masses involved. Electronic transitions happen at frequencies in the visible, ultraviolet or X-ray range. A summery of the different forms of polarization is shown in Fig. 5.1.

The THz spectroscopy range can therefore give valuable information about

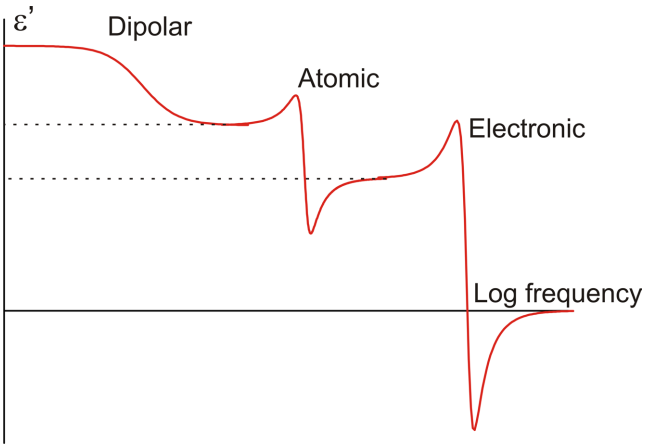

Figure 5.1: *Variation of real part of the dielectric function for simple dielectrics as a function of frequency. The different dynamics are described in the text.*

the fastest dipolar relaxation mechanisms based on the Debye model description as well as the intra- and intermolecular vibration modes based on the Lorentz oscillator model. However, the typical resonance frequencies of intramolecular bonds are in the infrared frequency region and can therefore not be probed by means of terahertz spectroscopy. Only resonance frequencies of intermolecular bonds between large groups of a molecule will fall into the terahertz frequency region. Intermolecular vibrations of the weakly bound molecular network, on the other hand, is often to be found in the terahertz frequency range . THz spectroscopy can also be used to probe phonon modes of crystalline samples [66].

The polarization P of the material is related to the electric field E in the following way,

$$P = \varepsilon_0(\hat{\varepsilon} - 1)E, \tag{5.1}$$

where ε_0 is the dielectric permittivity of free space and $\hat{\varepsilon}$ is the permittivity of the material relative to free space. P and E are normally expressed as vectors but in the following argument this is not needed. The time dependent polarization $P(t)$ has an instantaneous contribution P_1 an a time dependent contribution $P_2(t)$ [67]:

$$P(t) = P_1 + P_2(t). \tag{5.2}$$

The time dependent polarization $P_2(t)$ will increase from zero to a saturation value $P_2(\infty)$. Using the boundary conditions

- $\hat{\varepsilon} \to \varepsilon_\infty$ for $\omega \to \infty$ $(t = 0)$,
- $\hat{\varepsilon} \to \varepsilon_s$ for $\omega \to 0$ $(t \to \infty)$,

where ε_s is the static permittivity and ε_∞ is the permittivity in the high frequency limit. These boundary conditions give the static polarization and the polarization in the high frequency limit

$$P(0) = P_1 = \varepsilon_0(\varepsilon_\infty - 1)E, \tag{5.3}$$
$$P(\infty) = P_1 + P_2(\infty) = \varepsilon_0(\varepsilon_s - 1)E. \tag{5.4}$$

From Eqs. 5.3 and 5.4 it can be found that

$$P_2(\infty) = \varepsilon_0(\varepsilon_s - \varepsilon_\infty)E. \tag{5.5}$$

5.1 Lorentz oscillator model

One way to describe absorption and dispersion in a material is to assume the following: when propagating through the material, the electric field of an incident wave couple to the electric dipole moment of the material, represented by a set of damped harmonic oscillators. This model was first introduced by H. A. Lorentz (1853-1928) and is therefore also know as the *Lorentz oscillator model*.

The model assumes that the force binding two charges particles can be described by Hooke's law, i.e. it resembles a spring. The bound charges will oscillate around their equilibrium since the applied electric field forces the charges to move. A system like this can be modeled as a damped harmonic oscillator with resonant frequency ω_0 and damping coefficient γ. The equation of motion in the x direction for such a system is given by

$$\frac{d^2x}{dt^2} + \gamma\frac{dx}{dt} + \omega_0^2 x = \frac{q}{m}E(t), \tag{5.6}$$

where m is the (reduced) mass of charge q and $E(t)$ is the applied field. If the field is a monochromatic wave, $E(t) = E_0 exp[i\omega t]$, the solution of Eq. 5.6 is

$$x(t) = x_0 e^{i\omega t}, \qquad \text{where} \qquad x_0 = \frac{q}{m}\frac{E_0}{\omega_0^2 - \omega^2 + i\gamma\omega}. \tag{5.7}$$

With N dipoles per unit volume and the macroscopic electronic dipole moment expressed as $p(t) = q \cdot x(t)$, the contribution to the polarization will be

$$P(t) = Nqx(t) = \frac{q^2}{m}\frac{E_0 e^{i\omega t}}{\omega_0^2 - \omega^2 + i\gamma\omega} \equiv \varepsilon_0(\hat{\varepsilon} - 1)E_0 e^{i\omega t}. \tag{5.8}$$

Assuming that the total polarization consists of a static part and a time dependent part and following the definitions of Eqs. 5.3-5.5 the dielectric function can be expressed as

$$\hat{\varepsilon}(\omega) = \epsilon_\infty + \frac{A}{\omega_0^2 - \omega^2 + i\omega\gamma}, \qquad \text{where} \qquad A = \frac{Nq^2}{m\varepsilon_0\omega_0^2}. \tag{5.9}$$

The dielectric function in Eq. 5.11 can easily be split up into a real and imaginary part

$$\hat{\varepsilon}'(\omega) = \epsilon_\infty + \frac{A(\omega_0^2 - \omega^2)}{(\omega_0^2 - \omega^2)^2 + \gamma^2\omega^2}, \qquad \hat{\varepsilon}''(\omega) = \frac{A\gamma\omega}{(\omega_0^2 - \omega^2)^2 + \gamma^2\omega^2}. \quad (5.10)$$

In Fig. 5.2 the real and imaginary part of the dielectric function for a Lorentzian dipole oscillator are shown.

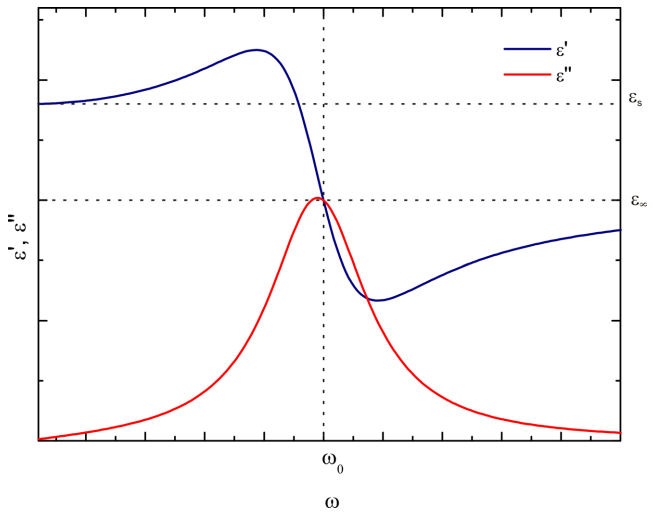

Figure 5.2: *Real (blue) and imaginary (red) part of the dielectric function for a Lorentzian dipole oscillator.*

Typically, a medium will have several resonant frequencies, ranging from the low frequency intermolecular vibrations to high frequency electronic transitions. Multiple vibration modes which are independent of each other can then be expressed as a sum of Lorentzian dipole oscillators. In this case, the dielectric function will be

$$\hat{\varepsilon}(\omega) = \epsilon_\infty + \sum_{k=1}^{M} \frac{A_k}{\omega_k^2 - \omega^2 + i\gamma_k\omega}, \quad (5.11)$$

where ω_k is the resonant frequency for the k-th vibration with the amplitude A_k and damping coefficient γ_k.

5.2 Dipolar relaxation and the Debye model

Peter Debye (1884-1966) developed in the 1920s a model to describe theoretically the dipole relaxation of non-interacting polar liquids [68]. To describe dipolar relaxation we first consider a *static* electric field E and assume that the time dependent polarization $P_2(t)$ decays exponentially,

$$P_2(t) = P_2(\infty)\left[1 - e^{t/\tau}\right], \quad (5.12)$$

where τ is the time constant (or the relaxation time). The time derivative of $P_2(t)$ can be written as

$$\frac{dP_2(t)}{dt} = \frac{P_2(\infty) - P_2(t)}{\tau}. \tag{5.13}$$

If a *time dependent* electric field $E = E_0 exp[i\omega t]$ is considered $P_2(\infty)$ is no longer a constant but will be time dependent since it is proportional to the applied field as seen in Eq. 5.5. The time derivative of $P_2(t)$ will then be

$$\frac{dP_2(t)}{dt} = \frac{\varepsilon_0(\varepsilon_s - \varepsilon_\infty)E_0 \cdot e^{i\omega t} - P_2(t)}{\tau}, \tag{5.14}$$

which has the solution

$$P_2(t) = C \cdot e^{-t/\tau} + \frac{\varepsilon_0(\varepsilon_s - \varepsilon_\infty)E(t)}{1 + i\omega\tau}. \tag{5.15}$$

The first term of Eq. 5.15, $Cexp(-t/\tau)$, will decay quickly and can thus be disregarded. The total polarization $P(t)$ is now given by a sum of the steady state polarization P_1 given in Eq. 5.3 and the time dependent polarization $P_2(t)$ given in Eq. 5.15. Substituting this sum into Eq. 5.1 gives the *Debye equation*

$$\hat{\varepsilon}(\omega) = \varepsilon_\infty + \frac{\varepsilon_s - \varepsilon_\infty}{1 + i\omega\tau}. \tag{5.16}$$

The Debye equation can easily be divided into a real and imaginary part

$$\varepsilon'(\omega) = \varepsilon_\infty + \frac{\varepsilon_s - \varepsilon_\infty}{1 + (\omega\tau)^2} \quad , \quad \varepsilon''(\omega) = \frac{(\varepsilon_s - \varepsilon_\infty)\omega\tau}{1 + (\omega\tau)^2}, \tag{5.17}$$

where $\hat{\varepsilon} = \varepsilon' - i\varepsilon''$. Since the Debye equation describes a first order process it can alternatively be derived by observing the analogy system of an electrical RC-circuit [69].

Many material deviate from this ideal behavior to a greater or lesser extend due to the complexity of the material. Due to this fact, the Debye model has been moderated in several ways since its introduction. Numerous empirical models or distribution functions have been proposed to model these deviations and the most popular can be summarized in the following equation [69]

$$\hat{\varepsilon}(\omega) = \varepsilon_\infty + \frac{\varepsilon_s - \varepsilon_\infty}{[1 + i(\omega\tau)^{1-\alpha}]^\beta}, \tag{5.18}$$

where $0 \leq \alpha \leq 1$, $\beta = 1$ is called Cole-Cole relaxation [70], $\alpha = 0$, $0 \leq \beta \leq 1$ is called Davidson-Cole relaxation [71] and $0 \leq \alpha \leq 1$, $0 \leq \beta \leq 1$ is called Havriliak-Negami relaxation [72]. Fig. 5.3 depicts the real and imaginary parts of Debye, Cole-Cole and Cole-Davidson relaxation behavior.

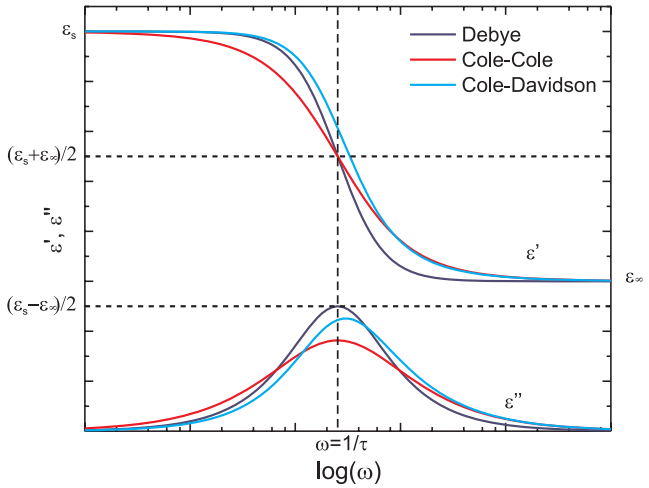

Figure 5.3: *Real and imaginary parts of Debye (dark blue), Cole-Cole (red) and Cole-Davidson (cyan) relaxation.*

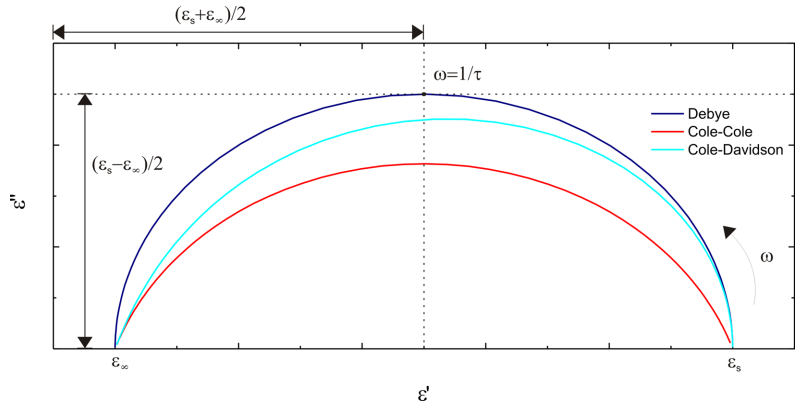

Figure 5.4: *Cole-Cole diagrams of Debye (dark blue), Cole-Cole (red) and Cole-Davidson (cyan) relaxation.*

Another way to plot the dielectric relaxation is in a so-called Cole-Cole diagram where the imaginary part ε'' is plotted against the real part ε' [70]. Cole-Cole diagrams of the three relaxation types depicted in Fig. 5.3 are shown in Fig. 5.4.

Debye type relaxation will here form a semicircle while Cole-Cole type relaxation will result in a semicircular arc and Cole-Davidson relaxation in a skewed semicircle.

Multiple relaxation processes in materials often occur. The simplest approximation to described these relaxation processes is to assume multiple first order processes which will lead to a sum of multiple Debye processes (or de-

viations of Debye processes)

$$\varepsilon(\omega) = \varepsilon_\infty + \sum_{j=1}^{N} \frac{\Delta\varepsilon_j}{1 + i\omega\tau_j}. \tag{5.19}$$

In general, the dielectric function of a polar liquid can thus be expressed in terms relaxation processes at lower frequencies and inter- and/or intramolecular vibrational modes at higher frequencies. If it is assumed that N relaxation processes takes place simultaneous with M vibration modes, the general dielectric function can be expressed as

$$\varepsilon(\omega) = \varepsilon_\infty + \sum_{j=1}^{N} \frac{\Delta\varepsilon_j}{[1 + (i\omega\tau_j)^{1-\alpha}]^\beta} + \sum_{k=1}^{M} \frac{A_k}{\omega_k^2 - \omega^2 + i\omega\gamma_k}. \tag{5.20}$$

5.3 Dielectric properties of water in inverse micelles

When two or more immiscible liquids are mixed it is defined as an emulsion, e.g. a mixture of water and oil. Emulsions can generally be divided into two groups: oil-in-water (o/w) emulsions where small amounts of oil is dispersed in a continuous medium of water and water-in-oil (w/o) emulsions which is the opposite case.

Because of the interfacial tension between oil and water, an emulsion will be thermodynamically unstable and seek to minimize the interfacial tension between oil and water making the interfacial area between water and oil as small as possible. The result will be that the emulsion will separate into layers, or large regions, of water and oil. Adding a surfactant will lower the interfacial tension between the fluid interfaces meaning that the driving force for coalescence is reduced which will increase the solubility of the liquids [73].

A surfactant will typically consist of a lipophilic part and a hydrophilic part. Since the lipophilic part often consists of CH-chains this is commonly referred to the *tail* of the surfactant while the hydrophilic part is referred to as the *head* of the surfactant. An example of a surfactant can be seen in Fig. 5.5 where the molecular structure of AOT (sodium bis(2-ethylhexyl)sulfosuccionate) is shown.

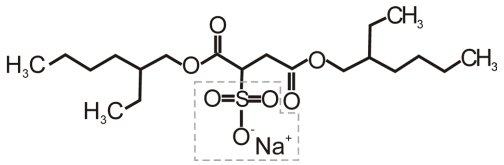

FIGURE 5.5: *Molecular structure of the surfactant AOT. The gray box indicates the hydrophilic head of the molecule and the two CH-chains are its lipophilic tails.*

If sufficient surfactant is added to the continuous phase, aggregation of surfactant molecules, also known as micelles, will form. Depending on the concentrations of the liquids and the surfactant the emulsion can be thermodynamically stable.

In this section we will focus on inclusions of water in oil, i.e. a w/o emulsion. In Fig. 5.6 an inverse micelle is depicted. Water makes up the interior of the micelles which are dispersed in oil. The name *inverse* (or reverse) refers to that the hydrophilic heads of the surfactant are facing the center of the micelle.

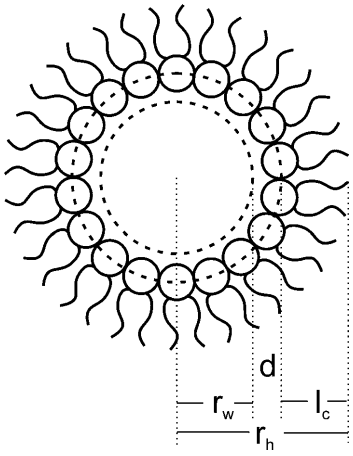

Figure 5.6: *Schematic of an inverse micelle with an aqueous core where d is the thickness of the bound water, r_w is the radius of the water core inside the micelle, r_h is the micelle radius and l_c is the thickness of the surfactant monolayer.*

A mixture of oil, water and surfactant will not always result in the formation of micelles. This is illustrated in Fig. 5.7 where the phase diagram for the water, AOT, *n*-heptane system is shown [74]. A mixture of 10 % water, 30 % AOT and 60 % heptane is shown in order to illustrate how to interpret a phase diagram. The shaded region (I) shows which compositions that will result in inverse micellar formation. The regions of (II), (III), (IV), and (V) represent the liquid crystal, the bicontinuous phase, the o/w microemulsion, and the separated phases, respectively.

The broken line in the phase diagram represents mixtures with 15 % water. The nature of water in inverse micelles is different from that of bulk water because of the interfacial interactions between the water molecules and the surrounding molecules.

In a heterogeneous system as described above the dielectric properties of the medium will be altered due to interfacial polarization effects. This is known as *dielectric dispersion*. According to considerations originally carried out by Maxwell [75], the equivalent dielectric function of two concentric spheres,

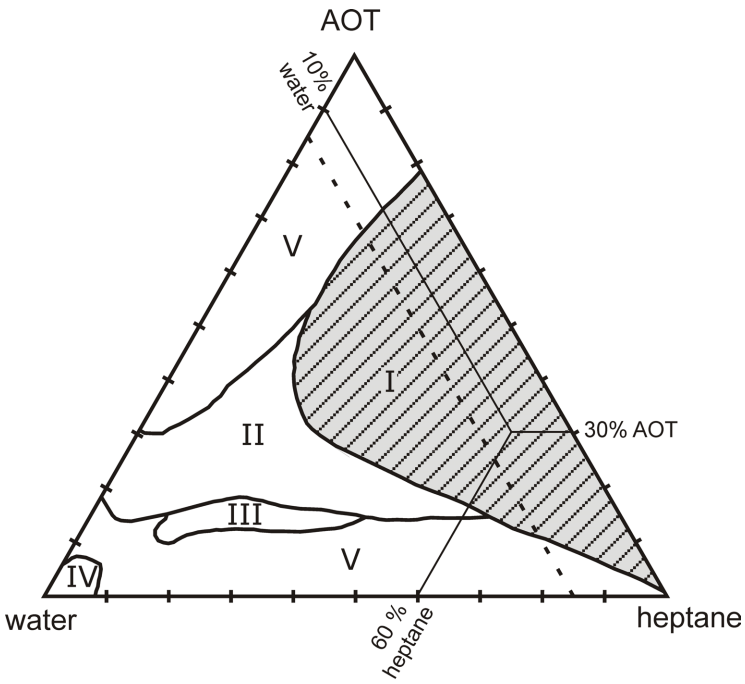

FIGURE 5.7: *Phase diagram (w/w %) composed of water, AOT and n-heptane with 5 different regions which are described in the text. The broken line indicates mixtures with 15 % water.*

which could be a micelle consisting of a shell and a core, can be expressed as [76]

$$\varepsilon_{micelle} = \varepsilon_{shell} \frac{2(1-f)\varepsilon_{shell} + (1+2f)\varepsilon_{core}}{(2+f)\varepsilon_{shell} + (1-f)\varepsilon_{core}}, \tag{5.21}$$

where f is the volume fraction of the core, $\varepsilon_{micelle}$, ε_{shell} and ε_{core} are the dielectric functions of the micelle, the shell and the core, respectively. Wagner reformulated Maxwell's considerations and took both the real and imaginary part of the dielectric function into account, and thus Eq. 5.21 is know as the *Maxwell-Wagner equation*. Eq. 5.21 can also be used to describe the total dielectric function of many dispersed spheres in a continuous medium (in that case $\varepsilon_{solution} = \varepsilon_{micelle}$, $\varepsilon_{background} = \varepsilon_{shell}$ and $\varepsilon_{sphere} = \varepsilon_{core}$ in Eq. 5.21). However, this does only hold for very dilute systems. For more concentrated systems, where interactions between the inclusions occur, Hanai have formulated an extension of the Maxwell-Wagner equation [77, 78]

$$\frac{\varepsilon_{solution} - \varepsilon_{micelle}}{\varepsilon_{background} - \varepsilon_{micelle}} \left(\frac{\varepsilon_{background}}{\varepsilon_{solution}}\right)^{1/3} = 1 - \phi. \tag{5.22}$$

Here ϕ is the volume fraction of the inclusions, in this case micelles, in the solution.

It should be noted that the Maxwell-Wagner equation and the Hanai equation only are two of many different formulations to describe the effective dielectric function of mixtures [79].

Suppose the dielectric function of the background $\varepsilon_{background}$ and the volume fraction ϕ of the micelle in the solution are known. It is then possible to decouple the dielectric function of the entire micelle $\varepsilon_{micelle}$ from the measured dielectric function of the solution $\varepsilon_{solution}$ based on Eq. 5.22.

Since it is the dielectric function of the water we are interested in we have to decouple the dielectric function of the micelle which consists of both a core of water and a shell of surfactant. The dielectric function of the surfactant ε_{shell} can be found by measuring a solution containing empty micelles, i.e. micelles with no water inside. In this case $\varepsilon_{shell} = \varepsilon_{micelle}$ in Eq. 5.22. Now it is possible, by applying the Maxwell-Wagner equation (Eq.5.21), to find the dielectric function of the aqueous core ε_{core} based on the measurements of the hydrated micelle samples.

Naturally, Eqs. 5.21-5.22 are based on some assumptions. Both equations assume that the inclusions are spherical with abrupt interfaces between the different media. Furthermore, it is necessary to assume that the dielectric properties of the continuous medium is unaffected by the inclusions in order to extract the dielectric function of the core medium. The model also ignores the size dispersion of the micelles.

Part II

Experiments

Chapter 6

Ethanol and sucrose solutions in water

Water and ethanol are maybe the most important and well-studied liquids i natural sciences. In spite of the simple geometry of these molecules a lot is still left to understand to obtain a complete picture of these molecules and their dynamics, both as neat components and as mixtures of them. Previously, Kitahara and coworkers used transmission THz-TDS to determine the dielectric functions of ethanol-water mixtures and they observed a huge difference between the dielectric function of water and that of ethanol in the THz spectral range [80]. The most apparent application of this knowledge is to use it to determine the ethanol concentration in an ethanol-water mixture.

In this Chapter measurements on ethanol-water mixtures including commercial beverages will be discussed. Furthermore, the influence of presence of sucrose in the mixture and carbonation will be investigated [52].

6.1 Experimental details

The measurements were performed in a reflection THz spectrometer (described in Chapter 4.3) with photoconductive generation and detection of THz radiation (described in Chapter 3.1). The pulsed laser (HighQ) used had a wavelength $\lambda = 800$ nm, an average power P_{av}=400 mW, a pulse width of $\sim$ 100 fs and a repetition rate of 75 MHz. Deionized water and ethanol (Sigma Aldrich, 99.5 % purity) were used without any further purification.

6.2 Ethanol concentrations in ethanol-water mixtures

The real and imaginary part of the dielectric function (hereafter denoted ε' and ε'', respectively) of water and ethanol, respectively, measured at room

temperature (20 °C) are shown in Fig. 6.1.

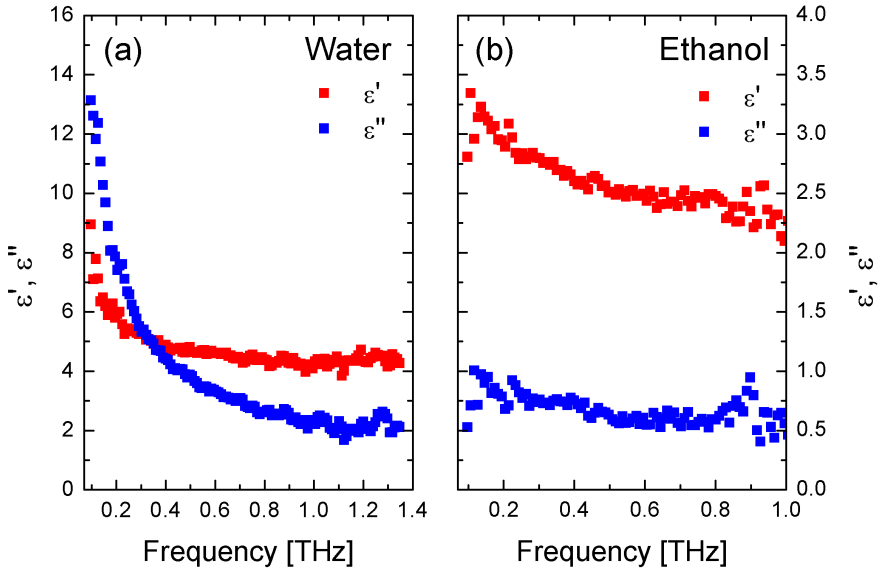

Figure 6.1: *Real (red squares) and imaginary (blue squares) part of the dielectric functions of (a) water and (b) ethanol at 20° C.*

Water is measured in the 0.1-1.4 THz range while ethanol is only measured in the 0.1-1.0 THz range since the spectrometer is less sensitive for less absorbing materials as discussed in Chapter 4.5. A detailed discussion of the dielectric functions of water and ethanol will be given in Chapter 7 and will not be discussed further in this Chapter. Fig. 6.1 illustrates the differences between the dielectric functions of water an ethanol. At 1 THz ε' of water is nearly twice of that of ethanol, while ε'' of water is almost the quadruple of that of ethanol and even more for lower frequencies.

ε' and ε'' of ethanol-water mixtures measured at room temperature in the 0.1-1.1 THz range where the ethanol concentration is varied in 5% w/w (weight/weight) steps from 0% to 100% are shown in Fig. 6.2.

Both ε' and ε'' show an evident ethanol concentration dependency. This dependency is most pronounced at low concentrations and strongest for ε''. There is a good agreement between our results and previous THz measurements on water [50, 60, 80, 81], ethanol [80, 81] and mixtures of ethanol and water [80].

6.3 Determination of unknown concentrations

The gradual change of ε' and ε'' suggests that it is possible to determine an unknown ethanol concentration by comparing its dielectric function to the reference curves in Fig. 6.2 given that they are measured under the same

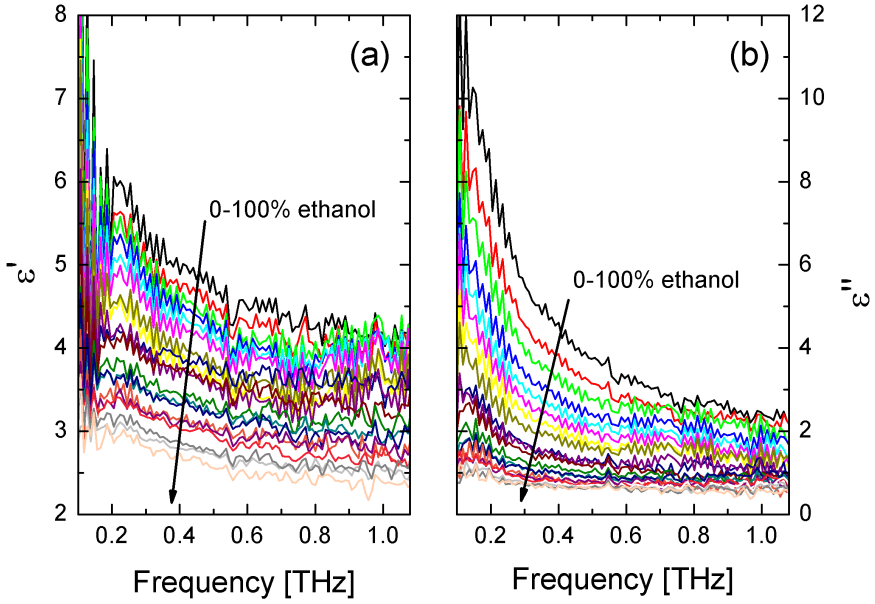

FIGURE 6.2: *(a) Real and (b) imaginary part of the dielectric functions of ethanol-water mixtures measured at room temperature in the 0.1-1.1 THz range. The ethanol concentration is varied in 5% w/w steps from 0% to 100%.*

ambient conditions. The most thorough way to do this would be by applying multivariate data analysis [82]. However, since this is a two-component system where there is an obvious connection between the ethanol concentration and the values of ε' and ε'' a more simple approach is chosen. In Fig. 6.3 the average values of ε' and ε'' in the 0.15-1.0 THz are plotted as a function of the ethanol concentration.

The solid lines are phenomenological exponential fits to the average values of ε' and ε'' (hereafter denoted $\bar{\varepsilon'}$ and $\bar{\varepsilon''}$, respectively) of the form

$$\bar{\varepsilon'}(x_{EtOH}) = A + B \cdot e^{Cx_{EtOH}}, \tag{6.1}$$

$$\bar{\varepsilon''}(x_{EtOH}) = D + F \cdot e^{Gx_{EtOH}}, \tag{6.2}$$

where x_{EtOH} is the ethanol concentration (w/w) and with the fitting parameters $A = 0.137$ (kept fixed), $B = 4.554 \pm 0.029$, $C = -0.623 \pm 0.013$, $D = 0.501 \pm 0.052$, $F = 3.534 \pm 0.053$, and $G = -3.177 \pm 0.140$ obtained by a standard nonlinear curve fitting procedure.

The ideal behavior of a mixture implies that the complex refractive indices of the individual neat components can be added in the following way [83–85]

$$\hat{n}_{ideal}(\omega) = \sum_{j=1}^{M} \frac{c_j^{mix}}{c_j^{neat}} \hat{n}_j(\omega), \tag{6.3}$$

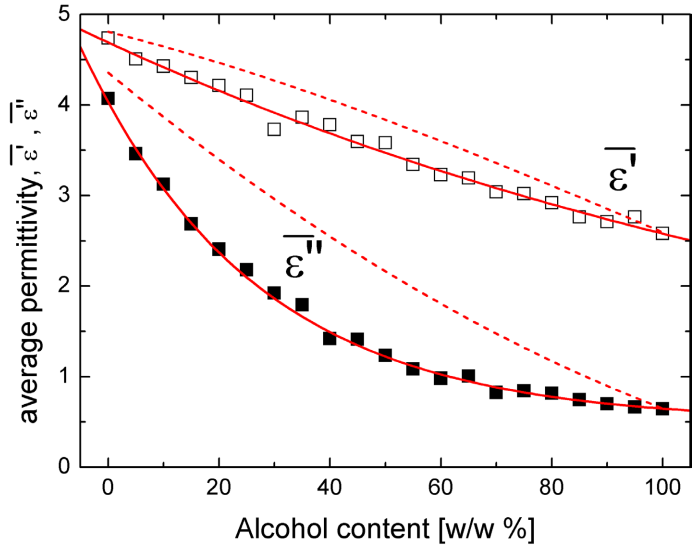

Figure 6.3: *The average values of the real ($\bar{\varepsilon}'$) and imaginary ($\bar{\varepsilon}''$) parts of the dielectric functions of ethanol-water mixtures as functions of the ethanol concentration. The solid lines are phenomenological fits to the average values and the dashed lines show the ideal behavior of the mixtures.*

where $\hat{n}_{ideal}$ is the complex refractive index of the ideal mixture, c_j^{mix} and c_j^{neat} are the concentrations of the j-th component in the mixture and in a neat sample of the component, respectively, and $\hat{n}_j$ is the complex refractive index of the j-th neat component. This way of adding the complex refractive indices will also take small nonidealities in the volume of mixing which actually is the case for ethanol-water mixtures as illustrated in Fig. 6.4.

Commercial beers, wines and liquors, which characteristics are listed in Tab. 6.1, were measured in the same fashion as the 21 reference curves and $\bar{\varepsilon}'$ and $\bar{\varepsilon}''$ were calculated. The labeled alcohol contents were converted to w/w %.

Table 6.1: *Commercial beverages measured with reflection THz-TDS.*

Beverage	Labeled alcohol concentration [w/w %]	Country	Color
Light beer	0.1	Denmark	Light brown
Pilsner	4.0	Denmark	Light brown
Porter	6.1	Denmark	Dark brown
White wine	8.8	France	Light yellow
Cream liquor	13.7	Ireland	Light brown
Bitter	37	Germany	Dark brown
Absinthe	52	Bulgaria	Green

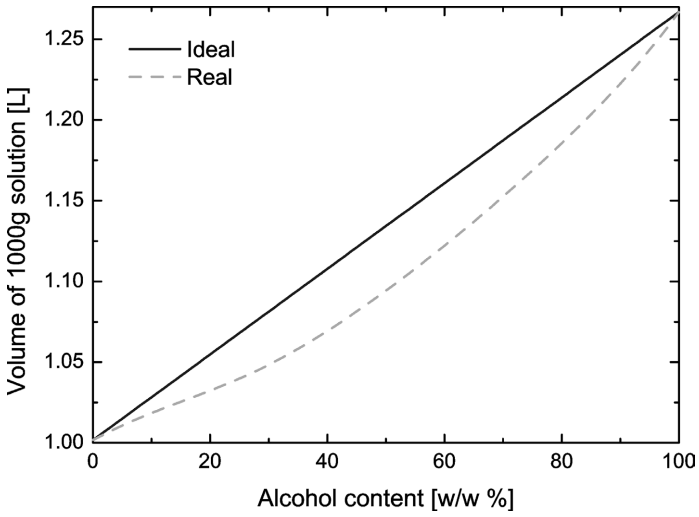

FIGURE 6.4: *Ideal (dark blue) and real (red) volume of a mixture of ethanol and water with a total mass of 1000g.*

By inverting Eqs. 6.1 and 6.2 one can estimate the ethanol concentration from $\bar{\varepsilon}'$ and $\bar{\varepsilon}''$ for an unknown sample. This was done for each of the 21 reference measurements. Fig. 6.5 shows a plot of the actual versus the predicted ethanol concentration for the reference measurements (black squares) and measurements on the commercial beverages (blue stars) listed in Tab. 6.1.

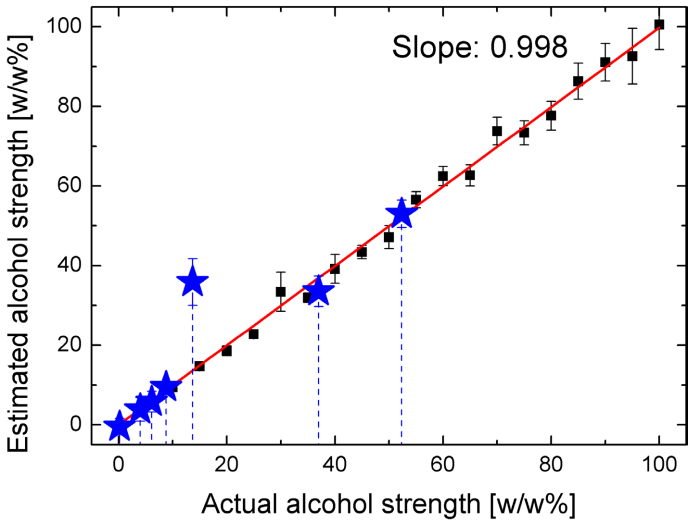

FIGURE 6.5: *Predicted versus actual ethanol concentration of ethanol-water mixtures (black squares) and commercial beverages (blue stars).*

The error bars indicate the standard deviation of each estimate calculated from the standard deviation of the constants in Eqs. 6.1 and 6.2 and the standard deviation of $\bar{\varepsilon}'$ and $\bar{\varepsilon}''$. The standard deviation of the reference points is approximately 1% for low ethanol concentration whereas it is several percent for high ethanol concentrations due to the decreasing slope of Eq. 6.2 at high ethanol concentrations. The red curve, which goes through origin and has a slope of 0.998, is a linear fit to the reference points. This indicates that the prediction of the ethanol content is very close to the actual ethanol content.

The commercial beverages are predicted to be within 1% of the labeled values with the exception of the cream liquor. However, this particular beverage fails the main assumption that only ethanol leads to a reduction of ε' and ε'' since the cream also will have this effect. Thus, this simple model will overestimate the ethanol content of the cream liquor.

6.4 Sucrose solutions in water

The measurements on the commercial beverages suggest that coloration of the sample, carbonation as well as content of sugar and sediments have little or no influence on this measurement technique. To further investigate this, a series of measurement on sucrose solutions in water was performed. ε' and ε'' for sucrose-water solutions in the 0-75% (w/w) range in 5% steps are shown in Fig. 6.6.

The highest concentrations required a slight heating but all measurements were carried out at room temperature and no precipitation of crystalline sucrose was observed during the measurements. The real part of the dielectric function shows only a weak dependency on the sucrose content which is contrary to ε' of the ethanol-water mixtures where presence of ethanol decreased ε'. The imaginary part of the dielectric function shows, on the other hand, a strong dependence on the sucrose content which also was the case for the ε' dependency of ethanol content in the ethanol-water mixtures.

Again, to determine an unknown concentration of sucrose one can in a similar fashion as in the case of the water-ethanol mixtures determine $\bar{\varepsilon}'$ and $\bar{\varepsilon}''$ for the different sucrose solutions. This is shown in Fig. 6.7 where $\bar{\varepsilon}'$ and $\bar{\varepsilon}''$ calculated in the range of 0.15-1.1 THz are shown as a function of the sucrose concentration.

Up to a sucrose concentration of 40%, $\bar{\varepsilon}'$ is nearly constant and it decreases slightly with the sucrose concentration above 40%. However, $\bar{\varepsilon}''$ shows a pronounced linear dependence on the sucrose content. The red line are

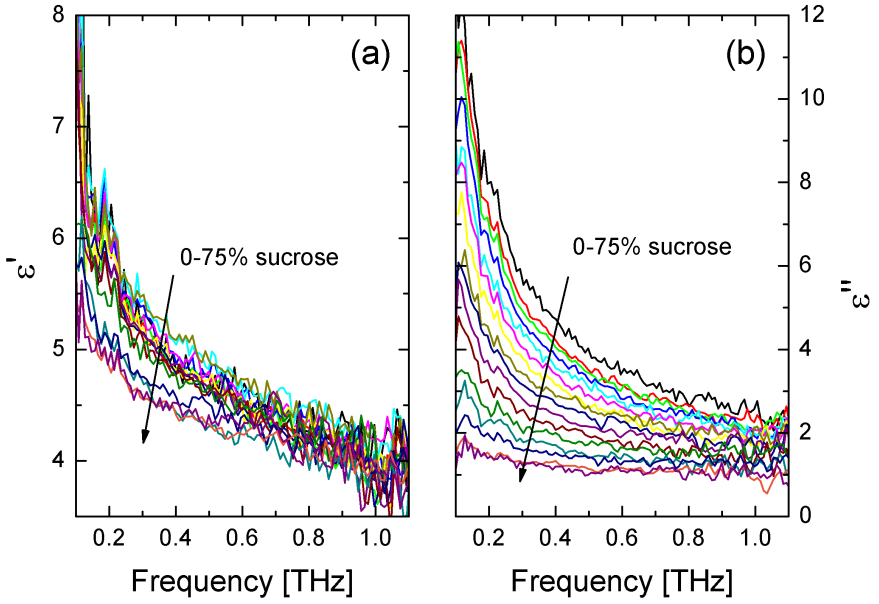

FIGURE 6.6: *(a) Real and (b) imaginary part of the dielectric functions of sucrose-water solutions measured at room temperature in the 0.1-1.1 THz range. The sucrose concentration is varied in 5% w/w steps from 0% to 75%.*

phenomenological linear fits of the form

$$\epsilon'(x_{sucrose}) = \begin{cases} A' , & x_{sucrose} < 40\% \\ B' - C' x_{sucrose} , & x_{sucrose} \geq 40\% \end{cases} \quad (6.4)$$

$$\epsilon''(x_{sucrose}) = D' - F' x_{sucrose}, \quad (6.5)$$

with the fitting parameters $A' = 4.763 \pm 0.032$, $B' = 0.00978 \pm 0.0024$, $C' = 5.05 \pm 0.14$, $D' = 4.11 \pm 0.03$ and $F' = 0.0415 \pm 0.0007$.

6.5 Effect of carbonation and sediments

Carbonation of the liquids would indeed influence a transmission measurement since the air bubbles would scatter the THz light because of their comparable size to the wavelength. However, because of the geometry of the setup the air bubbles will seek to the surface and therefore not be present at the probed interface. Hence, measurements on carbonated liquids can be conducted with basically the same accuracy as still liquids. In Fig. 6.8a ε' and ε'' of deionized water (black curve), carbonated mineral water (red curve) and decarbonated mineral water (blue curve) are depicted. Fig. 6.8b shows ε' and ε'' of deionized water (black curve), carbonated soft drink with an approximate sucrose content of 15% (red curve), and the same soft drink decarbonized (blue curve).

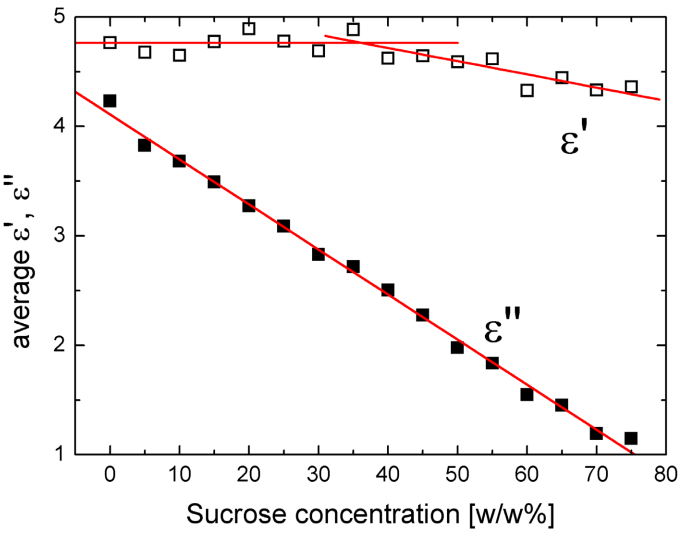

Figure 6.7: *The average values of $\bar{\varepsilon}'$ and $\bar{\varepsilon}''$ parts of the dielectric functions of sucrose-water solutions as functions of the sucrose concentration. The solid lines are phenomenological fits to the average values.*

The originally carbonated mineral water and soft drink were decarbonized by thorough shaking.

Figure 6.8a shows no difference between carbonated mineral water and the same mineral water with the gas removed. This suggests that the bubbles does not influence the measurements, probably because the bubbles rapidly escape from the probed Si-sample interface compared to the probing time. A closer look reveals that the deionized water has a slightly lower ε' compared to that of mineral water. Since the presence of bubbles at the interface not is the cause for this, it is most likely due to temperature fluctuations in the laboratory. This is due to the fact that the complex refractive index of silicon as well as water depend on the temperature [50, 60].

In Fig. 6.8b it is seen again that the presence of bubbles in the soft drink have minimal influence on the dielectric function. ε' of deionized water is lower than that of the soft drink and ε'' is higher than that of the soft drink. This difference can be ascribed to the sugar content of the soft drink.

Coloration of the sample can cause trouble for other optical spectroscopic techniques, where the wavelength is comparable to the visible wavelengths. However, the coloration of the sample have no influence on the results in THz spectroscopy. Furthermore, small sediments will only have little influence as long as they are smaller than the THz wavelength (1 THz = 300 μm).

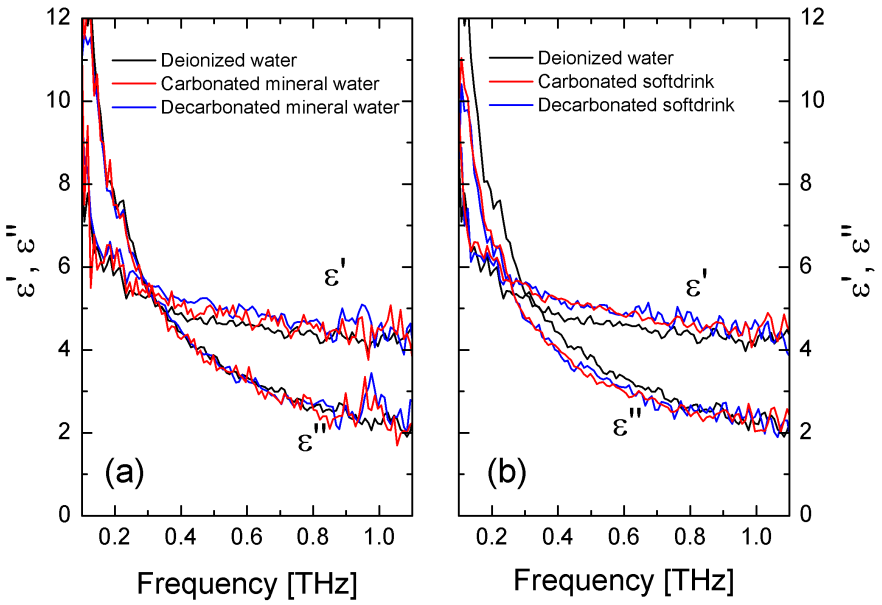

FIGURE 6.8: *Real and imaginary part of the dielectric function for (a) deionized water (black curve), carbonated mineral water (red curve) and the same mineral water decarbonized (blue curve) and (b) deionized water (black curve), a carbonated soft drink (red curve) and the same soft drink decarbonized (blue curve).*

6.6 Simultaneous determination of ethanol and sucrose content

In Section 6.4 it was demonstrated that small amounts of sucrose have little or no influence on ε'. Since adding alcohol to water will decrease ε', this information can in principle be used to *simultaneous* determination of the sucrose and ethanol contents of sucrose-ethanol-water mixtures.

Figure 6.9 shows ε' and ε'' of deionized water, an ethanol-water mixture (20% ethanol), a sucrose-water solution (20% sucrose) and two sucrose-ethanol-water solutions (10% sucrose, 20% ethanol and 20% sucrose, 20% ethanol). It is seen that only ethanol causes a decrease of in the case of ε' whereas the presence of both sucrose and ethanol lead to a decrease of ε''.

In order to determine the sucrose and ethanol contents of sucrose-ethanol-water mixtures it is assumed that $\bar{\varepsilon}'$ and $\bar{\varepsilon}''$ of the mixtures can be described as a sum of the individual modifications originating from ethanol and sucrose, respectively. For moderate amounts of ethanol and sucrose Eqs. 6.1-6.5 can then be combined to

$$\bar{\varepsilon}'(x_{EtOH}, x_{sucrose}) = A + B \cdot e^{Cx_{EtOH}}, \tag{6.6}$$

$$\bar{\varepsilon}''(x_{EtOH}, x_{sucrose}) = D + F \cdot e^{Gx_{EtOH}} - F'x_{sucrose}. \tag{6.7}$$

From this simple model the 10%-sucrose-20%-ethanol solution was pre-

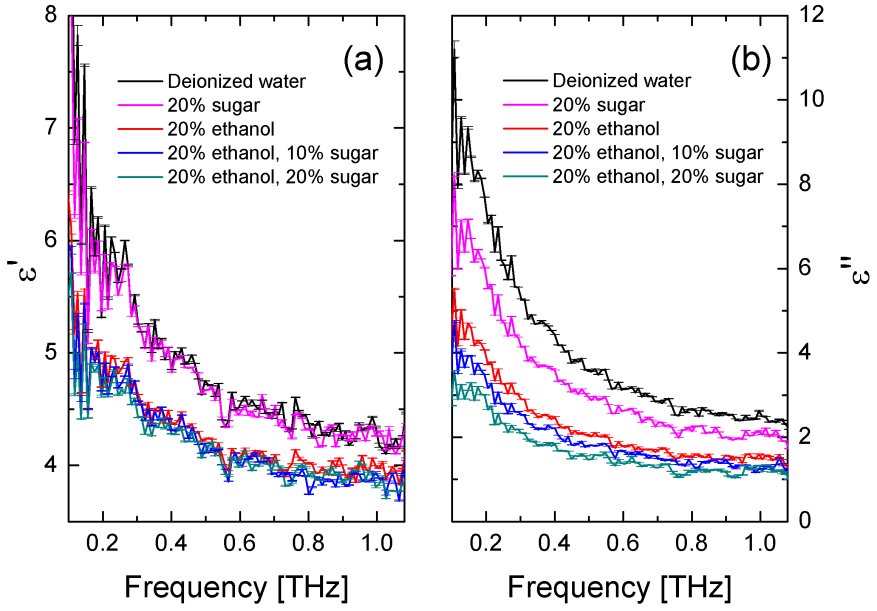

Figure 6.9: *ε' and ε'' of deionized water, an ethanol-water mixture (20% ethanol), a sucrose-water solution (20% sucrose) and two sucrose-ethanol-water solutions (10% sucrose, 20% ethanol and 20% sucrose, 20% ethanol).*

dicted to contain (13.6±2.5)% sucrose and (18.6±1.1)% ethanol. The 20%-sucrose-20%-ethanol solution was predicted to contain (19.4±2.5)% sucrose and (19.4±1.1)% ethanol.

The simultaneous determination of the unknown concentrations of two components, in this case ethanol and sucrose, is possible through this simple method because both ε' and ε'' can be calculated directly from the measurement. Thus, the unknown concentrations of two components are also the maximum number of components that can be determined from this simple method. Multiple component determination will require a more thorough analysis method, i.e. multivariate data analysis.

6.7 Conclusion

Based on reflection THz-TDS it was in this Chapter demonstrated that the different dielectric functions of water and ethanol can be used to determine unknown concentration of ethanol based on reference spectra of ethanol-water mixtures. The same method also turned out to be useful to determine the alcohol content of commercial beverages where color, carbonation, sediments and moderate amounts of sugar showed little or no influence on the result. For low ethanol contents the predicted values were within 1% of the actual value and for higher ethanol concentrations it was within a few percent.

The fact that both the real and the imaginary part of the dielectric function are determined directly in THz-TDS makes it possible to determine the concentration of up to two components. It was demonstrated how to extract the concentrations of sucrose and ethanol in sucrose-ethanol-water solutions with an accuracy of a few percent. The simple model requires that no other components (besides the two unknown) in the liquid contributes significantly to changes of the dielectric function of the solvent and that changes of the dielectric function derived from the presence of two unknown components can be described as the sum of the individual contributions.

Chapter 7

Dielectric relaxation of ethanol-water mixtures

In this Chapter we will discuss the measurements of the dielectric function of ethanol-water mixtures. We make use of data from a very broad frequency range, by combination of our own results and already published data recorded in the microwave range with a combination of time-domain reflectometry (TDR) and waveguide interfeometry by Sato and Buchner [86], who has made their original data available to us. By combining the two sets of data we are able to cover the wide frequency range 100 MHz - 2.5 THz, and thus we are able to perform accurate fits to the experimental data, covering the full range of dielectric relaxation [87].

Here we are interested in binary mixtures of water and ethanol over the full mixing ratio range from pure water (mole fraction $x_{EtOH} = 0$) to pure ethanol (mole fraction $x_{EtOH} = 1$). The thermodynamic properties of water-ethanol mixtures have been investigated in great detail, partly due to the fact that this specific mixture is very important from a technological and also cultural point of view, and partly because of many intriguing properties of the (at first glance) rather simple system.

We find that the combination of already published data recorded in the region below 100 GHz with our broadband THz data up to 2.5 THz, combined with the knowledge of recently published data on liquid water in the frequency range up to 7 THz, allows a consistent modeling of the dielectric spectrum of the mixture from MHz frequencies up to the onset of intermolecular vibrational bands. The modeling, based on a combination of Debye relaxation terms and a heavily damped, high-frequency vibrational mode (Eq. 5.20), allows us to correlate the extracted relaxation times, relaxation strengths, and vibrational properties with the thermodynamic properties of the mixtures.

Pure water is believed to structure itself with hydrogen-bonded clusters of molecules extending throughout a substantial fraction of the liquid volume

and with a rather small fraction of water molecules as monomers or small clusters [88]. Pure ethanol, on the other hand, is reported to structure itself into smaller aggregates with of varying length, with cluster sizes ranging from monomers to tens of molecules, either in the form of linear or cyclic chains of hydrogen-bonded molecules, as demonstrated by molecular dynamics (MD) simulations [88] and Monte Carlo simulations [89]. The structure of liquid ethanol-water mixtures is believed to exhibit some degree of clustering of the ethanol molecules and the water molecules, respectively. Several MD simulations offer insight into this microscopic structuring [88, 90].

When ethanol is added to a volume of water, the extensive hydrogen-bonded network of water molecules is disrupted, and new chemical bonds (hydrogen bonds) are formed between the ethanol molecules, between water and ethanol molecules, and between water molecules. Thus the water-ethanol mixture is heterogenous at the microscopic level [88].

The formation and breaking of the intermolecular hydrogen bonds in the mixture can be seen as a chemical reaction, and as these processes are dependent on the mixing ratio, it leads to a complicated dependence of the thermodynamic properties on the mixing ratio and on the temperature.

7.1 Experimental details

The experimental method used for the recording of our THz data is based on ATR terahertz time-domain spectroscopy, as described in Chapter 4.4 and also described in detail elsewhere [57, 60, 91].

Briefly, the THz pulses are generated by focussing synchronous, optical pulses from a femtosecond fibre laser (IMRA femtolite, $\lambda = 780$ nm, P_{av}=20 mW, pulse width of ~ 90 fs, repetition rate of 50 MHz) onto a biased photoconductive GaAs dipole antenna and detected by use of electro-optic sampling in a <110>-oriented ZnTe crystal. A silicon Dove prism placed in the focus point of the THz beam [57]. The principles of generation and detection of pulsed THz radiation as well as the principles of THz time-domain spectroscopy are described in Chapters 3 and 4. Distilled water (Wako Pure Chemical Industries, Ltd.) and ethanol (Nacalai Tesque, Inc., 99.5% purity) were used without further purification. Water-cooled Peltier elements were used to keep a constant temperature of 25°C±0.5°C of the liquid.

The Fresnel reflection coefficients were obtained from the Fourier transformed temporal waveforms with and without a sample, respectively and these coefficients were used to calculate the complex dielectric function of ethanol/water mixtures at 25°C for ten different fractions of ethanol, X_{EtOH} = 0.00 (H_2O), 0.04, 0.08, 0.11, 0.18, 0.30, 0.50, 0.70, 0.90, and 1.00 (C_2H_5OH).

7.2 Measurement of the dielectric function of ethanol-water mixtures

Figures 7.1(a) and 7.1(b) show the real and imaginary part of the complex dielectric function, $\hat{\varepsilon} = \varepsilon' - i\varepsilon''$, of different mixtures of ethanol (C_2H_5OH) and water (H_2O) as a function of frequency in the region 0.2–2.5 THz.

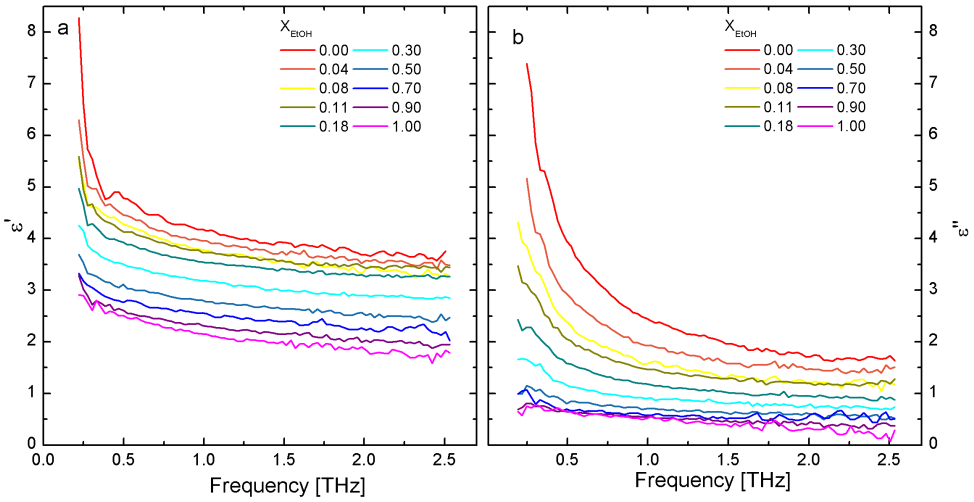

FIGURE 7.1: *(a) Real and (b) imaginary part of the complex dielectric function of 10 different ethanol/water mixtures at 298 K (25° C).*

The measurements presented here are in good agreement with the substantial number of investigations of liquid water in the THz range [50, 52, 60, 80, 81, 92–94], on liquid ethanol [52, 80, 81], and on mixtures of ethanol and water [52, 80].

Since the slow relaxation processes in the microwave region contribute substantially to the complex dielectric function it is necessary to take these into account. Sato and Buchner have previously measured the complex dielectric functions of samples identical to this work in the frequency range 0.1–89 GHz using time-domain reflectometry (TDR) and waveguide interferometry [86]. We have included the measurements of Sato and Buchner in our analysis and thereby covering more than four decades of frequency, from 10^{-4} – 2.5 THz. As examples, Fig. 7.2 shows the complex dielectric function of (a) 18% and (b) 50% ethanol/water mixtures. One can clearly see that in order to describe all the relaxation processes in ethanol/water mixtures it is necessary to include data from the microwave region as well as the THz region.

Different microscopic pictures of the different relaxation processes in liquid water have been suggested. The slow relaxation time τ_1 has been described as rotational relaxation within a hydrogen-bonded cluster, or water self-diffusion

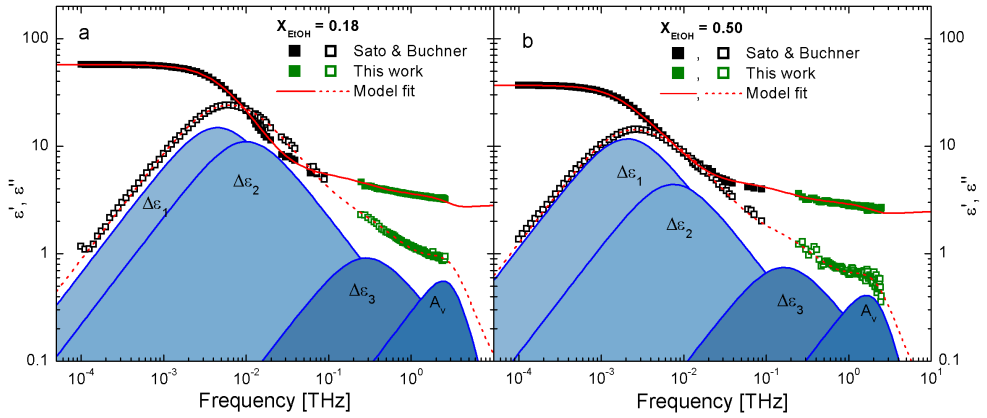

Figure 7.2: *Real (solid symbols) and imaginary (open symbols) part of the complex dielectric function of (a) 11% and (b) 50% ethanol/water mixtures at 298 K (25°). Data recorded in the present work are shown in green color, and data from Sato and Buchner [86] are shown in black color. The fitted dielectric function is shown by solid (real part) and dashed (imaginary part) curves, respectively. The contributions to ε'' from the three relaxation processes and the vibrational term are shown in blue colors.*

understood as hopping between occupied and vacant sites in the tetrahedral water structure [95]. According to Gaiduk and Vij [96] the faster relaxation time τ_2 is related to an overdamped bending vibration coupled to stretching vibration of individual water molecules while the hydrogen bonds exist. Gaiduk and Vij also mention that the motion of the hydrogen-bonded water molecules is overdamped, and the motion of the water molecules is thus more chaotic than for a orientational relaxation [96]. An even faster relaxation process has been suggested, possibly associated with free rotation of weakly hydrogen-bonded water molecules or water molecules with broken hydrogen bonds [97]. However, recent spectroscopic data indicate that the fast processes in water are better described as a damped intermolecular stretch vibration [60].

Irrespective of the nature of the various relaxation processes, it is important to note that the Debye model that incorporates several relaxation processes is based on the assumption that these relaxation processes are independent of each other, and take place in a parallel fashion [98]. This assumption is not obvious, and a deeper insight into the fundamental nature of the relaxation processes in the mixture requires a combination of MD simulation, spectroscopy, and analytical considerations.

7.3 Fitting of data

We use a nonlinear fitting procedure based on the Levenberg-Marquardt algorithm [99] to estimate the dielectric parameters by simultaneous fitting to the real and imaginary part of the complex dielectric function, and find that

the complex dielectric function of ethanol/water mixtures can be decomposed into three relaxation components and a vibrational term, i.e. we use Eq. 5.20 with $N = 3$ and $M = 1$,

$$\varepsilon(\omega) = \varepsilon_\infty + \sum_{j=1}^{N} \frac{\Delta\varepsilon_j}{1 + i\omega\tau_j} + \sum_{k=1}^{M} \frac{A_k}{\omega_k^2 - \omega^2 + i\omega\gamma_k}. \tag{7.1}$$

The fitting parameters and a discussion of the fitting procedure can be found in Appendix A.

Thus our fitting parameters are ε_s, $\Delta\varepsilon_1$, $\Delta\varepsilon_2$, $\Delta\varepsilon_3$, and ε_∞ and τ_1, τ_2, and τ_3, and finally the vibrational amplitude A_v, angular frequency ω_v, and damping γ_v. It should be pointed out that several of the constants are linked with each other as can be seen by considering the total dielectric strength,

$$\begin{aligned} \varepsilon_s - \varepsilon_\infty &= \Delta\varepsilon_1 + \Delta\varepsilon_2 + \Delta\varepsilon_3 + \frac{A_v}{\omega_v^2} \\ &= (\varepsilon_s - \varepsilon_1) + (\varepsilon_1 - \varepsilon_2) \\ &\quad + (\varepsilon_2 - \frac{A_v}{\omega_v^2} - \varepsilon_\infty) + \frac{A_v}{\omega_v^2}, \end{aligned} \tag{7.2}$$

where ε_1 and ε_2 are the low frequency limits of the intermediate and fast Debye relaxation components, respectively. Liquid water and the 4% mixture can be described by use of only two Debye terms and one vibration term, i.e. $\varepsilon_1(x_{EtOH} = 0) = \varepsilon_2(x_{EtOH} = 0)$, and our measurement of liquid ethanol show no sign of an intermolecular stretching vibration, i.e. $A_v(x_{EtOH} = 1) = 0$.

Yada *et al.* recently measured the temperature dependence of the complex dielectric function of water and heavy water with ATR THz spectroscopy [60] up to 3.5 THz, and combined their data with microwave data [100, 101] and far-infrared data [92]. They found that the complex dielectric function of liquid water at room temperature can be decomposed in four components: a slow relaxation mode at $\tau_1 = 9.4$ ps, a fast relaxation mode at $\tau_2 = 0.25$ ps, an intermolecular stretching vibration mode at ~ 5 THz, and an intermolecular libration mode at ~ 15 THz. The effect of isotopic substitution on the intermolecular stretch vibration was recently studied, also by Yada *et al.*, where the frequency range of their ATR technique was pushed to 7 THz [59].

Because of the bandwidth limitation (< 2.5 THz) in the present work we have not included the intermolecular libration mode in our model.

In Tab. 7.1 we compare our fitting results for water with results from the literature. Although variations are seen between the various results, there is a good consistency between the fitted parameters.

In Tab. 7.2 our fitting parameters for liquid ethanol are shown together with previous results from Kindt *et al.* [81] and Sato *et al.* [86]. Both groups have used a triple Debye model to describe the relaxation processes of ethanol. Our data is consistent with the work of Kindt *et al.* while Sato *et al.* report higher values of the high frequency components (τ_3 and ε_∞) which also leads

Table 7.1: *Comparison of relaxation parameters of water*

Water	ε_s	$\Delta\varepsilon_1$	τ_1 [ps]	$\Delta\varepsilon_3$	τ_3 [ps]
This work	78.3	72.3	8.34	2.12	0.36
Rønne *et al.*[50]†	80.6♯	72.1	8.5	1.9	0.17
Sato *et al.*[86]	78.3	72.2	8.32	2.14	0.39
Yada *et al.*[60]‡	79.9♯	74.9	9.43	1.63	0.25
		$A_v/(2\pi)$ [THz^2]	$\omega_v/2\pi$ [THz]	$\gamma_v/2\pi$ [THz]	ε_∞
This work		28.4	5.01	7.06	2.68
Rønne *et al.*[50]†		–	–	–	3.3
Sato *et al.*[86]		–	–	–	3.96
Yada *et al.*[60]‡		31.5	5.30	5.35	2.50*

†Measured at 19°C. ♯Fixed. ‡Measured at 20°C.

*Including amplitude of intermolecular libration mode.

to a shift of the intermediate component (τ_2), most probably due to the lack of high-frequency data in their fitting procedure.

Table 7.2: *Comparison of relaxation parameters of ethanol*

Ethanol	ε_s	$\Delta\varepsilon_1$	τ_1 [ps]	$\Delta\varepsilon_2$	τ_2 [ps]	$\Delta\varepsilon_3$	τ_3 [ps]	ε_∞
This work	24.4	20.0	163	1.40	4.51	1.21	0.33	1.85
Kindt *et al.*[81]†	24.4♯	20.2	161	1.43	3.3	0.79	0.22	1.93
Sato *et al.*[86]	24.5	20.0	165	0.74	10.4	1.19	1.69	2.60

†Measured at room temperature. ♯Fixed.

Previously, several deviations of the Debye model have been used to describe the slow dielectric relaxation process in ethanol/water mixtures as discussed in Chapter 5.2. Generalizations such as Cole-Cole relaxation [70, 86, 102], Davidson-Cole relaxation [71, 86, 102, 103], and Havriliak-Negami relaxation [72, 86, 102] have been reported. However, we find it sufficient to use the standard Debye model as this gives nearly flat residuals close to zero and a reduced chi-squared $\chi^2 \leq 7 \cdot 10^{-3}$ in the entire measurable frequency range for all mixtures.

The fitted dielectric functions of the different ethanol/water mixtures are shown in Fig. 7.3.

In Figs. 7.4-7.7 we summarize all the fitting parameters based on Eq. 7.1 with $N = 3$ and $M = 1$ as function of the ethanol concentration x_{EtOH}.

In Fig. 7.4 it is seen that the static dielectric constant (ε_s) decreases with

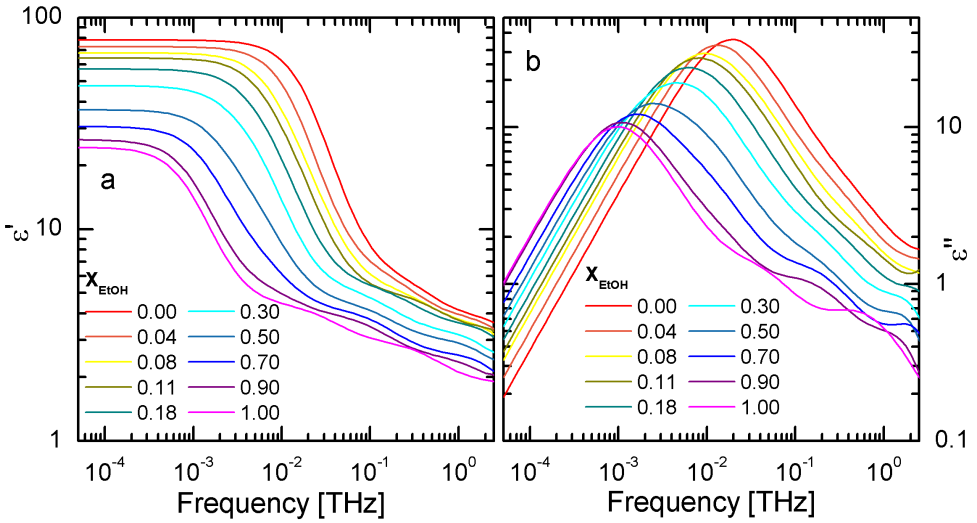

FIGURE 7.3: *Fitted curves of (a) the real and (b) the imaginary part of the complex dielectric functions for different ethanol/water mixtures by using Eq. 7.1 with $N = 3$ and $M = 1$.*

increasing ethanol concentration as observed previously [80, 86, 102–104]. Also the high-frequency permittivity is seen to decrease monotonically with increasing alcohol concentration.

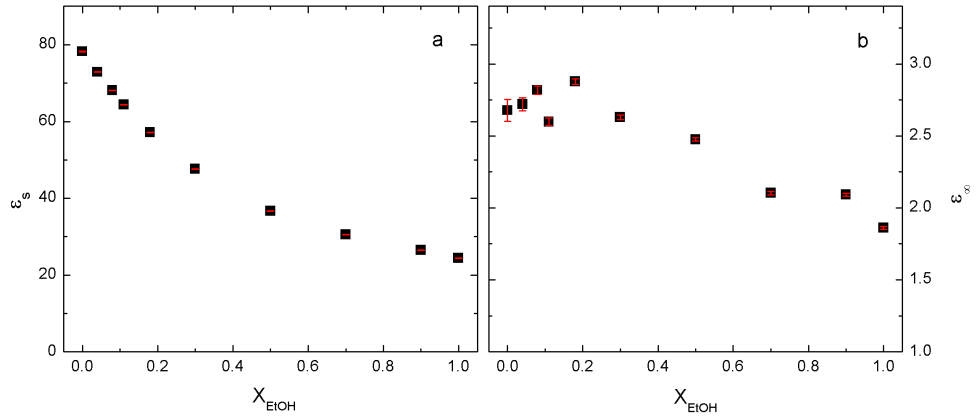

FIGURE 7.4: *Fitted values and standard deviations of (a) the static dielectric constant, ε_s, and (b) the dielectric constant in the high frequency limit, ε_∞, of ethanol/water mixtures as a function of ethanol fraction X_{EtOH}.*

In Fig. 7.5 the relaxation amplitudes, normalized to the total contribution to the dielectric constant from the relaxation terms ($\varepsilon_s - \varepsilon_\infty$) are shown as functions of the ethanol concentration.

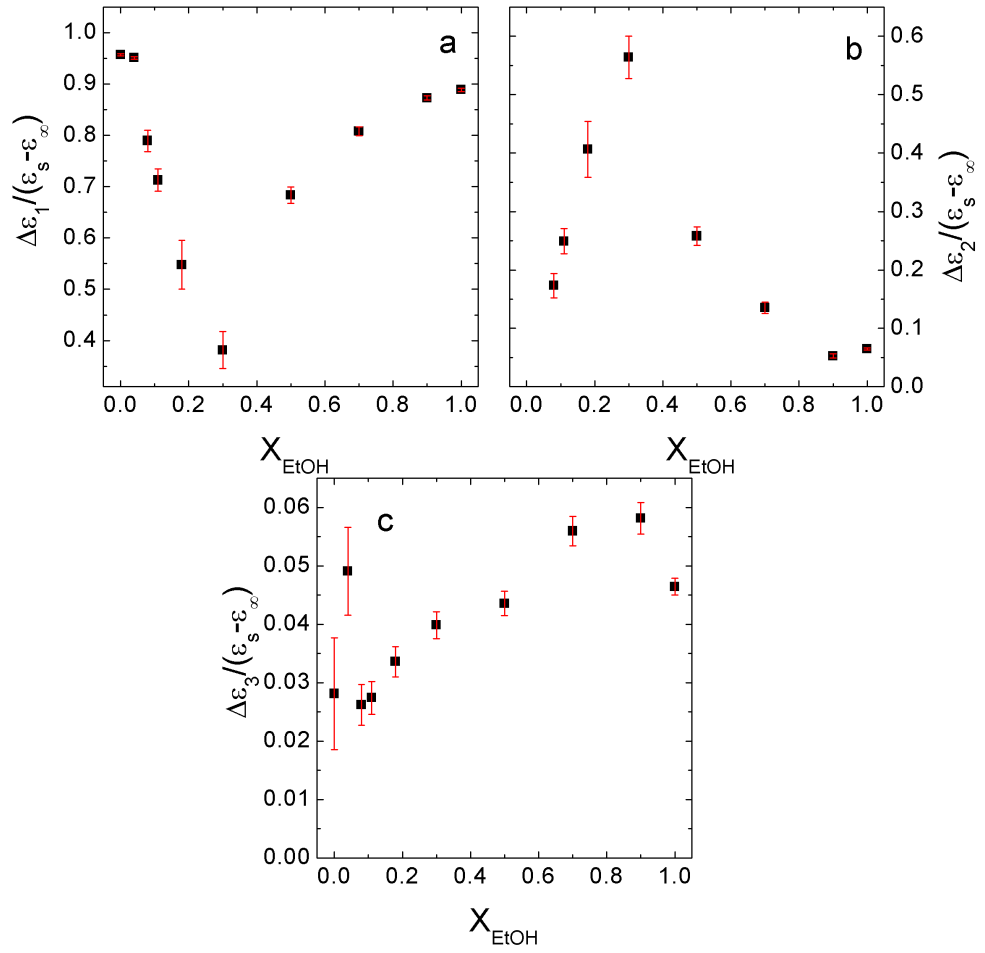

Figure 7.5: *Debye relaxation strengths (a) $\Delta\varepsilon_1$, (b) $\Delta\varepsilon_2$, and (c) $\Delta\varepsilon_3$ of ethanol/water mixtures as functions of the ethanol concentration.*

It is seen that the slow relaxation process is the most prominent contributing $35-96\%$ to the total dielectric strength. The intermediate and fast process contributes $6.2-55\%$ and $2.4-5.8\%$ to the total dielectric strength, respectively. The slow component shows a minimum near an ethanol concentration of 30% where it contributes to only one third of the dielectric strength whereas for pure water and pure ethanol it contributes to almost all of the dielectric function. The intermediate process show a similar sequence but with opposite sign and contributes to more than half of the dielectric function in a 30% ethanol/water mixture. This indicates that the slow and intermediate process are strongly correlated. We ensured that the opposite trends seen in the concentration dependencies of $\Delta\varepsilon_1$ and $\Delta\varepsilon_2$ was not due to simple mathematical interdependence of the variables. An example of the correlation between the different variables are given in Appendix A.

In Fig. 7.6 we show the concentration dependence of the three relaxation times in the model. Figure 7.6(a) shows that the slow relaxation time, τ_1, has a nearly linear dependence of the ethanol concentration, in agreement with previous studies. In general, previous studies in the low frequency region firmly characterizes the slow relaxation process [86, 102–104] due to the facts that (a) this process occurs within their spectral range and (b) that the slow relaxation process is the most dominant of all the relaxation processes.

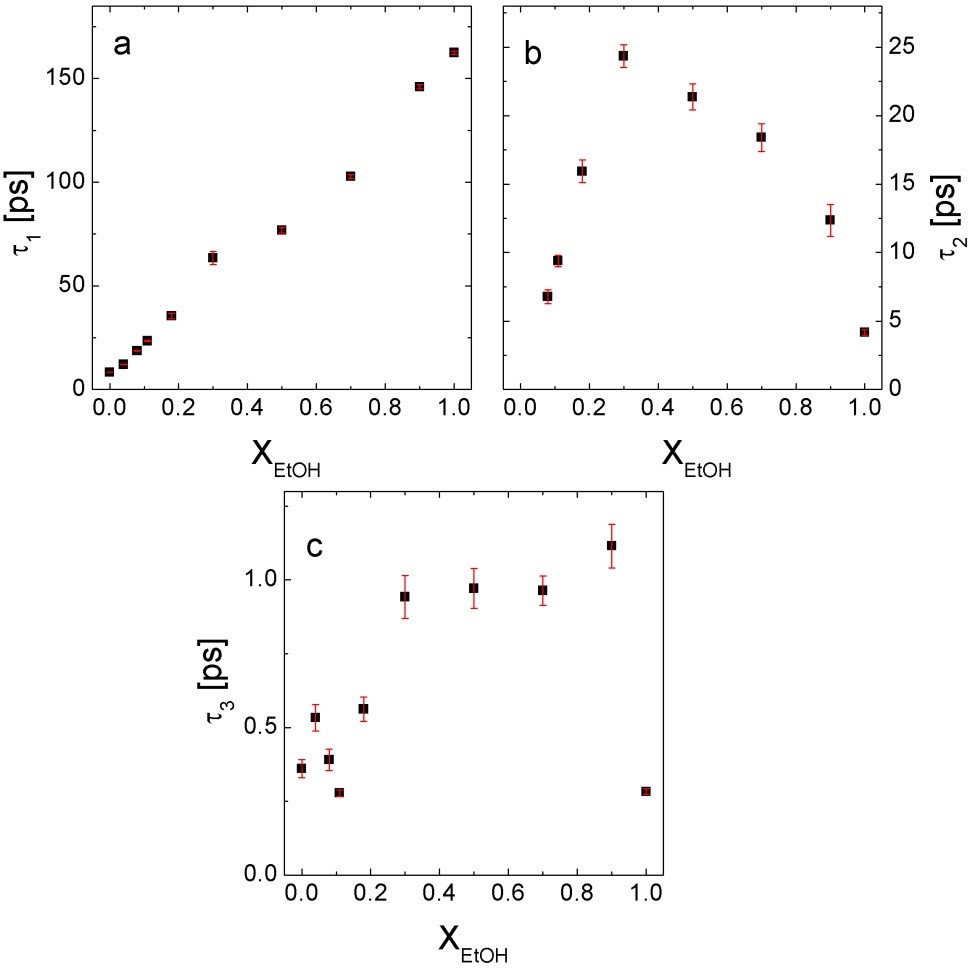

FIGURE 7.6: *Debye relaxation times (a) τ_1, (b) τ_2, and (c) τ_3 of ethanol/water mixtures as a function of ethanol concentration.*

Figures 7.6(b) and 7.6(c) show the concentration dependence of the intermediate (τ_2) and fast (τ_3) relaxation processes. In contrast to the behavior of τ_1, both τ_2 and τ_3 display a non-monotonous behavior with ethanol concentration, with a maximum of τ_2 at $x_{EtOH} \approx 0.3 - 0.4$.

The parameters for the intermolecular stretching vibration mode are plot-

ted in Fig. 7.7. As previously mentioned, the vibration parameters of water are consistent with the findings of Yada *et al.*

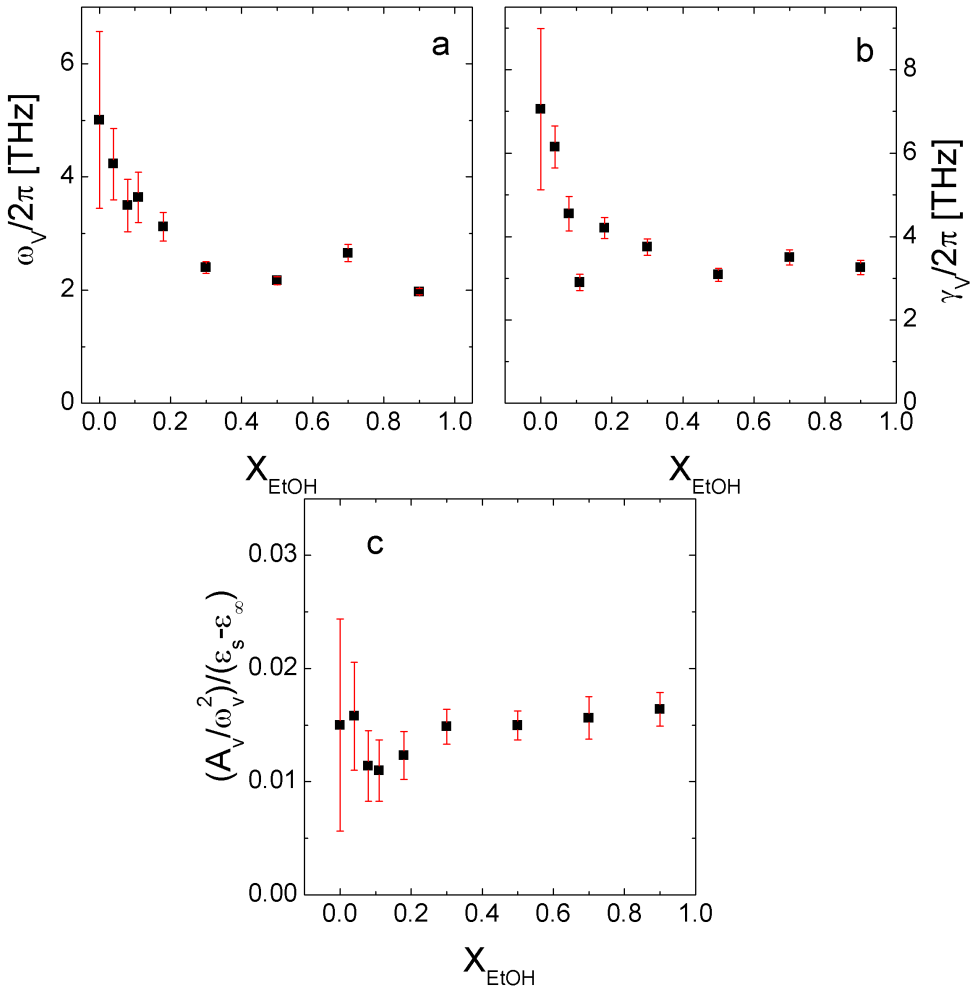

Figure 7.7: *(a) Resonance frequency, (b) damping constant, and (c) vibration strength of the intermolecular stretching vibration of ethanol/water mixtures as a function of ethanol concentration.*

Since intermolecular vibrations occur in pure water they are also bound to be present in ethanol/water mixtures to some extent. In the water-rich region the vibrational mode shifts to lower frequencies as the ethanol concentration increases and it levels out above 30% to a frequency around 2.5 THz. One possible explanation of the frequency decrease could be that when ethanol is added to water some of the water molecules participating in the intermolecular vibrational motion will be substituted with heavier ethanol molecules resulting with an overall frequency drop. At this stage it is not clear why

the resonance frequency remains fixed at higher ethanol concentrations. However, it is interesting to note that the resonance frequency remains fixed for concentrations above that which coincides with the region where there is a minimum in the mixing enthalpy (indicating that most hydrogen bonds are formed per added molecule), and approximately where the self-diffusion and mutual diffusion coefficients display their minima, as discussed above.

For pure ethanol our data indicate that the vibrational mode no longer contributes to the dielectric function, indicating that water must be present in order to observe the effects of the mode.

7.4 Comparison with thermodynamic properties

The mixing of ethanol and water at room temperature is an exothermic process, meaning that energy is released when the two components are mixed. The amount of released energy per mole of added ethanol, also called the mixing enthalpy ΔH^M, depends on the ethanol concentration [105], and is thus an important indicator of the formation and breaking of intermolecular hydrogen bonds during the mixing process. Interestingly, there seems to be a strong correlation between $\Delta\varepsilon_1, \varepsilon_2$ and ΔH^M of the solution.

Figure 7.8 shows the concentration dependence of the mixing enthalpy ΔH for ethanol/water mixtures (red curve) together with the relative strengths of the slow (black squares) and intermediate (blue circles) relaxation processes.

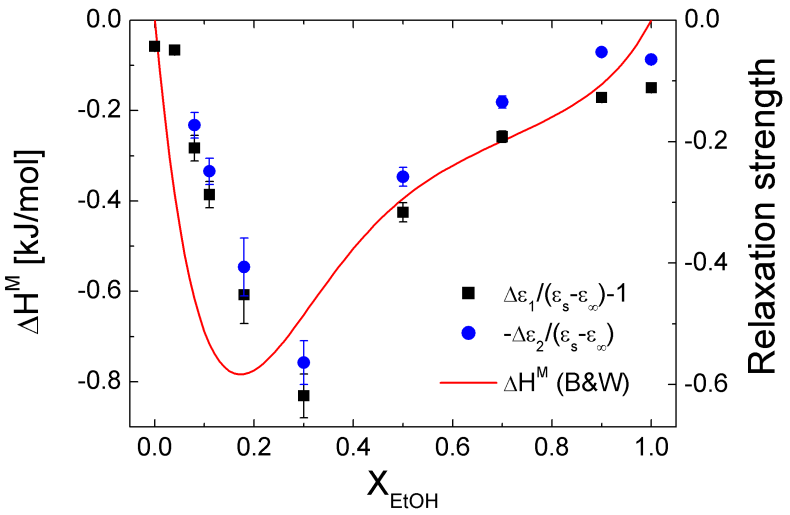

FIGURE 7.8: *Mixing enthalpy of ethanol/water mixtures (red curve, from [106]) and the relaxation strengths of the slow Debye process (black points) and the intermediate Debye process (blue points) as a function of ethanol concentration.*

Similar to the concentration dependence of the mixing enthalpy, the mixing

volume (volume change per added ethanol) of ethanol-water mixtures display a non-monotonous behavior. In Fig. 7.9 we plot the normalized mixing volume $\Delta V_{mix}/n_T$ (solid, red curve), where n_T is the total number of molecules in the mixture, as function of x_{EtOH}. In the same graph we show the normalized values of τ_2 and τ_3 (black and blue squares, respectively). It is apparent that there is a strong correlation between the mixing volume and the time constants of the intermediate and fast relaxation processes.

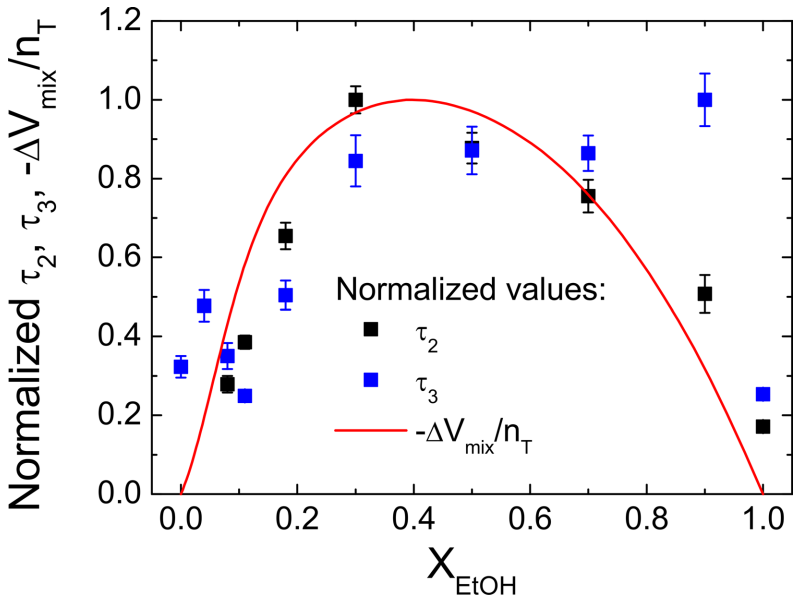

Figure 7.9: *Mixing volume of ethanol-water mixtures (solid, red curve) and the time constants τ_2 (black squares) and τ_3 (blue squares) as a function of ethanol concentration.*

The reduction of the volume during the mixing process indicates a closer packing of the molecules in the liquid. Although detailed numerical simulation of this process is required, we speculate that the correlation between $\Delta V_{mix}/n_T$ and τ_2, τ_3 is consistent with a slowing down of the relaxation processes due to less space available for the relaxation processes. This speculation would then indicate that the intermediate as well as the fast relaxation processes are of intermolecular nature.

MD simulations [90] and experimental data [107] show that the mutual diffusion coefficients for ethanol-water mixtures are smallest in the region near $x_{EtOH} = 0.3$, and the self-diffusion coefficients of water in ethanol-water mixtures is smallest in the region near $x_{EtOH} = 0.4$.

7.5 Conclusion

Water remains a liquid with many intriguing properties. The physical and optical properties of water and other polar liquids in the THz frequency range has been studied both by precise molecular dynamics simulations and by optical spectroscopy, with simulation results indicating that there is a connection between the microscopic dynamics and structure of the liquid and its thermodynamic properties. The link between optical experiments and the dynamics of the liquid is often to apply a phenomenological relaxation model to the dielectric spectrum of the liquid, and thus obtain information about the strength of the relaxation processes and their characteristic time constants. The most prominent modeling tool for this purpose is the Debye model, often with the inclusion of several relaxation processes which are then assumed to take place in a parallel fashion. This approach has given the possibility of identifying several relaxation processes in water and ethanol-water mixtures.

Broadband spectroscopy that includes information about the lowest frequency intermolecular vibrational modes of the liquid has made it possible to combine data from DC measurements, the microwave regime, and the low and high THz regime, to obtain complete coverage of the frequency range that contains all the relaxation processes.

In this Chapter we have used such an approach to combine already published microwave data with our measurements of the dielectric function of water, ethanol-water mixtures and ethanol. Water and low concentrated (4 %) ethanol-water mixtures were found to be well described by the Debye relaxation model with two Debye relaxation terms while ethanol and ethanol-water mixtures were found to be well described by three Debye relaxation terms. In the case of water and water-ethanol mixtures, the presence of the lowest intermolecular vibrational mode influences our data, and this mode was included in the modeling.

We found that the characteristics of the relaxation processes (relaxation strength and relaxation time constants) are correlated with the macroscopic thermodynamic properties of the liquid. Specifically it seems like there is a strong correlation between the mixing volume of ethanol-water mixtures and the intermediate and fast relaxation times - the smaller the mixing volume, the slower these relaxation times appear to be. Similarly, the largest enthalpy of mixing of ethanol-water mixtures appear at an ethanol concentration where the strength of the slow relaxation process is smallest and the strength of the intermediate relaxation process is highest.

We believe that our data and the links to the thermodynamic properties of the liquids could serve as inspiration for molecular dynamics simulations that may help to shed further light on the intriguing microscopic dynamics of the liquids that we have studied.

Chapter 8

Water in inverse micelles

In this Chapter we have investigated the optical properties of water confined in nanometer-sized inverse micelles. We show that the optical properties of the confined water are dependent on the water pool size. We also discuss the optical properties of different vegetable oils, lard as well as butter and use these properties to deduce the optical properties of water in butter.

Zhang and Grischkowsky have previously measured the optical properties of water confined in a parallel plate waveguide by THz-TDS. They demonstrated that the absorption coefficient and refractive index of 20 nm water layers are consistent with those of bulk water [108]. Thus, confinement of water does not in itself necessarily alter the optical properties of the confined water. However, the surrounding environment is of great importance. Arikawa *et al.* measured the number of hydrated water molecules surrounding a sucrose molecule in sucrose-water solutions. These hydrated water molecules exhibit a slowing down of their dielectric response compared to that of bulk water [61]. Previous work by the group of Mittleman observed that the THz absorption spectrum of water confined in nanometer-sized inverse micelles shoved a pronounced resonance due to surface modes [109–111].

8.1 Experimental details

The experimental method used to measure the the optical properties of the samples is based on variable cell transmission THz-TDS and photoconductive switches were used to generate and detect the coherent THz pulses. The generation and detection of THz pulses as well as the principles of THz-TDS are described in Chapters 3-4. All measurements were performed at room temperature.

AOT (sodium bis(2-ethylhexyl)sulfosuccionate, $C_{20}H_{37}NaO_7S$, Sigma, purity $\geq$99%, ρ =1.21 g/mL, M=444.56 g/mol) was kept in a vacuum desiccator for at least 24 hours before use in order to remove water residuals in the surfac-

tant. Deionized water (H_2O, ρ =1.00 g/mL, M=18.02 g/mol) and n-heptane (C_7H_{16}, anhydrous, Sigma, 99% purity, ρ =0.684 g/mL, M=100.21 g/mol) were used without any further purification. If w defines the molar ratio of water and surfactant,

$$w = \frac{[H_2O]}{[AOT]}, \tag{8.1}$$

and we set the concentration of water in the mixture to 15% (v/v) and let the mass of heptane be 20 g, then the content of each of the components can be found for any given w as illustrated in Tab. 8.1. There is a nearly linear relationship between w and the micelle radius [112]. For each solution with a given w ($w = 10$, $w = 20$, $w = 25$, $w = 35$ in Tab. 8.1) a reference solution was prepared identical to the sample except with no water (Ref.10, Ref.20, Ref.25, Ref.35 in Tab. 8.1).

Table 8.1: *Water-AOT-heptane micelle composition where $m_{heptane}$, m_{water} and m_{AOT} are the masses of heptane, water and AOT, respectively, in the mixture. The volume fraction of water in the hydrated samples is 15 %.*

sample	$m_{heptane}$ [g]	m_{water} [g]	m_{AOT} [g]
Ref.10	20.00	0	19.89
w=10	20.00	8.06	19.89
Ref.20	20.00	0	7.76
w=20	20.00	6.29	7.76
Ref.25	20.00	0	5.95
w=25	20.00	6.03	5.95
Ref.35	20.00	0	4.06
w=35	20.00	5.75	4.06

The water content of the micelle system has been set to 15 % deliberately in the attempt to create a model system which has a water content comparable to daily life food products.

Butter products, oils and lard (pig fat) were bought in a local grocery store and used without any preparation. The water content of the butter products were determined by weight before and after heating at 100°C for 24 hours.

8.2 Water-AOT-heptane mixtures

The mixture of heptane, water and AOT is a classic three components system which has been studied by molecular dynamic simulations [113] and a variety of different experimental methods, e.g. THz spectroscopy [109–111, 114], steady-state [115] and time-resolved infrared spectroscopy [116], and neutron

scattering [117]. This system forms stable inverse (w/o) microemulsions without the complications introduced by additional cosurfactant. Such a cosurfactant is required by many other reverse microemulsion systems. This simplification makes the alkane-water-AOT system a model system for studying inverse microemulsions [112, 118, 119].

The molecular structure of AOT have been shown previously, in Fig. 5.5. AOT is an anionic surfactant which gives rise to a negatively charged surfactant ion, hence anionic, and a positively charged counterion, in this case Na^+, upon dissolution in water.

Spectra of the dielectric function for several micelle samples of water-AOT-heptane are shown in Fig. 8.1. Also shown for comparison are their corresponding reference (AOT-heptane) samples as well as neat heptane.

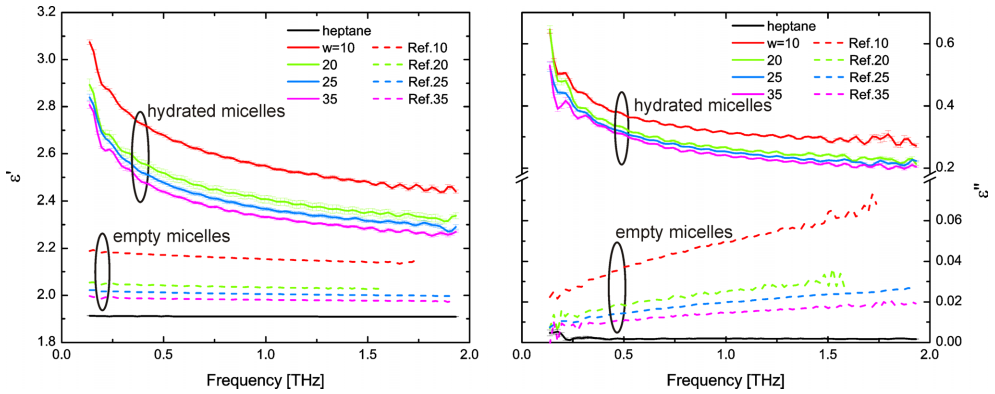

FIGURE 8.1: *Real (left) and imaginary (right) part of the complex dielectric function of water-AOT-heptane samples (hydrated micelles, solid lines) , reference samples of AOT-heptane (empty micelles, broken lines) and heptane (black solid lines). The sample compositions are given in Tab. 8.1.*

From Fig. 8.1 it can be seen that the presence of AOT leads to an increase of both the real and the imaginary part of the dielectric function. The presence of water leads to a further increase which is not surprising since the dielectric function of water is much larger than that of heptane as seen in Figs. 4.7 and 4.14.

Since we are interested in the dielectric function of the water in the micelles we have to decouple the dielectric function of the entire system. To extract the dielectric function of water we must account for the dielectric effects of the surfactant (AOT) and the solvent (heptane) as well as the spherical geometry. This decoupling procedure is described in Chapter 5.3. As described here, the model rests on several assumptions. First of all it assumes spherical geometry with no size dispersion. Previous measurements on this system show that this is a reasonable approximation [112, 120]. Moreover, the model also assumes that the dielectric function of neither the continuous phase (hep-

tane) nor the surfactant shell is altered when water is added. Again, this is a reasonable approximation since the geometry of the surfactant molecules is not strongly altered by hydration [110]. Finally, it assumes abrupt interfaces. The water-AOT interface has been studied by molecular dynamic simulations which indicate that this interface is only a few angstrom thick [113]. The thickness of the exterior AOT-heptane interface involving the tail of the surfactant is in the order of ∼12 Å, but is however less well characterized [121].

The water in the micelles can basically be characterized as either "bound" or "free" water. The bound water is found in the vicinity of the surfactant shell and this region is up to a few monolayers thick. The free water is in the center of the micelle and behaves like bulk water. Thus, the smallest micelles are dominated by the bound water whereas the larger micelles will be dominated by the free water [113, 122].

Some characteristic parameters for water-AOT-heptane mixtures are shown in Tab. 8.2. An empty micelle will have a diameter of approximately 10 Å [112] plus the length of the surfactant tail of approximately 12 Å. The finite core diameter of an empty micelle indicate that the shell is more than one layer thick [121].

Table 8.2: *Water-AOT-heptane micelle parameters. ϕ is the volume fraction of the micelle in the solution (Eq. 5.22), f is the volume fraction of the water core in the micelle (Eq. 5.21), and r_w denotes the radius of the micelle core.*

w	r_w [nm] †	ϕ	f
10	1.75	0.46	0.33
20	3.00	0.30	0.50
25	3.55	0.27	0.55
35	4.75	0.24	0.63

†Data taken from Ref. [112].

The first step in extracting the dielectric properties of water is to determine the dielectric properties of the surfactant shell. From measurements on neat heptane and the empty samples (AOT-heptane), the dielectric properties of the shell can be found from Eq. 5.22. The real and imaginary part of the extracted dielectric function of surfactant shells in the 4 different reference samples are shown in Fig. 8.2.

The surfactant shells in the different samples show almost identical dielectric properties as expected. We believe that the small differences can be attributed thermal fluctuations in the laboratory and uncertainty on the determination of the sample thickness.

The second step is to determine the dielectric properties of the entire micelle. Based on measurements on neat heptane and this time the water-AOT-heptane samples, the dielectric properties of the micelle can be found from Eq. 5.22. The third and final step is then to decouple the dielectric

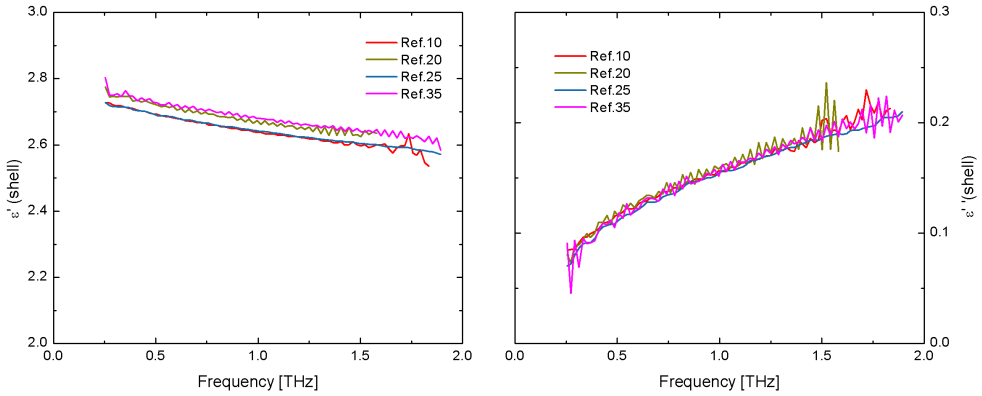

FIGURE 8.2: *Real (left) and imaginary (right) part of the complex dielectric function of the surfactant shell. All samples are without water.*

properties of the micelle and since the dielectric properties of the shell is known, the dielectric properties of the water inside the micelle can be found from Eq. 5.21.

The spectra of the extracted dielectric function of water are shown in Fig. 8.3 and compared to the dielectric properties of bulk water. The equivalent optical properties of water in micelles are shown in Fig. 8.4.

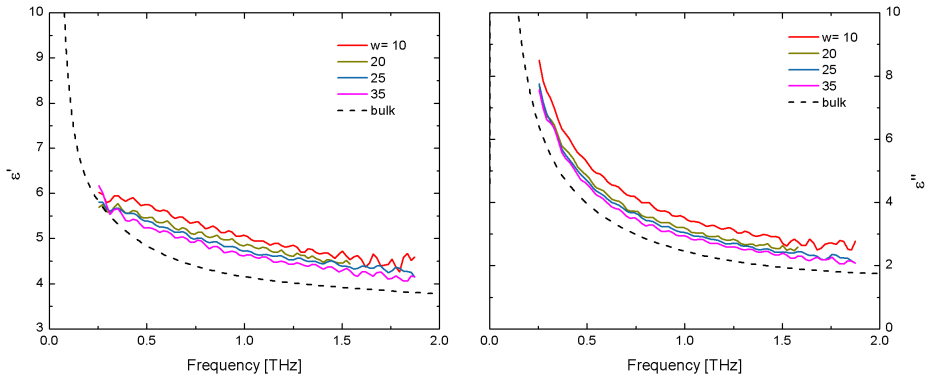

FIGURE 8.3: *Real (left) and imaginary (right) part of the extracted complex dielectric function of water in inverse micelle with the w values shown. The broken line represents a fit of bulk water (parameters from Tab 7.1).*

We observe an increase of both the dielectric properties as well as the optical properties compared to those of bulk water. The smallest micelles (w=10) exhibit the largest change compared to bulk water and as the micelles grow they resembles more and more the properties of bulk water. Any differences between these results and the properties of bulk water can be assigned to the

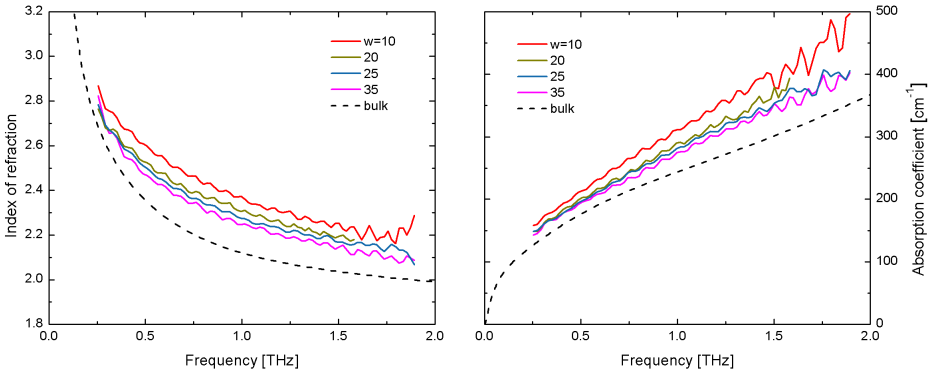

Figure 8.4: *Extracted refractive index (left) and absorption coefficient (right) of water in inverse micelle with the w values shown. The broken line represents a fit of bulk water (parameters from Tab. 7.1).*

modified environment.

Our findings are contrary to those of Mittleman *et al.* [109–111]. They observed huge resonance peaks in the absorption spectra due to surface modes of the micelles. We believe that the differences between our observations and those of Mittleman and coworkers are of two reasons. (I) The micelles in our samples make up 1/4 - 1/2 of the total volume of the solution compared to the 6 % Mittleman *et al.* used. Thus, the surface modes in our sample could be damped due to inter-micelle interactions. (II) We used AOT directly after vacuum desiccation while Mittleman *et al.* additionally purified their AOT before use. In fact, they found this purification process crucial in order to obtain their results.

The same group also did some measurements without this purification of AOT [114]. If we compare our observations of the refractive indices they are very similar to those of Mittleman *et al.*. They also observed that water in the smallest micelles had the largest absorption coefficient. However, at frequencies lower than 0.8 THz the absorption was lower than that of bulk water while it was higher for frequencies exceeding 0.8 THz. We believe that this difference can be attributed to the analyzing model. Mittleman *et al.* assumed the optical properties of water could be found based on additive Lambert-Beer-type optical properties of the sample.

In Fig. 8.5 we have illustrated the two different models for one of the sample discussed previously. The two models are different, since interfacial interactions are neglected when assuming Lambert-Beer-type optical properties of the sample.

The fact that we use an anionic surfactant implies that we have water pools containing Na^+ counterions. The molar concentrations of the counterions are $M_{w=10} \simeq 2.23$, $M_{w=20} \simeq 0.87$, $M_{w=25} \simeq 0.67$ and $M_{w=35} \simeq 0.45$ for the

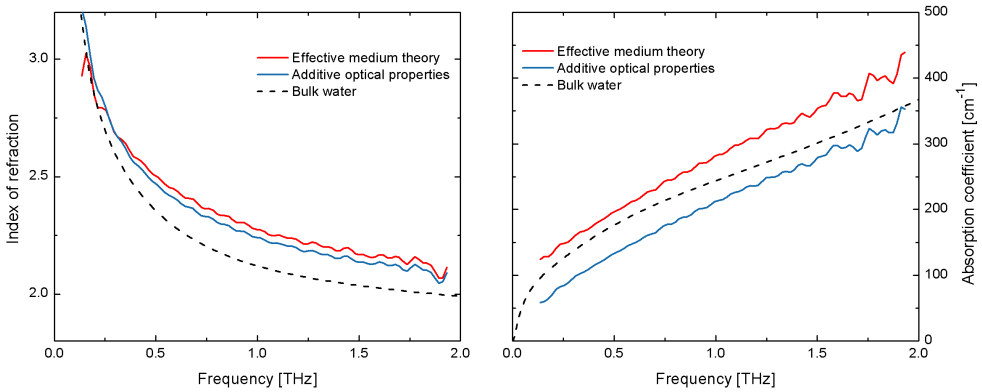

FIGURE 8.5: *Comparison of models for the w=25 sample. The red line is based on effective medium theory (Eq. 5.21-5.22) and the blue line shows additive Lambert-Beer-type optical properties. The broken line represents a fit of bulk water (parameters from Tab. 7.1).*

four solutions which compositions are given in 8.1. Xu *et. al* have investigated the absorption coefficients of both NaCl and GuHCl solutions in water, respectively, in the 0.15-0.69 THz range [123]. For moderate amounts of salts dissolved in water they report an increase of the absorption coefficient compared to that of bulk water which is consistent with measurements of other research groups [124, 125]. Despite the molecular and structural differences between NaCl and GuHCl they observed no significant difference between their THz absorbance. For a 5M NaCl solution they observed an overall increase of the absorption coefficient compared to that of bulk water. At 0.5 THz this increase was $\sim$25 cm^{-1}. A simple approach would then be to estimate the contribution from the salt to the total absorption coefficient to be in the order of $\sim$5 cm^{-1} M^{-1}. If we estimate the contribution in the same manner, based on the concentration of counterions, we get $\Delta\alpha_{w=10} \simeq$17 cm^{-1} M^{-1}, $\Delta\alpha_{w=20} \simeq$31 cm^{-1} M^{-1}, $\Delta\alpha_{w=25} \simeq$31 cm^{-1} M^{-1} and $\Delta\alpha_{w=35} \simeq$45 cm^{-1} M^{-1} at 0.5 THz. Since the relative change of the absorption coefficient is largest for the most diluted solutions this does not seem like a plausible explanation for the increase of the absorption coefficient. However, it is likely that the existence of Na^+ counterions will affect the absorption but not to the extend we observe here.

8.3 Butter

In our daily life we are surrounded by emulsions, e.g. from food and pharmaceutical products. In this section we will use the model based on effective medium theory to extract the optical properties of water in butter. This sys-

tem share two characteristics with the above described water-AOT-heptane system: The water content of butter is about 15 % and butter is an w/o emulsion. There are however also a number of dissimilarities. The water droplet size in butter is not expected to be monodisperse but is reported to be in the order of 1-25 μm in diameter, i.e. a factor of 1000 greater than the water droplets in the water-AOT-heptane system. [126].

Conventional butter is made from churning of cow milk. It consists of approximately 80% (v/v) fat, 16% water, 3% proteins and 1% salt. The size distribution of the water droplets influence many factors, e.g. the taste, shelf life and consistency of the butter [126]. Near-infrared spectroscopy combined with multivariate data analysis is the standard way to determine the major components in dairy products [127, 128]. Several methods, including confocal scanning laser microscopy and nuclear magnetic resonance spectroscopy, have been used to determine the water droplet size distribution in butter [129, 130]. Common for these methods are that they can measure droplet sizes down to approximately 0.65 μm and rely on mathematical models of the particle size distributions to estimate the number of smaller droplets.

The refractive index and absorption coefficient of two commercial butter products are shown in Fig. 8.6.

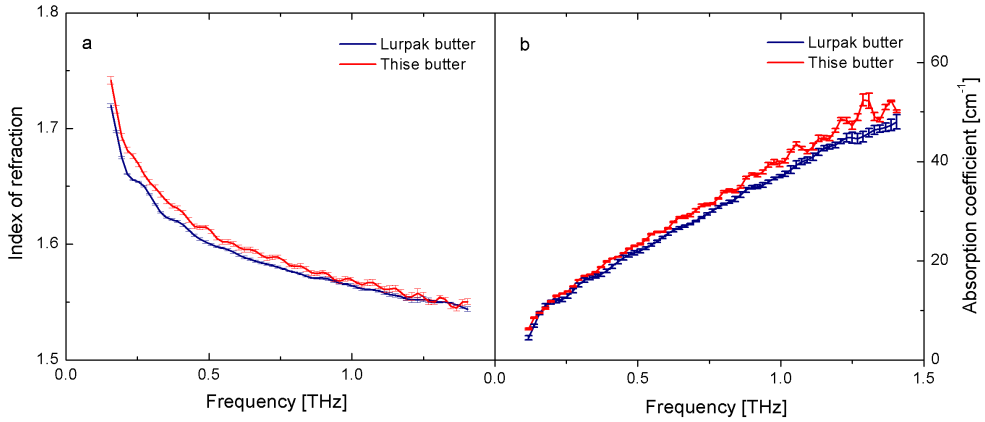

Figure 8.6: *(a) Refractive index and (b) absorption coefficient of two butter products: Lurpak (dark blue) and Thise (red).*

Butter from the same package was dried in an oven for 24h at 100°C in order to determine the water content. The water content of Thise was found to be 16.0 % (w/w) while it for Lurpak was 14.7 % (w/w). The higher optical properties of Thise compared to Lurpak can be attributed to its higher water content.

It was not possible to obtain and measure on neither a reference sample containing everything except water nor a background solution containing only the butter fat. However, we characterized several types of vegetable oils and

animal fats. Some representative measurements of the dielectric and optical properties of two types of vegetable oils, grapeseed and rapeseed oil, and one type of animal fat, lard, are shown in Fig. 8.7.

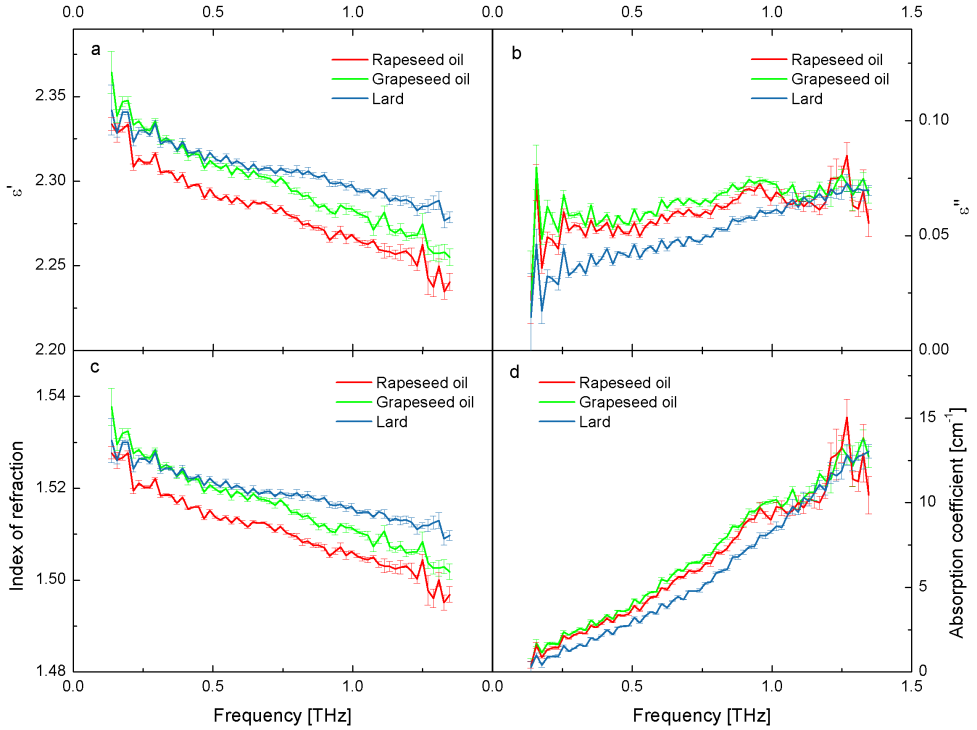

FIGURE 8.7: *(a) Real and (b) imaginary part of the dielectric function as well as (c) refractive index and (d) absorption coefficient of rapeseed oil (red), grapeseed oil (green) and lard (blue).*

In general, the dielectric and optical properties of the different oils and fats follow the same trend, even though the oils are in a liquid form while the lard is in a solid form. The real part of the dielectric function is decreasing with increasing frequency while the imaginary part of the dielectric function is close to zero, but a small increase with increasing frequency can be observed. Li and Yao have measured the optical properties of olive oil [131]. We observe a similar absorption coefficient as they have measured. The refractive indices of our oils are however slightly higher compared to their measurements (1.51-1.52 compared to 1.47).

Returning again to the measurements on butter, we have to make several assumptions in order to extract the water contribution to the total optical properties of butter. First, we use our measurements on lard as the background measurement. Since our measurements on different oils and fats show that they have similar optical properties, this seems as a fair assumption. Next,

we assume that the optical properties of the protein is similar to that of AOT. This is a crude assumption but the content of proteins only make up 3 % of the butter and it has therefore minimal influence on the optical properties.

The extracted dielectric and optical properties of water in Lurpak butter are shown in Fig. 8.8 and compared to that of bulk water.

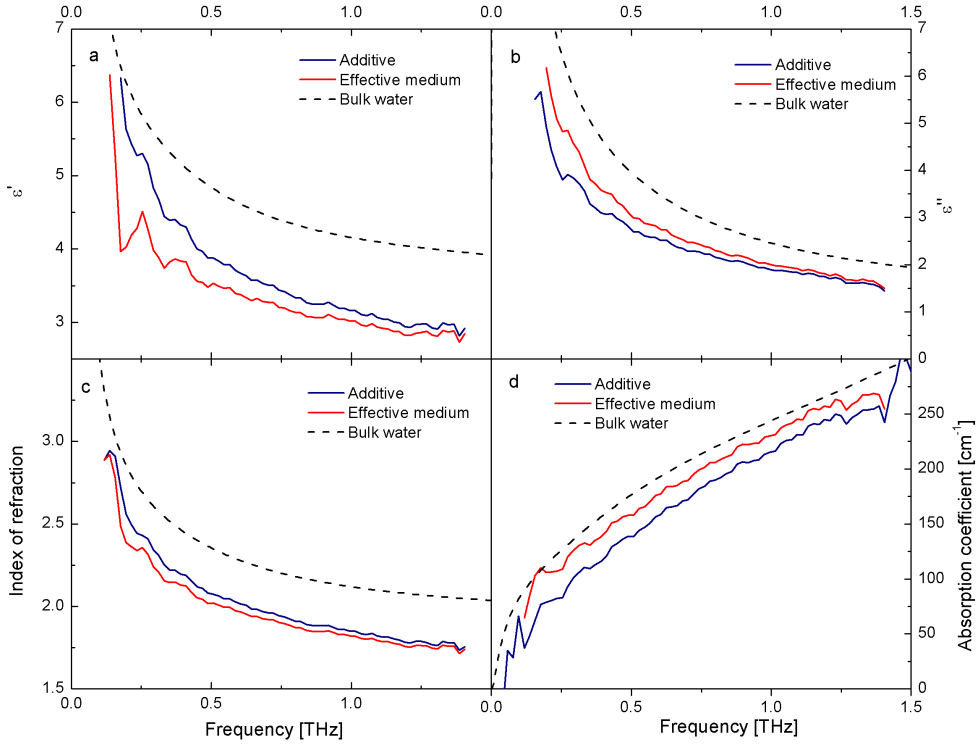

Figure 8.8: *Extracted (a) real and (b) imaginary part of the dielectric function as well as (c) refractive index and (d) absorption coefficient of water in Lurpak butter. The dark blue line is based on effective medium theory (Eq. 5.21-5.22) and the red line shows additive Lambert-Beer-type optical properties. The broken line represents a fit of bulk water (parameters from Tab. 7.1).*

We assumed for simplicity that the butter contained the measured water content (14.7% (w/w)), 3 % (w/w) proteins which makes up the shell, and the rest is fat. Similar results for the Thise butter were obtained but not shown here. We also obtained similar results when substituting the dielectric properties of lard with those of grapeseed oil or rapeseed oil. The blue curves represent additive Lambert-Beer-type optical properties while the red curves is based on effective medium theory as described in Eqs. 5.21-5.22. The low frequency spectral features, especially seen in ε', originate from standing waves in the transmission cell.

We observe that both the complex dielectric function as well as the optical

properties of water in butter are lower than those of bulk water in the 0.2-1.5 THz frequency range. The reported size distribution of the water pools in butter should imply that the majority of the water is bulk water. However, we observe a clear reduction of both the real and imaginary part of the dielectric function for the water in butter compared to those of bulk water. This indicate one of two (or a combination of two) possibilities: (a) the region of bound water is far larger than in the water-AOT-heptane system where the thickness of the bound water layer has been estimated to be only a few monolayers, and/or (b) the size distribution of the water pools has a notable contribution from very small micelles ($d \ll 1\mu m$).

The water content determination by heating can lead to an overestimate since other ingredients might have evaporated as well. However, unless the water content is grossly overestimated it can not explain the difference between the dielectric properties of water in butter and those of bulk water. In fact, the model is fairly rigid. Changing the water concentration (14.7%±2%) only gives a small change of the imaginary part of the dielectric function while we observe practically no changes of the real part of the dielectric function.

We have not taken scattering of the THz radiation into account in spite of the fact that the larger water droplets could lead to scattering, especially of the highest frequency components. However, if scattering occurs it will lead to an increase of the apparent optical properties shown in Fig. 8.8.

The optical properties of water in inverse micelles in the water-AOT-heptane system is contrary to those of water in butter. The water in the micellar model system shows a higher absorption coefficient and refractive index compared to those of bulk water, while the optical properties of water in butter are lower. As previously mentioned, Mittleman *et al.* observed huge resonance peaks in the absorption spectra due to surface modes of the micelles [109–111]. We speculate that in our case these resonant peaks are broadened and contribute to and overall monotonous increase of the absorption coefficient. The lower absorption coefficient and refractive index of water in butter compared to those of bulk water indicate that a fair amount of bound water is present in butter.

8.4 Conclusion

In this Chapter we have discussed the dielectric and optical properties of confined water in two systems: 1) nanometer-sized water pools in inverse micelles in a water-AOT-heptane system and 2) water in butter. In both cases we made use of effective medium theory in order to extract the dielectric properties of the water in each system. All the water-AOT-heptane samples contained 15% water (v/v), which is comparable to the water content of butter. We also characterized different vegetable oils and lard.

The confined water pools in inverse micelles in the water-AOT-heptane

system exhibit an increase of the absorption coefficient and the refractive index compared to those of bulk water. This increase is largest for the smallest micelles and as the micelles grow they resembles more and more the properties of bulk water. Any differences between these results and the properties of bulk water can be assigned to the modified environment. The bound water fraction of the total water content in the micelles are largest for the smallest micelles. This fact, together with a small contribution from the Na^+ counterions in the water, can explain the increase of the optical properties of the confined water compared to those of bulk water. Contrary to the results reported by Mittleman *et al.* we observe no surface vibrational modes of the water pools. This is probably due to the facts that (a) we have a high concentration of micelles, which will lead to a damping of these modes and (b) we used the surfactant directly after vacuum desiccation while Mittleman *et al.* additionally purified their surfactant before use. In fact, they found this purification process crucial in order to obtain their results.

The absorption coefficient and refractive index of water in butter was lower than those of bulk water. This indicates that a substantial part of the water in butter can be characterized as bound water. The water pool sizes in butter is reported to be in the order of 1–25 μm in diameter which suggests either that the thickness of the bound water shell also are in the μm range, or that the size distribution of the water pools has a notable contribution from very small micelles ($d \ll 1\mu m$).

The optical properties of water in inverse micelles in the water-AOT-heptane system are different from those of water in butter. The system of water-AOT-heptane is therefore not a suitable model system to describe the dynamics of water in butter.

Chapter 9

Inspection of liquids in bottles

THz radiation penetrates packing materials and clothing. Therefore the use of THz radiation for identification of hidden chemicals has been exploited, at least at the demonstration level. Such potential applications rely on specific spectral features arising from the lowest vibrational modes of the crystal lattice of the chemical substance. Hence the focus have been on inspection of dry, crystalline chemicals.

Liquids have a broadband dielectric response in the far infrared, without sharp and specific spectral features. Polar liquids interact strongly with THz radiation because of the intermolecular hydrogen bonding network. In comparison, nonpolar liquids show a much weaker interaction with THz radiation. While the lack of distinct spectral features hinder specific identification of a liquid, the contrast between polar and nonpolar liquids can be exploited for classification of a liquid. Ikeda *et al.* demonstrated that THz transmission spectroscopy can be used to distinguish between water and inflammable liquids, even through a plastic bottle [132]. Broad *et al.* used near-infrared spectroscopy to determine the distribution of ingredients in multicomponent pharmaceutical liquids, through the wall of amber plastic bottles [133]. Common to these two examples are that although identification is carried out through the plastic bottle wall, the methods rely on a known propagation distance through the liquid, and a transmission measurement.

In this Chapter an alternative method for the characterization and classification of liquids inside bottles will be described. This method eliminates the requirement of a transmission measurement, and at the same time is less sensitive to false negative tests in a scenario where bottles are screened for dangerous (e.g. inflammable or explosive) liquids. It will also be shown that the method can be used to determine the alcohol content of an aqueous liquid inside a bottle [54].

9.1 Experimental details

The method is based on the reflection of an ultrashort, broadband THz pulse from the surface of a bottle, as illustrated in Fig. 9.1.

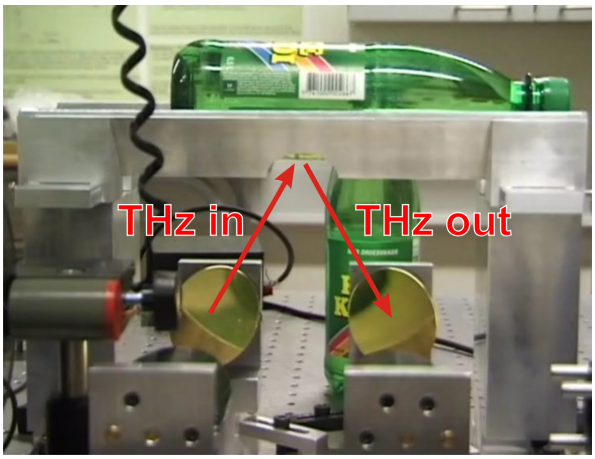

Figure 9.1: *Self-referenced reflection THz-TDS of liquids in a PET bottle.*

The THz pulse is generated and detected in a standard manner, using photoconductive dipole antennas by synchronous pulses from a femtosecond laser as described in Chapter 3.1. The principles of reflection THz-TDS are explained in Chapter 4, where the silicon slab now is exchanged with a bottle. As explained here we make use of the two reflections returned from the bottle, namely the *reference* reflection from the outer surface of the bottle, and the *sample* reflection, returned from the inner surface of the bottle material which is in contact with the liquid. Fig. 9.2 shows some of the complications that might arise when performing measurements on real bottle shapes.

A good identification system should be insensitive to whether the measurement is carried out on the bare bottle, through the label, at the edge of a label, or even through a detached piece of label.

The thickness of the bottle material as well as the topology of the bottle surface will influence the measurement. The thickness of the bottle material determines the temporal separation of the reflected reference and sample pulses, whereas the local topology strongly influences the temporal shape of both the returned pulses.

9.2 Characterization of bottle materials

Most commercial plastic bottles are made of poly(ethylene terephthalate), or PET. In Fig. 9.3 we show the optical properties (absorption coefficient and

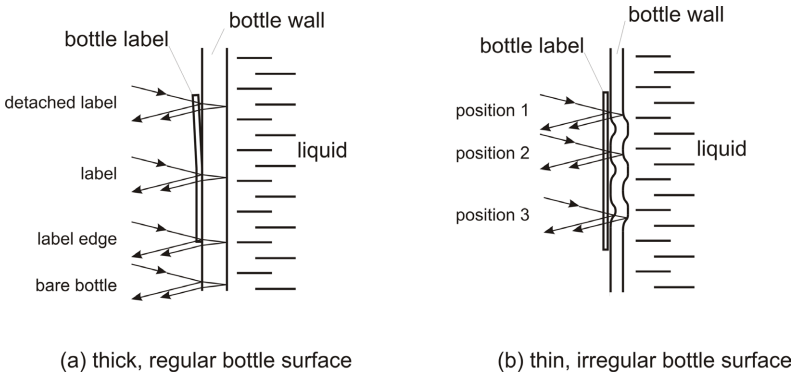

FIGURE 9.2: *Definitions of the geometry associated with reflection of the THz signal from a bottle. (a) A thick, regular bottle shape with a paper label and (b) a thin, irregular bottle shape with a loosely attached polymer label.*

index of refraction) in the THz range of different types of PET, compared to those of PMMA, or plexiglass.

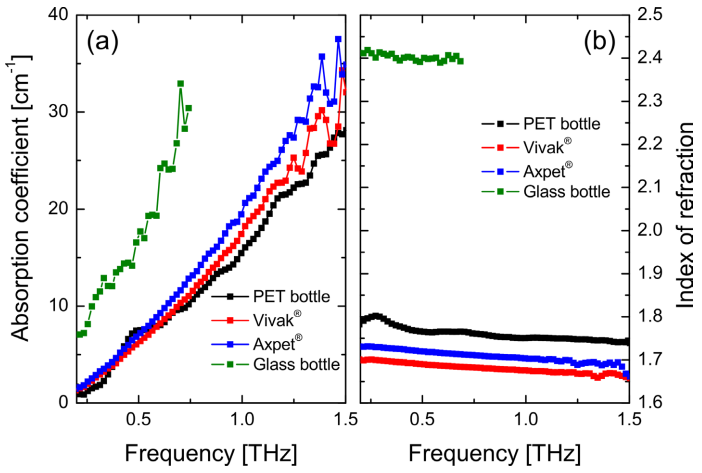

FIGURE 9.3: *(a) THz absorption coefficient and (b) index of refraction of PET, in the form of a soft drink bottle (black curves), Vivak® (red curves) and Axpet® (blue curves). The absorption and index of the glass bottle used in this study (dark olive curves) are also shown. All measurements are carried out at room temperature.*

The measurements were performed with a standard transmission THz-TDS system. We recorded the optical properties of two commercial polymers Axpet® and Vivak® as well as material cut out from a standard soft drink bottle from one of the major international brands. The absorption spectra of the different PET varieties are similar, and increase monotonically with frequency within our measurement bandwidth. The refractive indices of the

PET varieties are similar, to within 0.1.

In Fig. 9.3 we also show the optical properties of glass cut out from a typical glass bottle. The absorption and index of refraction are shown up to 0.75 THz. Above this frequency the measurement was limited by the available dynamic range of the spectrometer [64].

The absorption coefficient of the glass used in our experiments is higher than the absorption of PET, and the index of refraction of the glass is also higher than that of PET. We note that the optical properties of PET is not too different from those of commercial glasses recently studied by Naftaly and Miles [134]. A more significant difference between PET and glass bottles is the larger wall thickness that in general is required to ensure the mechanical strength of glass bottles, compared to PET bottles. A typical PET bottle for carbonated soft drinks has a wall thickness of 0.65 mm, whereas the wall thickness of a glass bottle with the same volume is 3-4 mm. This, together with the somewhat higher absorption of glass compared to PET, leads to approximately an order of magnitude smaller transmission through a glass bottle wall compared to that of a PET bottle wall.

9.3 Inspection of liquids inside labeled bottles

We will now investigate the possibility of inspection of the properties of a liquid through the wall of a bottle, possibly covered by paper or plastic labels. For this purpose we filled a PET bottle (0.65 mm wall thickness) with water, and recorded the reflected THz signal from the bottle, with the THz beam incident at various locations on the bottle surface, as illustrated in Fig. 9.2. Later the measurements were repeated with isopropanol in the bottle. Isopropanol is a flammable liquid with a slightly lower index of refraction and slightly lower absorption coefficient than ethanol. Hence the data shown in this section may indicate how a low-index, volatile liquid can be distinguished from a high-index, non-volatile liquid.

Fig. 9.4a shows the THz signal reflected from a bare part of the bottle (blue, lower trace), from a position on the bottle completely covered by a paper label (red, middle trace), and from a position on the bottle partly covered by a paper label (green, upper trace). In Fig. 9.4b the reflected signals from similar positions on the same bottle filled with isopropanol are shown. In this plot an additional trace is shown, recorded at a position on the bottle where the label was detached from the bottle.

In all the situations considered in Fig. 9.4a the reflected signal consists of a reference signal and a sample signal, well separated from each other and with a relatively constant temporal shape. Even when the signal is reflected at a point near the edge of the label the signal shape is intact. The additional optical path through the label can be observed as a slight additional delay of the sample signal with respect to the reference signal, compared to the

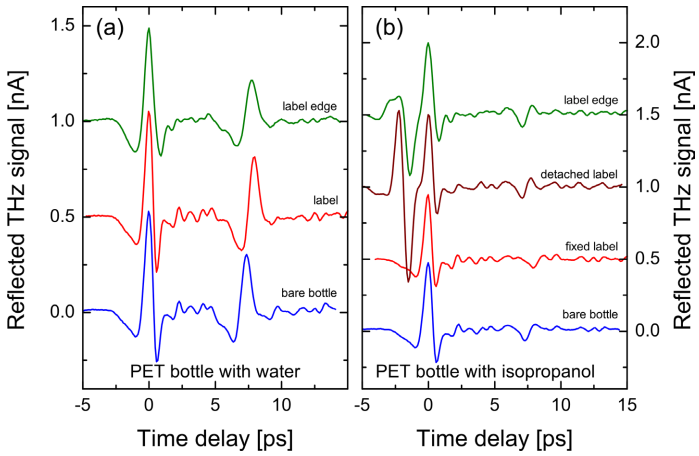

FIGURE 9.4: *Reflected THz signals from a PET bottle containing (a) water and (b) isopropanol. The different traces show the reflected signal from a position on the bare bottle, from a position at the edge of the paper label, and from a position on the label.*

reflected signal from the bare bottle.

The set of measurements on the isopropanol-filled bottle, shown in Fig. 9.4b again show a clear separation between the reference signal and the sample signal. As expected the sample signal is significantly lower than that in Fig. 9.4a. In addition the reference signal is strongly modified when the THz beam samples a position on the bottle with a detached label. Here the reference signal splits up due to the additional dielectric interfaces in the beam path. A similar, although less pronounced splitting is observed when we sample at the edge of the label. The reference signal recorded from the edge of the label is different from the similar measurement shown in Fig. 9.4a. We took no special precautions to reflect off the exact same location of the bottle in these two situations, so the difference in the reference signal is representative of the spread in signal shapes that might be encountered in the general case.

The influence of atmospheric absorption is seen clearly as additional oscillations in all traces shown in Fig. 9.4. The experiments were carried out outside of the purged chamber of the THz-TDS system, with a THz beam path of 81 cm. Especially when investigating low-index liquids inside the PET container it is seen that the additional oscillations caused by the atmospheric absorption to some extent masks the sample reflection, hence making quantitative measurements difficult. This problem can, however, be minimized by reducing the THz beam path to an absolute minimum, for instance by integrating the THz emitter and detector in a handheld unit that can be brought into contact or to close proximity of the bottle.

Measurements on thinner PET bottles will lead to a smaller separation of

the reference and sample signals, as shown in Fig. 9.5. Here measurements are carried out on a 0.17 mm PET bottle, typically used for still drinking water.

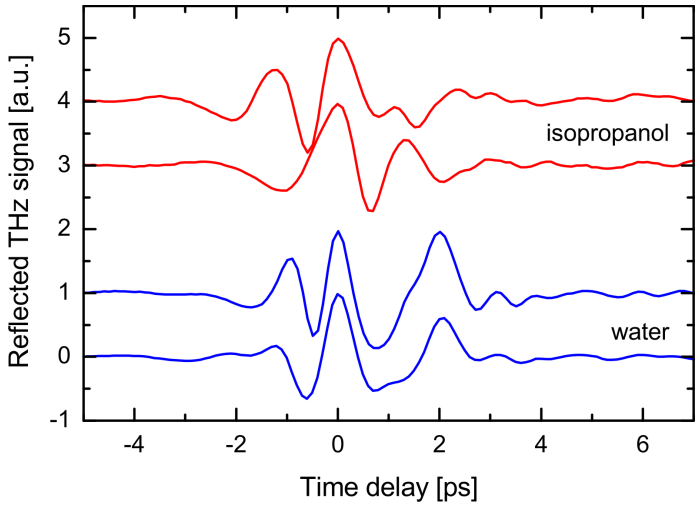

Figure 9.5: *Reflected THz signals from a thin (0.17 mm wall thickness) PET bottle containing water (lower two traces, shown in blue color) and and the same bottle containing isopropanol (upper two traces, shown in red color). Each trace was recorded at a new position on the bottle.*

The two lower traces, shown in blue color, show reflected signals from a bottle containing water, and sampled at two different positions on the bottle surface, through the thin plastic label of the bottle. The two top traces, shown in red color, are similar traces recorded at two different positions on the same bottle filled with isopropanol. The variation among the reference signals in the four traces is significant, and the small temporal separation between the reference and sample signal makes a clear distinction between the two signals difficult. However, in spite of the more complicated signal structure compared to reflections from a thicker bottle, the signature of the water is still strong, and easy to distinguish from the isopropanol traces.

9.4 Simulation of reflected THz signals from bottles

In this section we will present a numerical simulation of the properties of the reflected THz signal from a bottle containing an aqueous solution of ethanol, and show how the reflected signal can be used to predict the alcohol content of the solution.

The reflected THz pulse sequence from the bottle wall can be described in terms of the Fresnel reflection and transmission coefficients of the interfaces

of the bottle material which are given in Chapter 2.2. These coefficients are determined by the incidence angle and the optical properties of the bottle material and the liquid in the bootle. The reflected field from the outer surface $E_{ref}(\omega)$ and the reflected field from the inner surface in contact with the liquid, $E_{sam}(\omega)$ can be expressed as

$$E_{ref}(\omega) = E_i(\omega)(\hat{r}_{12}^{\parallel} + \hat{r}_{12}^{\perp}), \quad (9.1)$$

$$E_{sam}(\omega) = E_i(\omega)e^{-\alpha_2(\omega)d_{eff}-2in_2(\omega)\omega d_{eff}/c} \cdot (\hat{r}_{23}^{\parallel}\hat{t}_{12}^{\parallel}\hat{t}_{21}^{\parallel} + \hat{r}_{23}^{\perp}\hat{t}_{12}^{\perp}\hat{t}_{21}^{\perp}), \quad (9.2)$$

which are also discussed in detail in Chapter 4.3. The complex index of refraction of the bottle material is defined in the usual manner, $\hat{n}_2 = n_2 - i\alpha_2 c/2\omega$, and the calibration term $A_{cal}exp[i\phi] = 1$

The optical properties of the alcohol-water mixture can be described in terms of the Debye model as described in Chapters 5 and 7. Based on the dielectric functions of the ethanol-water mixtures presented in Chapter 7, it is possible to make a parameterized, phenomenological model of the dielectric function of ethanol-water mixtures as a function of the ethanol concentration for all mass fractions x_{EtOH}. This parametrization is shown in Appendix B. The optical properties of the bottle materials are also parameterized and further described in Appendix B.

In Fig. 9.6 the real and imaginary parts of the calculated dielectric function of water-ethanol mixtures are shown with solid lines, as function of frequency and ethanol mass fraction. Also shown are the measured real and imaginary parts of the dielectric function of neat water and of neat ethanol.

9.5 Inspection of alcohol strength through a bottle wall

Here we use the self-referencing reflection principle to investigate the optical properties of a liquid, without removing the liquid from its bottle.

In Fig. 9.7a we show the result of a simulation of the return signal from a 0.65 mm PET bottle containing different water-ethanol mixtures. As input pulse for the simulation we used the signal measured in our reflection spectrometer with the PET bottle replaced by a plane, metallic mirror. We applied Eqs. 9.1 and 9.2, using the Fresnel equations which are calculated using the optical properties of PET and the water-ethanol mixtures discussed above.

The simulation results show that we should expect a strong sample reflection from a PET bottle containing neat water, and that this reflection should diminish in amplitude with increasing alcohol concentration. Additionally we observe a significant reshaping of the shape of the sample signal. The dispersion of the water-ethanol mixture changes with composition of the mixture. For the highest alcohol concentrations there will be a frequency within our bandwidth with perfect index match between the PET and the liquid mixture. Hence this reshaping is expected.

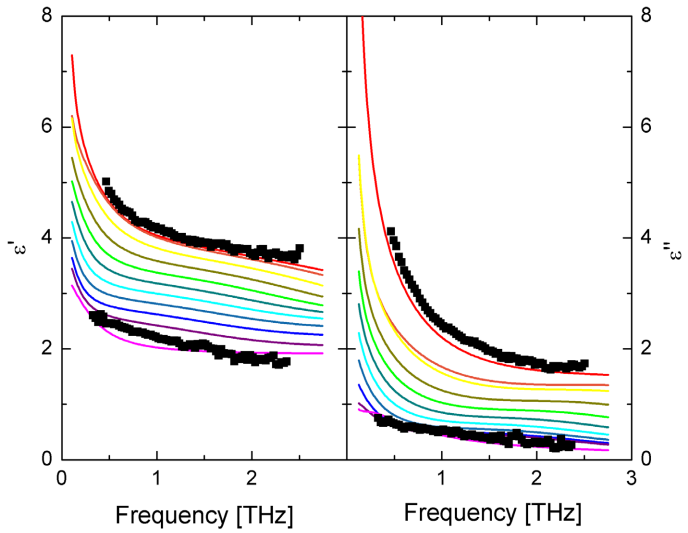

Figure 9.6: *(solid lines) (a) Real and (b) imaginary part of the modeled dielectric function of water-ethanol mixtures, in 10% increments. The experimental data for neat water and neat ethanol were recorded by ATR THz-TDS. Experimental data for water and ethanol is shown with solid squares.*

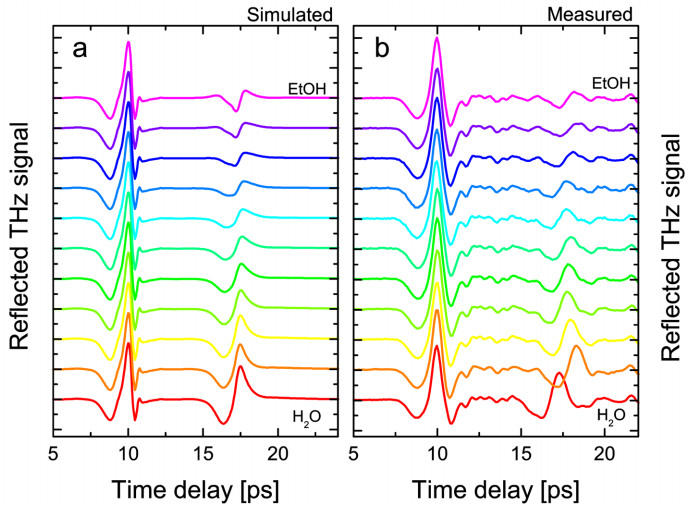

Figure 9.7: *(a) Simulated and (b) measured reflected THz signal from a PET bottle with 0.65 mm wall thickness, containing mixtures of water and ethanol. The red, lower traces represent the reflection from neat water and each successive curve represents a 10% increase in ethanol mass fraction.*

Fig. 9.7b shows the experimental results, obtained under the same conditions as used in the simulation shown in Fig. 9.7a, i.e. with a PET bottle of

0.65 mm wall thickness. The PET bottle was removed from the spectrometer between each measurement, for replacement of the liquid. The measurements were carried out at approximately the same spot on the bottle, through the paper label glued to the bottle. No special precautions were taken to ensure the exact same measurement conditions for each scan. The effect of small differences between each scan is seen as slight deviations of the temporal position of the sample reflection with respect to the reference reflection due to variations of the bottle wall thickness. The experiment reproduces the simulation quite well. We observe a decreasing amplitude of the sample signal with respect to the reference signal with increasing alcohol strength as well as a significant reshaping of the sample signal. The additional oscillations present in the experimental traces in comparison to the simulated traces are due to water vapor in the THz beam path.

The good agreement between simulation and experiment demonstrated in Fig. 9.7 indicates that the experimental details left out of the simulation, such as the relatively low radius of curvature of the bottle, the paper label, and the irregular surface, do not significantly influence the result of the measurements. These geometrical factors will influence the reference signal and the sample signal in approximately the same manner, and hence the ratio of the two signals will be stable against changes in the geometry of the experiment.

In Fig. 9.8 we show the result of a simulation of the reflected signal from a 3.0 mm glass bottle containing different water-ethanol mixtures. The simulation was carried out as described above, using the optical properties of the glass material shown in Fig. 9.3.

The thicker glass wall compared to the PET bottle, together with the higher index, leads to a delay of 50 ps of the sample signal with respect to the reference signal. The increased wall thickness results in strong attenuation of the sample signal with respect to the reference signal. In contrast to the return signal from the PET bottle, we observe only a modest dependence of the sample signal strength on the alcohol concentration of the liquid. We do, however, observe a significant reshaping of the sample signal that resembles a sign change of the signal, or a 180-degree phase shift. The average refractive index of the glass is located between the refractive indices of neat water and of neat ethanol. Hence, neglecting the frequency dependence of the refractive indices, the sign of the sample signal with respect to the reference signal should change from positive to negative with increasing ethanol concentration. The deviation from the pure sign change is mainly caused by the frequency dependence of the refractive indices of the liquid.

Figure 9.9 shows the result of a measurement carried out under the same conditions as the simulation of the reflected signal from the glass bottle.

There is a good agreement between the simulation results and the experimental data. Experimentally we observe the sample signal 50 ps after the reference signal, and we observe a strong attenuation of the sample signal. The attenuation is slightly weaker than seen in the simulation. We believe

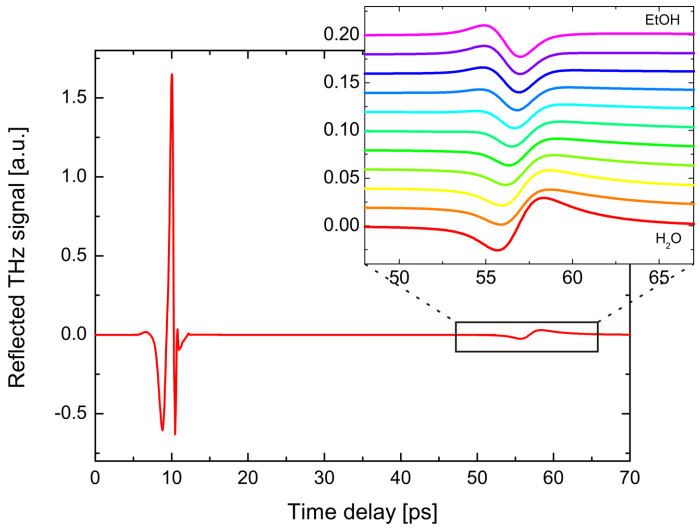

Figure 9.8: *Simulated reflected THz signal from a glass bottle with 3.0 mm wall thickness, containing neat water. The inset shows the shape of the second reflection in dependence of the ethanol concentration in the mixture. The red, lower trace represents the reflection from neat water and each successive curve represents a 10% increase in ethanol mass fraction.*

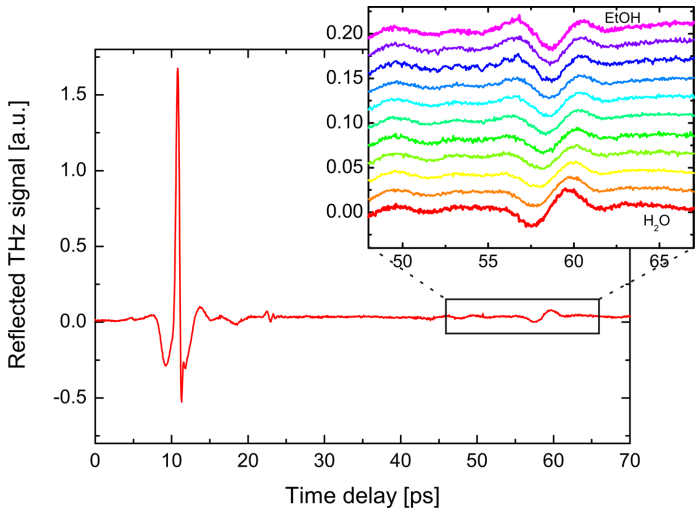

Figure 9.9: *Measured reflected THz signal from a glass bottle with 3.0 mm wall thickness, containing neat water. The inset shows the shape of the second reflection in dependence of the ethanol concentration in the mixture. The red, lower trace represents the reflection from neat water and each successive curve represents a 10% increase in ethanol mass fraction.*

that the weaker apparent attenuation could be caused by impurities in the glass which have decreased the absorption. The optical path difference between the two reflection planes is 14.4 mm, and the THz beam is incident on the glass bottle at an incidence angle of 30 degrees, focused by an off-axis paraboloidal mirror with an effective focal length of 101.6 mm. Hence the added propagation distance through the glass will lead to some deviation away from the ideal THz propagation axis of the part of the THz signal that is reflected from the glass-liquid interface.

The dependence of the reflected sample signal both from the PET bottle and from the glass bottle on the alcohol concentration suggests that the alcohol concentration x of the liquid inside the bottle can be determined by the ratio of the integrated field strength of the sample pulse and that of the reference pulse. In Fig. 9.10 we show this ratio R, defined as

$$R(x) = \sqrt{\frac{\sum E^2_{sam,x}(t_i)}{\sum E^2_{ref,x}(t_j)}} \tag{9.3}$$

where the summation indices i and j are chosen so that the sum covers the full sample- and reference pulses, respectively. The solid, black squares represent the measured ratios, whereas the solid red curves represent the result of the simulation discussed above. Figure 9.10a shows the results for the PET bottle and Fig. 9.10b shows the results for the glass bottle.

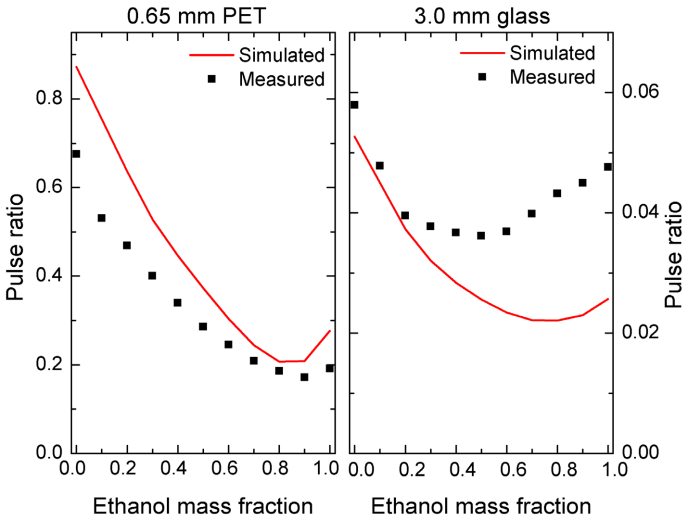

FIGURE 9.10: *The ratio of the strengths of the second to the first pulse reflected off an (a) 0.65 mm PET bottle and (b) a 3.0 mm glass bottle, as functions of the ethanol concentration of the water-ethanol mixture in the bottles. Red curves represent a simulation, square symbols represent measurements.*

The agreement between the experimentally determined ratio and the simulated one is good for the PET bottle, and the monotonous dependence of the ratio on the alcohol concentration allows the determination of unknown alcohol concentrations [52], at least for alcohol concentrations up to 80%. Interestingly both the simulated and measured $R(x)$ increases slightly at the highest alcohol concentrations, indicating that for the highest alcohol concentrations the index of refraction of the liquid crosses that of the PET material. The minimum of the ratio at 90% alcohol concentration corresponds to the best possible index match between the bottle wall and the liquid. The permittivity of PET is 3.06 (see Fig. 9.3b). Inspection of Fig. 9.6 confirms that the highest alcohol concentrations results in a permittivity of the liquid below this value.

For the glass bottle, the measured ratio is higher than the simulated one. The possible reasons for the higher measured ratios are discussed above. The dependence of the ratio on the alcohol content is similar for the simulated and the measured data. The higher refractive index of the glass material shifts the minimum $R(x)$ to lower alcohol concentrations, and results in the observed non-monotonous behavior of $R(x)$. This makes an unambiguous determination of unknown alcohol concentrations in a glass bottle difficult, at least if the ratio R is used as the only estimator.

However, inspection of the progression of the sample signal with alcohol concentration makes it clear that additional information about the composition of the liquid is stored in the significant reshaping of the sample signal. If we for instance use the difference between the sample signal from the bottle filled with the alcohol solution and that from the same bottle with water, $E_{diff,x}(t) = E_{sam,x}(t) - E_{sam,H_2O}(t)$, we can calculate a difference ratio $R_{diff}(x)$ similar to the ratio defined in Eq. 9.3 to obtain a signal with a strength that depends monotonously on the alcohol concentration x,

$$R_{diff}(x) = \sqrt{\frac{\sum E^2_{diff,x}(t_i)}{\sum E^2_{ref,x}(t_j)}} \tag{9.4}$$

In Fig. 9.11a we plot the sample difference signal $E_{diff,x}(t)$ with varying alcohol concentration x. In contrast to the sample signals themselves, the shape of the difference signals is independent of the alcohol concentration, whereas the difference signal strength increases monotonously with alcohol concentration. This indicates that the difference signal is mainly due to the change of the real part of the refractive index of the liquid, and that the additional phase shift associated with changes in the imaginary part of the refractive index has little influence on the reflected signal shape. In Fig. 9.11b the ratio $R_{diff}(x)$ is plotted as function of the alcohol concentration in the bottle. This difference ratio increases monotonously with the alcohol concentration, and is hence useful for the determination of unknown alcohol concentrations in the bottle. The difference ratio shown in Fig. 9.11 never reaches zero, even for the

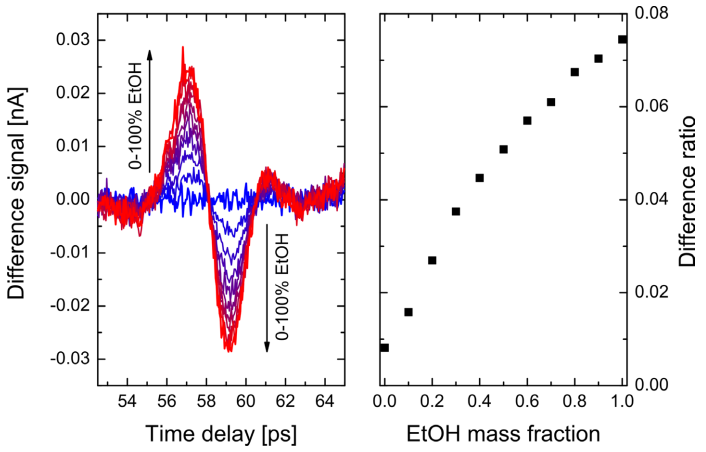

FIGURE 9.11: *(a) Time traces of the the difference sample signal reflected from a glass bottle for various ethanol concentrations. (b) The ratio $R_{diff}(x)$ of the strength of the difference signal with respect to the reference signal, as function of alcohol concentration.*

measurement on neat water. This is due to experimental noise, which is not averaged out in the calculation of the difference ratio since the square of the instantaneous field strength is used in the summations.

9.6 Conclusion

We have described a method for contact-free inspection of liquids inside bottles. The method relies on the reflection of a THz transient from the bottle. It works by a comparison of the two signals reflected from the bottle; one reflection from the outer surface of the bottle wall and one reflection from the inner surface, in contact with the liquid, of the bottle wall. The automatic generation of a reference signal from the outer bottle surface is useful as a validity check of the measurement. In contrast to a transmission measurement, where the lack of a transmitted signal in principle can be due to either strong absorption or a misalignment of the system, the lack of any reflected signal clearly indicates an error in the measurement. In a calibrated system the strength of the outer reflection can also be used for automatic identification of the bottle material, based on its index of refraction.

Our experimental and numerical results showed that the method works on both PET bottles and glass bottles. The capability to inspect the content of a glass bottle depends critically on the thickness of the glass, due to the strong absorption of THz waves in the glass material. Hence the dynamic range of the THz detection system is important for the maximum thickness of the glass

material. An estimate of the maximal thickness of the glass material is

$$d_{max} \approx \frac{1}{\alpha} \ln(DR) \tag{9.5}$$

where DR is the dynamic range of the detection system and *alpha* is the absorption coefficient of the glass material at the frequency where the dynamic range is defined. For the measurements presented in this work ($DR \approx 1000$ and $\alpha \approx 20$ cm^{-1}) we find $d_{max} \approx 0.35$ cm.

The concentration of alcohol solutions in PET bottles could be determined by a measurement of the ratio $R(x)$. For the same solutions in glass bottles the simple ratio $R(x)$ is no longer sufficient for an unambiguous determination of the alcohol strength. The difference ratio $R_{diff}(x)$ was introduced to allow determination of unknown alcohol concentrations in a glass bottle. This modified method can then be applied in situations where it is possible to obtain a reflected signal from a similar bottle containing either neat water or neat ethanol.

Conclusion and outlook

Conclusion

In this thesis we present and discuss terahertz time-domain spectroscopy (THz-TDS) applied to food model systems. The theory behind is found in Chapters 2–5 while the experimental outcome of this research is presented in Chapters 6–9. The main results and conclusions are summarized here.

THz transmission, reflection and attenuated total reflection spectroscopy

The analysis of measurements based on THz transmission, reflection and attenuated total reflection (ATR) spectroscopy all relies on the Fresnel equations. This means that all methods, in principle, will yield the equivalent information about the optical properties of the sample. In Chapter 4.5 it was demonstrated that the best suitable method depends on the sample under investigation. It was demonstrated that transmission spectroscopy is well suited for investigation of low absorbing samples while ATR spectroscopy is superior when it comes to measurements on high absorbing samples.

In case of transmission spectroscopy the sensitivity of the spectrometer relies on the thickness of the sample and there is an optimal sample thickness where the sensitivity is largest. This optimal sample thickness should however be weighted against the possibility of multiple reflections which will complicate the analysis.

Even though the ATR spectroscopy method was showed to be superior to the reflection method when it comes to spectroscopy, the latter method is still useful in many cases, e.g. in stand-off detection systems, imaging systems, contact-free spectroscopy of hazardous samples.

The dynamic range of the spectrometer and the sample thickness determine the maximum detectable absorption coefficient and thus the bandwidth of the system in the case of transmission geometry. In case of ATR and reflection geometry the maximum detectable absorption will depend on the phase accuracy and amplitude accuracy. This limit will typically lie well above absorption coefficients that are normally encountered in dielectric and semiconductor materials.

There is a fundamental difference between the THz spectroscopy methods. In THz transmission spectroscopy the THz radiation interacts with a volume of the sample, whereas the THz radiation in both of the THz reflection spectroscopy techniques interacts with the sample in the vicinity of its surface. This difference implies that the reflection technique is very vulnerable to changes in the vicinity of the surface of the sample, e.g. when phases separate in emulsions. On the other hand the reflection geometry can be an advantage. This is seen in the case of measurements on carbonated liquids. The air bubbles is simply led away from the surface and are therefore not influencing the measurements.

Determination of ethanol and sucrose contents in aqueous mixtures

The dielectric responses of water and ethanol in the THz region are very dissimilar. While water, because of its weak hydrogen-bonded network, interacts strongly with the THz radiation the interaction of ethanol takes place to a less extend. Based on reflection THz time-domain spectroscopy it was discussed in Chapter 6 how the differences in the dielectric properties of water and ethanol can be used to determine the ethanol content of an ethanol-water solution, despite the lack of spectral features in the spectra. The method also turned out to be useful for determination of the alcohol content in commercial alcoholic liquids with little or no influence from the color, carbonation, sediments and moderate amounts of sugar of the sample. For low ethanol contents the predicted values were within 1% of the actual value and for higher ethanol concentrations it was within a few percent.

The fact that both the real and the imaginary part of the dielectric function are determined directly in THz-TDS makes it possible to determine the concentration of up to two components. It was demonstrated how to extract the concentrations of sucrose and ethanol in sucrose-ethanol-water solutions with an accuracy of a few percent. The simple model requires that no other components (besides the two unknown) in the liquid contributes significantly to changes of the dielectric function of the solvent and that changes of the dielectric function derived from the presence of two unknown components can be described as the sum of the individual contributions.

Dielectric properties of ethanol-water mixtures

In Chapter 7 the dielectric properties of ethanol-water mixtures with varying concentrations were measured with ATR THz-TDS and combined with previously published microwave data. This enabled us to cover the frequency range 100 MHz - 2.5 THz and thereby to obtain a complete coverage of the frequency range that contains all the relaxation processes and the lowest intermolecular vibration process.

Water and low concentrated (up to a molar fraction of 4 %) ethanol-water mixtures were found to be well described by the Debye relaxation model with two Debye relaxation terms while ethanol and ethanol-water mixtures were found to be well described by three Debye relaxation terms. In the case of water and water-ethanol mixtures, the presence of the lowest intermolecular vibrational mode influences our data, and this mode was included in the modeling.

We found that the characteristics of the relaxation processes (relaxation strength and relaxation time constants) are correlated with the macroscopic thermodynamic properties of the liquid. Specifically it seems like there is a strong correlation between the mixing volume of ethanol-water mixtures and the intermediate and fast relaxation times - the smaller the mixing volume, the slower these relaxation times appear to be. Similarly, the largest enthalpy of mixing of ethanol-water mixtures appear at an ethanol concentration where the strength of the slow relaxation process is smallest and the strength of the intermediate relaxation process is highest.

We believe that our data and the links to the thermodynamic properties of the liquids could serve as inspiration for molecular dynamics simulations that may help to shed further light on the intriguing microscopic dynamics of the liquids that we have studied. The use of terahertz time-domain spectroscopic techniques is an important tool for the detailed understanding of the relaxation dynamics of polar liquids, where processes important for the macroscopic thermodynamic properties of the liquids take place on the picosecond to sub-picosecond time scale.

The frequency coverage of the THz-TDS system is an important factor for the interpretation of the results. Based on the results presented in Chapter 7 it is obvious that it is not possible to rely solely on data in the low THz region, since the faster processes are not covered by such experiments. We therefore believe that the ongoing progress on the improvement on bandwidth of THz-TDS systems, for instance by ultrabroadband photoconductive emitters and detectors or novel nonlinear crystals for ultrabroadband THz generation and detection by electrooptic processes will be very important for the progress of the experimental verification of numerical results. Furthermore, the low-frequency range, up to 0.1 THz, which is well-covered by microwave dielectric spectroscopy, plays a major role. Thus, spectroscopic studies that include both microwave techniques and the broadband THz techniques are important in order to obtain a complete picture of the extremely broadband relaxation processes in polar liquids.

Confined water in inverse micelles

In Chapter 8 we discussed the dielectric and optical properties of confined water in two systems: 1) nanometer-sized water pools in inverse micelles in a water-AOT-heptane system and 2) water in butter. In both cases we made

use of effective medium theory in order to extract the dielectric properties of the water in each system. All the water-AOT-heptane samples contained 15% water (v/v), which is comparable to the water content of butter. We also characterized different vegetable oils and lard.

The confined water pools in inverse micelles in the water-AOT-heptane system exhibit an increase of the absorption coefficient and the refractive index compared to those of bulk water. This increase is largest for the smallest micelles and as the micelles grow they resembles more and more the properties of bulk water. Any differences between these results and the properties of bulk water can be assigned to the modified environment. The bound water fraction of the total water content in the micelles are largest for the smallest micelles. This fact, together with a small contribution from the Na^+ counterions in the water, can explain the increase of the optical properties of the confined water compared to those of bulk water. Contrary to the results reported by Mittleman *et al.* we observe no surface vibrational modes of the water pools. This is probably due to the facts that (a) we have a high concentration of micelles, which will lead to a damping of these modes and (b) we used the surfactant directly after vacuum desiccation while Mittleman *et al.* additionally purified their surfactant before use. In fact, they found this purification process crucial in order to obtain their results.

The absorption coefficient and refractive index of water in butter was lower than those of bulk water. This indicates that a substantial part of the water in butter can be characterized as bound water. The water pool sizes in butter is reported to be in the order of 1–25 μm in diameter which suggests either that the thickness of the bound water shell also are in the μm range, or that the size distribution of the water pools has a notable contribution from very small micelles ($d \ll 1\mu m$).

The optical properties of water in inverse micelles in the water-AOT-heptane system are different from those of water in butter. The system of water-AOT-heptane is therefore not a suitable model system to describe the dynamics of water in butter.

Inspection of liquids in bottles

In Chapter 9 we described a method for contact-free inspection of liquids inside bottles. The method relies on the reflection of a THz transient from the bottle. It works by a comparison of the two signals reflected from the bottle; one reflection from the outer surface of the bottle wall and one reflection from the inner surface, in contact with the liquid, of the bottle wall. The automatic generation of a reference signal from the outer bottle surface is useful as a validity check of the measurement. In contrast to a transmission measurement, where the lack of a transmitted signal in principle can be due to either strong absorption or a misalignment of the system, the lack of any reflected signal clearly indicates an error in the measurement.

Our experimental and numerical results showed that the method works on both PET bottles and glass bottles. The capability to inspect the content of a glass bottle depends critically on the thickness of the glass, due to the strong absorption of THz waves in the glass material. Hence the dynamic range of the THz detection system is important for the maximum thickness of the glass material.

The concentration of alcohol solutions in PET bottles could be determined by a measurement of the ratio $R(x)$. For the same solutions in glass bottles the simple ratio $R(x)$ is no longer sufficient for an unambiguous determination of the alcohol strength. The difference ratio $R_{diff}(x)$ was introduced to allow determination of unknown alcohol concentrations in a glass bottle. This modified method can then be applied in situations where it is possible to obtain a reflected signal from a similar bottle containing either neat water or neat ethanol.

Outlook

There is still room for improvements and progress in the field of terahertz spectroscopy both in general and in the field of subjects treated in this thesis.

THz transmission, reflection and attenuated total reflection spectroscopy

The frequency coverage of the THz-TDS system is an important factor for the interpretation of measurements. We therefore believe that the ongoing progress on the improvement on bandwidth of THz-TDS systems, for instance by ultrabroadband photoconductive emitters and detectors or novel nonlinear crystals for ultrabroadband THz generation and detection by electrooptic processes will be very important for the progress of the experimental verification of numerical results.

The development of high power THz radiation is also important in order to do nonlinear spectroscopy to gain additional information about the sample under investigation.

It is also essential to reduce the costs and lower the acquisition time of THz-TDS systems. Therefore is the ongoing development of e.g. fiber coupled systems at telecom wavelengths is crucial in order to move analysis systems based on THz out from the laboratories to the industry.

The field of THz spectroscopy has still a lot to gain by adapting techniques from more mature spectroscopic methods. For example it would be interesting to implement multiple reflection ATR spectroscopy which is known from infrared spectroscopy. Such a geometry would allow the THz radiation to interact multiple times with the sample which could lead to more detailed measurements.

Determination of ethanol and sucrose contents in aqueous mixtures

With simple analysis of an aqueous sample we showed that unknown concentrations of up to two components could be determined. For more complex systems, the obvious way forward is to combine the THz measurements with multivariate data analysis which is widely used in other spectral ranges.

There is also a need for continuous investigation of the actual physical processes that occur when components are mixed.

Dielectric properties of ethanol-water mixtures

As previously mentioned, the frequency coverage of the THz-TDS system is an important factor for the interpretation of the results. Based on the results presented in Chapter 7 it is obvious that it is not possible to rely solely on data in the low THz region, since the faster processes are not covered by such experiments. Furthermore, the low-frequency range, up to 0.1 THz, which is well-covered by microwave dielectric spectroscopy, plays a major role. Thus, spectroscopic studies that include both microwave techniques and the broadband THz techniques are important in order to obtain a complete picture of the extremely broadband relaxation processes in polar liquids.

The correlations between the characteristics of the relaxation processes and the macroscopic thermodynamic properties of the liquid need to be investigated further in order to understand the origin of this correlation. This can for example be done by measurements at different temperatures which will change the thermodynamic properties of the system and through that shed further light on the possible link between the dielectric properties and the thermodynamic properties of various systems.

Different microscopic pictures of the different relaxation processes in liquid water as well as water-ethanol mixtures have been suggested. There is a need for further investigations, both experimental and by molecular dynamic simulations, in order to understand the actual processes taking place.

Confined water in inverse micelles

The measurements presented in Chapter 8 showed that the optical properties of water in inverse micelles in the water-AOT-heptane system are different from those of water in butter. The system of water-AOT-heptane is therefore not a suitable model system to describe the dynamics of water in butter. It would therefore be interesting to produce a model system that resembles butter in a better way.

The role of counterions in the inverse micellar water pools does also need further attention. In Chapter 8 we used an anionic surfactant. However, it is possible to use cationic surfactants and non-ionic surfactants to deal with this subject.

We used a simple model for water with some crude assumptions. There is room for improvements of this model, e.g. by incorporating the size distribution water pools in butter. In order to use THz spectroscopy to analyze butter in general more butter samples need to be investigated. In this case multivariate data analysis will be a helpful tool to determine different quantities of butter. Moreover, it would be interesting to investigate other types of dairy products with THz spectroscopy.

Inspection of liquids in bottles

In order for the THz system to be implemented for liquid inspection, e.g. for security applications, more liquids need to be characterized. Further characterization of various bottle materials is also necessary.

The atmospheric absorption is clearly seen in our measurements. This problem can, however, be minimized by reducing the THz beam path to an absolute minimum, for instance by integrating the THz emitter and detector in a handheld unit that can be brought into contact or to close proximity of the bottle.

Bibliography

[1] P. Smith, D. Auston, and M. Nuss, "Subpicosecond photoconducting dipole antennas," *IEEE J. Quantum Electron.*, vol. 24, no. 2, pp. 255–260, 1988.

[2] C. Fattinger and D. Grischkowsky, "Terahertz beams," *Appl. Phys. Lett.*, vol. 54, no. 6, pp. 490–492, 1989.

[3] D. J. Segelstein, "The complex refractive index of water," Master's thesis, University of Missouri-Kansas City, 1981. Data can be found at http://www.philiplaven.com/p20.html.

[4] M. Born and E. Wolf, *Principles of optics: Electromagnetiv theory of propagation, interference and diffraction of light*. Cambridge University Press, 7th ed., 1999.

[5] E. Hecht, *Optics*. Adison Wesley, 4th ed., 2002.

[6] J. E. Chamberlain, M. N. Afsar, J. B. Hasted, M. S. Zafar, and G. J. Davies, "Dispersion of alcohols and water in the submillimetre waveband," *Nature*, vol. 255, pp. 319–321, 1975.

[7] T. S. Hartwick, D. T. Hodges, D. H. Barker, and F. B. Foote, "Far infrared imagery," *Appl. Opt.*, vol. 15, no. 8, pp. 1919–1922, 1976.

[8] M. Afsar, J. Hasted, and J. Chamberlain, "New techniques for dispersive fourier transform spectrometry of liquids," *Infrared Phys.*, vol. 16, no. 1–2, pp. 301–310, 1976.

[9] S. E. Harris, B. J. McMurtry, and A. E. Siegman, "Modulation and direct demodulation of coherent and incoherent light at a microwave frequency," *Appl. Phys. Lett.*, vol. 1, no. 2, pp. 37–39, 1962.

[10] M. Bass, P. A. Franken, J. F. Ward, and G. Weinreich, "Optical rectification," *Phys. Rev. Lett.*, vol. 9, no. 11, pp. 446–448, 1962.

[11] J. A. Valdmanis, G. Mourou, and C. W. Gabel, "Picosecond electro-optic sampling system," *Appl. Phys. Lett.*, vol. 41, no. 3, pp. 211–212, 1982.

[12] L. Xu, X.-C. Zhang, and D. H. Auston, "Terahertz beam generation by femtosecond optical pulses in electro-optic materials," *Appl. Phys. Lett.*, vol. 61, no. 15, pp. 1784–1786, 1992.

[13] X.-C. Zhang, Y. Jin, and X. F. Ma, "Coherent measurement of thz optical rectification from electro-optic crystals," *Appl. Phys. Lett.*, vol. 61, no. 23, 1992.

[14] X.-C. Zhang, X. F. Ma, Y. Jin, T.-M. Lu, E. P. Boden, P. D. Phelps, K. R. Stewart, and C. P. Yakymyshyn, "Terahertz optical rectification from a nonlinear organic crystal," *Appl. Phys. Lett.*, vol. 61, no. 26, pp. 3080–3082, 1992.

[15] Q. Wu and X.-C. Zhang, "Free-space electro-optic sampling of terahertz beams," *Appl. Phys. Lett.*, vol. 67, no. 24, pp. 3523–3525, 1995.

[16] P. U. Jepsen, C. Winnewisser, M. Schall, V. Schyja, S. R. Keiding, and H. Helm, "Detection of thz pulses by phase retardation in lithium tantalate," *Phys. Rev. E*, vol. 53, no. 4, pp. R3052–R3054, 1996.

[17] A. Nahata, A. S. Weling, and T. F. Heinz, "A wideband coherent terahertz spectroscopy system using optical rectification and electro-optic sampling," *Appl. Phys. Lett.*, vol. 69, no. 16, 1996.

[18] K. A. McIntosh, E. R. Brown, K. B. Nichols, O. B. McMahon, W. F. DiNatale, and T. M. Lyszczarz, "Terahertz photomixing with diode lasers in low-temperature-grown GaAs," *Appl. Phys. Lett.*, vol. 67, no. 26, pp. 3844–3846, 1995.

[19] B. S. Williams, "Terahertz quantum-cascade lasers," *Nature Photonics*, vol. 1, pp. 517–525, 2007.

[20] J. Murphy and S. Krinsky, "Millimeter wave coherent synchrotron radiation in the SXLS phase I electron storage ring," *Nucl. Instrum. Methods Phys. Res., Sect. A*, vol. 346, no. 3, pp. 571–577, 1994.

[21] J. Hebling, K.-L. Yeh, M. C. Hoffmann, B. Bartal, and K. A. Nelson, "Generation of high-power terahertz pulses by tilted-pulse-front excitation and their application possibilities," *J. Opt. Soc. Am. B*, vol. 25, no. 7, pp. 6–19, 2008.

[22] C. Kübler, R. Huber, and A. Leitenstorfer, "Ultrabroadband terahertz pulses: generation and field-resolved detection," *Semicond. Sci. Technol.*, vol. 20, no. 7, pp. 128–133, 2005.

[23] P. Siegel, "Terahertz technology," *IEEE Trans. Microwave Theory Tech.*, vol. 50, no. 3, pp. 910–928, 2002.

[24] S. Dexheimer, ed., *Terahertz Spectroscopy: Principles and Applications*. CRC Press, 2007.

[25] P. U. Jepsen, R. H. Jacobsen, and S. R. Keiding, "Generation and detection of terahertz pulses from biased semiconductor antennas," *J. Opt. Soc. Am. B*, vol. 13, no. 11, pp. 2424–2436, 1996.

[26] C. Ludwig and J. Kuhl, "Studies of the temporal and spectral shape of terahertz pulses generated from photoconducting switches," *Appl. Phys. Lett.*, vol. 69, no. 9, pp. 1194–1196, 1996.

[27] H.-M. Heiliger, M. Vosseburger, H. G. Roskos, H. Kurz, R. Hey, and K. Ploog, "Application of liftoff low-temperature-grown GaAs on transparent substrates for THz signal generation," *Appl. Phys. Lett.*, vol. 69, no. 19, pp. 2903–2905, 1996.

[28] M. Tani, S. Matsuura, K. Sakai, and S. ichi Nakashima, "Emission characteristics of photoconductive antennas based on low-temperature-grown GaAs and semi-insulating GaAs," *Appl. Opt.*, vol. 36, no. 30, pp. 7853–7859, 1997.

[29] K. P. H. Lui and F. A. Hegmann, "Ultrafast carrier relaxation in radiation-damaged silicon on sapphire studied by optical-pump–terahertz-probe experiments," *Appl. Phys. Lett.*, vol. 78, no. 22, pp. 3478–3480, 2001.

[30] S. E. Ralph and D. Grischkowsky, "Trap-enhanced electric fields in semi-insulators: The role of electrical and optical carrier injection," *Appl. Phys. Lett.*, vol. 59, no. 16, pp. 1972–1974, 1991.

[31] M. van Exter, C. Fattinger, and D. Grischkowsky, "High-brightness terahertz beams characterized with an ultrafast detector," *Appl. Phys. Lett.*, vol. 55, no. 4, pp. 337–339, 1989.

[32] D. Grischkowsky, S. Keiding, M. van Exter, and C. Fattinger, "Far-infrared time-domain spectroscopy with terahertz beams of dielectrics and semiconductors," *J. Opt. Soc. Am. B*, vol. 7, no. 10, pp. 2006–2015, 1990.

[33] P. N. Butcher and D. Cotter, *The Elements of Nonlinear Optics*. Cambridge University Press, 1990.

[34] A. Rice, Y. Jin, X. F. Ma, X.-C. Zhang, D. Bliss, J. Larkin, and M. Alexander, "Terahertz optical rectification from <110> zinc-blende crystals," *Appl. Phys. Lett.*, vol. 64, no. 11, pp. 1324–1326, 1994.

[35] D. Turchinovich, *Study of Ultrafast Polarization and Carrier Dynamics in Semiconductor Nanostructures: a THz Spectroscopy Approach.* PhD thesis, University of Freiburg, May 2004.

[36] P. C. M. Planken, H.-K. Nienhuys, H. J. Bakker, and T. Wenckenbach, "Measurement and calculation of the orientation dependence of terahertz detection in ZnTe," *J. Opt. Soc. Am. B*, vol. 18, no. 3, 2001.

[37] N. C. J. van der Valk, T. Wenckenbach, and P. C. M. Planken, "Full mathematical description of electro-optic detection in optically isotropic crystals," *J. Opt. Soc. Am. B*, vol. 21, no. 3, 2004.

[38] Y.-S. Lee, *Principles of Terahertz Science and Technology.* Springer, 2009.

[39] According to search on ISI Web of Knowledge^{SM}.

[40] M. van Exter, C. Fattinger, and D. Grischkowsky, "Terahertz time-domain spectroscopy of water vapor," *Opt. Lett.*, vol. 14, no. 20, pp. 1128–1130, 1989.

[41] C. A. Schmuttenmaer, "Exploring dynamics in the far-infrared with terahertz spectroscopy," *Chem. Rev.*, vol. 104, no. 4, pp. 1759–1780, 2004.

[42] D. G. Cooke, *Time-resolved terahertz spectroscopy of bulk and nanoscale semiconductors.* PhD thesis, University of Alberta, 2007.

[43] R. Piesiewicz, C. Jansen, S. Wietzke, D. Mittleman, M. Koch, and T. Kürner, "Properties of building and plastic materials in the THz range," *Int. J. Infrared Milli. Waves*, vol. 28, no. 5, pp. 363–371, 2007.

[44] L. Duvillaret, F. Garet, and J.-L. Coutaz, "A reliable method for extraction of material parameters in terahertz time-domain spectroscopy," *IEEE J. Selected Top. Quantum Electron.*, vol. 2, no. 3, pp. 739–746, 1996.

[45] L. Duvillaret, F. Garet, and J.-L. Coutaz, "Highly precise determination of optical constants and sample thickness in terahertz time-domain spectroscopy," *Appl. Opt.*, vol. 38, no. 2, pp. 409–415, 1999.

[46] T. D. Dorney, R. G. Baraniuk, and D. M. Mittleman, "Material parameter estimation with terahertz time-domain spectroscopy," *J. Opt. Soc. Am. A*, vol. 18, no. 7, pp. 1562–1571, 2001.

[47] W. Withayachumnankul, B. Ferguson, T. Rainsford, S. Mickan, and D. Abbott, "Direct Fabry-Pérot effect removal," *Fluctuation Noise Lett.*, vol. 6, no. 2, pp. 227–239, 2006.

[48] M. Naftaly and R. Miles, "A method for removing etalon oscillations from THz time-domain spectra," *Optics Communications*, vol. 280, no. 2, pp. 291 – 295, 2007.

[49] L. Thrane, R. Jacobsen, P. U. Jepsen, and S. Keiding, "THz reflection spectroscopy of liquid water," *Chem. Phys. Lett.*, vol. 240, no. 4, pp. 330–333, 1995.

[50] C. Rønne, L. Thrane, P.-O. Astrand, A. Wallqvist, K. V. Mikkelsen, and S. R. Keiding, "Investigation of the temperature dependence of dielectric relaxation in liquid water by THz reflection spectroscopy and molecular dynamics simulation," *J. Chem. Phys.*, vol. 107, no. 14, pp. 5319–5331, 1997.

[51] C. Rønne, *Intermolecular Liquid Dynamics Studied by THz-Spectroscopy*. PhD thesis, Aarhus University, 2000.

[52] P. U. Jepsen, U. Møller, and H. Merbold, "Investigation of aqueous alcohol and sugar solutions with reflection terahertz time-domain spectroscopy," *Opt. Express*, vol. 15, no. 22, pp. 14717–14737, 2007.

[53] J. Dai, J. Zhang, W. Zhang, and D. Grischkowsky, "Terahertz time-domain spectroscopy characterization of the far-infrared absorption and index of refraction of high-resistivity, float-zone silicon," *J. Opt. Soc. Am. B*, vol. 21, no. 7, pp. 1379–1386, 2004.

[54] P. U. Jepsen, J. K. Jensen, and U. Møller, "Characterization of aqueous alcohol solutions in bottles with thz reflection spectroscopy," *Opt. Express*, vol. 16, no. 13, pp. 9318–9331, 2008.

[55] S. Huang, P. C. Ashworth, K. W. Kan, Y. Chen, V. P. Wallace, Y. ting Zhang, and E. Pickwell-MacPherson, "Improved sample characterization in terahertz reflection imaging and spectroscopy," *Opt. Express*, vol. 17, no. 5, pp. 3848–3854, 2009.

[56] H. Hirori, M. Nagai, and K. Tanaka, "Destructive interference effect on surface plasmon resonance in terahertz attenuated total reflection," *Opt. Express*, vol. 13, no. 26, pp. 10801–10814, 2005.

[57] M. Nagai, H. Yada, T. Arikawa, and K. Tanaka, "Terahertz time-domain attenuated total reflection spectroscopy in water and biological solution," *Int. J. Infrared Milli. Waves*, vol. 27, pp. 505–515, 2006.

[58] S. R. Keiding and D. Grischkowsky, "Measurements of the phase shift and reshaping of terahertz pulses due to total internal reflection," *Opt. Lett.*, vol. 15, no. 1, pp. 48–50, 1990.

[59] H. Yada, M. Nagai, and K. Tanaka, "The intermolecular stretching vibration mode in water isotopes investigated with broadband terahertz time-domain spectroscopy," *Chem. Phys. Lett.*, vol. 473, no. 4-6, pp. 279 – 283, 2009.

[60] H. Yada, M. Nagai, and K. Tanaka, "Origin of the fast relaxation component of water and heavy water revealed by terahertz time-domain attenuated total reflection spectroscopy," *Chem. Phys. Lett.*, vol. 464, no. 4-6, pp. 166 – 170, 2008.

[61] T. Arikawa, M. Nagai, and K. Tanaka, "Characterizing hydration state in solution using terahertz time-domain attenuated total reflection spectroscopy," *Chem. Phys. Lett.*, vol. 457, pp. 12–17, 2008.

[62] Y. Ogawa, L. Cheng, S. Hayashi, and K. Fukunaga, "Attenuated total reflection spectra of aqueous glycine in the terahertz region," *IEICE Electronics Express*, vol. 6, no. 2, pp. 117–121, 2009.

[63] N. J. Harrick, *Internal Reflection Spectroscopy.* Interscience Publishers, 1967.

[64] P. U. Jepsen and B. M. Fischer, "Dynamic range in terahertz time-domain transmission and reflection spectroscopy," *Opt. Lett.*, vol. 30, no. 1, pp. 29–31, 2005.

[65] R. Pethig, *Dielectric and Electronic Properties of Biological Materials.* John Wiley and Sons, 1979.

[66] B. M. Fischer, *Broadband THz Time-Domain Spectroscopy of Biomolecules - A Comprehensive Study of the Dielectric Properties of Biomaterials in the Far-Infrared.* PhD thesis, University of Freiburg, 2005.

[67] P. J. Harrop, *Dielectrics.* Butterworth, 1972.

[68] P. J. W. Debye, *Polar Molecules.* Chemical Catalog Inc., New York, 1929.

[69] G. G. Raju, *Dielectrics in Electric Fields.* Marcel Dekker, 2003.

[70] K. S. Cole and R. H. Cole, "Dispersion and absorption in dielectrics I. Alternating current characteristics," *J. Chem. Phys.*, vol. 9, no. 4, pp. 341–351, 1941.

[71] D. W. Davidson and R. H. Cole, "Dielectric relaxation in glycerol, propylene glycol, and n-propanol," *J. Chem. Phys.*, vol. 19, no. 12, pp. 1484–1490, 1951.

[72] S. Havriliak and S. Negami, "A complex plane representation of dielectric and mechanical relaxation processes in some polymers," *Polymer*, vol. 8, pp. 161–210, 1967.

[73] D. G. Dalgleish, *Food Emulsions: Their Structures and Properties*, ch. 1. In *Food Emulsions Fourth Edition, Revised and Expanded*, edited by S. E. Friberg, K. Larsson, and J. Sjöblom, Marcel Dekker, 2004.

[74] Y. Luan, G. Xu, G. Dai, Z. Sun, and H. Liang, "The interaction between poly(vinylpyrrolidone) and reversed micelles of water/AOT/ n-heptane," *Colloid Polym. Sci.*, vol. 282, no. 2, pp. 110–118, 2003.

[75] J. C. Maxwell, *A Treatise on Electricity and Magnetism*. Oxford, Clarendon Press, 1873.

[76] T. Hanai, K. Asami, and N. Koizumi, "Dielectric theory of concentrated suspensions of shell-spheres in particular reference to the analysis of biological cell suspensions," *Bull. Inst. Chem. Res., Kyoto Univ.*, vol. 57, no. 4, 1979.

[77] T. Hanai, "Theory of the dielectric dispersion due to the interfacial polarization and its application to emulsions," *Kolloid Z.*, vol. 171, no. 23, 1960.

[78] T. Hanai, T. Imakita, and N. Koizumi, "Analysis of dielectric relaxations of w/o emulsions in the light of theories of interfacial polarization," *Colloid Polym. Sci.*, vol. 260, no. 11, pp. 1029–1034, 1982.

[79] F. S. Barnes and R. Greenwood, eds., *Handbook of Biological Effects of Electromagnetic Fields: Bioengineering and Biophysical Aspects of Electromagnetic Fields*. CRC Press, 2007.

[80] H. Kitahara, T. Yagi, K. Mano, M. W. Takeda, S. Kojima, and S. Nishizawa, "Dielectric characteristics of water solutions of ethanol in the terahertz region," *J. Korean Phys. Soc.*, vol. 46, no. 1, pp. 82–85, 2005.

[81] J. T. Kindt and C. A. Schmuttenmaer, "Far-infrared dielectric properties of polar liquids probed by femtosecond terahertz pulse spectroscopy," *J. Phys. Chem.*, vol. 100, no. 24, pp. 10373–10379, 1996.

[82] L. Eriksson, E. Johansson, N. Kettaneh-World, and S. World, *Multi- and Megavariate Data Analysis: Principles and Applications*. Umetrics Academy, 2001.

[83] T. Tassaing, Y. Danten, M. Besnard, E. Zoïdis, and J. Yarwood, "A far infrared study of benzene-fluorinated benzene binary mixtures," *Chem. Phys.*, vol. 184, no. 1-3, pp. 225–231, 1994.

[84] A. C. Dean S. Venables and C. A. Schmuttenmaer, "Structure and dynamics of nonaqueous mixtures of dipolar liquids. I. Infrared and far-infrared spectroscopy," *J. Chem. Phys.*, vol. 113, pp. 3243–3248, 2000.

[85] D. S. Venables and C. A. Schmuttenmaer, "Spectroscopy and dynamics of mixtures of water with acetone, acetonitrile, and methanol," *J. Chem. Phys.*, vol. 113, pp. 11222–11236, 2000.

[86] T. Sato and R. Buchner, "Dielectric relaxation processes in ethanol/water mixtures," *J. Phys. Chem. A*, vol. 108, pp. 5007–5015, 2004.

[87] U. Møller, D. G. Cooke, K. Tanaka, and P. U. Jepsen, "Terahertz reflection spectroscopy of Debye relaxation in polar liquids [Invited]," *J. Opt. Soc. Am. B*, vol. 26, no. 9, pp. A113–A125, 2009.

[88] S. Y. Noskov, G. Lamoureux, and B. Roux, "Molecular dynamics study of hydration in ethanol-water mixtures using a polarizable force field," *J. Phys. Chem. B*, vol. 109, no. 14, pp. 6705–6713, 2005.

[89] M. Tomšič, A. Jamnik, G. Fritz-Popovski, O. Glatter, and L. Vlček, "Structural properties of pure simple alcohols from ethanol, propanol, butanol, pentanol, to hexanol: Comparing Monte Carlo simulations with experimental SAXS data," *J. Phys. Chem. B*, vol. 111, no. 7, pp. 1738–1751, 2007.

[90] C. Zhang and X. Yang, "Molecular dynamics simulation of ethanol/water mixtures for structure and diffusion properties," *Fluid Phase Equilibria*, vol. 231, no. 1, pp. 1 – 10, 2005.

[91] H. Hirori, K. Yamashita, M. Nagai, and K. Tanaka, "Attenuated total reflection spectroscopy in time domain using terahertz coherent pulses," *Jpn. J. Appl. Phys.*, vol. 43, no. 10A, p. 1287, 2004.

[92] M. N. Afsar and J. B. Hasted, "Measurements of the optical constants of liquid H_2O and D_2O between 6 and 450 cm^{-1}," *J. Opt. Soc. Am.*, vol. 67, no. 7, pp. 902–904, 1977.

[93] J. B. Hasted, S. K. Husain, F. A. M. Frescura, and J. R. Birch, "The temperature variation of the near millimetre wavelength optical constants of water," *Infrared Phys.*, vol. 27, no. 1, pp. 11–15, 1987.

[94] J. Barthel, K. Bachhuber, R. Buchner, and H. Hetzenauer, "Dielectric spectra of some common solvents in the microwave region. Water and lower alcohols," *Chem. Phys. Lett.*, vol. 165, no. 4, pp. 369–373, 1990.

[95] N. Agmon, "Tetrahedral displacement: the molecular mechanism behind the Debye relaxation in water," *J. Phys. Chem.*, vol. 100, no. 3, pp. 1072–1080, 1996.

[96] V. I. Gaiduk and J. K. Vij, "The concept of two stochastic processes in liquid water and analytical theory of the complex permittivity in the wavenumber range 0–1000 cm^{-1}," *Phys. Chem. Chem. Phys.*, vol. 3, pp. 5173–5181, 2001.

[97] A. Beneduci, "Which is the effective time scale of the fast debye relaxation process in water?," *J. Mol. Liq.*, vol. 138, no. 1-3, pp. 55 – 60, 2008.

[98] R. M. Hill and L. A. Dissado, "Debye and non-debye relaxation," *J. Phys. C: Solid State Phys.*, vol. 18, no. 19, pp. 3829–3836, 1985.

[99] K. Madsen, H. Nielsen, and O. Tingleff, *Methods for Non-linear Least Squares Problems*. Informatics and Mathematical Modelling, Technical University of Denmark, second ed., 2004.

[100] U. Kaatze, "Complex permittivity of water as a function of frequency and temperature," *J. Chem. Eng. Data*, vol. 34, no. 4, pp. 371–374, 1989.

[101] J. M. Alison and R. J. Sheppard, "A precision waveguide system for the measurement of complex permittivity of lossy liquids and solid tissues in the frequency range 29 GHz to 90 GHz - III. The liquid system for 57 to 82 GHz: an investigation into water and formamide," *Meas. Sci. Technol.*, vol. 2, no. 10, pp. 975–979, 1991.

[102] T. Sato, A. Chiba, and R. Nozaki, "Dynamical aspects of mixing schemes in ethanol–water mixtures in terms of the excess partial molar activation free energy, enthalpy, and entropy of the dielectric relaxation process," *J. Chem. Phys.*, vol. 110, no. 5, pp. 2508–2521, 1999.

[103] S. Mashimo, S. Kuwabara, S. Yagihara, and K. Higasi, "The dielectric relaxation of mixtures of water and primary alcohol," *J. Chem. Phys.*, vol. 90, no. 6, pp. 3292–3294, 1989.

[104] P. Petong, R. Pottel, and U. Kaatze, "Water-ethanol mixtures at different compositions and temperatures. a dieletric relaxation study," *J. Phys. Chem. A*, vol. 104, no. 32, pp. 7420–7428, 2000.

[105] R. Chang, *Physical Chemistry for the Chemical and Biological Sciences*. University Science Books, third ed., 2000.

[106] J. A. Boyne and A. G. Williamson, "Enthalpies of mixture of ethanol and water at 25°C," *J. Chem. Eng. Data*, vol. 12, no. 3, pp. 318–318, 1967.

[107] M. T. Tyn and W. F. Calus, "Temperature and concentration dependence of mutual diffusion coefficients of some binary liquid systems," *J. Chem. Eng. Data*, vol. 20, no. 3, pp. 310–316, 1975.

[108] J. Zhang and D. Grischkowsky, "Waveguide terahertz time-domain spectroscopy of nanometer water layers," *Opt. Lett.*, vol. 29, no. 14, pp. 1617–1619, 2004.

[109] J. E. Boyd, A. Briskman, V. L. Colvin, and D. M. Mittleman, "Direct observation of terahertz surface modes in nanometer-sized liquid water pools," *Phys. Rev. Lett.*, vol. 87, no. 14, p. 147401, 2001.

[110] J. E. Boyd, A. Briskman, C. M. Sayes, D. Mittleman, , and V. Colvin, "Terahertz vibrational modes of inverse micelles," *J. Phys. Chem. B*, vol. 106, no. 24, pp. 6346–6353, 2002.

[111] J. E. Boyd, A. Briskman, A. Mikhail, V. Colvin, and D. Mittelman, *Size-Dependent Dielectric Properties of Liquid Water Clusters.*, ch. 21. In *Liquid Dynamics: Experiment, Simulation, and Theory*, edited by J. T. Fourkas, American Chemical Society, 2002.

[112] J. Sjöblom, ed., *Emulsions and Emulsion Stability.* CRC Press, second ed., 2006.

[113] J. Faeder and B. M. Ladanyi, "Molecular dynamics simulations of the interior of aqueous reverse micelles," *J. Phys. Chem. B*, vol. 104, no. 5, pp. 1033–1046, 2000.

[114] D. M. Mittleman, M. C. Nuss, and V. L. Colvin, "Terahertz spectroscopy of water in inverse micelles," *Chem. Phys. Lett.*, vol. 275, no. 3-4, pp. 332 – 338, 1997.

[115] A. S. Giuseppe Onori, "IR investigations of water structure in Aerosol OT reverse micellar aggregates," *J. Phys. Chem.*, vol. 97, no. 20, pp. 5430–5434, 1993.

[116] D. Cringus, J. Lindner, M. T. Milder, M. S. Pshenichnikov, P. Vöhringer, and D. A. Wiersma, "Femtosecond water dynamics in reverse-micellar nanodroplets," *Chem. Phys. Lett.*, vol. 408, no. 1-3, pp. 162 – 168, 2005.

[117] M. R. Harpham, B. M. Ladanyi, N. E. Levinger, and K. W. Herwig, "Water motion in reverse micelles studied by quasielastic neutron scattering and molecular dynamics simulations," *J. Chem. Phys.*, vol. 121, no. 16, pp. 7855–7868, 2004.

[118] T. K. De and A. Maitra, "Solution behaviour of aerosol ot in non-polar solvents," *Adv. Colloid Interface Sci.*, vol. 59, pp. 95–193, 1995.

[119] J. J. Silber, A. Biasutti, E. Abuin, and E. Lissi, "Interactions of small molecules with reverse micelles," *Adv. Colloid Interface Sci*, vol. 82, no. 1-3, pp. 189 – 252, 1999.

[120] M. Zulauf and H. F. Eicke, "Inverted micelles and microemulsions in the ternary system water/aerosol-OT/isooctane as studied by photon correlation spectroscopy," *J. Phys. Chem.*, vol. 83, no. 4, 1979.

[121] A. Maitra, "Determination of size parameters of water-Aerosol OT-oil reverse micelles from their nuclear magnetic resonance data," *J. Phys. Chem.*, vol. 88, no. 21, pp. 5122–5125, 1984.

[122] N. E. Levinger and L. A. Swafford, "Ultrafast dynamics in reverse micelles," *Annu. Rev. Phys. Chem.*, vol. 60, no. 1, pp. 385–406, 2009.

[123] J. Xu, K. W. Plaxco, S. J. Allen, J. E. Bjarnason, and E. R. Brown, "0.15–3.72 THz absorption of aqueous salts and saline solutions," *Appl. Phys. Lett.*, vol. 90, no. 3, p. 031908, 2007.

[124] T. Meissner and F. Wentz, "The complex dielectric constant of pure and sea water from microwave satellite observations," *IEEE Trans. Geosci. Remote Sens.*, vol. 42, no. 9, pp. 1836–1849, 2004.

[125] H. P. Merbold, "Terahertz time-domain spectroscopy of aqueous systems in reflection geometry and construction of polarisation-sensitive phtoconductive terahertz antennas," Master's thesis, Albert-Ludwigs-Universität Freiburg, 2006.

[126] P. Walstra, J. T. M. Wouters, and T. J. Geurts, *Dairy Science and Technology*, ch. 18. CRC Press, second ed., 2006.

[127] M. Hermida, J. M. Gonzalez, M. Sanchez, and J. L. Rodriguez-Otero, "Moisture, solids-non-fat and fat analysis in butter by near infrared spectroscopy," *Int. Dairy J.*, vol. 11, no. 1-2, pp. 93 – 98, 2001.

[128] P. C. Heussen, H.-G. Janssen, I. B. Samwel, and J. P. van Duynhoven, "The use of multivariate modelling of near infrared spectra to predict the butter fat content of spreads," *Anal. Chim. Acta*, vol. 595, no. 1-2, pp. 176 – 181, 2007.

[129] G. Van Dalen, "Determination of the water droplet size distribution of fat spreads using confocal scanning laser microscopy," *J. Microsc.*, vol. 208, no. 2, pp. 116–133, 2002.

[130] K. Van lent, B. Vanlerberghe, P. Van Oostveldt, O. Thas, and P. Van der Meeren, "Determination of water droplet size distribution in butter: Pulsed field gradient NMR in comparison with confocal scanning laser microscopy," *Int. Dairy J.*, vol. 18, no. 1, pp. 12 – 22, 2008.

[131] J. Li and J. Yao, "Highly precise determination of optical constants in olive oil using terahertz time-domain spectroscopy," vol. 7277, p. 727707, SPIE, 2008.

[132] T. Ikeda, A. Matsushita, M. Tatsuno, Y. Minami, M. Yamaguchi, K. Yamamoto, M. Tani, and M. Hangyo, "Investigation of inflammable liquids by terahertz spectroscopy," *Appl. Phys. Lett.*, vol. 87, no. 3, p. 034105, 2005.

[133] N. W. Broad, R. D. Jee, A. C. Moffat, M. J. Eaves, W. C. Mann, and W. Dziki, "Non-invasive determination of ethanol, propylene glycol and water in a multi-component pharmaceutical oral liquid by direct measurement through amber plastic bottles using fourier transform near-infrared spectroscopy," *The Analyst*, vol. 125, pp. 2054–2058, 2000.

[134] M. Naftaly and R. E. Miles, "Terahertz time-domain spectroscopy of silicate glasses and the relationship to material properties," *J. Appl. Phys.*, vol. 102, no. 4, p. 043517, 2007.

Acknowledgements

My Ph.D. studies would not have been possible without the help of many people who I am indebted to.

In particular I would like to thank my supervisor Professor **Peter Uhd Jepsen**, the group leader of the Terahertz Technologies & Biophotonics Group, DTU Fotonik - Department of Photonics Engineering, Technical University of Denmark. He introduced me to the world of terahertz and has been an ongoing source of inspiration throughout my time at DTU. Peter's door has always been open and he always found time to discuss and help with any problem I might have had. I also want to thank my other supervisor, Senior Scientist **Jacob Riis Folkenberg** from FOSS Analytical A/S. His knowledge about food analysis and other spectroscopic techniques has helped a lot.

A special thanks goes to the technical and administrative staff and of course the THz group members, especially **Finn Eichhorn** and **Rasmus Kjelsmark Olsson** for their help in the lab and numerous on- and off-topic discussions, Assistant Professor **David G. Cooke** for instructing me on the use of the high power laser, **Hannes Merbold** from whom I inherited the first THz setup and **Jens Kristian Jensen** for doing some of the measurements.

I am also very grateful to Professor **Koichiro Tanaka** who enabled my 4 month stay in his group at Kyoto University, Japan. I also thank the members of the Tanaka group, especially **Mukesh Jewariya**, **Yosuke Minowa** and **Megumi Hashiguchi** who helped to install me in Kyoto and translated Japanese documents for me as well as Dr. **Hiroyuki Yada** and Dr. **Takashi Arikawa** who helped me in the lab and let me use their setups.

Thanks to Dr. **Takaaki Sato** and apl. Professor **Richard Buchner** for providing me with data from their measurements on ethanol-water mixtures.

This work would also not have bee possible without the support from my family and friends. Thanks to my girlfriend **Louise** for bearing with me in the occasionally stressful times.

Finally, I acknowledge the financial support for my PhD project from FOSS Analytical A/S, DTU Fotonik and the Ministry of Science, Technology and Innovation. I also acknowledge the funding from the Japanese based Global Center of Excellence (GCOE) which made it possible for me to go to Japan for 4 months.

Appendices

Appendix **A**

Fitting parameters of ethanol-water mixtures

In Chapter 7 the dielectric properties of ethanol-water mixtures is discussed. The complex dielectric function of ethanol-water mixtures at 25°C for ten different fractions of ethanol, X_{EtOH} = 0.00 (H_2O), 0.04, 0.08, 0.11, 0.18, 0.30, 0.50, 0.70, 0.90, and 1.00 (C_2H_5OH) were calculated. In this Appendix the fitting parameters are given.

We make use of data from a very broad frequency range, by combination of our own results and already published data recorded in the microwave range with a combination of time-domain reflectometry (TDR) and waveguide interfeometry by Sato and Buchner [86], who has made their original data available to us. By combining the two sets of data we are able to cover the wide frequency range 100 MHz - 2.5 THz, and thus we are able to perform accurate fits to the experimental data, covering the full range of dielectric relaxation.

As discussed in Chapter 7 ethanol-water mixtures can be described by

$$\varepsilon(\omega) = \varepsilon_\infty + \sum_{j=1}^{N} \frac{\Delta\varepsilon_j}{1 + i\omega\tau_j} + \sum_{k=1}^{M} \frac{A_k}{\omega_k^2 - \omega^2 + i\omega\gamma_k}. \tag{A.1}$$

For water and 4% ethanol-water mixture N=2 and M=1, for ethanol N=3 and M=0 and for all other mixtures N=3 and M=1.

The fitting parameters and their standard deviations are given in Tabs. A.1-A.2.

The model fitting is based on a Levenberg-Marquardt algorithm [99], which is a least squares fitting method. The residuals, i.e. the difference between the measured and modeled points, as a function of the frequency are shown for the 50 % ethanol-water mixture in Fig. A.1.

The purpose of the nonlinear curve fitting procedure is to find the absolute minimum value of χ^2. The χ^2 is obtained by dividing the residual sum of

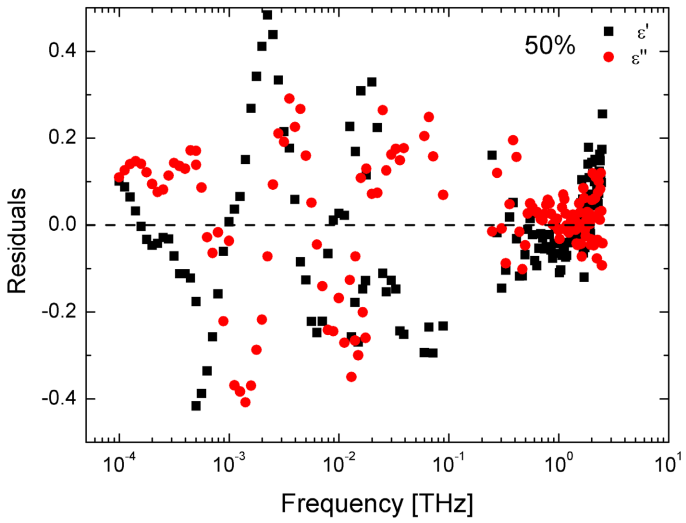

Figure A.1: *Residual plot of 50 % ethanol-water mixture.*

squares by the degrees of freedom. Starting from an initial value the parameter value is adjusted so that the residual sum of squares value is reduced. The fit has converged when $\Delta\chi^2 \leq$tolerance. When this happens the fit is said to converge.

To illustrate the dependency of a fitting parameter with respect to another, one can compute the correlation between them. The correlation matrix for the fitting parameters of the 50 % ethanol-water mixtures are shown in Tab. A.3. The correlation indicates the linear dependency between two random variables. If the correlation is 1 or -1 the variables are perfectly correlated. The sign of correlation indicates the direction of association. A negative correlation means that the change of one variable will cause the other variable to change in the opposite direction. If the correlation is positive, change of one variable will cause the other variable to change in the same direction. A correlation of 0 means that the two variables are independent of each other.

In Tab. A.3 it is seen that all parameters, with the exceptions of ε_s and ε_∞, are strongly correlated to at least one other parameter. Not surprisingly, the correlated parameters are part of the same term (the same relaxation / vibration) in Eq. A.1. It is also seen that the low frequency parameters are more or less independent of the high frequency parameters.

TABLE A.1: *Fitting parameters of ethanol-water mixtures.*

mol	vol	mass	ε_s	±	ε_1	±	$\varepsilon_s - \varepsilon_\infty$	±	$\Delta\varepsilon_1$	±	$\frac{\Delta\varepsilon_1}{(\varepsilon_s-\varepsilon_\infty)}$	±
0	0	0	78.25	0.0719	5.94	0.1080	75.58	0.1046	72.32	0.1297	0.9569	0.0022
4	12.03	9.63	72.89	0.0923	6.164	0.1173	70.17	0.1033	66.72	0.1493	0.9509	0.0026
8	22.45	18.19	68.06	0.0713	16.56	1.365	65.24	0.0770	51.50	1.367	0.7894	0.0210
11	29.38	24.02	64.37	0.0583	20.35	1.344	61.77	0.0645	44.03	1.345	0.7127	0.0218
18	43.03	35.95	57.11	0.0754	27.40	2.582	54.23	0.0776	29.70	2.583	0.5477	0.0476
30	60.26	52.29	47.60	0.0809	30.45	1.625	44.97	0.0823	17.15	1.627	0.3813	0.0362
50	78.64	71.89	36.68	0.0641	13.30	0.5285	34.21	0.0653	23.38	0.5324	0.6836	0.0156
70	90.00	85.65	30.56	0.0518	7.569	0.2471	28.46	0.0530	22.99	0.2525	0.8079	0.0090
90	97.35	95.84	26.47	0.0537	5.196	0.0671	24.38	0.0545	21.28	0.0859	0.8727	0.0040
100	100	100	24.41	0.0524	4.368	0.0234	22.55	0.0535	20.05	0.0574	0.8888	0.0033

mol	ε_2	±	$\Delta\varepsilon_2$	±	$\frac{\Delta\varepsilon_2}{(\varepsilon_s-\varepsilon_\infty)}$	±	ε_∞	±	$\Delta\varepsilon_3$	±	$\frac{\Delta\varepsilon_3}{(\varepsilon_s-\varepsilon_\infty)}$	±
0	–	–	–	–	–	–	2.677	0.0760	2.125	0.7209	0.0281	0.0095
4	–	–	–	–	–	–	2.712	0.0464	2.335	0.3571	0.0491	0.0075
8	5.273	0.0969	11.29	1.369	0.1730	0.0210	2.818	0.0290	1.711	0.2271	0.0262	0.0035
11	4.970	0.0406	15.38	1.344	0.2489	0.0218	2.599	0.0275	1.694	0.1738	0.0274	0.0028
18	5.367	0.0781	22.04	2.583	0.4064	0.0476	2.877	0.0183	1.822	0.1394	0.0336	0.0026
30	5.090	0.0727	25.37	1.627	0.5640	0.0361	2.629	0.0152	1.792	0.1017	0.0399	0.0023
50	4.478	0.0553	8.821	0.5314	0.2579	0.0155	2.475	0.0123	1.491	0.0716	0.0436	0.0021
70	3.429	0.2516	0.13493	0.0099	2.103	0.0113	1.592	0.0724	0.0560	0.0026	0.0560	0.0026
90	3.911	0.0542	1.285	0.0862	0.0527	0.0035	2.093	0.0094	1.418	0.0658	0.0582	0.0027
100	2.908	0.0305	1.460	0.0384	0.0647	0.0017	1.861	0.0106	1.047	0.0323	0.0464	0.0014

Table A.2: *Fitting parameters of ethanol-water mixtures (con't).*

mol	τ_1	$\pm$	τ_2	$\pm$	τ_3	$\pm$	A_v	$\pm$	ω_v	$\pm$	γ_v	$\pm$	χ^2
0	8.339	0.0256	–	–	0.3602	0.0308	28.44	1.261	5.008	1.561	7.056	1.930	0.0050
4	12.07	0.0446	–	–	0.5327	0.0445	19.83	0.8189	4.229	0.6312	6.147	0.5061	0.0073
8	18.70	0.2712	6.787	0.5073	0.3909	0.0366	9.082	0.6240	3.494	0.4622	4.550	0.4137	0.0050
11	23.49	0.3600	9.386	0.4185	0.2776	0.0118	8.990	0.2505	3.641	0.4446	2.900	0.193	0.0028
18	35.51	1.305	15.93	0.8233	0.5623	0.0410	6.502	0.3567	3.120	0.2521	4.203	0.2536	0.0044
30	63.45	3.066	24.35	0.8373	0.9423	0.0722	3.851	0.2304	2.400	0.1020	3.747	0.1965	0.0058
50	76.90	1.294	21.36	0.9535	0.9715	0.0672	2.406	0.1417	2.167	0.0672	3.081	0.1571	0.0044
70	102.8	0.9050	18.40	1.008	0.9637	0.0500	3.130	0.1099	2.652	0.1525	3.500	0.1851	0.0031
90	146.1	0.9180	12.36	1.169	1.115	0.0746	1.557	0.1143	1.972	0.05189	3.257	0.172	0.0033
100	162.5	0.7469	4.175	0.1953	0.2825	0.0094	–	–	–	–	–	–	0.0035

TABLE A.3: *Correlation matrix of the 50 % ethanol-water mixture fitting parameters.*

	ε_s	τ_1	ε_1	τ_2	ε_2	τ_3	ε_∞	A_v	ω_v	γ_v
ε_s	1	0.210	0.172	0.156	0.250	0.267	0.042	0.213	0.075	0.180
τ_1	0.210	1	0.935	0.826	0.350	0.239	0.057	0.013	-0.020	-0.003
ε_1	0.172	0.935	1	0.949	0.476	0.339	0.078	0.044	-0.016	0.019
τ_2	0.156	0.826	0.949	1	0.609	0.432	0.097	0.037	-0.030	0.007
ε_2	0.250	0.350	0.476	0.609	1	0.849	0.184	0.276	0.036	0.199
τ_3	0.267	0.239	0.339	0.432	0.849	1	0.229	0.324	-0.023	0.219
ε_∞	0.0416	0.0569	0.078	0.097	0.184	0.229	1	-0.442	-0.622	-0.561
A_v	0.213	0.013	0.044	0.0368	0.276	0.324	-0.442	1	0.873	0.956
ω_v	0.075	-0.020	-0.016	-0.030	0.036	-0.023	-0.622	0.873	1	0.875
γ_v	0.180	-0.003	0.019	0.007	0.199	0.219	-0.561	0.956	0.875	1

Appendix **B**

Fitting parameters for liquid inspection inside bottles

In Chapter 9 it was demonstrated how one can simulate the reflected reference pulse from outside a bottle and the reflected sample pulse from inside the bottle, based on the knowledge of the optical properties of the bottle material and the dielectric function of the liquid inside the bottle.

In this Appendix the fitting parameters are given.

B.1 Optical properties of bottle materials

The measurements of the optical properties of glass and PET are shown in Fig. 9.3. These measurements are fitted to a straight line and extrapolated to cover the $0.1 \geq \nu \geq 2.5$ THz frequency range,

$$n_{PET}(\nu) = 1.807 - 0.0390 \cdot \nu \quad [THz] \tag{B.1}$$

$$\alpha_{PET}(\nu) = 19.11 \cdot \nu \quad [THz] \tag{B.2}$$

$$n_{glass}(\nu) = 2.413 - 0.0249 \cdot \nu \quad [THz] \tag{B.3}$$

$$\alpha_{glass}(\nu) = 36.86 \cdot \nu \quad [THz] \tag{B.4}$$

B.2 Parameters for ethanol-water mixtures

Based on data from 10 ethanol-water mixtures with different ethanol concentration described in Chapter 7 and Appendix A we have made a phenomenological parametrization of the dielectric function in order to determine the dielectric function for any given concentration of ethanol in an ethanol-water mixture.

As discussed in Chapter 7 ethanol-water mixtures can be described by

$$\varepsilon(\omega) = \varepsilon_\infty + \sum_{j=1}^{N} \frac{\Delta\varepsilon_j}{1 + i\omega\tau_j} + \sum_{k=1}^{M} \frac{A_k}{\omega_k^2 - \omega^2 + i\omega\gamma_k}. \tag{B.5}$$

For water and up to 10% ethanol in ethanol-water mixtures N=2 and M=1, for ethanol N=3 and M=0 and for all other mixtures N=3 and M=1. With x as the ethanol mass fraction Eq. B.5 can be parameterized to

$$\begin{aligned}
\Delta\varepsilon_1 &= 17.43 + 59.70 \cdot e^{-x/0.279}, \\
\Delta\varepsilon_2 &= \begin{cases} 0\ , & x < 0.1 \\ -6.78 + 34.55 \cdot x + 575.0 \cdot x^2 & \\ -1719 \cdot x^3 + 1589 \cdot x^4 - 471.2 \cdot x^5\ , & x \geq 0.1 \end{cases} \\
\Delta\varepsilon_3 &= 2.112 - 0.829 \cdot x, \\
\varepsilon_\infty &= 2.662 + 0.813 \cdot x - 1.575 \cdot x^2, \\
\tau_1 &= -8.635 + 19.09 \cdot e^{x/0.461}, & [ps] \\
\tau_2 &= -14.38 + 127.7 \cdot x - 106.4 \cdot x^2, & [ps] \\
\tau_3 &= 0.418 - 1.443 \cdot x + 11.44 \cdot x^2 - 28.21 \cdot x^3 + 36.51 \cdot x^4 - 18.24 \cdot x^5, & [ps] \\
A_1 &= \begin{cases} 1.611 + 27.18 \cdot e^{-x/0.186}\ , & x < 0.95 \\ 0\ , & x \geq 0.95 \end{cases} & [(2\pi THz)^2] \\
\omega_1 &= 2.026 + 2.972 \cdot e^{-x/0.319}, & [2\pi THz] \\
\gamma_1 &= 3.314 + 3.947 \cdot e^{-x/0.153}. & [2\pi THz]
\end{aligned} \tag{B.6}$$

The parametrization is carried out without any regard for the actual physical processes.

Appendix C

Publications

The author of this thesis has contributed to the following journal publications, conference contributions and book chapters during his Ph.D. project:

Journal publications

1. Uffe Møller, David G. Cooke, Koichiro Tanaka, and Peter Uhd Jepsen, "*Terahertz reflection spectroscopy of Debye relaxation in polar liquids [Invited]*", J. Opt. Soc. Am. B **26**, A113–A125 (2009).

2. Peter Uhd Jepsen, Jens Kristian Jensen, and Uffe Møller, "*Characterization of aqueous alcohol solutions in bottles with THz reflection spectroscopy*", Opt. Express **16**, 9318-9331 (2008).

3. Peter Uhd Jepsen, Uffe Møller, and Hannes Merbold, "*Investigation of aqueous alcohol and sugar solutions with reflection terahertz time-domain spectroscopy*", Opt. Express **15**, 14717-14737 (2007).

Conference contributions

4. Uffe Møller, Jacob Riis Folkenberg, Peter Uhd Jepsen and Koichiro Tanaka, "*Dielectric relaxation processes in ethanol/water mixtures*", Danish Physical Society Nordic Meeting, Kgs. Lyngby, Denmark (2009) (talk).

5. Peter Uhd Jepsen, David Cooke, and Uffe Møller, "*THz spectroscopy of liquids - applications and future challenges*", Optical Terahertz Science and Technology Topical Meeting and Tabletop Exhibit, Santa Barbara, CA, USA (2009) (invited talk).

6. Uffe Møller, Hiriyuki Yada, Takashi Arikawa, Jacob Riis Folkenberg, Peter Uhd Jepsen, and Koichiro Tanaka, "*Dielectric relaxation processes in ethanol/water mixtures measured with attenuated total reflection terahertz time-domain spectroscopy*", Optical Terahertz Science and Technol-

ogy Topical Meeting and Tabletop Exhibit, Santa Barbara, CA, USA (2009) (poster).

7. Uffe Møller, Jens Kristian Jensen, David Cooke, and Peter Uhd Jepsen, "*Investigation of liquids and solids with THz time-domain spectroscopy*", IEICE Meeting on THz Electronic Devices, Sendai, Japan (2008) (invited talk + proceeding).

8. Uffe Møller, Jacob Riis Folkenberg, and Peter Uhd Jepsen, "*Absorption properties of water-in-oil emulsions in the low THz frequency range*", European Optical Socieety Annual Meeting, Paris, France (2008) (poster).

9. Uffe Møller, Jens Kristian Jensen, Finn Eichhorn, Jacob Riis Folkenberg, and Peter Uhd Jepsen, "*Determination of alcohol concentration in plastic bottles with THz reflection spectroscopy*", FoodDTU Conference, Technical University of Denmark, Kgs. Lyngby, Denmark (2008) (poster).

10. Uffe Møller, Jens Kristian Jensen, Jacob Riis Folkenberg and Peter Uhd Jepsen, "*Characterization of liquids in commercial plastic and glass bottles with THz reflection spectroscopy*", Danish Physical Society Annual Meeting, Nyborg, Denmark (2008) (talk).

11. Uffe Møller, Hannes Merbold, Jacob Riis Folkenberg, and Peter Uhd Jepsen, "*Determination of Alcohol Concentration in Aqueous Solutions and Food Analysis using Reflection Terahertz Time-Domain Spectroscopy*", Optical Terahertz Science and Technology Topical Meeting and Tabletop Exhibit, Orlando, Florida, USA (2007) (talk).

12. Uffe Møller, Hannes Merbold, Jacob Riis Folkenberg, and Peter Uhd Jepsen, "*Terahertz Time-domain Spectroscopy: A New Way to Determine Alcohol Concentrations in Aqueous Solutions*", Danish Physical Society Annual Meeting, Nyborg, Denmark (2007) (talk).

13. Uffe Møller, Hannes Merbold, Jacob Riis Folkenberg, and Peter Uhd Jepsen, "*Determination of Alcohol- and Sugar Concentration In Aqueous Solutions Using Reflection Terahertz Time-domain Spectroscopy*", Joint 32nd International Conference on Infrared & Millimetre Waves and 15th International Conference on Terahertz Electronics: IRMMWTHz 2007, Cardiff, UK (2007) (poster).

14. Uffe Møller, Jacob Riis Folkenberg, and Peter Uhd Jepsen, "*Terahertz Spectroscopy and Its Application in Food Analysis*", FoodDTU Opening Conference, Technical University of Denmark, Kgs. Lyngby, Denmark (2007) (poster).

15. Peter Uhd Jepsen, Uffe Møller, Finn Eichhorn, Hannes Merbold, Jacob Riis Folkenberg, and Steward Clark, "*Terahertz Time-domain Spectroscopy of*

Crystalline and Aqueous Systems", CLEO/QELS, Baltimore, Maryland, USA (2007) (invited talk).

16. Peter Uhd Jepsen, Uffe Møller, David Cooke, and Jacob Riis Folkenberg, "*Ingredients Analysis of Aqueous Solutions and Food Products with Reflection THz spectroscopy*", Frontiers in Optics/Laser Science XXIII, Rochester, New York, USA (2007) (invited talk).

17. Peter Uhd Jepsen, Uffe Møller, Finn Eichhorn, Hannes Merbold, Jacob Riis Folkenberg, and Steward Clark, "*Terahertz Time-domain Spectroscopy and Modelling of Crystalline and Aqueous Systems*", Presented at: Royal Netherlands Academy of Arts and Sciences: Colloquium on Terahertz Science, Amsterdam, The Netherlands (2007) (invited talk).

18. Finn Eichhorn, Uffe Møller, Jens E. Pedersen, C.F. Pedersen, and Peter Uhd Jepsen, "*Tunable Dual-wavelength DFB Fibre Laser System for kHz-linewidth Terahertz Generation by Photo-mixing*", Danish Physical Society Annual Meeting, Nyborg, Denmark (2007) (poster).

Book chapters

19. David Cooke, Dmitry Turchinovich, Uffe Møller, Finn Eichhorn, and Peter Uhd Jepsen, "*Nyt lys på ukendt land: Terahertz teknologi*", Chapter 4 in: "*Optiske Horisonter: en rejse på kommunikationsteknologiens vinger*", pp. 67-91, one2one, Odense, COM DTU, Denmark (2007) (Danish high school book).

Appendix **D**

Published and submitted journal papers

The following published and submitted journal papers can be found in this appendix:

1. Peter Uhd Jepsen, Uffe Møller, and Hannes Merbold, "*Investigation of aqueous alcohol and sugar solutions with reflection terahertz time-domain spectroscopy*", Opt. Express **15**, 14717-14737 (2007).

2. Peter Uhd Jepsen, Jens Kristian Jensen, and Uffe Møller, "*Characterization of aqueous alcohol solutions in bottles with THz reflection spectroscopy*", Opt. Express **16**, 9318-9331 (2008).

3. Uffe Møller, David G. Cooke, Koichiro Tanaka, and Peter Uhd Jepsen, "*Terahertz reflection spectroscopy of Debye relaxation in polar liquids [Invited]*", J. Opt. Soc. Am. B **26**, A113–A125 (2009).

.

Investigation of aqueous alcohol and sugar solutions with reflection terahertz time-domain spectroscopy

Peter Uhd Jepsen,[1] **Uffe Møller**[1] **and Hannes Merbold**[2]

[1]*COM•DTU - Department of Communications, Optics and Materials, Technical University of Denmark, DK-2800 Kongens Lyngby, Denmark*
[2]*Department of Molecular and Optical Physics, Institute of Mathematics and Physics, University of Freiburg, D-79104 Freiburg, Germany*
jepsen@com.dtu.dk

Abstract: We give a detailed analysis of a general realization of reflection terahertz time-domain spectroscopy. The method is self-referenced and applicable at all incidence angles and for all polarizations of the incident terahertz radiation. Hence it is a general method for the determination of the dielectric properties of especially liquids in environments where transmission measurements are difficult. We investigate the dielectric properties in the 0.1-1.0 THz frequency range of liquids using reflection terahertz time-domain spectroscopy. We apply the technique for the determination of alcohol and sugar concentration of commercial alcoholic beverages and liquors. The special geometry of the experiment allows measurement on sparkling beverages.

OCIS codes: (300.6495) Spectroscopy, terahertz; (220.2740) Geometric optical design; (120.4825) Optical time-domain reflectometry

References and links

1. L. Thrane, R. H. Jacobsen, P. Uhd Jepsen, and S. R. Keiding, "THz reflection spectroscopy of liquid water," Chem. Phys. Lett. **240,** 330 (1995)
2. C. Rønne, L. Thrane, P.-O. Åstrand, A. Wallqvist, K. V. Mikkelsen, and S. R. Keiding, "Investigation of the temperature dependence of dielectric relaxation in liquid water by THz reflection spectroscopy and molecular dynamics simulation," J. Chem. Phys. **107,** 5319 (1997)
3. J. Dai, J. Zhang, W. Zhang, and D. Grischkowsky, "Terahertz time-domain spectroscopy characterization of the far-infrared absorption and index of refraction of high-resistivity, float-zone silicon," J. Opt. Soc. Am. B **21,** 1379 (2004)
4. D. Grischkowsky, S. Keiding, M. van Exter, and Ch. Fattinger, "Far-infrared time-domain spectroscopy with terahertz beams of dielectrics and semiconductors," J. Opt. Soc. Am. B **7,** 2006 (1990)
5. H. Hirori, K. Yamashita, M. Nagai, and K. Tanaka, "Attenuated total reflection spectroscopy in time domain using terahertz coherent pulses," Jpn. J. Appl. Phys. **43,** L1287 (2004)
6. A. Dobroiu, R. Beigang, C. Otani, and K. Kawase, "Monolithic Fabry-Perot resonator for the measurement of optical constants in the terahertz range," Appl. Phys. Lett. **86,** 261107 (2005)
7. P. Uhd Jepsen and B. M. Fischer, "Dynamic range in terahertz time-domain transmission and reflection spectroscopy," Opt. Lett. **30,** 29 (2005)
8. T.-I. Jeon and D. Grischkowsky, "Characterization of optically dense, doped semiconductors by reflection THz time domain spectroscopy," Appl. Phys. Lett. **72,** 3032 (1998)
9. C. Rønne, *Intermolecular liquid dynamics studied by THz-spectroscopy*, Ph.D. Thesis, Aarhus University (2000)
10. J. Barthel, K. Bachhuber, R. Buchner, and H. Hetzenauer, "Dielectric spectra of some common solvents in the microwave region. Water and lower alcohols," Chem. Phys. Lett. **165,** 369 (1990)

#87328 - $15.00 USD Received 7 Sep 2007; revised 23 Oct 2007; accepted 23 Oct 2007; published 24 Oct 2007

11. J. T. Kindt and C. A. Schmuttenmaer, "Far-infrared dielectric properties of polar liquids probed by femtosecond terahertz pulse spectroscopy," J. Phys. Chem. **100,** 10373 (1996)
12. H. Kitahara, T. Yagi, K. Mano, M. Wada Takeda, S. Kojima, and S. Nishizawa, "Dielectric characteristics of water solutions of ethanol in the terahertz region," J. Korean Phys. Soc. **46,** 82 (2005)
13. M. Nagel, M. Först, and H. Kurz, "THz biosensing devices: fundamentals and technology," J. Phys. Condens. Matter **18,** S601 (2006)
14. P. Uhd Jepsen, R. H. Jacobsen, and S. R. Keiding, "Generation and detection of terahertz pulses from biased semiconductor antennas," J. Opt. Soc. Am. B **13,** 2424 (1996)
15. L. Duvillaret, F. Garet, and J.-L. Coutaz, "A reliable method for extraction of material parameters in terahertz time-domain spectroscopy," IEEE J. Sel. Top. Quantum Electron. **2,** 739 (1996)
16. T. Tassaing, Y. Danten, M. Besnard, E. Zoidis, and J. Yarwood, "A far infrared study of benzene-fluorinated benzene binary mixtures," Chem. Phys. **184,** 225 (1994)
17. B. N. Flanders, R. A. Cheville, D. Grischkowsky, and N. F. Scherer, "Pulsed terahertz transmission spectroscopy of liquid $CHCl_3$, CCl_4, and their mixtures," J. Phys. Chem. **100,** 11824 (1996)
18. D. S. Venables, A. Chiu, and C. A. Schmuttenmaer, "Structure and dynamics of nonaqueous mixtures of dipolar liquids. I. Infrared and far-infrared spectroscopy," J. Chem. Phys. **113,** 3243 (2000)
19. D. S. Venables and C. A. Schmuttenmaer, "Spectroscopy and dynamics of mixtures of water with acetone, acetonitrile, and methanol," J. Chem. Phys. **113,** 11222 (2000)

1. Introduction

Terahertz time-domain spectroscopy (THz-TDS) is a method for the determination of the real and imaginary part of the dielectric function, or the absorption coefficient and index of refraction. This method has found extended use in a wide range of research fields, including studies of carrier dynamics in semiconductors, low-frequency vibrational modes in molecular crystals, and low-energy interactions in polar and nonpolar liquids.

THz-TDS can be performed both as a transmission measurement and as a reflection measurement. The transmission geometry is easiest to implement, and the majority of data reported in the literature has been obtained with transmission setups. However, since THz-TDS is a phase-sensitive technique a determination of the complex reflection coefficient of a sample by reflection spectroscopy yields the equivalent information about the dielectric function of the sample. Reflection THz-TDS has earlier been used for investigations of the temperature dependence of the dielectric properties of water [1, 2], and recently Hirori *et al.* used attenuated total internal reflection THz-TDS to study the optical properties of semiconductor materials and liquid water [5]. Dubroiu *et al.* have shown that the loss factor of a monolithic Fabry-Perot resonator is modified by sample material in contact with the total internal reflection facet of the resonator, and that this mechanism can be used to determine the alcohol content in aqueous solutions [6]. The dynamic range and noise limitations in transmission and reflection THz-TDS measurements were investigated by Jepsen and Fischer [7].

Both transmission- and reflection spectroscopy requires a reference spectrum, recorded under known conditions, in order to extract quantitative information about the dielectric function of a sample. In transmission spectroscopy this reference measurement is typically recorded without a sample in the beam path, or by varying the thickness of a liquid sample. Since both the reference- and sample signal shapes depend on both spectrometer alignment and the generation- and detection process, a reference signal is preferably recorded for each measurement, hence doubling the required data acquisition time. In reflection spectroscopy, the reference signal can be recorded by replacing the sample with a known reflector, for instance a metal mirror. This approach is very sensitive to the precise placement of the reference mirror with respect to the sample surface, and in practice, some compensation in the analysis is required [8]. Another method, which eliminates the need to replace the sample surface with a metal mirror, was described by Thrane *et al.* [1], who placed the sample, in that case water, in contact with a thick silicon window. In this geometry both the reference- and the sample signals are available in a single recording, obtained as the reflection from the air/silicon interface and the silicon/sample

#87328 - $15.00 USD Received 7 Sep 2007; revised 23 Oct 2007; accepted 23 Oct 2007; published 24 Oct 2007

interface, respectively. The normal incidence of the THz signal onto the window requires an experimental setup which includes a beamsplitter in the THz beam path, and hence the detected signal is reduced significantly in amplitude. This complication can be avoided by choosing a non-normal incidence angle, at the expense of complicating the procedure for extraction of the dielectric function of the sample material. Rønne treated this problem, and described an iterative process for the calculation of the dielectric function [9].

Inspired by that work we derive here expressions that can be used for the calculation of the dielectric function of a sample material in contact with a transparent window material such as silicon, without limitations to the incidence angle and polarization state of the incident THz field. This analysis is crucial for the correct evaluation of quantitative spectroscopic results from THz reflection spectrometers. Since this method records both the reference- and the sample signals in the same scan, it may be referred to as self-referenced reflection THz time-domain spectroscopy.

Following the discussion of the analysis of the reflection spectroscopy, we will illustrate its applicability in the characterization of the dielectric properties of water-ethanol mixtures, and in particular we will present a method for the determination of the alcohol concentration in commercial beverages and liquors, independent of the presence of other components such as flavor, color, organic precipitates, as well as carbonation of the beverage. We will also investigate the influence of higher concentrations of sugar in the solutions, and finally demonstrate that the method can be used for the simultaneous determination of both alcohol- and sugar concentration in a solution.

2. Self-referenced THz reflection spectroscopy

In this section we will describe the method for extraction of the dielectric function in a reflection setup, in the general situation with arbitrary incidence angle as well as arbitrary incident polarization angle of the electric field.

2.1. Full analysis

The reflection coefficient is most conveniently defined for the two orthogonal components of the electric field *parallel* to the incidence plane of the sample window and *perpendicular* to the incidence plane of the sample window. In the general case the polarization of the electric field may have any angle with respect to the incidence plane. The polarization may also be circular or elliptical. The spectrometer layout that we will describe in the following features linear polarization of the incident electric field. Typical pulsed THz emitters, such as photoconductive dipole antennas and electro-optic crystals, normally generate linearly polarized radiation. The state of the polarization throughout the spectrometer is then defined by the geometrical arrangement of the mirrors that control the beam path. Any out-of-plane reflection of the THz beam in the spectrometer will lead to a rotation of the polarization. In addition, any differences in the reflection coefficients between *s*- and *p*-polarized light at reflective surfaces in the spectrometer will also modify the state of polarization of the light.

The optical path of the THz beam inside our spectrometer is illustrated in Fig. 1.

This particular geometry is based on a standard transmission spectrometer with an intermediate focus. In this geometry the THz beam is guided and focused by off-axis paraboloidal mirrors with equal effective focal lengths f. The mirrors are placed in a $f-2f-f$ geometry both before and after the intermediate focus. The incidence planes of these mirrors are shown as gray rectangles in Fig. 1. This arrangement ensures a 1:1 imaging of the emitter plane onto the sample window and further onto the detector. The four off-axis paraboloidal mirrors and the THz emitter and detector all lie is the same plane, which we will denote the main plane of the spectrometer. The beam path is indicated by the red lines in Fig. 1.

#87328 - $15.00 USD Received 7 Sep 2007; revised 23 Oct 2007; accepted 23 Oct 2007; published 24 Oct 2007

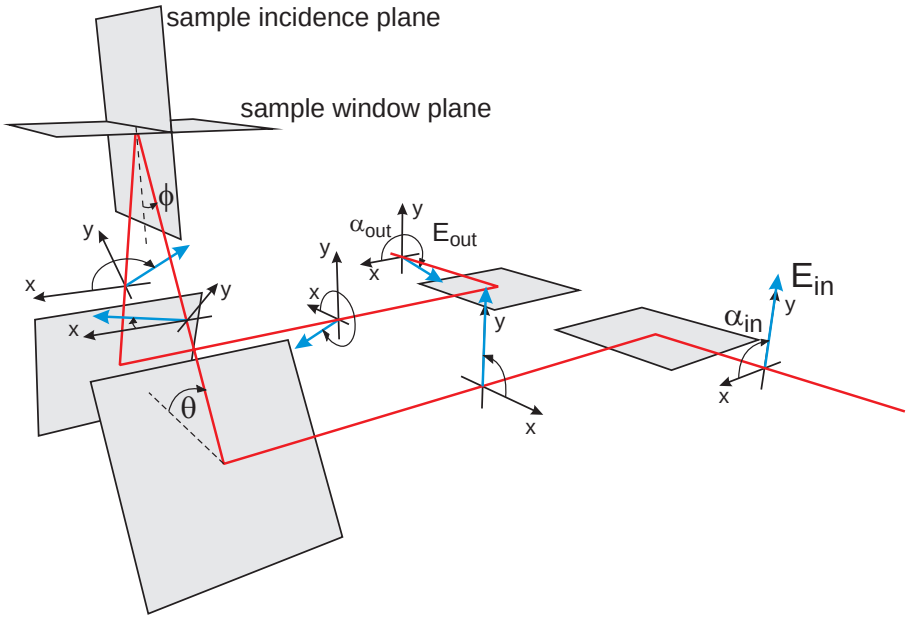

Fig. 1. Beam path of the reflection spectrometer. The gray rectangles indicate the incidence planes of the four off-axis paraboloidal mirrors. The sample window is elevated from the main plane of the spectrometer by rotation of the incidence planes before and after the sample. The vectors shown in blue color illustrate the polarization of an initially vertically polarized THz field through the spectrometer.

The reflection geometry is realized by elevating the sample plane out of the main plane of the spectrometer, to a height h by rotation of the off-axis paraboloidal mirrors before and after the sample. This done in a manner that preserves the distances f from the sample surface to the two rotated mirrors. We have used an elevation angle $\theta = 60^\circ$, as indicated in Fig. 1. This means that the angle of incidence on the sample window is $\phi = 30^\circ$.

We can follow the polarization through the spectrometer by application of the Jones matrix formalism. Here it is useful to recall that in the principal coordinate system of the reflection plane, the polarization vector is changed according to

$$\begin{pmatrix} E'_{\parallel} \\ E'_{\perp} \end{pmatrix} = \begin{pmatrix} -r_{\parallel} & 0 \\ 0 & r_{\perp} \end{pmatrix} \begin{pmatrix} E_{\parallel} \\ E_{\perp} \end{pmatrix} , \tag{1}$$

where the negative sign on $r_{\parallel}$ describes the geometrical mirroring of the polarization vector in the plane perpendicular to the incidence plane. For most metals at THz frequencies, the reflection coefficients $r_{\parallel} \approx -1$ and $r_{\perp} \approx -1$. In a system with several reflective surfaces, the beam may be directed out of the incidence plane of the previous mirror. This is the case in the spectrometer described here. The polarization change is easiest described in the principal coordinate system of each new incidence plane. The transformation to this coordinate system from the previous incidence plane is described by the rotation matrix

$$M(\theta) = \begin{pmatrix} \cos\theta & \sin\theta \\ -\sin\theta & \cos\theta \end{pmatrix} , \tag{2}$$

where θ is the rotation angle of the current incidence plane with respect to that of the previous reflection.

#87328 - $15.00 USD Received 7 Sep 2007; revised 23 Oct 2007; accepted 23 Oct 2007; published 24 Oct 2007

Using this standard formalism we can determine the polarization of the incident THz field in the incidence plane of the sample window, and determine the THz polarization state at the THz detector. In the specific situation described here, the THz beam is reflected at an angle $\theta = 60$ degrees out of the plane. The polarization of the THz beam in the detector plane is then $\alpha' = 180^\circ + 2\theta - \alpha$, where α is the polarization angle of the input THz field, with respect to horizontal. The polarization is traced through our spectrometer as represented by the blue vectors in Fig. 1.

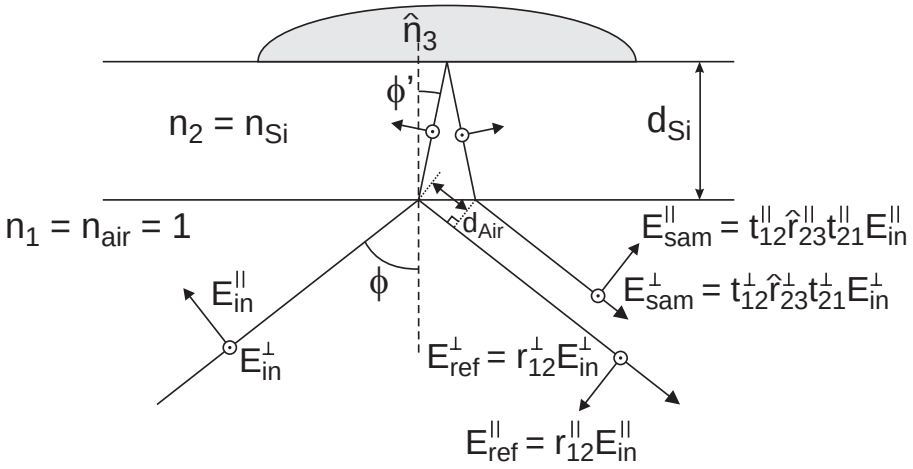

Fig. 2. Detailed view of the reflection geometry at the window which splits the input THz signal into a reference part and a sample part.

In addition to the geometrical rotation of the polarization rotation, the different reflection coefficients of the *s*- and *p*-components of the field at the sample window will lead to an additional phase retardation between the two components of the polarization in that reflection plane. General expressions for the two electric field components at the output plane of the spectrometer can be derived for arbitrary input polarizations, and for arbitrary geometries of the beam path in the spectrometer.

The window material should have known dielectric properties. High-purity silicon has a constant index of refraction of 3.425 and negligible absorption at room temperature in the spectral range relevant for this work [2]. More recent work [3] has reported a very precise value of 3.4175, in line with the first THz-TDS characterization of crystalline silicon [4], which reported a value of 3.4177 at room temperature.

The high index of refraction is ideal for the purpose since it results in a normal-incidence field reflection coefficient of -0.54. This gives a good balance between the signal strength of the reference reflection and the sample reflection.

The known dielectric properties of the window material can be used to solve an important problem in the experimental geometry. As indicated in Fig. 2 the sample beam is displaced slightly with respect to the reference beam after propagation through the window material. This will influence the shape of the detected sample signal since the coupling to the detector antenna will be different if the propagation axis is not identical to that of the reference signal. This effect is difficult to take into account in a strictly formal manner, but nevertheless the effect of the displacement can be taken into account in a more empirical way [9], by imposing an additional frequency-dependent amplitude calibration factor $A_{cal}(\omega)$ and phase shift $\Delta_{cal}(\omega)$ to the sample signal.

#87328 - $15.00 USD Received 7 Sep 2007; revised 23 Oct 2007; accepted 23 Oct 2007; published 24 Oct 2007

The components of the electric field at the output plane are then

$$\vec{E}_{out}^{ref} = \frac{1}{2}E_{in}\begin{pmatrix} (r_{12}^{\parallel}-r_{12}^{\perp})\cos\alpha-(r_{12}^{\parallel}+r_{12}^{\perp})\cos(\alpha-2\theta) \\ (r_{12}^{\parallel}-r_{12}^{\perp})\sin\alpha+(r_{12}^{\parallel}+r_{12}^{\perp})\sin(\alpha-2\theta) \end{pmatrix}, \tag{3}$$

$$\vec{E}_{out}^{sam} = \frac{1}{2}E_{in}A_{cal}\exp(i\Delta_{cal})\exp(2in_2\omega d_{eff}/c) \times \begin{pmatrix} (\hat{r}_{23}^{\parallel}t_{12}^{\parallel}t_{21}^{\parallel}-\hat{r}_{23}^{\perp}t_{12}^{\perp}t_{21}^{\perp})\cos\alpha-(\hat{r}_{23}^{\parallel}t_{12}^{\parallel}t_{21}^{\parallel}+\hat{r}_{23}^{\perp}t_{12}^{\perp}t_{21}^{\perp})\cos(\alpha-2\theta) \\ (\hat{r}_{23}^{\parallel}t_{12}^{\parallel}t_{21}^{\parallel}-\hat{r}_{23}^{\perp}t_{12}^{\perp}t_{21}^{\perp})\sin\alpha+(\hat{r}_{23}^{\parallel}t_{12}^{\parallel}t_{21}^{\parallel}+\hat{r}_{23}^{\perp}t_{12}^{\perp}t_{21}^{\perp})\sin(\alpha-2\theta) \end{pmatrix}. \tag{4}$$

The effective single-pass propagation length d_{eff} through the sample window is calculated by considering the optical path difference OP between the reference beam and the sample beam, measured from the point of entrance into the sample window to the same phase front of the two output beams. We find that

$$OP = \frac{2n_2 d_{Si}}{\cos\phi'} - d_{air} = \frac{2n_2 d_{Si}}{\cos\phi'}(1-\sin^2\phi') = 2n_s d_{Si}\left(1-\frac{\sin^2\phi}{n_s^2}\right). \tag{5}$$

Hence we can define

$$d_{eff} = d_{Si}\left(1-\frac{\sin^2\phi}{n_s^2}\right). \tag{6}$$

From these general equations it is possible to describe the polarization of the electric field in a wide range of spectrometer geometries. In the following we will investigate the special case $\alpha = 90^\circ$ (vertical input polarization) and an elevation angle $\theta = 60^\circ$. For the purpose of testing the analysis method discussed here, a reflection spectrometer was constructed with these parameters. In this special case, the ratios of the horizontal and vertical components of the electric field reflected from the window-sample interface and the air-window interface, respectively, are

$$\frac{E_{out,x}^{sam}}{E_{out,x}^{ref}} = \frac{\hat{r}_{23,sam}^{\parallel}t_{12}^{\parallel}t_{21}^{\parallel}+\hat{r}_{23,sam}^{\perp}t_{12}^{\perp}t_{21}^{\perp}}{r_{12}^{\parallel}+r_{12}^{\perp}}A_{cal}\exp(i\Delta_{cal})\exp(2in_2\omega d_{eff}/c) \tag{7}$$

$$\frac{E_{out,y}^{sam}}{E_{out,y}^{ref}} = \frac{\hat{r}_{23,sam}^{\parallel}t_{12}^{\parallel}t_{21}^{\parallel}-3\hat{r}_{23,sam}^{\perp}t_{12}^{\perp}t_{21}^{\perp}}{r_{12}^{\parallel}-3r_{12}^{\perp}}A_{cal}\exp(i\Delta_{cal})\exp(2in_2\omega d_{eff}/c). \tag{8}$$

From this point we will assume that the detector is oriented to detect the x-component of the output field, and drop the subscript x. A typical measurement of the signal trace in this geometry is shown in Fig. 3. The two signals in the trace are the reference signal from the lower interface between air and the silicon window and then, 46 ps later, the sample signal from the reflection at the interface between the silicon window and the sample material, in this case air. This time delay between the reference pulse and the sample pulse is due to the propagation distance of the pulse through the 2.00-mm thick silicon window. The pulses are generated and detected by ultrafast photoconductive switching and sampling, respectively [14]. The temporal separation of the two signals allows an easy separation of the reference and sample signals for the subsequent analysis.

The ratio of the spectra of the sample- and the reference signals is shown in Fig. 4, together with the spectrum of the phase difference between the two signals. The phase difference has been corrected for the accumulated phase due to the propagation distance, $2n_2\omega d_{eff}/c$.

We expect a sign reversal between the two signals since the reference signal is reflected at an interface to a denser medium while the sample signal is reflected at an interface to a less

#87328 - $15.00 USD Received 7 Sep 2007; revised 23 Oct 2007; accepted 23 Oct 2007; published 24 Oct 2007

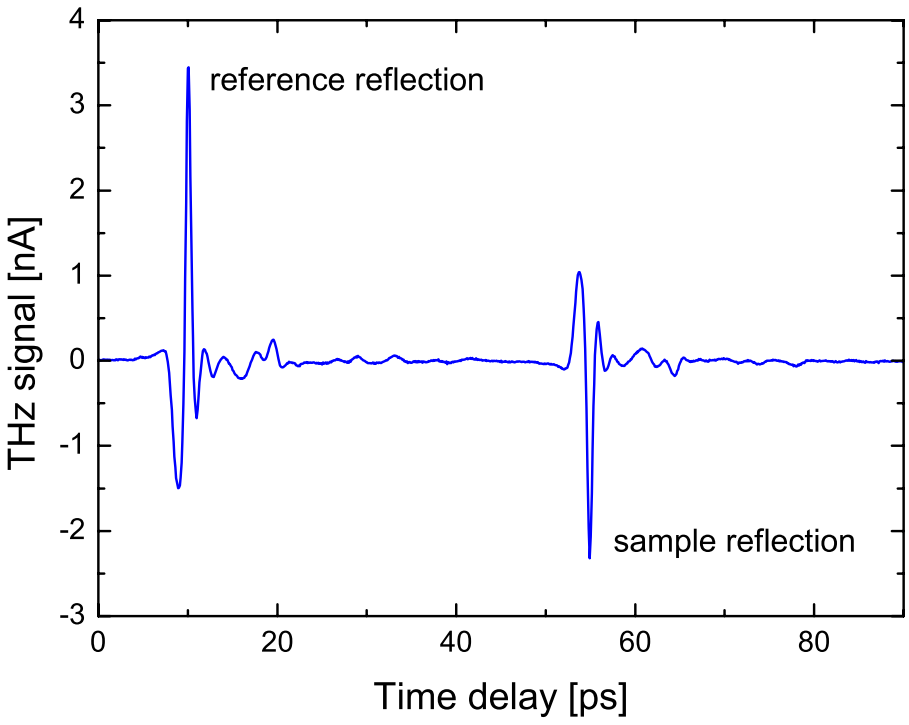

Fig. 3. The THz signal trace recorded in a spectrometer with vertical input polarization ($\alpha = 90^\circ$) and elevation angle $\theta = 60^\circ$. The reference signal is the reflection from the air-silicon interface, and the sample signal is the reflection from the opposite interface between silicon and the sample material, in this case air.

dense medium. This is indicated as the theoretical value π in Fig. 4(b). The measured phase difference is close to this expected value, but nevertheless we observe some differences. The same is the case for the ratio of the amplitudes of the two reflections, shown in Fig. 4(a). The expected ratio of the amplitudes is given by the prefactor in Eq. (7), which has the numerical value 0.697 for our geometry.

The calibration factor $A_{cal}\exp(i\Delta_{cal})$ can be determined by a measurement with air in contact with the window,

$$A_{cal}\exp(i\Delta_{cal}) = \frac{E_{out}^{air}}{E_{out}^{ref}} \frac{r_{12}^{\parallel} + r_{12}^{\perp}}{r_{23,air}^{\parallel} t_{12}^{\parallel} t_{21}^{\parallel} + r_{23,air}^{\perp} t_{12}^{\perp} t_{21}^{\perp}} \exp(-2in_2\omega d_{eff}/c) \tag{9}$$

The amplitude and phase of the calibration factor is shown in Fig. 5. The amplitude of the calibration factor oscillates around unity, and the phase of the calibration factor oscillates around zero. The amplitude of the oscillations indicate that the inclusion of this correction factor in the subsequent analysis is indeed important.

If Eq. (9) is now reinserted into the expression for the sample to reference ratio, now obtained from an unknown sample, one gets

$$A_{sam}\exp(i\Delta_{sam}) \equiv \frac{E_{out}^{sam}}{E_{out}^{ref}} = \frac{\hat{r}_{23,sam}^{\parallel} t_{12}^{\parallel} t_{21}^{\parallel} + \hat{r}_{23,sam}^{\perp} t_{12}^{\perp} t_{21}^{\perp}}{r_{23,air}^{\parallel} t_{12}^{\parallel} t_{21}^{\parallel} + r_{23,air}^{\perp} t_{12}^{\perp} t_{21}^{\perp}} \frac{E_{out}^{air}}{E_{out}^{ref}} \tag{10}$$

#87328 - $15.00 USD Received 7 Sep 2007; revised 23 Oct 2007; accepted 23 Oct 2007; published 24 Oct 2007

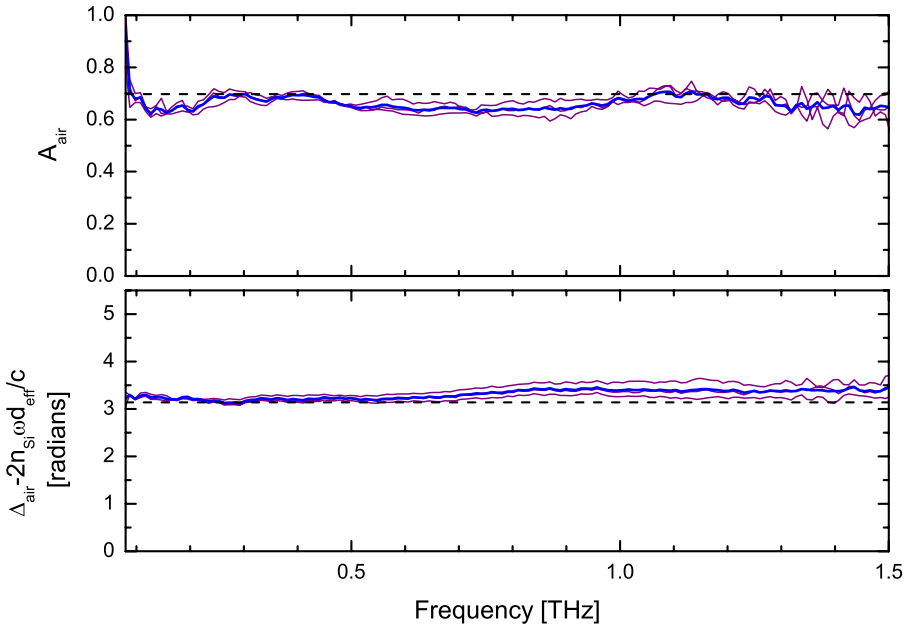

Fig. 4. (a) Amplitude ratio and (b) phase difference between the sample- and reference signal in Fig. 3. The phase difference has been corrected for the accumulated phase due to propagation through the window material. The thin, purple curves show three individual measurements, and the thick, blue curves show the average of these. The dashed lines indicate the theoretical amplitude ratio and phase difference.

The complex index of refraction $\hat{n}_3$ of the sample material can now be found by solving either Eq. (7) or Eq. (8) with respect to $\hat{n}_3$. For this purpose, the functional form of the various reflection- and transmission coefficients must be known. These coefficients are functions of the incidence angle at the respective interfaces. When expressed in terms of the incidence angle $\phi = 90^\circ - \theta$ at the first air-window interface these coefficients can be written as

$$r_{12}^{\parallel} = \frac{-n_2^2\cos\phi + \sqrt{n_2^2 - \sin^2\phi}}{n_2^2\cos\phi + \sqrt{n_2^2 - \sin^2\phi}}, \tag{11}$$

$$r_{12}^{\perp} = \frac{\cos\phi - \sqrt{n_2^2 - \sin^2\phi}}{\cos\phi + \sqrt{n_2^2 - \sin^2\phi}}, \tag{12}$$

$$t_{12}^{\parallel} = \frac{2\cos\phi}{n_2\cos\phi + \sqrt{1 - \sin^2\phi/n_2^2}}, \tag{13}$$

$$t_{12}^{\perp} = \frac{2\cos\phi}{\cos\phi + n_2\sqrt{1 - \sin^2\phi/n_2^2}}, \tag{14}$$

$$t_{21}^{\parallel} = \frac{2n_2\sqrt{1 - \sin^2\phi/n_2^2}}{n_2\cos\phi + \sqrt{1 - \sin^2\phi/n_2^2}}, \tag{15}$$

#87328 - $15.00 USD Received 7 Sep 2007; revised 23 Oct 2007; accepted 23 Oct 2007; published 24 Oct 2007

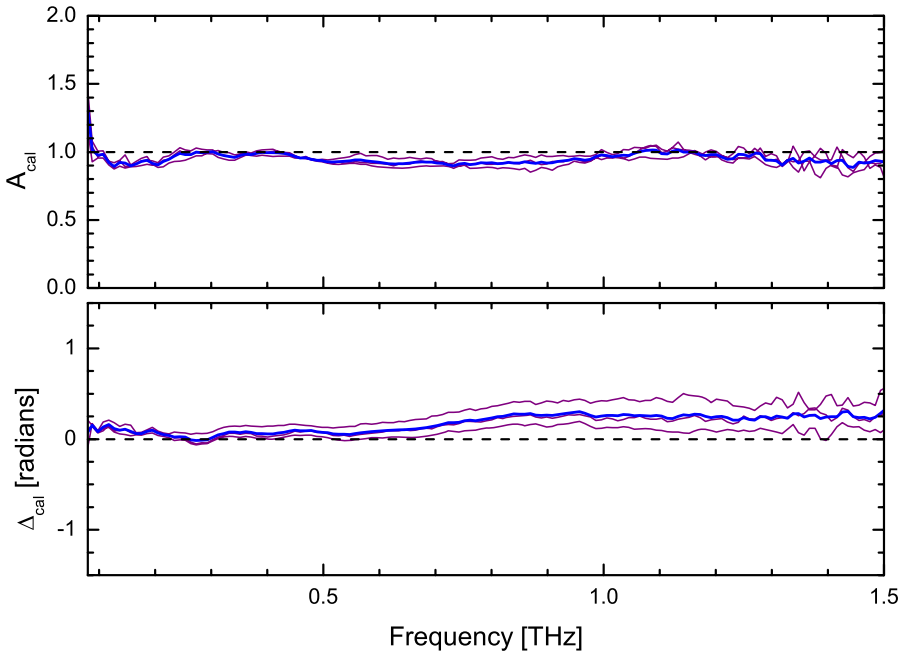

Fig. 5. Amplitude $A(\nu)$ and phase $\Delta(\nu)$ of the calibration factor of our spectrometer with $\theta = 60^\circ$ and $\alpha = 90^\circ$ (vertical input polarization). The thin, purple curves show three individual measurements, and the thick, blue curves show the average of these.

$$t_{21}^{\perp} = \frac{2n_2\sqrt{1-\sin^2\phi/n_2^2}}{\cos\phi + n_2\sqrt{1-\sin^2\phi/n_2^2}}, \tag{16}$$

$$\hat{r}_{23}^{\parallel} = \frac{-\hat{n}_3^2\sqrt{n_2^2-\sin^2\phi} + n_2^2\sqrt{\hat{n}_3^2-\sin^2\phi}}{\hat{n}_3^2\sqrt{n_2^2-\sin^2\phi} + n_2^2\sqrt{\hat{n}_3^2-\sin^2\phi}}, \tag{17}$$

$$\hat{r}_{23}^{\perp} = \frac{\sqrt{n_2^2-\sin^2\phi} - \sqrt{\hat{n}_3^2-\sin^2\phi}}{\sqrt{n_2^2-\sin^2\phi} + \sqrt{\hat{n}_3^2-\sin^2\phi}}. \tag{18}$$

Inserting these expressions into Eq. (10) results in an expression relating the ratio of the sample- and reference signals and complex index of refraction of the sample material. For a given geometry (incidence angle, window thickness and window refractive index) the sample refractive index is found as the single physically meaningful root of a fourth-order polynomial expression. The solution can be written in closed form if the various coefficients are evaluated numerically for the specific configuration. Due to the complexity of the solution we will not write it out here.

Alternatively the solution can be obtained by an iterative procedure [15], using the values estimated using magic angles (see next section) as initial guess.

The complex index of refraction is related to the dielectric function of the material through the relation $\hat{\varepsilon}_3 = \varepsilon_3' + i\varepsilon_3'' = \hat{n}_3^2 = (n_3 + i\kappa_3)^2$. In the data analysis in the subsequent sections we will focus on the dielectric function instead of the complex index of refraction.

#87328 - $15.00 USD Received 7 Sep 2007; revised 23 Oct 2007; accepted 23 Oct 2007; published 24 Oct 2007

If we remove the sample material from the silicon window, it is possible to perform an accuracy check of the system. In Fig. 6 we show the resulting apparent real and imaginary part of the dielectric function of air. The real part of the apparent dielectric function of air is located

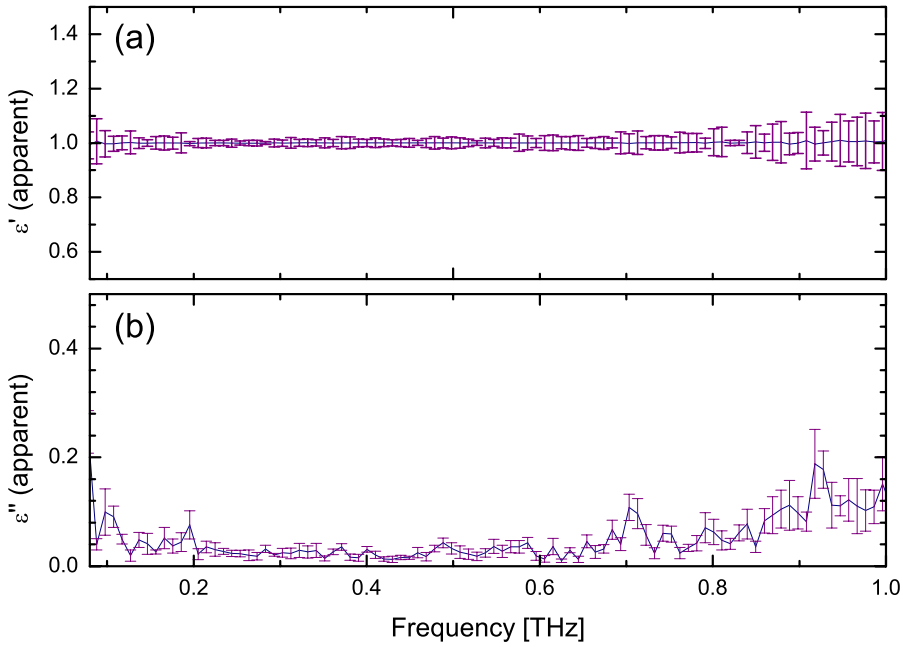

Fig. 6. The apparent (a) real and (b) imaginary part of the dielectric function of air, as measured with the reflection spectrometer. The error bars indicate the standard deviation of the average value of 5 sequential measurements.

very near the expected value $\varepsilon'_{air} = 1$, and for low frequencies, the apparent imaginary part of the dielectric function of air, ε''_{air}, is close to zero, as expected. However, ε''_{air} increases slightly at higher frequencies. This increase is caused by small uncertainties in the detected phase of the sample signal, compared to the reference measurement. This source of error seems to be most important for samples with a very small absorption, as will be discussed in Section 2.3.

2.2. Analysis using magic angles

The complexity of the analysis arises from the presence of both *s*- and *p*-polarized light at the sample interface. For a given elevation angle θ, a pure *s*- or *p*-polarization at the sample interface can be obtained by appropriate rotation of the input polarization ($\alpha = 60^\circ$ gives pure *s*-polarization and $\alpha = -30^\circ$ gives pure *p*-polarization). In these cases the extraction of the complex index of refraction of the sample material becomes significantly simpler than for the situation where both *s*- and *p*-components are present at the reflection.

For an incident polarization angle of $\alpha = 60^\circ$ the ratio of the *x*- and *y*-projections of the output field are identical, and can be expressed as of the sample and reference signals are

$$A^{\perp}_{sam} \exp(i\Delta^{\perp}_{sam}) = \frac{\hat{r}^{\perp}_{23,sam}}{r^{\perp}_{23,air}} \frac{E^{air}_{out}}{E^{ref}_{out}} \,. \tag{19}$$

Correspondingly, for $\alpha = -30^\circ$, the ratio of the *x*- and *y*-components of the output field are

#87328 - $15.00 USD Received 7 Sep 2007; revised 23 Oct 2007; accepted 23 Oct 2007; published 24 Oct 2007

identical, and can be expressed as

$$A^{\parallel}_{sam}\exp(i\Delta^{\parallel}_{sam}) = \frac{\hat{r}^{\parallel}_{23,sam}}{r^{\parallel}_{23,air}}\frac{E^{air}_{out}}{E^{ref}_{out}} \ . \tag{20}$$

Although the *ratio* of the *x*- and *y*-components of the output field are the same in these expressions, the *overall* signal strength, and consequently also the signal-to-noise ratio, can be optimized by aligning the polarization axis of the detector with the polarization of the output field.

As an example, if the emitter is mounted so that it results in an input polarization $\alpha = 60^\circ$, the complex index of refraction of the sample material can be found to be

$$\hat{n}_{sam} = \frac{\sqrt{(1-\hat{r}_{23,sam})^2 n_2^2 + 4\hat{r}_{23,sam}\sin^2\phi}}{1+\hat{r}_{23,sam}} \ , \tag{21}$$

where $\hat{r}_{23,sam}$ is found by inverting Eq. (19). The imaginary part of the index of refraction (the extinction coefficient) is related to the absorption coefficient, $\hat{n}_{23,sam} = n + i\kappa = n + i\alpha c/2\omega$.

2.3. Verification of the accuracy of the spectrometer

In the next section we will describe an application of the reflection spectrometer. In order to verify the accuracy of the analysis method described in the previous sections, we performed a calibration measurement with deionized water and pure ethanol as sample materials. The spectrometer was set up with the input polarization $\alpha = 90^\circ$ and elevation angle $\theta = 60^\circ$, and hence the full analysis with mixed polarization at the sample interface has been applied.

In order to compare our results with already published data the dielectric functions measured for water and ethanol, respectively, are shown in Fig. 7. The real and imaginary part of the dielectric function are defined as $\varepsilon' + i\varepsilon'' = (n+i\kappa)^2$. The dielectric spectrum of water has been analyzed applying the double Debye model with two relaxation times [10, 11, 2],

$$\varepsilon(\omega) = \frac{\varepsilon_s - \varepsilon_1}{1 - i\omega\tau_1} + \frac{\varepsilon_1 - \varepsilon_\infty}{1 - i\omega\tau_2} + \varepsilon_\infty \ . \tag{22}$$

Likewise, the dielectric spectrum of ethanol has previously been analyzed using the triple Debye model [10, 11],

$$\varepsilon(\omega) = \frac{\varepsilon_s - \varepsilon_1}{1 - i\omega\tau_1} + \frac{\varepsilon_1 - \varepsilon_2}{1 - i\omega\tau_2} + \frac{\varepsilon_2 - \varepsilon_\infty}{1 - i\omega\tau_3} + \varepsilon_\infty \ , \tag{23}$$

where three relaxation times are required for a satisfactory agreement between experimental data and the model. In Table 1 we compare the fitting parameters obtained using our data and data from the literature [10, 11, 2].

In our analysis of the water dielectric spectrum we have kept the value of the static permittivity ε_s constant at the value determined in microwave experiments by Barthel *et al.* [10]. Because of the rapid increase of the dielectric function at low frequencies we cannot reliably fit the value of ε_s from our experimental data. Similarly, during the fitting of the triple Debye model to our experimental ethanol data, we kept the values of ε_s, ε_1, and τ_1 fixed at the values reported by Barthel *et al.* [10].

The good agreement between the result of our analysis and published values of the Debye parameters confirms that the spectrometer configuration in reflection geometry with both *s*- and *p*-polarized THz light incident on the sample window at non-normal incidence, together with the analysis outlined above, can precisely characterize the dielectric properties of liquids.

#87328 - $15.00 USD Received 7 Sep 2007; revised 23 Oct 2007; accepted 23 Oct 2007; published 24 Oct 2007

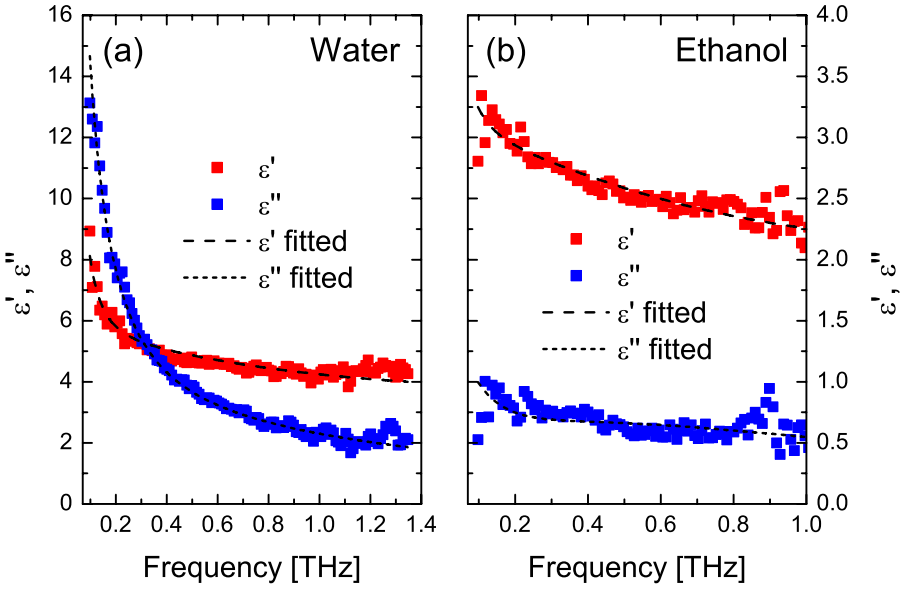

Fig. 7. The real (red symbols) and imaginary (blue symbols) part of the dielectric function of (a) water and (b) ethanol recorded at a temperature of 20°C. The fitted curves are described in the text.

3. Reflection spectroscopy of ethanol-water solutions

The analysis outlined in the previous sections will now be applied to spectroscopy of aqueous solutions of ethanol and sucrose. The results in Fig. 7 demonstrate the significant difference in the dielectric properties of pure water and pure ethanol in the THz range. Kitahara *et al.* used transmission THz-TDS to determine the dielectric function of water-ethanol mixtures [12]. Recently, Nagel et al. used a corrugated parallel-plate waveguide chip to measure the real and imaginary parts of the refractive index in water-ethanol mixtures [13].

We prepared a series of 21 samples of water-ethanol mixtures with varying alcohol content from 0% to 100%, increased in 5%-steps. Each of these samples were then characterized with our reflection setup. The temperature of the sample material was determined by the ambient temperature of the laboratory, and remained stable within 1-2 Kelvin during the measurements. The real and imaginary parts (in the following denoted ε' and ε'', respectively) of the dielectric function in the frequency range 0.1-1.1 THz of these mixtures are shown in Fig. 8.

Both ε' and ε'' show a pronounced dependence on the alcohol concentration. The effect is strongest on ε''. We also note the gradual and monotonic change of the dielectric function from that of pure water to that of pure ethanol, in agreement with the dielectric spectra based on transmission measurements reported by Kitahara *et al.* [12].

The pronounced dependence of ε' and ε'' on the alcohol concentration suggests that we can determine the alcohol concentration of an aqueous solution of alcohol by comparing the dielectric function of the unknown sample to the reference curves in Fig. 8. Chemometric approaches such as principal components analysis would be a standard method for this determination. However, due to the lack of distinct spectral features only a single, or at most two, principal components of the spectra will contain useful information. Therefore we will apply a simpler approach, with basically the same accuracy. In Fig. 9 we have plotted the average value over the frequency range 0.15-1.0 THz of ε' and ε'', as functions of the ethanol concentration

#87328 - $15.00 USD Received 7 Sep 2007; revised 23 Oct 2007; accepted 23 Oct 2007; published 24 Oct 2007

Table 1. Comparison with existing literature of Debye model parameters for water and ethanol. Values marked with $\star$ have been kept fixed in the fitting process. The reported uncertainties are the standard deviations of the estimated parameter values.

Water, double Debye model parameters

	This work	Kindt *et al.* [11]	Rønne *et al.* [2]	Barthel *et al.* [10]
ε_s	$78.36^\star$	$78.36^\star$	$80.58^\star$	78.36
τ_1 [ps]	7.89 ± 0.06	8.24 ± 0.40	8.5 ± 0.4	8.32
ε_1	5.16 ± 0.06	4.93 ± 0.54	5.2 ± 0.1	6.18
τ_2 [ps]	0.181 ± 0.014	0.180 ± 0.014	0.170 ± 0.04	1.02
ε_∞	3.49 ± 0.07	3.48 ± 0.70	3.3 ± 0.3	4.49

Ethanol, triple Debye model parameters

	This work	Kindt *et al.* [11]	Barthel *et al.* [10]
ε_s	$24.35^\star$	$24.35^\star$	24.35
τ_1 [ps]	$163^\star$	161	163
ε_1	$4.49^\star$	4.15	4.49
τ_2 [ps]	3.01 ± 0.21	3.3	8.97
ε_2	2.91 ± 0.04	2.72	3.82
τ_3 [ps]	0.235 ± 0.018	0.22	1.81
ε_∞	1.949 ± 0.034	1.93	2.29

in the solution.

The solid curves are phenomenological fits to the average values of ε' and ε'', in the following denoted $\overline{\varepsilon'}$ and $\overline{\varepsilon''}$ in the frequency range 0.15-1.0 THz. We used an exponential function to fit both curves,

$$\overline{\varepsilon'}(x) = A' + B' \exp(-C'x) \,, \tag{24}$$

$$\overline{\varepsilon''}(x) = A'' + B'' \exp(-C''x) \,, \tag{25}$$

with the fitting parameters $A' = 0.137$ (kept fixed), $B' = 4.554 \pm 0.029$, $C' = 0.623 \pm 0.013$, $A'' = 0.501 \pm 0.052$, $B'' = 3.534 \pm 0.053$, and $C'' = 3.177 \pm 0.14$, obtained by a standard non-linear least-squares curve fitting routine.

In the case of ideal additivity of the contributions to the total optical attenuation and dispersion from the two components of the mixture, we expect [16, 18, 19] the complex index of refraction to be of the form

$$\hat{n}_{ideal}(\nu) = \frac{c^{mix}_{H_2O}}{c^{neat}_{H_2O}} \hat{n}_{H_2O}(\nu) + \frac{c^{mix}_{EtOH}}{c^{neat}_{EtOH}} \hat{n}_{EtOH}(\nu) \,, \tag{26}$$

where c_i^{mix} is the concentration of component i in the mixture and c_i^{neat} is the concentration of the component i in a neat sample of the component. The dashed lines in Fig. 9 shows the ideal behavior of the average dielectric function of the mixtures. These curves were calculated by using the absorption coefficient and index of refraction of neat water and neat ethanol, respectively, to calculate the effective complex index of refraction $\hat{n}_{ideal}(\nu)$ for each mixing ratio,

#87328 - $15.00 USD Received 7 Sep 2007; revised 23 Oct 2007; accepted 23 Oct 2007; published 24 Oct 2007

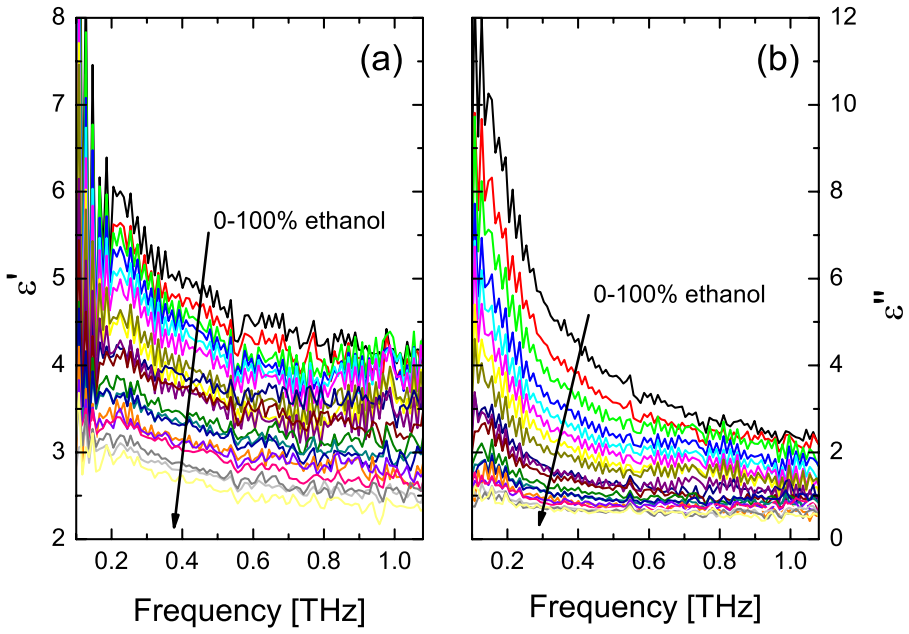

Fig. 8. The (a) real and (b) imaginary part of the dielectric function at room temperature of water-ethanol mixtures in the 0.1-1.1 THz range. The alcohol concentration is varied from 0% to 100% in 5%-steps.

using Eq. (26). Subsequently the dielectric function $\overline{\varepsilon'}_{ideal}(x)$ and hence $\overline{\varepsilon''}_{ideal}(x)$ could be calculated.

The observed behavior of both $\overline{\varepsilon'}$ and $\overline{\varepsilon''}$ is markedly different from the ideal mixing behavior. we observe that both $\overline{\varepsilon'}$ and $\overline{\varepsilon''}$ are smaller than expected from the ideal additivity hypothesis.

In a infrared study of mixtures of benzene and fluorinated benzene [16], Tassaing *et al.* concluded that only insignificant deviation from the additivity hypothesis was observed, although the authors mention a deviation below 30 cm^{-1}. Flanders *et al.* [17] studied mixtures of $CHCl_3$ and CCl_4, and found an increasing deviation from the ideal mixing behavior with increasing polar nature of the mixture. Venables *et al.* discussed mixtures of acetone/methanol, acetone/acetonitrile, and methanol/acetonitrile [18] and saw small deviations from the ideal additivity only in acetone/acetonitrile mixtures. In another study, Venables and Schmuttenmaer observed significant deviations from ideal additivity in water/acetone, water/acetonitrile, and water/methanol mixtures [19], specifically with a lower absorption coefficient and index of refraction of the mixture than expected for a mixture showing ideal additivity. Our observation of non-ideal mixing behaviour in a mixture of polar liquids is hence in agreement with the trend of already published observations.

If an unknown solution of ethanol in water is characterized by our setup, we can in a similar fashion determine $\overline{\varepsilon'}$ and $\overline{\varepsilon''}$. Inverting Eqs. (24) and (25) and forming the average of the two determinations of x, results in an estimate of the alcohol concentration of the unknown solution. This procedure was carried out on samples with ethanol concentrations from 0% to 100%, resulting in the correlation diagram shown in Fig. 10. The estimated alcohol concentration of the 21 samples with pure water and pure ethanol is shown as black symbols. The error bars are the standard deviations of each estimate, determined by the standard deviations of the fitted constants in Eqs. (24) and (25) as well as the standard deviations of $\overline{\varepsilon'}$ and $\overline{\varepsilon''}$ of the sample.

#87328 - $15.00 USD Received 7 Sep 2007; revised 23 Oct 2007; accepted 23 Oct 2007; published 24 Oct 2007

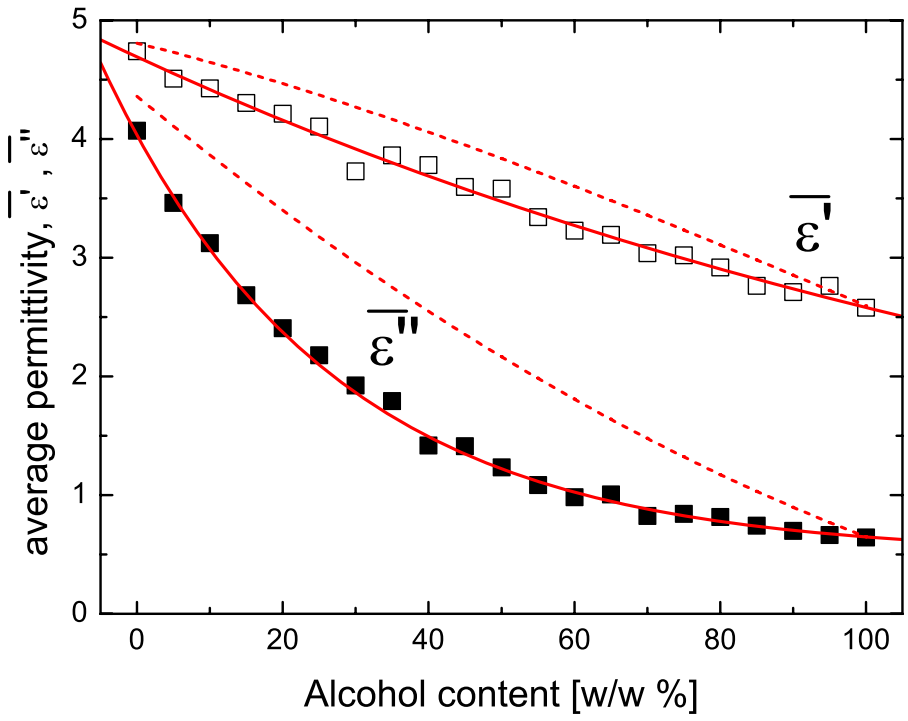

Fig. 9. The average value of the real and imaginary part of the dielectric function of water-ethanol mixtures in the 0.15-1.0 THz range, as function of the ethanol concentration. Solid curves are phenomenological fits to the experimental data, and the dashed lines show the ideal behavior of the mixtures.

The correlation between the reported and the estimated alcohol concentration is close to unity, with a slope of the best fit through the origin of 0.998. The standard deviation of the estimated values is approximately 1% at low alcohol concentrations, but increase to several % at higher concentrations. This is due to the decreasing slope of Eq. (25) at high alcohol concentrations.

Also shown in Fig. 10 are the estimated alcohol concentrations of a selection of commercial beverages and liquors, with alcohol strengths, converted from the labeling of the bottle to weight percentage, of 0.1% (alcohol-free beer), 4% (Danish Pilsner), 6.1% (Danish Porter beer), 8.8% (French white wine), 13.7% (Irish cream liquor), 37% (German Bitter), and 52% (Bulgarian Absinthe). The blue star-shaped symbols show the estimated concentrations versus the concentrations according to the labeling.

The estimated alcohol concentrations of the commercial alcohols are predicted with an accuracy of better than 1% with respect to the labeled alcohol strength, with the notable exception of the cream liquor. However, for this special liquor this strong deviation is to be expected since the content of cream leads to a significant reduction of both $\overline{\varepsilon'}$ and $\overline{\varepsilon''}$. Hence the initial assumption, that only alcohol contributes to the reduction of $\overline{\varepsilon'}$ and $\overline{\varepsilon''}$ is not valid for this type of liquor.

3.1. Influence of carbonation and sugar

It could be expected that measurements on carbonated solutions, such as softdrinks and sparkling wines, would be a special challenge for an optical detection technique. Transmis-

#87328 - $15.00 USD Received 7 Sep 2007; revised 23 Oct 2007; accepted 23 Oct 2007; published 24 Oct 2007

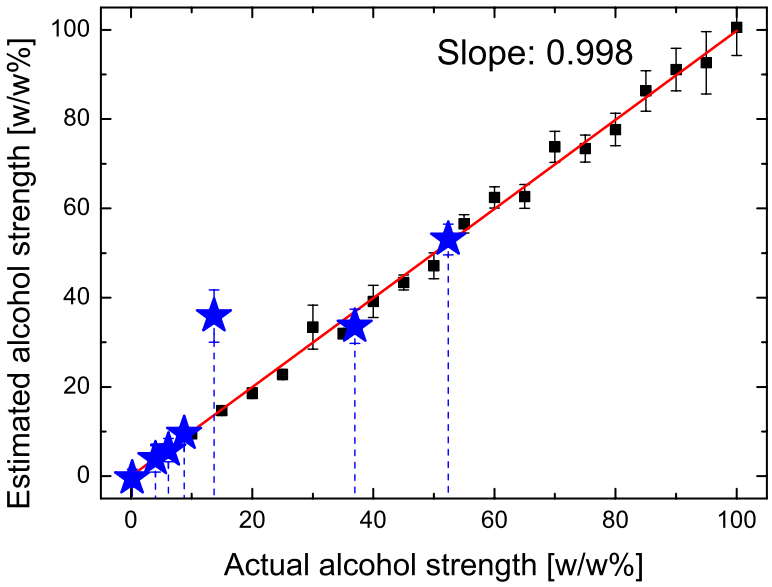

Fig. 10. The correlation between the known and the predicted concentration of ethanol in mixtures of deionized water and ethanol (black symbols) and commercial alcoholic beverages and liquors (blue, star-shaped symbols).

sion measurements would indeed be influenced by the presence of gas bubbles in the liquid due to strong and random scattering of the light on the bubbles.

The special configuration of the sample window, where the interface between the window and the liquid is oriented horizontally, allows bubbles formed in the sample liquid to rapidly escape the interface region. Hence carbonated liquids can be characterized with virtually the same accuracy as still samples. This is demonstrated in Fig. 11(a), where the dielectric function of pure water (black curve) is compared to that of carbonated mineral water (red curve) and the same carbonated water with the gas removed by vigorous shaking of the bottle prior to the measurements (blue curve). During the measurement on the carbonated water sample the formation and release of numerous gas bubbles was clearly visible.

The close resemblance of the spectra in Fig. 11 shows that the influence of carbonation on the reflection measurement of the dielectric properties is minimal. The reason why the influence on the measurements is so small is most likely that the time from formation of the gas bubble to its release from the interface is very short compared to the measurement time. At the same time, the large area of the sample interface reduces the probability that the gas bubbles are formed at the area sampled by the THz beam.

A closer look at Fig. 11(a) reveals that the real part of the dielectric function of the carbonated water is slightly larger than that of deionized water. Since this slight increase of $\overline{\varepsilon'}$ is the same for carbonated and decarbonated water, we rule out the formation of bubbles at the sample interface as the cause of this increase. More likely, the temperature of the sample material has varied slightly between the time of the measurement of the deionized water and the time of the

#87328 - $15.00 USD Received 7 Sep 2007; revised 23 Oct 2007; accepted 23 Oct 2007; published 24 Oct 2007

measurement of the carbonated and decarbonated water. The temperature is known to have a pronounced effect on the dielectric function of water in the THz range [2].

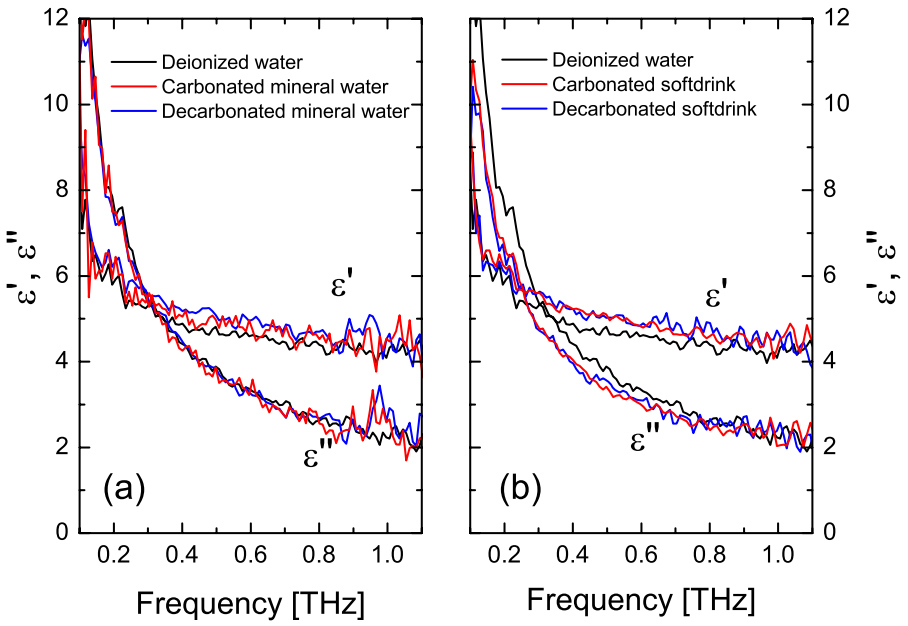

Fig. 11. The real and imaginary part of the dielectric function at room temperature of (a) deionized water, carbonated mineral water, and mineral water with gas removed, and (b) deionized water, a typical carbonated softdrink, and the same softdrink with the gas removed.

We repeated the measurements on various brands of carbonated water, and found that there is no significant and reproducible difference between the dielectric functions of the carbonated water and that of deionized water.

The influence of the sugar content in a commercial, carbonated softdrink on the dielectric function is investigated in Fig. 11(b). Here the dielectric function of the carbonated softdrink (red curve) and the same softdrink with the gas removed (blue curve), again by vigorous shaking of the bottle prior to the measurement, are shown. Again the formation of bubbles at the interface to the sample window seems to have minimal influence on the measurement. However, the real part of the dielectric function of the softdrink is higher than that of deionized water (black curve), and the imaginary part of the dielectric function is lower than that of deionized water, especially at frequencies below 0.7 THz. This difference can be attributed to the sugar content of the softdrink. In Fig. 12 we show the dielectric function of aqueous solutions of sucrose, for sucrose concentrations between 0 and 75% by weight. Preparation of the highest concentrations required a slight heating of the solution in order to dissolve the sucrose, but all measurements are carried out with the sample material at room temperature and without precipitation of sucrose crystals.

The real part of the dielectric function of aqueous solutions of sucrose shows only a weak dependence on the sucrose concentration. The imaginary part of the dielectric function, however, displays a significant dependence on the sucrose concentration. This is in contrast to the effect of mixing ethanol and water, where a pronounced dependence on the ethanol concentration was observed in both the real and imaginary part of the dielectric function of the solution.

#87328 - $15.00 USD Received 7 Sep 2007; revised 23 Oct 2007; accepted 23 Oct 2007; published 24 Oct 2007

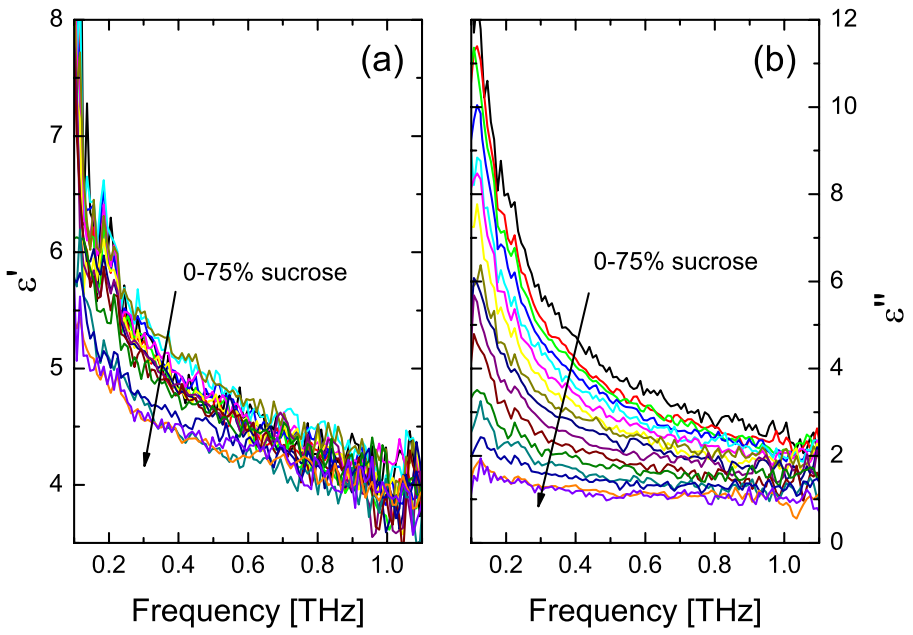

Fig. 12. The real and imaginary part of the dielectric function at room temperature of aqueous sucrose solutions, with sucrose concentrations from 0% to 75% by weight, measured in 5%-intervals.

The dependence on sucrose concentration of the average dielectric function in the frequency range 0.15-1.0 THz of the sucrose solutions is shown in Fig. 13.

The real part of the dielectric function of the sucrose solutions is seen to be basically independent of the sucrose concentration up to concentrations of approximately 40% by weight. At higher concentrations, a slight decrease of ε' is observed. The same plot shows a linear decrease of ε'' with increasing sucrose concentration. The red curves in Fig. 13 are linear fits to the data, using the functions

$$\varepsilon'(y) = \begin{cases} D' , & y < 40\% \\ -E'y + F' , & y \geq 40\% \end{cases} \quad (27)$$

$$\varepsilon''(y) = -E''y + F'' \quad (28)$$

with the fitting parameters $D' = 4.763 \pm 0.032$, $E' = 5.05 \pm 0.14$, $F' = 0.00978 \pm 0.0024$, $E'' = 0.0415 \pm 0.0007$, and $F'' = 4.11 \pm 0.03$.

3.2. Simultaneous determination of alcohol and sugar concentration

Having demonstrated that the dielectric function of an aqueous solution is sensitive both to the ethanol content and to the sucrose content we will now investigate if the technique can be used for the *simultaneous* determination of the concentration of both these components in an aqueous solution. The basis for this approach is that the modification of the dielectric function of the solution can be described as a sum of the individual modifications arising from the alcohol content and from the sugar content. Clearly this is an assumption that may only hold over a limited range of concentrations of alcohol and sugar. However, most commercial beverages and liquors contain a relatively small concentration of sugar.

#87328 - $15.00 USD Received 7 Sep 2007; revised 23 Oct 2007; accepted 23 Oct 2007; published 24 Oct 2007

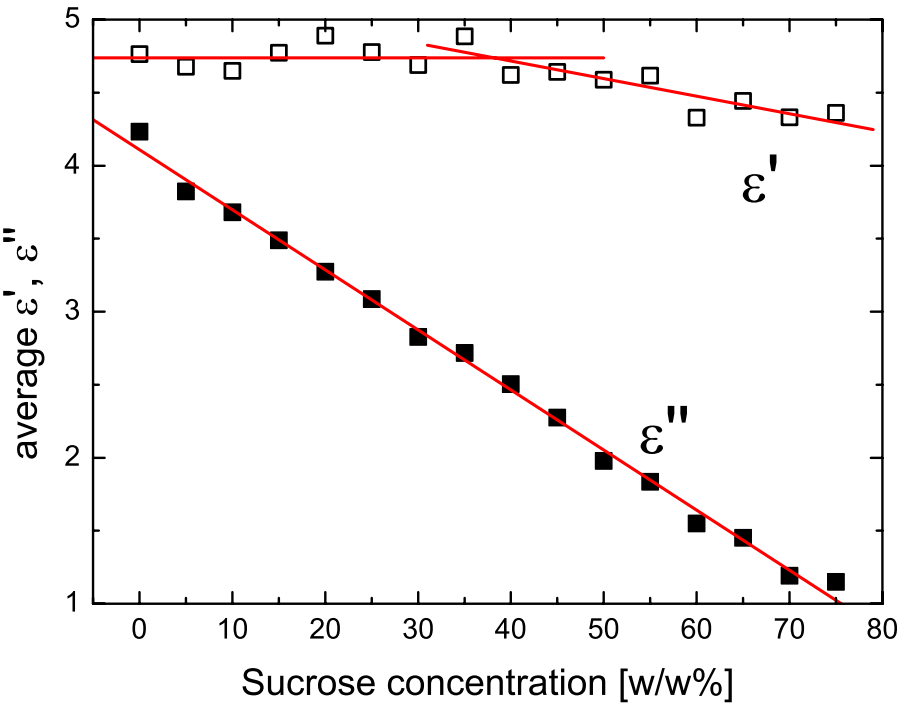

Fig. 13. The average value of the real and imaginary part of the dielectric function in the frequency interval 0.15-1.0 THz of aqueous sucrose solutions as function of the sucrose concentration. The solid curves are phenomenological fits, as discussed in the text.

In Fig. 14 the real and imaginary part of the dielectric function for mixtures of sucrose and ethanol in water are shown together with the dielectric functions of pure water, a water-ethanol solution, and a water-sucrose solution. Clearly the addition of up to 20% sucrose to the pure water as well as to the alcohol solution has little effect on the real part of the dielectric function of the solution. The effect of adding 10 and 20% sucrose to the solutions is however clearly seen in the lowering of the imaginary part of the dielectric function of the solution.

If we denote the ethanol concentration x and the sucrose concentration y, the above analysis indicates that the average dielectric function in the frequency interval 0.15-1.0 THz of a solution of ethanol and sugar in water can be written as

$$\varepsilon'(x,y) = A' + B'\exp(-C'x) \quad (29)$$

$$\varepsilon''(x,y) = A'' + B''\exp(-C''x) - E''y \quad (30)$$

where the constants in these equations are the same as given earlier. When using this analysis on the dielectric functions of the sucrose-ethanol solutions in Fig. 14 we obtain a fairly good agreement between the known concentrations of sucrose and ethanol and the concentrations predicted by the model. Specifically, the 10%-sucrose-20%-ethanol solution was predicted to contain (13.6 ± 2.5)% sucrose and (18.6 ± 1.1)% ethanol. The 20%-sucrose-20%-ethanol solution was predicted to contain (19.4 ± 2.5)% sucrose and (19.4 ± 1.1)% ethanol.

The extraction of the concentration of two components in the solution is possible because we measure both the real and imaginary part of the dielectric function. Two components is the

#87328 - $15.00 USD Received 7 Sep 2007; revised 23 Oct 2007; accepted 23 Oct 2007; published 24 Oct 2007

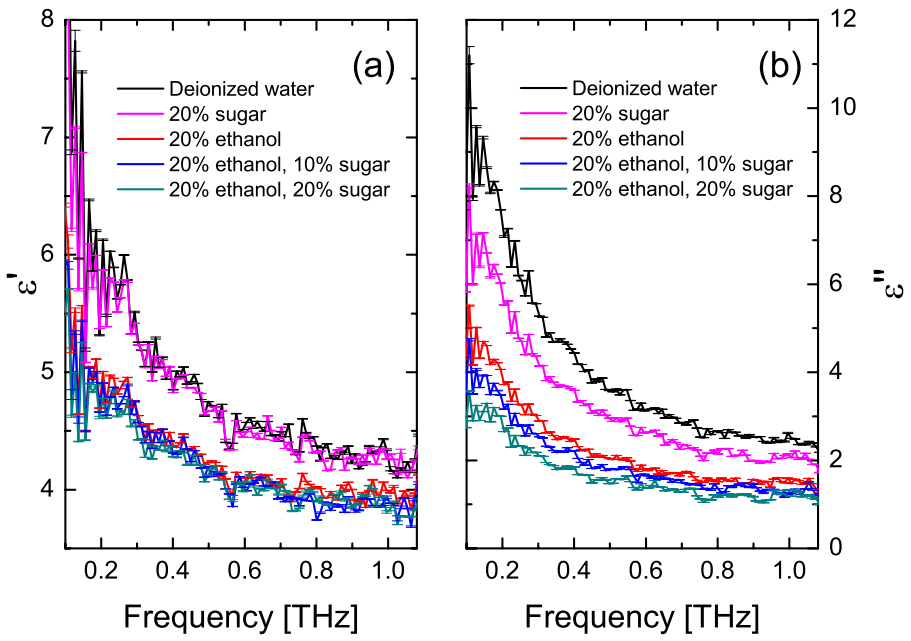

Fig. 14. The real and imaginary part of the dielectric function of pure water, a 20% sucrose solution, a 20% ethanol solution, and two solutions containing 10 and 20% sucrose and 20% ethanol.

maximum number of components that can be quantified with the method applied here, and the method requires that (a) no other components in the liquid contributes significantly to changes of the dielectric function of the solvent (here water) and (b) that changes of the dielectric function owing to the presence of two components can be described as the sum of the individual contributions. The quantification of even more complex mixtures of components would require specific signatures in the dielectric spectrum. The presence of such signatures would effectively increase the dimensionality of the data set, and chemometric approaches would become efficient. We have carried out a rigorous principal components analysis on the data presented here and found that the lack of distinct spectral features in the dielectric functions resulted in the same accuracy as the method applied above.

4. Conclusions

We have analyzed a method for the extraction of the dielectric function of a sample in the THz region by self-referenced reflection THz time-domain spectroscopy. The analysis takes an arbitrary incidence angle, as well as arbitrary input polarization of the THz field into account, and we validated the data extraction procedure in a comparison between our measurement of the dielectric functions of liquid water and ethanol and reported data in the literature.

We then devised a method for the determination of the alcohol content in water-alcohol mixtures, based on the THz dielectric properties of the mixture. Interestingly, this method can also be used to determine the alcohol concentration in commercial beverages and liquors. The accuracy of the method was found to be highest at low alcohol concentrations. The accuracy is mainly determined by the signal-to-noise level of the spectrometer.

The simultaneous measurement of both the real and the imaginary part of the dielectric func-

#87328 - $15.00 USD Received 7 Sep 2007; revised 23 Oct 2007; accepted 23 Oct 2007; published 24 Oct 2007

tion gives the possibility of determination of two ingredients in an aqueous solution, even in the absence of spectral features in the dielectric function of the sample. We demonstrated that it is possible to determine both alcohol and sugar content with an accuracy of a few percent in the concentration range typically found in commercial beverages and liquors.

We expect that stabilization of the sample temperature will further increase the accuracy of the method, making the method interesting for commercial applications.

This work was supported in part by the Danish Natural Science Research Council and the EU Integrated Project TeraNova.

#87328 - $15.00 USD Received 7 Sep 2007; revised 23 Oct 2007; accepted 23 Oct 2007; published 24 Oct 2007

.

Characterization of aqueous alcohol solutions in bottles with THz reflection spectroscopy

Peter Uhd Jepsen, Jens Kristian Jensen, and Uffe Møller

DTU Fotonik - Department of Photonics Engineering, Technical University of Denmark, DK-2800 Kongens Lyngby, Denmark

jepsen@com.dtu.dk

Abstract: We demonstrate a method based on self-referenced THz time-domain spectroscopy for inspection of aqueous liquids, and in particular alcohol solutions, inside closed containers. We demonstrate that it is possible to determine the alcohol content of an aqueous solution, and that liquids can be classified as either harmless or inflammable. The method operates in reflection mode with the result that liquids opaque to THz radiation can be characterized with little influence of the bottle shape. The method works with plastic bottles as well as glass bottles, with absorption of THz radiation by the plastic or the glass being the limiting factor. The reflection mode allows for automatic control of the validity of the measurement. The method will be useful in liquid scanning systems at security checkpoints.

OCIS codes: (300.6495) Spectroscopy, terahertz; (220.2740) Geometric optical design; (120.4825) Optical time-domain reflectometry

References and links

1. T. Ikeda, A. Matsushita, M. Tatsuno, Y. Minami, M. Yamaguchi, K. Yamamoto, M. Tani, and M. Hangyo, "Investigation of inflammable liquids by terahertz spectroscopy," Appl. Phys. Lett. **87,** 034105 (2005)
2. N. W. Broad, R. D. Jee, A. C. Moffat, M. J. Eaves, W. C. Mann, and W. Dziki, "Non-invasive determination of ethanol, propylene glycol and water in a multi-component pharmaceutical oral liquid by direct measurement through amber plastic bottles using Fourier transform near-infrared spectroscopy," The Analyst **125,** 2054 (2000)
3. S. Dexheimer (ed.) *Terahertz Spectroscopy: Principles and Applications* (CRC Press, 2007)
4. P. Uhd Jepsen, U. Møller, and H. Merbold, "Investigation of aqueous alcohol and sugar solutions with reflection terahertz time-domain spectroscopy," Opt. Express **15,** 14717 (2007)
5. P. Uhd Jepsen and B. M. Fischer, "Dynamic range in terahertz time-domain transmission and reflection spectroscopy," Opt. Lett. **30,** 29 (2005)
6. M. Naftaly and R. E. Miles, "Terahertz time-domain spectroscopy of silicate glasses and the relationship to material properties," J. Appl. Phys. **102,** 043517 (2007)
7. H. Kitahara, T. Yagi, K. Mano, M. Wada Takeda, S. Kojima, and S. Nishizawa, "Dielectric characteristics of water solutions of ethanol in the terahertz region," J. Korean Phys. Soc. **46,** 82 (2005)
8. J.-Z. Bao, M. L. Swicord, and C. C. Davis, "Microwave dielectric characterization of binary mixtures of water, methanol, and ethanol," J. Chem. Phys. **104,** 4441 (1996)
9. T. Sato and R. Buchner, "Dielectric relaxation processes in ethanol/water mixtures," J. Phys. Chem. A **108,** 5007 (2004)

1. Introduction

In the recent years THz radiation, and in particular pulsed, broadband THz radiation, has been applied for demonstrations of imaging with chemical recognition capabilities. The lowest vibra-

#95613 - $15.00 USD Received 29 Apr 2008; revised 6 Jun 2008; accepted 6 Jun 2008; published 9 Jun 2008

tional modes of molecules in their crystalline environment fall in the THz range, so broadband THz spectroscopy is a versatile tool for identification of chemical substances in the crystalline or polycrystalline state. Strongly bound molecular crystals (typically hydrogen-bonded systems such as saccharides) display a strong coupling between phonon modes and molecular vibrational modes. In weakly bound molecular crystals, on the other hand, the vibrational modes are more separated into pure phonon modes and pure molecular modes.

THz radiation penetrates packing materials and clothing. Therefore the use of THz radiation for identification of hidden chemicals has been exploited, at least at the demonstration level. Such potential applications rely on specific spectral features arising from the lowest vibrational modes of the crystal lattice of the chemical substance. Hence the focus have been on inspection of dry, crystalline chemicals.

Liquids have a broadband dielectric response in the far infrared, without sharp and specific spectral features. Polar liquids interact strongly with THz radiation because of the intermolecular hydrogen bonding network. In comparison, nonpolar liquids show a much weaker interaction with THz radiation. While the lack of distinct spectral features hinder specific identification of a liquid, the contrast between polar and nonpolar liquids can be exploited for classification of a liquid. Ikeda *et al.* demonstrated that THz transmission spectroscopy can be used to distinguish between water and inflammable liquids, even through a plastic bottle [1]. Broad *et al.* used near-infrared spectroscopy to determine the distribution of ingredients in multicomponent pharmaceutical liquids, through the wall of amber plastic bottles [2]. Common to these two examples are that although identification is carried out through the plastic bottle wall, the methods rely on a known propagation distance through the liquid, and a transmission measurement.

Here we present an alternative method for the characterization and classification of liquids inside bottles that removes the requirement of a transmission measurement, and at the same time is less sensitive to false negative tests in a scenario where bottles are screened for dangerous (e.g. inflammable or explosive) liquids. We also show that the method can be used to determine the alcohol content of an aqueous liquid inside a bottle.

2. Experimental details

The method is based on the reflection of an ultrashort, broadband THz pulse from the surface of a bottle, as illustrated in Fig. (1). The THz pulse is generated and detected in a standard manner, using photoconductive dipole antennas excited and gated, respectively, by synchronous pulses from a femtosecond laser. The principles of generation and detection of pulsed THz radiation as well as the principles of THz time-domain spectroscopy are described for instance in [3]. As described in detail in a recent publication[4] we make use of the two reflections returned from the bottle, namely the *reference* reflection from the outer surface of the bottle, and the *sample* reflection, returned from the inner surface of the bottle material which is in contact with the liquid. Fig. (1) shows some of the complications that might arise when performing measurements on real bottle shapes. A good identification system should be insensitive to whether the measurement is carried out on the bare bottle, through the label, at the edge of a label, or even through a detached piece of label.

The thickness of the bottle material as well as the topology of the bottle surface will influence the measurement. The thickness of the bottle material determines the temporal separation of the reflected reference and sample pulses, whereas the local topology strongly influences the temporal shape of both the returned pulses.

3. Characterization of bottle materials

Most commercial plastic bottles are made of poly(ethylene terephthalate), or PET. In Fig. (2) we show the optical properties (absorption coefficient and index of refraction) in the THz range

#95613 - $15.00 USD Received 29 Apr 2008; revised 6 Jun 2008; accepted 6 Jun 2008; published 9 Jun 2008

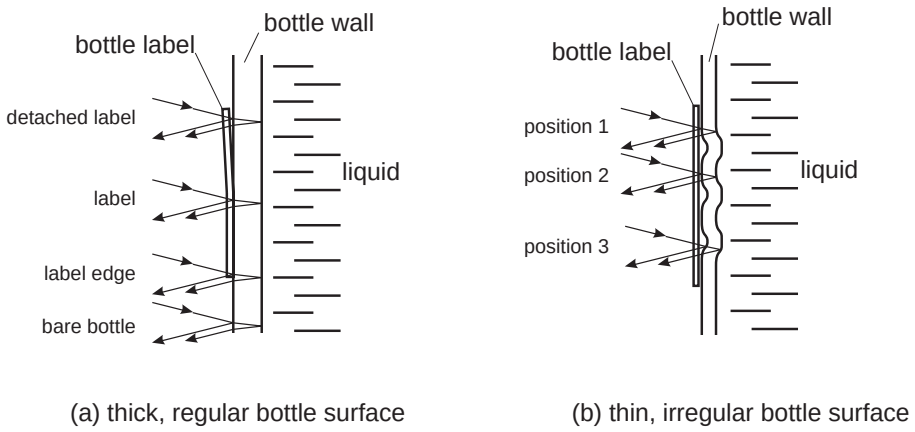

Fig. 1. Definitions of the geometry associated with reflection of the THz signal from a bottle. (a) A thick, regular bottle shape with a paper label and (b) a thin, irregular bottle shape with a loosely attached polymer label.

of different types of PET, compared to those of PMMA, or plexiglass.

The measurements were performed with a standard transmission THz-TDS system. We recorded the optical properties of two commercial polymers Axpet® and Vivak® as well as material cut out from a standard softdrink bottle from one of the major international brands. The absorption spectra of the different PET varieties are similar, and increase monotonically with frequency within our measurement bandwidth. The refractive indices of the PET varieties are similar, to within 0.1.

In Fig. (2) we also show the optical properties of glass cut out from a typical glass bottle. The absorption and index of refraction are shown up to 0.75 THz. Above this frequency the measurement was limited by the available dynamic range of the spectrometer [5].

The absorption coefficient of the glass used in our experiments is higher than the absorption of PET, and the index of refraction of the glass is also higher than that of PET. We note that the optical properties of PET is not too different from those of commercial glasses recently studied by Naftaly and Miles [6]. A more significant difference between PET and glass bottles is the larger wall thickness that in general is required to ensure the mechanical strength of glass bottles, compared to PET bottles. A typical PET bottle for carbonated softdrinks has a wall thickness of 0.65 mm, whereas the wall thickness of a glass bottle with the same volume is 3-4 mm. This, together with the somewhat higher absorption of glass compared to PET, leads to approximately an order of magnitude smaller transmission through a glass bottle wall compared to that of a PET bottle wall.

4. Inspection of liquids inside labeled bottles

We will now investigate the possibility of inspection of the properties of a liquid through the wall of a bottle, possibly covered by paper or plastic labels. For this purpose we filled a PET bottle (0.65 mm wall thickness) with water, and recorded the reflected THz signal from the bottle, with the THz beam incident at various locations on the bottle surface, as illustrated in Fig. (1). Later the measurements were repeated with isopropanol in the bottle. Isopropanol is a flammable liquid with a slightly lower index of refraction and slightly lower absorption coefficient than ethanol. Hence the data shown in this section may indicate how a low-index, volatile liquid can be distinguished from a high-index, non-volatile liquid.

#95613 - $15.00 USD Received 29 Apr 2008; revised 6 Jun 2008; accepted 6 Jun 2008; published 9 Jun 2008

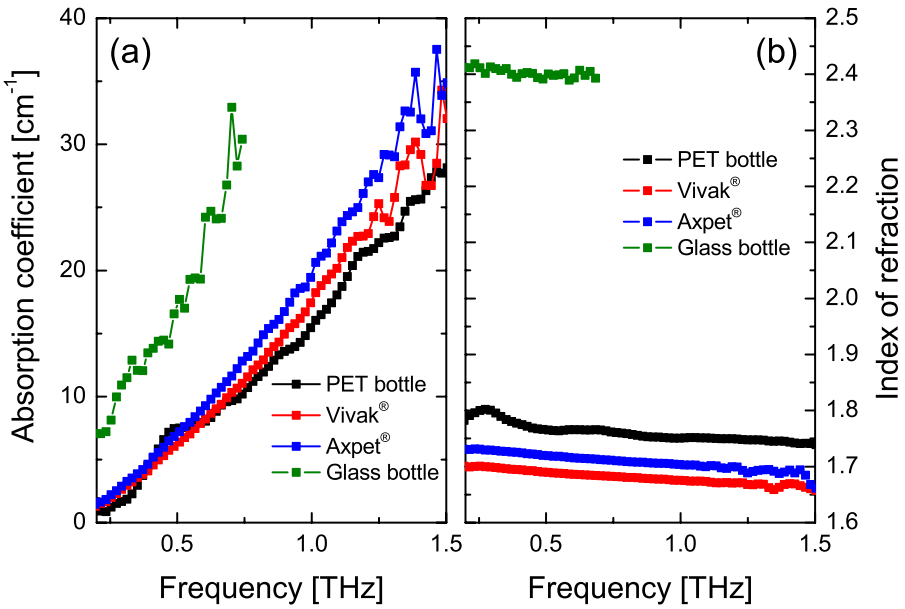

Fig. 2. (a) THz absorption coefficient and (b) index of refraction of PET, in the form of a softdrink bottle (black curves), Vivak®(red curves) and Axpet®(blue curves). The absorption and index of the glass bottle used in this study (dark olive curves) are also shown. All measurements are carried out at room temperature.

Figure 3(a) shows the THz signal reflected from a bare part of the bottle (blue, lower trace), from a position on the bottle completely covered by a paper label (red, middle trace), and from a position on the bottle partly covered by a paper label (green, upper trace). In Fig. 3(b) the reflected signals from similar positions on the same bottle filled with isopropanol are shown. In this plot an additional trace is shown, recorded at a position on the bottle where the label was detached from the bottle.

In all the situations considered in Fig. 3(a) the reflected signal consists of a reference signal and a sample signal, well separated from each other and with a relatively constant temporal shape. Even when the signal is reflected at a point near the edge of the label the signal shape is intact. The additional optical path through the label can be observed as a slight additional delay of the sample signal with respect to the reference signal, compared to the reflected signal from the bare bottle.

The set of measurements on the isopropanol-filled bottle, shown in Fig. 3(b) again show a clear separation between the reference signal and the sample signal. As expected the sample signal is significantly lower than that in Fig. 3(a). In addition the reference signal is strongly modified when the THz beam samples a position on the bottle with a detached label. Here the reference signal splits up due to the additional dielectric interfaces in the beam path. A similar, although less pronounced splitting is observed when we sample at the edge of the label. The reference signal recorded from the edge of the label is different from the similar measurement shown in Fig. 3(a). We took no special precautions to reflect off the exact same location of the bottle in these two situations, so the difference in the reference signal is representative of the spread in signal shapes that might be encountered in the general case.

The influence of atmospheric absorption is seen clearly as additional oscillations in all traces shown in Fig. (3). The experiments were carried out outside of the purged chamber of the THz-

#95613 - $15.00 USD Received 29 Apr 2008; revised 6 Jun 2008; accepted 6 Jun 2008; published 9 Jun 2008

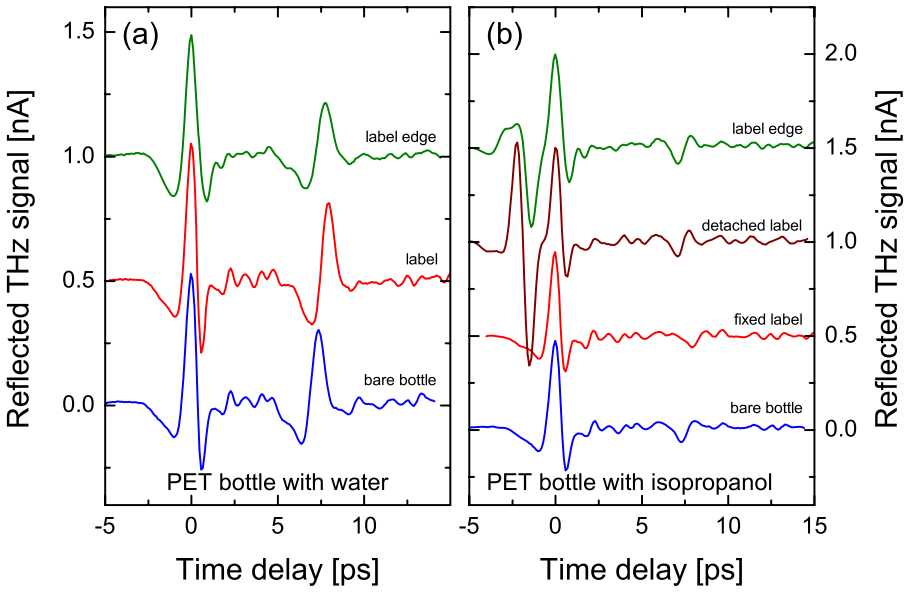

Fig. 3. Reflected THz signals from a PET bottle containing (a) water and (b) isopropanol. The different traces show the reflected signal from a position on the bare bottle, from a position at the edge of the paper label, and from a position on the label.

TDS system, with a THz beam path of 80 cm. Especially when investigating low-index liquids inside the PET container it is seen that the additional oscillations caused by the atmospheric absorption to some extent masks the sample reflection, hence making quantitative measurements difficult. This problem can, however, be minimized by reducing the THz beam path to an absolute minimum, for instance by integrating the THz emitter and detector in a handheld unit that can be brought into contact or to close proximity of the bottle.

Measurements on thinner PET bottles will lead to a smaller separation of the reference and sample signals, as shown in Fig. (4). Here measurements are carried out on a 0.17-mm PET bottle, typically used for still drinking water.

The two lower traces, shown in blue color, show reflected signals from a bottle containing water, and sampled at two different positions on the bottle surface, through the thin plastic label of the bottle. The two top traces, shown in red color, are similar traces recorded at two different positions on the same bottle filled with isopropanol. The variation among the reference signals in the four traces is significant, and the small temporal separation between the reference and sample signal makes a clear distinction between the two signals difficult. However, in spite of the more complicated signal structure compared to reflections from a thicker bottle, the signature of the water is still strong, and easy to distinguish from the isopropanol traces.

5. Simulation of reflected THz signals from bottles

In this section we will present a numerical simulation of the properties of the reflected THz signal from a bottle containing an aqueous solution of ethanol, and show how the reflected signal can be used to predict the alcohol content of the solution.

The reflected THz pulse sequence from the bottle wall can be described in terms of the Fresnel reflection and transmission coefficients of the interfaces of the bottle material. These coefficients are determined by the incidence angle and the optical properties of the bottle mate-

#95613 - $15.00 USD Received 29 Apr 2008; revised 6 Jun 2008; accepted 6 Jun 2008; published 9 Jun 2008

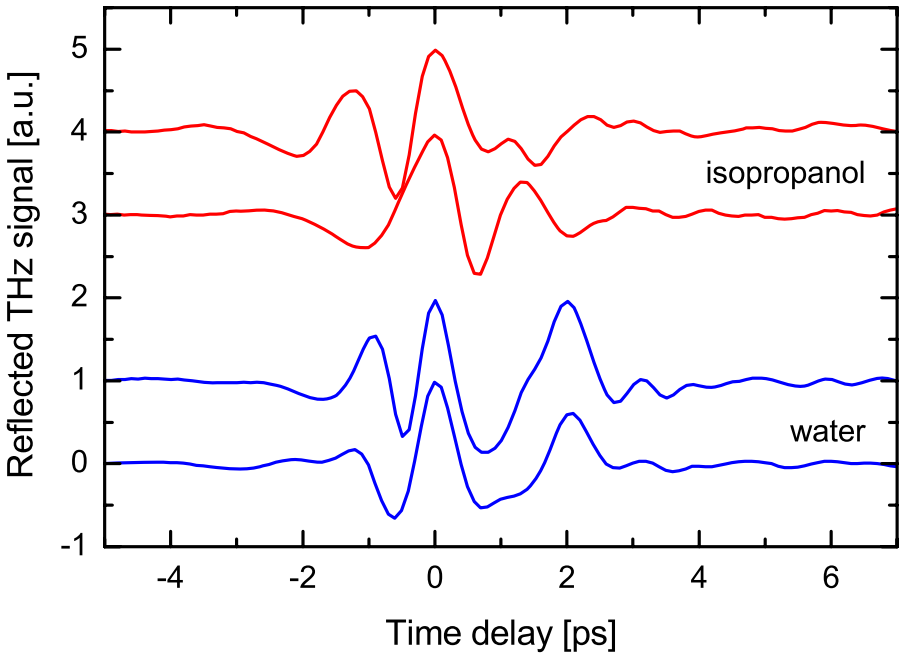

Fig. 4. Reflected THz signals from a thin (0.17 mm wall thickness) PET bottle containing water (lower two traces, shown in blue color) and and the same bottle containing isopropanol (upper two traces, shown in red color). Each trace was recorded at a new position on the bottle.

rial and the liquid in the bootle. The reflected field at the angular frequency $\omega = 2\pi\nu$ from the outer surface $E_{ref}(\omega)$ and the reflected field from the inner surface in contact with the liquid, $E_{sam}(\omega)$, are given by

$$E_{ref}(\omega) = \hat{r}_{12}E_{in}(\omega) \quad (1)$$

$$E_{sam}(\omega) = \hat{t}_{12}\hat{t}_{21}\hat{r}_{23}\exp\left(-\alpha_2 d_{eff} + 2in_2\omega d_{eff}/c\right) . \quad (2)$$

Here α_2 and n_2 are the absorption coefficient and index of refraction of the bottle material, respectively. The effective path length through the bottle wall, d_{eff}, is defined by the material thickness and the incidence angle. The complex index of refraction of the bottle material is defined in the usual manner, $\hat{n}_2 = n_2 + i\alpha_2 c/2\omega$. For simplicity we will assume that the incident field is TM-polarized.

The reflection and transmission coefficients can be expressed in terms of the external incidence angle ϕ as

$$\hat{r}_{12} = \frac{-\hat{n}_2^2\cos\phi + \sqrt{\hat{n}_2^2 - \sin^2\phi}}{\hat{n}_2^2\cos\phi + \sqrt{\hat{n}_2^2 - \sin^2\phi}} , \quad (3)$$

$$\hat{t}_{12} = \frac{2\cos\phi}{\hat{n}_2\cos\phi + \sqrt{1 - \sin^2\phi/\hat{n}_2^2}} , \quad (4)$$

#95613 - $15.00 USD Received 29 Apr 2008; revised 6 Jun 2008; accepted 6 Jun 2008; published 9 Jun 2008

$$\hat{t}_{21} = \frac{2\hat{n}_2\sqrt{1-\sin^2\phi/\hat{n}_2^2}}{\hat{n}_2\cos\phi+\sqrt{1-\sin^2\phi/\hat{n}_2^2}}, \quad (5)$$

$$\hat{r}_{23} = \frac{-\hat{n}_3^2\sqrt{\hat{n}_2^2-\sin^2\phi}+\hat{n}_2^2\sqrt{\hat{n}_3^2-\sin^2\phi}}{\hat{n}_3^2\sqrt{\hat{n}_2^2-\sin^2\phi}+\hat{n}_2^2\sqrt{\hat{n}_3^2-\sin^2\phi}}. \quad (6)$$

The optical properties of the alcohol-water mixture can be described in terms of the Debye model. The Debye model describes the low-frequency and far-infrared dielectric properties of polar liquids within the framework of one or more relaxation processes, each described by a relaxation time τ_i and a dielectric strength $\Delta\varepsilon_i$. The dielectric function of the liquid is then

$$\hat{\varepsilon}(\omega) = \varepsilon_\infty + \sum \frac{\Delta\varepsilon_i}{1-i\omega\tau_i} \quad (7)$$

In the literature it has been common to apply two relaxation times (the double Debye model) for the description of the dielectric properties of water, whereas three relaxation processes (the triple Debye model) seem to be required to reproduce the dielectric properties of alcohol. Kitahara *et al.* [7] measured the dielectric function of alcohol/water mixtures, using transmission THz time-domain spectroscopy. They used the triple Debye model to fit all their data in the frequency range 0.1-1 THz. We recently published similar data, obtained by reflection THz time-domain spectroscopy [4], covering approximately the same frequency range. The low-frequency part of the dielectric relaxation spectrum of water-alcohol mixtures is difficult to characterize with THz-TDS. Bao *et al.* published an analysis of the dielectric relaxation spectrum of water/ethanol mixtures in the range 45 MHz - 26 GHz [8], and Sato and Buchner recently published a comprehensive study in the range up to 89 GHz of water/alcohol mixtures[9]. In spite of the available data in the literature there is no consensus on the fitting parameters describing the dielectric function of water-alcohol mixtures. The low-frequency studies by Sato and Buchner [9] seem to overestimate ε_∞ and overestimate the fastest relaxation time τ_3, due to the lack of data at high frequencies, but that study and also the study by Bao *et al.* [8] firmly characterize the slowest relaxation process. The fitting procedure used by Kitahara *et al.* results in unphysically low values of ε_∞ and extremely fast relaxation processes, of the order of 30-50 fs.

Hence the parameters that give a good agreement between the triple Debye model and the experimental data are not the same in the < 0.1 THz region and in the 0.1-1 THz region. Therefore a goal for future THz research is the recording of the full dielectric function of water-ethanol mixtures at higher frequencies, up to 10 THz.

In spite of these fundamental difficulties with the interpretation of the dielectric function of water-ethanol mixtures we can nevertheless use the triple Debye model to set up a parameterized, phenomenological model for the dielectric function of the mixture for all mass fractions x_{EtOH} of ethanol. We have interpolated the fitted values for the parameters reported by Kitahara *et al.* and slightly modified the values of ε_∞ and $\Delta\varepsilon_2$ to reproduce the dielectric function of the neat liquids as recorded by reflection THz-TDS [4].

$$\begin{aligned}
\Delta\varepsilon_1(x_{EtOH}) &= 69.01 - 48.41x_{EtOH} \\
\Delta\varepsilon_2(x_{EtOH}) &= 2.01 - 0.62x_{EtOH} \\
\Delta\varepsilon_3(x_{EtOH}) &= 2.08 - 0.87x_{EtOH} \\
\varepsilon_\infty(x_{EtOH}) &= 2.10 - 0.76x_{EtOH} \\
\tau_1(x_{EtOH}) &= 9.02 + 68.78x_{EtOH}
\end{aligned}$$

#95613 - $15.00 USD Received 29 Apr 2008; revised 6 Jun 2008; accepted 6 Jun 2008; published 9 Jun 2008

$$\begin{aligned} \tau_2(x_{EtOH}) &= 0.80 + 0.73 x_{EtOH} \\ \tau_3(x_{EtOH}) &= 0.05 + 0.03 x_{EtOH} \end{aligned} \quad (8)$$

This parameterization is a simple linear interpolation between the parameter values for neat water and the parameter values for neat ethanol.

In Fig. (5) the real and imaginary parts of the calculated dielectric function of water-ethanol mixtures are shown with solid lines, as function of frequency and ethanol mass fraction. Also shown are the measured real and imaginary parts of the dielectric function of neat water and of neat ethanol.

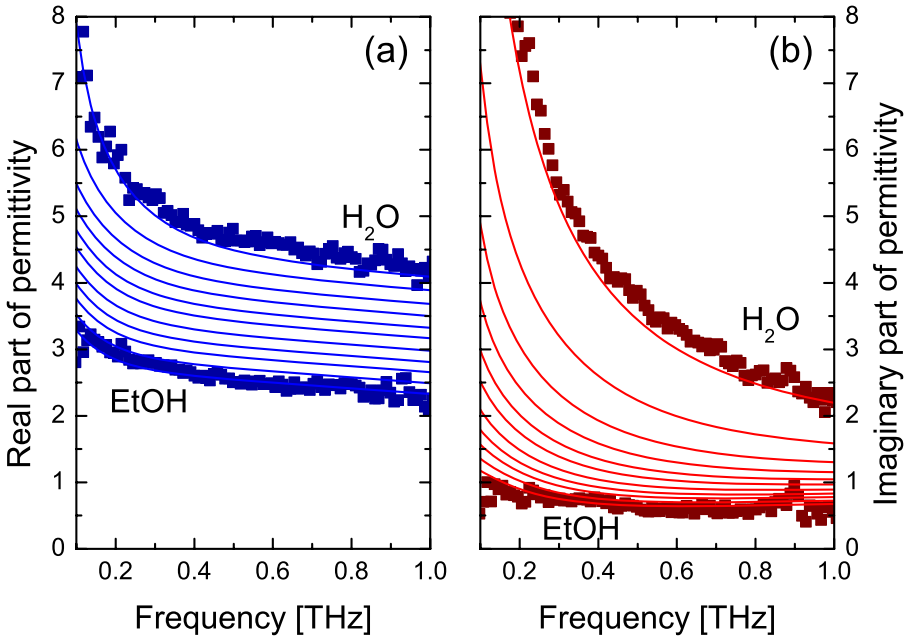

Fig. 5. (solid lines) (a) Real and (b) imaginary part of the modeled dielectric function of water-ethanol mixtures, in 10% increments. The experimental data for neat water and neat ethanol were recorded by reflection THz-TDS. Experimental data for water and ethanol is shown with solid squares.

In the following simulations we will use the triple Debye model with the parameters defined by Eqs. (8) to describe the dielectric properties of water-ethanol mixtures.

6. Inspection of alcohol strength through a bottle wall

We recently used a self-referenced reflection THz spectroscopy technique to determine the alcohol concentration of unknown mixtures of water and ethanol, by placing the liquid on a plane silicon window [4]. Here we use the same self-referencing principle to investigate the optical properties of a liquid, without removing the liquid from its bottle.

In Fig. 6(a) we show the result of a simulation of the return signal from a 0.65-mm PET bottle containing different water-ethanol mixtures. As input pulse for the simulation we used the signal measured in our reflection spectrometer with the PET bottle replaced by a plane, metallic mirror. We applied Eqs. (1) and (2), using the reflection- and transmission coefficients defined in Eqs. (3) - (6) which are calculated using the optical properties of PET and the water-ethanol mixtures discussed above.

#95613 - $15.00 USD Received 29 Apr 2008; revised 6 Jun 2008; accepted 6 Jun 2008; published 9 Jun 2008

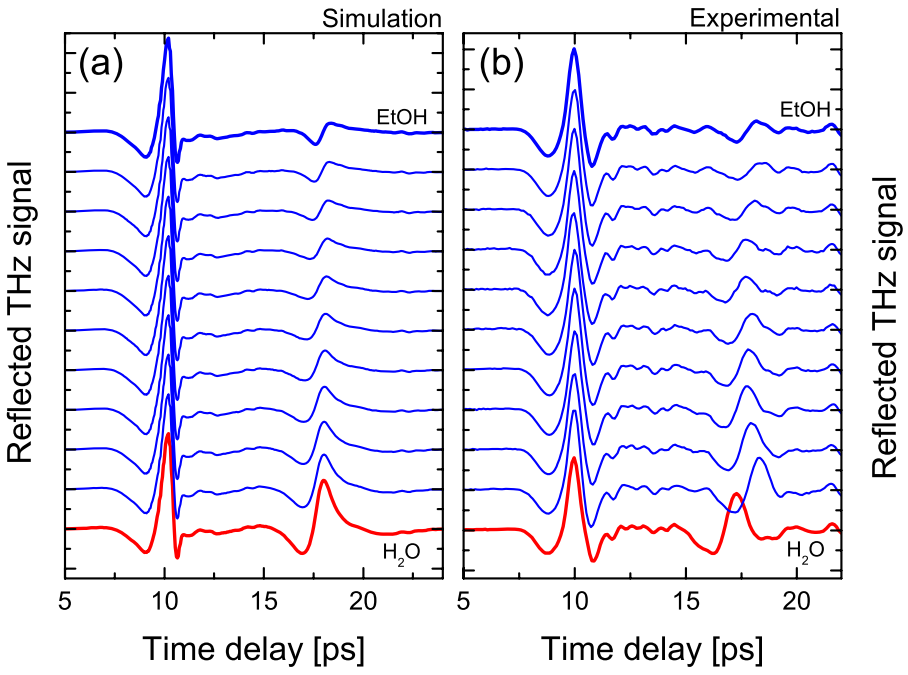

Fig. 6. (a) Simulated and (b) measured reflected THz signal from a PET bottle with 0.65 mm wall thickness, containing mixtures of water and ethanol. The red, lower traces represent the reflection from neat water and each successive curve represents a 10% increase in ethanol mass fraction.

The simulation results show that we should expect a strong sample reflection from a PET bottle containing neat water, and that this reflection should diminish in amplitude with increasing alcohol concentration. Additionally we observe a significant reshaping of the shape of the sample signal. The dispersion of the water-ethanol mixture changes with composition of the mixture. For the highest alcohol concentrations there will be a frequency within our bandwidth with perfect index match between the PET and the liquid mixture. Hence this reshaping is expected.

Figure 6(b) shows the experimental results, obtained under the same conditions as used in the simulation shown in Fig. 6(a), i.e. with a PET bottle of 0.65-mm wall thickness. The PET bottle was removed from the spectrometer between each measurement, for replacement of the liquid. The measurements were carried out at approximately the same spot on the bottle, through the paper label glued to the bottle. No special precautions was taken to ensure the exact same measurement conditions for each scan. The effect of small differences between each scan is seen as slight deviations of the temporal position of the sample reflection with respect to the reference reflection due to variations of the bottle wall thickness. The experiment reproduces the simulation quite well. We observe a decreasing amplitude of the sample signal with respect to the reference signal with increasing alcohol strength as well as a significant reshaping of the sample signal. The additional oscillations present in the experimental traces in comparison to the simulated traces are due to water vapor in the THz beam path.

The good agreement between simulation and experiment demonstrated in Fig. (6) indicates that the experimental details left out of the simulation, such as the relatively low radius of curvature of the bottle, the paper label, and the irregular surface, do not significantly influence

#95613 - $15.00 USD Received 29 Apr 2008; revised 6 Jun 2008; accepted 6 Jun 2008; published 9 Jun 2008

the result of the measurements. These geometrical factors will influence the reference signal and the sample signal in approximately the same manner, and hence the ratio of the two signals will be stable against changes in the geometry of the experiment.

In Fig. (7) we show the result of a simulation of the reflected signal from a 3.0-mm glass bottle containing different water-ethanol mixtures. The simulation was carried out as described above, using the optical properties of the glass material shown in Fig. (2).

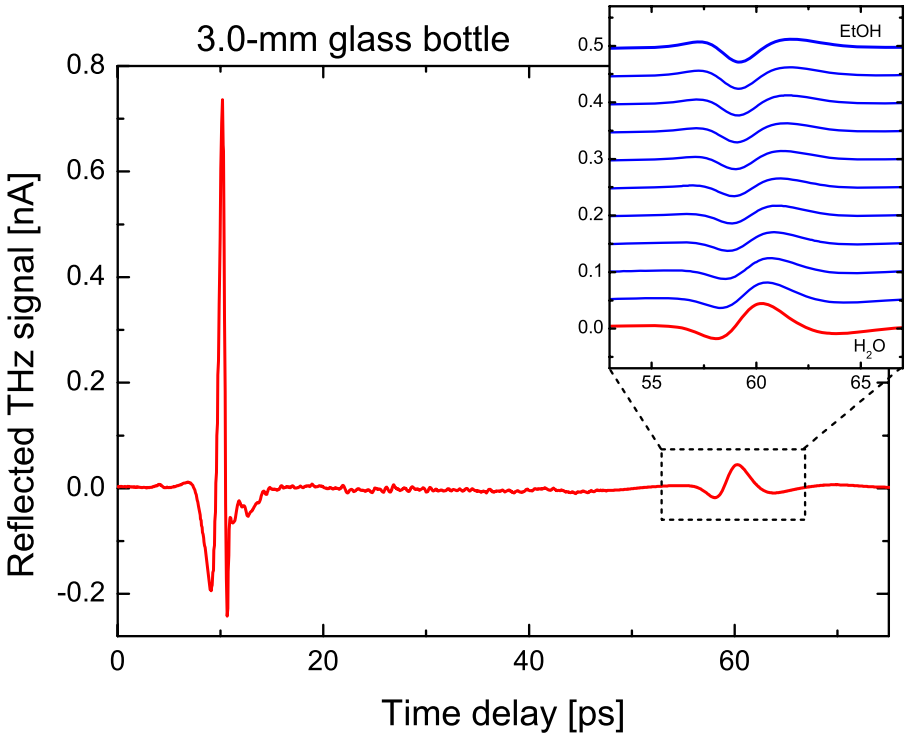

Fig. 7. *Simulated* reflected THz signal from a glass bottle with 3.0 mm wall thickness, containing neat water. The inset shows the shape of the second reflection in dependence of the ethanol concentration in the mixture. The red, lower trace represents the reflection from neat water and each successive curve represents a 10% increase in ethanol mass fraction.

The thicker glass wall compared to the PET bottle, together with the higher index, leads to a delay of 50 ps of the sample signal with respect to the reference signal. The increased wall thickness results in strong attenuation of the sample signal with respect to the reference signal. In contrast to the return signal from the PET bottle, we observe only a modest dependence of the sample signal strength on the alcohol concentration of the liquid. We do, however, observe a significant reshaping of the sample signal that resembles a sign change of the signal, or a 180-degree phase shift. The average refractive index of the glass is located between the refractive indices of neat water and of neat ethanol. Hence, neglecting the frequency dependence of the refractive indices, the sign of the sample signal with respect to the reference signal should change from positive to negative with increasing ethanol concentration. The deviation from the pure sign change is mainly caused by the frequency dependence of the refractive indices of the liquid.

Figure (8) shows the result of a measurement carried out under the same conditions as the

#95613 - $15.00 USD Received 29 Apr 2008; revised 6 Jun 2008; accepted 6 Jun 2008; published 9 Jun 2008

simulation of the reflected signal from the glass bottle.

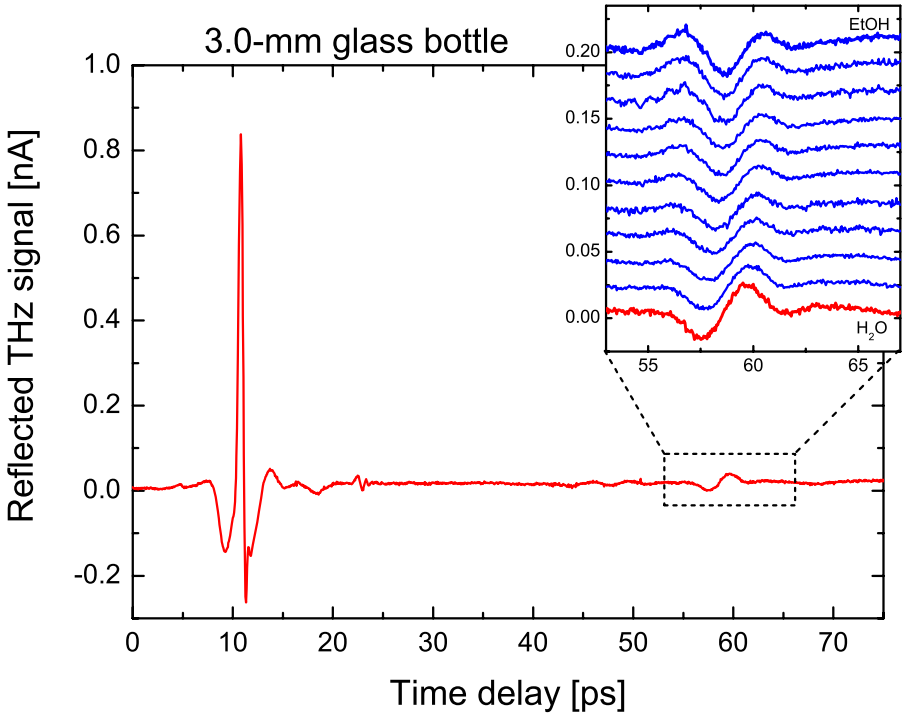

Fig. 8. *Measured* reflected THz signal from a glass bottle with 3.0 mm wall thickness, containing neat water. The inset shows the shape of the second reflection in dependence of the ethanol concentration in the mixture. The red, lower trace represents the reflection from neat water and each successive curve represents a 10% increase in ethanol mass fraction.

There is a good agreement between the simulation results and the experimental data. Experimentally we observe the sample signal 50 ps after the reference signal, and we observe a strong attenuation of the sample signal. The attenuation is slightly stronger than seen in the simulation. We believe that the stronger apparent attenuation could be caused by the displaced reflection plane at the glass-liquid interface with respect to the air-glass interface. The optical path difference between the two reflection planes is 14.4 mm, and the THz beam is incident on the glass bottle at an incidence angle of 30 degrees, focused by an off-axis paraboloidal mirror with an effective focal length of 101.6 mm. Hence the added propagation distance through the glass will lead to some deviation away from the ideal THz propagation axis of the part of the THz signal that is reflected from the glass-liquid interface.

The dependence of the reflected sample signal both from the PET bottle and from the glass bottle on the alcohol concentration suggests that the alcohol concentration x of the liquid inside the bottle can be determined by the ratio of the integrated field strength of the sample pulse and that of the reference pulse. In Fig. (9) we show this ratio R, defined as

$$R(x) = \sqrt{\frac{\sum E^2_{sam,x}(t_i)}{\sum E^2_{ref,x}(t_j)}} \tag{9}$$

where the summation indices i and j are chosen so that the sum covers the full sample- and reference pulses, respectively. The solid, black squares represent the measured ratios, whereas

#95613 - $15.00 USD Received 29 Apr 2008; revised 6 Jun 2008; accepted 6 Jun 2008; published 9 Jun 2008

the solid red curves represent the result of the simulation discussed above. Figure 9(a) shows the results for the PET bottle and Fig. 9(b) shows the results for the glass bottle.

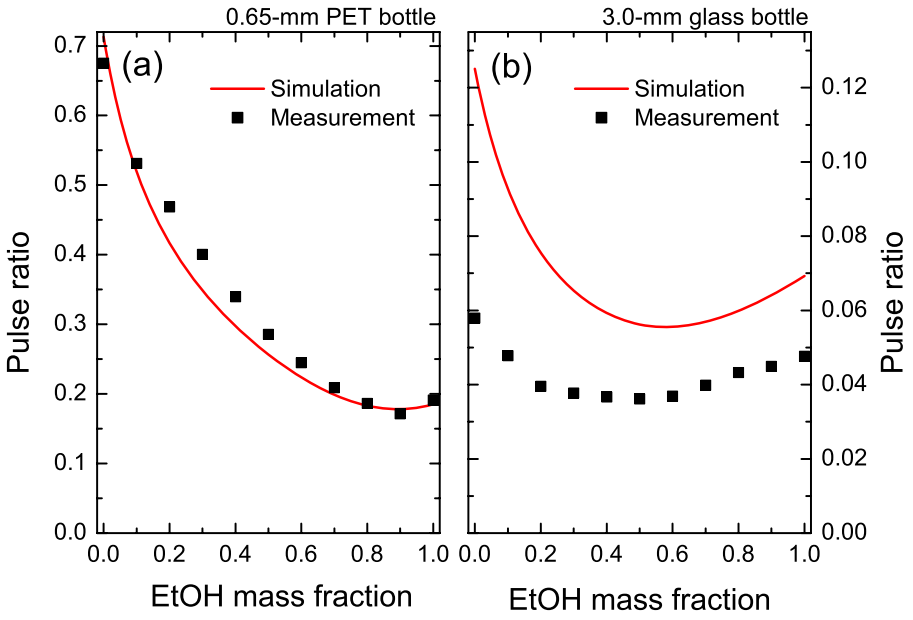

Fig. 9. The ratio of the strengths of the second to the first pulse reflected off an (a) 0.65 mm PET bottle and (b) a 3.0 mm glass bottle, as functions of the ethanol concentration of the water-ethanol mixture in the bottles. Red curves represent a simulation, square symbols represent measurements.

The agreement between the experimentally determined ratio and the simulated one is good for the PET bottle, and the monotonous dependence of the ratio on the alcohol concentration allows the determination of unknown alcohol concentrations [4], at least for alcohol concentrations up to 80%. Interestingly both the simulated and measured $R(x)$ increases slightly at the highest alcohol concentrations, indicating that for the highest alcohol concentrations the index of refraction of the liquid crosses that of the PET material. The minimum of the ratio at 90% alcohol concentration corresponds to the best possible index match between the bottle wall and the liquid. The permittivity of PET is 3.06 (see Fig. (2b)). Inspection of Fig. (5) confirms that the highest alcohol concentrations results in a permittivity of the liquid below this value.

For the glass bottle, the measured ratio is lower than the simulated one. The possible reasons for the lower measured ratios are discussed above. The dependence of the ratio on the alcohol content is similar for the simulated and the measured data. The higher refractive index of the glass material shifts the minimum $R(x)$ to lower alcohol concentrations, and results in the observed non-monotonous behavior of $R(x)$. This makes an unambiguous determination of unknown alcohol concentrations in a glass bottle difficult, at least if the ratio R is used as the only estimator.

However, inspection of the progression of the sample signal with alcohol concentration makes it clear that additional information about the composition of the liquid is stored in the significant reshaping of the sample signal. If we for instance use the difference between the sample signal from the bottle filled with the alcohol solution and that from the same bottle with water, $E_{diff,x}(t) = E_{sam,x}(t) - E_{sam,H_2O}(t)$, we can calculate a difference ratio $R_{diff}(x)$ similar

#95613 - $15.00 USD Received 29 Apr 2008; revised 6 Jun 2008; accepted 6 Jun 2008; published 9 Jun 2008

to the ratio defined in Eq. (9) to obtain a signal with a strength that depends monotonously on the alcohol concentration x,

$$R_{diff}(x) = \sqrt{\frac{\sum E^2_{diff,x}(t_i)}{\sum E^2_{ref,x}(t_j)}} \tag{10}$$

In Fig. 10(a) we plot the sample difference signal $E_{diff,x}(t)$ with varying alcohol concentration x. In contrast to the sample signals themselves, the shape of the difference signals is independent of the alcohol concentration, whereas the difference signal strength increases monotonously with alcohol concentration. This indicates that the difference signal is mainly due to the change of the real part of the refractive index of the liquid, and that the additional phase shift associated with changes in the imaginary part of the refractive index has little influence on the reflected signal shape. In Fig. 10(b) the ratio $R_{diff}(x)$ is plotted as function of the alcohol concentration in the bottle. This difference ratio increases monotonously with the alcohol concentration, and is hence useful for the determination of unknown alcohol concentrations in the bottle. The difference ratio shown in Fig. (10) never reaches zero, even for the measurement on neat water. This is due to experimental noise, which is not averaged out in the calculation of the difference ratio since the square of the instantaneous field strength is used in the summations.

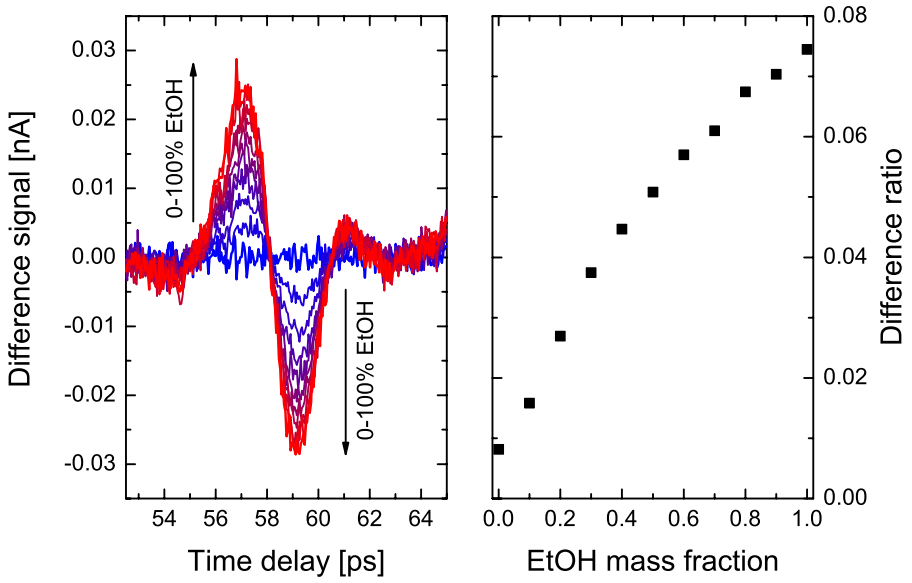

Fig. 10. (a) Time traces of the the difference sample signal reflected from a glass bottle for various ethanol concentrations. (b) The ratio $R_{diff}(x)$ of the strength of the difference signal with respect to the reference signal, as function of alcohol concentration.

7. Conclusions

We have described a method for contact-free inspection of liquids inside bottles. The method relies on the reflection of a THz transient from the bottle. It works by a comparison of the two signals reflected from the bottle; one reflection from the outer surface of the bottle wall and one reflection from the inner surface, in contact with the liquid, of the bottle wall. The automatic generation of a reference signal from the outer bottle surface is useful as a validity check of the

#95613 - $15.00 USD Received 29 Apr 2008; revised 6 Jun 2008; accepted 6 Jun 2008; published 9 Jun 2008

measurement. In contrast to a transmission measurement, where the lack of a transmitted signal in principle can be due to either strong absorption or a misalignment of the system, the lack of any reflected signal clearly indicates an error in the measurement. In a calibrated system the strength of the outer reflection can also be used for automatic identification of the bottle material, based on its index of refraction.

Our experimental and numerical results showed that the method works on both PET bottles and glass bottles. The capability to inspect the content of a glass bottle depends critically on the thickness of the glass, due to the strong absorption of THz waves in the glass material. Hence the dynamic range of the THz detection system is important for the maximum thickness of the glass material. An estimate of the maximal thickness of the glass material is

$$d_{max} \approx \frac{1}{\alpha} \ln(DR) \tag{11}$$

where DR is the dynamic range of the detection system and $alpha$ is the absorption coefficient of the glass material at the frequency where the dynamic range is defined. For the measurements presented in this work ($DR \approx 1000$ and $\alpha \approx 20$ cm^{-1}) we find $d_{max} \approx 0.35$ cm.

The concentration of alcohol solutions in PET bottles could be determined by a measurement of the ratio $R(x)$. For the same solutions in glass bottles the simple ratio $R(x)$ is no longer sufficient for an unambiguous determination of the alcohol strength. The difference ratio $R_{diff}(x)$ was introduced to allow determination of unknown alcohol concentrations in a glass bottle. This modified method can then be applied in situations where it is possible to obtain a reflected signal from a similar bottle containing either neat water or neat ethanol.

Acknowledgment

This work was supported by the EU Integrated Project TeraNova.

#95613 - $15.00 USD Received 29 Apr 2008; revised 6 Jun 2008; accepted 6 Jun 2008; published 9 Jun 2008

Terahertz reflection spectroscopy of Debye relaxation in polar liquids [Invited]

Uffe Møller,[1] David G. Cooke,[1] Koichiro Tanaka,[2,3] and Peter Uhd Jepsen[1,*]

[1]*DTU Fotonik—Department of Photonics Engineering, Technical University of Denmark, Ørsteds Plads, Bldg. 343, DK-2800 Kgs. Lyngby, Denmark*
[2]*Department of Physics, Graduate School of Science, Kyoto University, Kitashirakawa, Sakyo-ku, Kyoto 606-8502, Japan*
[3]*Institute for Integrated Cell-Material Sciences, Kyoto University, Yoshidakonoe-cho, Sakyo-ku, Kyoto 606-8501, Japan*
[*]*Corresponding author: puje@fotonik.dtu.dk*

Received August 13, 2009; accepted August 13, 2009;
posted August 17, 2009 (Doc. ID 115700); published August 28, 2009

Terahertz (THz) radiation interacts strongly with the intermolecular hydrogen-bond network in aqueous liquids. The dielectric properties of liquid water and aqueous solutions in the THz spectral region are closely linked to the microscopic dynamics of the liquid solution, and hence THz spectroscopy offers an important insight into fundamental intermolecular interactions in polar liquids. At the same time, the strong and characteristic interaction between THz radiation and liquids offers a methodology for the classification of liquids inside containers, and hence the THz region is suitable for remote detection of some of the properties of bottled liquids. Here we present a review of THz spectroscopy and modeling of water–ethanol mixtures, and establish a link between the dielectric function of water–ethanol mixtures and some of their thermodynamic properties. We then review how the knowledge of the dielectric function of aqueous mixtures can be used for inspection of liquids inside bottles. Finally we draw up some of the limits to the applicability of THz reflection spectroscopy in the identification of dangerous liquids.

OCIS codes: 300.6495, 120.4530, 010.4290, 120.4290.

1. INTRODUCTION

With the possible exception of ethanol, water is the most important liquid for mankind. Hence it is not surprising that the properties of water have been investigated since the beginning of science. In spite of the apparently simple geometry of the water molecule, liquid water has a range of surprising physical and thermodynamic properties, which include strong deviations from ideal mixing behavior, higher density than solid water (ice I), and exothermic mixing properties with certain other liquids that can form hydrogen bonds. All these properties stem, in one way or another, from the unique property of the water molecule to form a tetrahedral arrangement of hydrogen bonds to its neighboring molecules, thereby forming a highly dynamic network of virtually infinite extent of interconnected molecules.

The optical properties of bulk water have been investigated at all wavelengths normally associated with electromagnetic radiation. In Fig. 1 we show the absorption coefficient (on a logarithmic scale) and the index of refraction (on a linear scale) as function of frequency (lower, horizontal axis) or wavenumber (upper, horizontal axis) [1].

The gray area indicates the part of the THz spectrum typically accessed by THz time-domain spectroscopy (THz-TDS) techniques, and the visible region of the spectrum is indicated by the narrow bar. The figure shows that THz-TDS has access to the part of the dielectric response of water that lies below the vibrational bands in the infrared.

The large dipole moment of the water molecule in interplay with the dynamic intermolecular network of hydrogen bonds forms a highly complex many-body system. This system interacts collectively in a strong and characteristic manner with electro-magnetic radiation at microwave and THz frequencies. This is due to the fact that the typical time scales involved in relaxation dynamics of water molecules displaced or rotated from their equilibrium positions falls in the picosecond to subpicosecond range. Thus far-infrared or THz spectroscopy is a versatile tool for the study of the collective properties of water, in particular, and of hydrogen-bonded liquids in general.

When a molecule is solvated or dispersed in water, the water molecules will naturally rearrange themselves in order to accommodate the molecule. This rearrangement will influence the local structure of the dynamic intermolecular hydrogen bond network, and thus the THz dielectric properties will also change locally. This effect has been demonstrated in spectroscopic studies of sucrose in water, where an analysis based on the broadband dielectric properties of the solution in the THz range made it possible to measure the size of the solvation shell around the sucrose molecules [2]. Other experiments, using narrow-band THz radiation rather than a broadband spectroscopic source, have revealed the size of the solvation shell around proteins and carbohydrates solvated in water [3,4]. Related work on water contained in inverse micelles [5–7] demonstrated that nanometer-sized pools of water behave distinctively different from bulk water, due to mechanical resonances of the spherical water in-

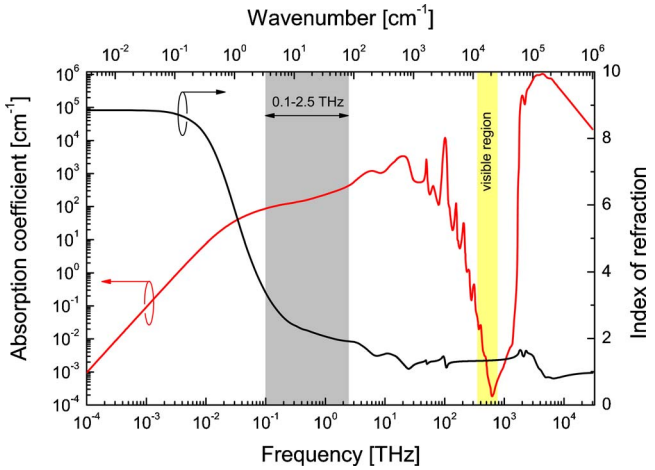

Fig. 1. (Color online) Absorption spectrum (red curve, logarithmic scale) and index of refraction (black curve, linear scale) as function of frequency (lower horizontal scale) and wavenumber (upper, horizontal scale). The gray area indicates the 0.1–2.5 THz region, and the narrow yellow shaded area indicates the visible part of the spectrum.

clusion. It was demonstrated that extended interfaces of liquid water with a thickness of a few nanometers, condensed on the surface of a parallel-plate waveguide, behaves like bulk water [8], whereas strong deviations from bulk behavior was observed in the dielectric spectrum of submonolayer films of water absorbed on the surface of hydrophilic aerogels [9]. All these reports clearly demonstrate that the three-dimensional environment of water molecules in the liquid state plays a defining role for the local dielectric response of the liquid at distances on the nanometer scale from solvated molecules or from interfaces. These works have also demonstrated that at distances greater than, for instance, the radius of the solvation shell surrounding a molecule in liquid water, the dielectric properties of the water solvent are identical, or at least in practice indistinguishable from the properties of bulk water. Importantly, this dielectric response can be sensed by spectroscopy in the THz frequency range.

The paper is organized as follows: In Section 2 we describe different methods based on reflection spectroscopy for the measurement of the full dielectric function of strongly absorbing liquids in the THz range. In Section 3 we then briefly discuss the derivation of the Debye model of dielectric relaxation. In Section 4 we then describe a detailed investigation of the dielectric function of water–ethanol mixtures. In the more applications-oriented Section 5 we describe how the dielectric properties of liquids can be inspected though the wall material of bottles, and in Section 6 we show selected examples of the application of reflection-type THz spectroscopy for characterization of liquids that may be classified as dangerous. These liquids include hydrogen peroxide, a strong oxidizing agent, as well as the liquid fuel components nitromethane and nitroethane.

2. EXPERIMENTAL METHODS FOR REFLECTION THz SPECTROSCOPY

With the invention of far-infrared Fourier transform infrared spectroscopy (FTIR) and later THz-TDS, spectroscopic investigations of liquid water in the far infrared has been a recurring topic for the past 30 years.

Spectroscopy of liquids is typically carried out in either a transmission geometry or in a reflection geometry, depending on the absorption strength of the liquid. The highest absorption coefficient that can be measured in a transmission experiment is limited by the dynamic range of the spectrometer, here defined as the frequency-dependent reference signal amplitude with respect to the noise floor of the experiment [10]. In contrast it is the signal-to-noise ratio of the spectrometer, i.e., frequency-dependent fluctuations of the signal strength, that determines the largest measurable absorption coefficient in a reflection experiment, since the absorption of the sample is detected as a small additional phase of the reflected signal [10].

Due to the rather strong absorption of polar liquids, and in particular of water, spectroscopy in the THz region of such liquids is typically carried out in a reflection geometry on bulk quantities of the liquid or by transmission through a very thin liquid layer. While THz transmission measurements of liquid water are certainly possible for thin water layers, the subsequent analysis becomes plagued with multiple reflections of the THz beam in the water cell, especially at low frequencies. In the region above 1 THz, transmission experiments are difficult due to strong absorption, and in recent work targeting the frequency range of 1–6 THz, reflection-type spectroscopy seems to be the method of choice. Here we will thus briefly review different techniques applied for reflection THz spectroscopy.

Historically, the technique of dispersive Fourier transform spectroscopy (DFTS) [11] was the first method for accurate determination of the full dielectric function of materials in the far infrared. Afsar and Hasted used DFTS [12] to characterize the full dielectric function of liquid water in the 0.2–13.5 THz range (6–450 cm^{-1}). In their spectroscopic setup, water was kept behind a single-crystal, high-resistivity silicon window, transparent to the far-infrared radiation but with sufficiently high and constant index of refraction [13] to also serve as a useful beam splitter for the THz radiation. The liquid cell was placed in one of the arms of the modified Michelson interferometer in the spectrometer, as illustrated schematically in Fig. 2(a). Hence phase-sensitive measurements were possible by measuring the interferogram $I(\tau)$ of the incoherent, broadband light source. This allowed a direct evaluation of both the real and the imaginary part of the frequency-dependent permittivity $\hat{\epsilon}(\nu)=\epsilon'(\nu)+i\epsilon''(\nu)$ from the experimental data.

In DFTS, temporally separated interferograms of the incoherent light reflected from the different dielectric interfaces in the sample arm of the spectrometer are recorded by scanning the position $\tau=2x/c$ of the mirror in the variable arm of the interferometer. The part of the interferogram $I_{wa}(\tau)$ associated with the window–air interface of the empty cell is used as a reference for the sample interferogram $I_{wl}(\tau)$ from the window–liquid interface of the filled liquid cell. The ratio of the Fourier transformations of these interferograms can then, in combination with the standard expressions for the Fresnel reflection

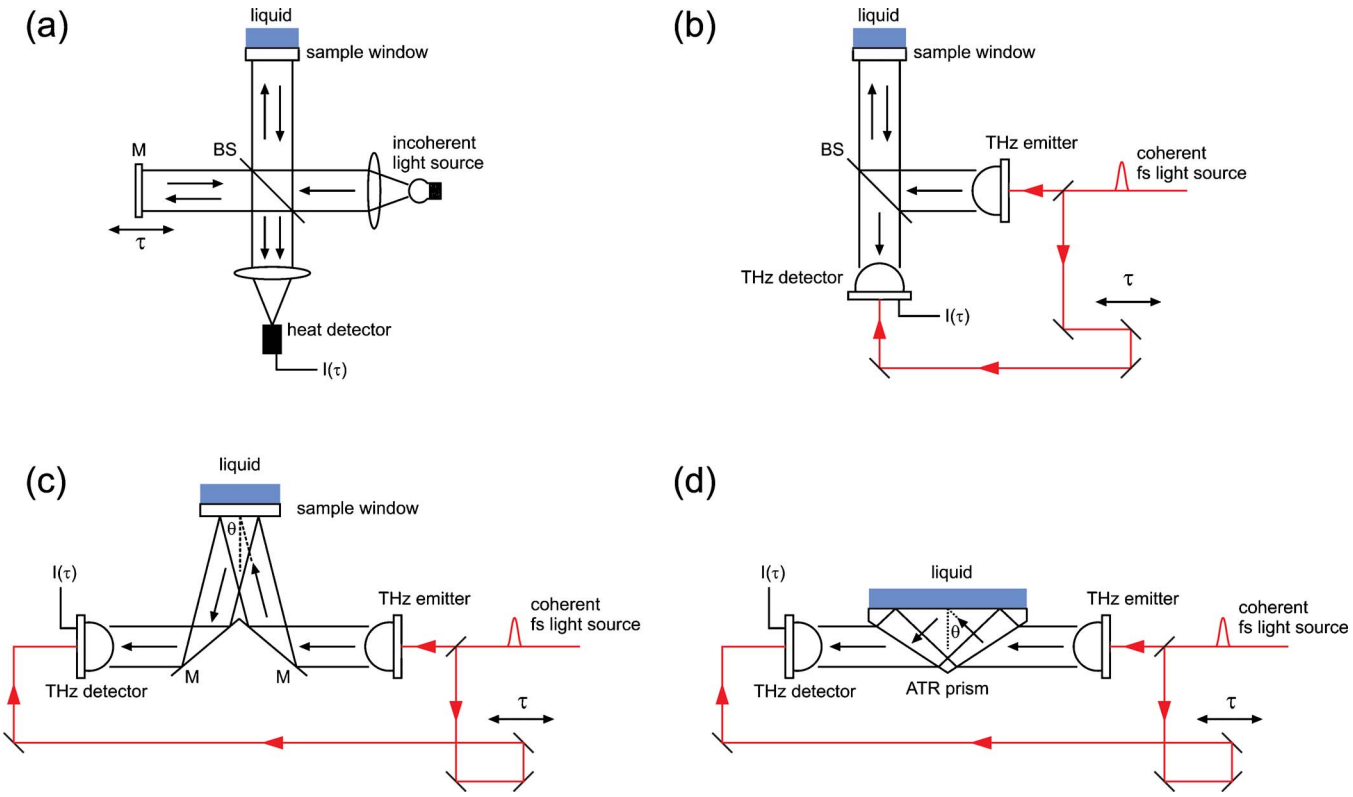

Fig. 2. (Color online) Experimental configurations for (a) dispersive Fourier transform spectroscopy (DFTS), (b) normal-incidence reflection THz time-domain spectroscopy (THz-TDS), (c) generalized reflection THz-TDS with an incidence angle θ, and (d) attenuated total reflection (ATR) THz-TDS with an internal angle θ larger than the total internal reflection angle.

coefficients at the interfaces, be used for the calculation of the optical properties of the liquid:

$$R\exp(i\phi)=\frac{\mathcal{F}\{I_{wl}(\tau)\}}{\mathcal{F}\{I_{wa}(\tau)\}}=\frac{\hat{I}_{wl}(\nu)}{\hat{I}_{wa}(\nu)}=\frac{\hat{r}_{wl}(\nu)}{r_{wa}(\nu)}$$

$$=\frac{(\hat{n}_l(\nu)-n_w(\nu))(1+n_w(\nu))}{(\hat{n}_l(\nu)+n_w(\nu))(1-n_w(\nu))},\qquad(1)$$

where R and ϕ are the measured amplitude and phase of the ratio of the two interferograms and $\mathcal{F}$ denotes the Fourier transformation. When inverted, Eq. (1) gives the complex index of refraction of the liquid, $\hat{n}_l(\nu)=n_l(\nu)+i\alpha_l(\nu)c/(4\pi\nu)$, assuming that the index of refraction n_w of the window material is known:

$$n_l=\frac{1-R^2\left(\frac{1-n_w}{1+n_w}\right)^2}{1+R^2\left(\frac{1-n_w}{1+n_w}\right)^2-2R\cos\phi\left(\frac{1-n_w}{1+n_w}\right)},\qquad(2)$$

$$\alpha_l=\frac{4\pi\nu}{c}\frac{2R\sin\phi\left(\frac{1-n_w}{1+n_w}\right)}{1+R^2\left(\frac{1-n_w}{1+n_w}\right)^2-2R\cos\phi\left(\frac{1-n_w}{1+n_w}\right)}.\qquad(3)$$

THz-TDS [14] is a modern spectroscopic technique with much of the same functionality as DFTS, and with several fundamental as well as practical advantages compared to FTIR spectroscopy. In THz-TDS a short burst of coherent light in the THz region is generated and detected either by the ultrafast photoconductive response in miniature photoconductive switches excited by femtosecond laser pulses [15] or by optical rectification of ultrafast laser pulses and free-space electro-optic sampling in a nonlinear crystal [16]. In both techniques, a femtosecond laser pulse train is split into two portions by a beamsplitter, where one portion is used for generation of the THz pulse, consisting typically of a single cycle of the electromagnetic field, and the second, delayed portion is used for time-resolved sampling of the electrical field of the THz signal.

Thrane *et al.* [17] established a reflection-type THz-TDS technique with an experimental arrangement of the liquid cell similar to that in [12], adapted to the technique of reflection THz-TDS, with normal incidence of the THz field onto the liquid surface. This experimental geometry is illustrated in Fig. 2(b). In the geometry shown here, the full set of spectroscopic data is obtained within the same temporal scan, by using the reflection from the interface between air and window material as the reference signal $E_r(\tau)$ and the reflection from the interface between the window and the liquid as the sample signal $E_s(\tau)$. The sample signal is separated in time from the reference signal due to the propagation delay of the sample signal

through the window material of thickness d_w. With normal incidence of the THz beam on the window, the ratio of the spectra of the sample and reference pulses is

$$\frac{\mathcal{F}\{E_s(\tau)\}}{\mathcal{F}\{E_r(\tau)\}} = \frac{\hat{E}_s(\nu)}{\hat{E}_r(\nu)} = \frac{t_{aw}t_{wa}}{r_{aw}} \exp\left(i\frac{4\pi n_w d_w \nu}{c}\right)\frac{\hat{n}_l - n_w}{\hat{n}_l + n_w} \Leftrightarrow R\exp(i\phi)$$

$$= \frac{\hat{E}_s(\nu)}{\hat{E}_r(\nu)}\frac{r_{aw}}{t_{aw}t_{wa}} \exp\left(-i\frac{4\pi n_w d_w \nu}{c}\right) = \frac{\hat{n}_l - n_w}{\hat{n}_l + n_w}, \quad (4)$$

where R and ϕ are the measured spectral amplitude and phase of the ratio of the sample- and reference signals, corrected for the transmission and reflection coefficients of the air–window interface and the acquired phase due to propagation through the window material.

Inverting Eq. (4) yields the index of refraction and absorption coefficient of the liquid:

$$n_l = \frac{n_w(1-R^2)}{1+R^2+2R\cos\phi}, \quad (5)$$

$$\alpha_l = \frac{4\pi n_w \nu}{c}\frac{-2R\sin\phi}{1+R^2+2R\cos\phi}. \quad (6)$$

The methodology described here for the calculation of the dielectric properties of the liquid can be extended to an analysis at non-normal incidence at an angle θ of the THz beam on the sample window. This experimental geometry is shown schematically in Fig. 2(c). Compared to normal-incidence reflection spectroscopy, the configuration with non-normal incidence of the THz beam has a significantly higher signal strength, since the THz beam splitter is no longer required. In this geometry the generalized reflection and transmission coefficients must be used, and also the polarization state of the THz beam becomes important [18]. Due to the many possible configurations, we refrain from presenting the full expressions for the determination of the optical constants of the liquid, but we refer to the discussion in [18].

The most sensitive method for determination of the full dielectric function of a strongly absorbing liquid is offered by attenuated total reflection (ATR) THz-TDS [19,20]. In this configuration the THz beam is transmitted through a Dove prism where it undergoes total internal reflection at a facet of the prism in contact with the liquid. The geometry of an ATR THz-TDS system is schematically shown in Fig. 2(d). The angle θ refers to the internal incidence angle of the THz beam onto the interface towards the liquid. The highest sensitivity to small changes in the dielectric properties of the sample is obtained when that incidence angle is larger than, but close to, the critical angle for total internal reflection. The measurement is carried out by recording a reference pulse $E_r(\tau)$ transmitted through the prism with air above the interface and subsequently a sample pulse $E_s(\tau)$ recorded with liquid in contact with the prism. The ratio of the spectra of these two signals is, as in the previous cases discussed here, analyzed in order to extract the complex index of refraction of the liquid. If we assume p-polarization of the THz light incident on the ATR interface we have [19]

$$R\exp(i\phi) = \frac{\mathcal{F}\{E_s(\tau)\}}{\mathcal{F}\{E_r(\tau)\}} = \frac{\hat{E}_s(\nu)}{\hat{E}_r(\nu)} = \frac{\hat{r}^p_{wl}}{\hat{r}^p_{wa}} \Leftrightarrow \hat{r}^p_{wl} = \hat{r}^p_{wa}R\exp(i\phi), \quad (7)$$

where R and ϕ again represent the amplitude and phase of the ratio of the spectra of the sample- and reference pulses.

Using the Fresnel reflection coefficients for total internal reflection of p-polarized light, Eq. (7) can be inverted to find an expression for the complex permittivity $\hat{\epsilon}_l = \epsilon_l' + i\epsilon_l'' \equiv \hat{n}_l^2$ [19]:

$$\hat{\epsilon}_l = \frac{B \pm \sqrt{B^2 - AB\sin^2 2\theta}}{2A\cos^2\theta}, \quad (8)$$

where $A=(\hat{r}^p_{wl}-1)^2$ and $B=(\hat{r}^p_{wl}+1)^2$. All typical material systems show a positive ϵ'' and hence the solution with $\epsilon_l'' > 0$ should be chosen.

3. DEBYE MODEL OF THE DIELECTRIC FUNCTION OF POLAR LIQUIDS

The most widely accepted phenomenological description of the complex frequency-dependent dielectric function $\hat{\epsilon}(\omega)$ of polar, nonconductive ($\sigma_{DC}=0$) liquids is based on the Debye model and extensions of the Debye model. Here we will briefly summarize a derivation of the Debye model of dielectric relaxation [21].

When a dielectric material is subject to a sudden electric field E then the induced total polarization P will have two contributions: the near-instantaneous electronic response P_1 and the slower dipolar response P_2. It is assumed that the rate of change of P_2 is proportional to the distance to the steady-state total polarization,

$$\frac{dP_2}{dt} = \frac{P - P_1 - P_2}{\tau}, \quad (9)$$

where τ is the characteristic relaxation time of the process. If an electric field is suddenly switched on at $t=0$ then the solution is

$$P_2(t) = (P - P_1)(1 - \exp(-t/\tau)), \quad (10)$$

showing the characteristic exponential behavior of the relaxation process in the Debye picture.

If a harmonic electric field at frequency ν, $E(t) = E_0\exp(-i2\pi\nu t)$, is applied to the material then the solution to Eq. (9) is

$$\frac{dP_2}{dt} = \frac{\epsilon_0(\epsilon_s - \epsilon_\infty)}{\tau}E_0\exp(i2\pi\nu t) - \frac{P_2}{t} \quad (11)$$

$$\Rightarrow P_2(t) = \frac{\epsilon_0(\epsilon_s - \epsilon_\infty)}{1 - i2\pi\nu\tau}E(t), \quad (12)$$

where it has been assumed that the total steady-state polarization is expressed as $P=\epsilon_0(\epsilon_s-1)E, \nu\to 0$ and the electronic polarization is $P_1=\epsilon_0(\epsilon_\infty-1)E$.

Using the known relation between the induced polarization and the applied field, $P=\epsilon_0(\epsilon-1)E$ we find the complex permittivity

$$\hat{\epsilon}(\nu)=\epsilon'(\nu)+i\epsilon''(\nu)=\epsilon_\infty+\frac{\epsilon_s-\epsilon_\infty}{1-i2\pi\nu\tau}. \quad (13)$$

From this derivation of the basic Debye permittivity spectrum it can be seen that, if several relaxation processes with different relaxation times take place in parallel, then the total dielectric function will be a simple sum of the individual contributions from each process.

Furthermore, in the general case the dielectric function of a polar liquid is determined by dielectric relaxation processes at the lowest frequencies and by vibrational modes (intermolecular and intramolecular) at higher frequencies. If we assume that N relaxation processes occur simultaneous with M homogeneously broadened vibrational modes then the general dielectric function can be expressed as

$$\hat{\epsilon}(\omega)=\sum_{j=1}^{N}\frac{\Delta\epsilon_j}{1-i\omega\tau_j}+\sum_{j=1}^{M}\frac{A_j}{\omega_j^2-\omega^2-i\omega\gamma_j}+\epsilon_\infty, \quad (14)$$

where the coefficients A_j are the vibrational amplitudes, $\omega_j/2\pi$ are the resonance frequencies, and γ_j are the damping rates of the jth vibrational mode.

As will be discussed in Section 4, up to three relaxation processes are required in the model in order to describe the dielectric response of ethanol and ethanol–water mixtures. The microscopic basis of the introduction of three relaxation processes is still debated in the literature, and it is important to note that it is not our goal to shed light on the fundamental question of the validity of the Debye model.

The Debye model with the incorporation of several relaxation processes is based on the assumption that these relaxation processes are independent of each other and take place in a parallel fashion [22]. This assumption is not obvious, and a deeper insight into the fundamental nature of the relaxation processes in the mixture requires a combination of molecular dynamics (MD) simulation, spectroscopy, and analytical considerations.

4. ATR SPECTROSCOPY OF WATER–ETHANOL MIXTURES

Here we are interested in binary mixtures of water and ethanol over the full mixing ratio range from pure water (mole fraction $x_{\mathrm{EtOH}}=0$) to pure ethanol (mole fraction $X_{\mathrm{EtOH}}=1$). The thermodynamic properties of water–ethanol mixtures have been investigated in great detail, partly due to the fact that this specific mixture is very important from a technological and also cultural point of view, and partly because of many intriguing properties of the (at first glance) rather simple system.

We will discuss the measurement of the dielectric function of water–ethanol mixtures. As an extension to our previous studies of water–ethanol mixtures [18,23] we make use of data from a very broad frequency range, by a combination of our own results and already published data recorded in the microwave range with a combination of time-domain reflectometry (TDR) and waveguide interfeometry by Sato and Buchner [24], who has made their original data available to us. By combining the two sets of data we are able to cover the wide frequency range 100 MHz–2.5 THz, and thus we are able to perform accurate fits to the experimental data, covering the full range of dielectric relaxation.

The experimental method used for the recording of our THz data is based on ATR spectroscopy, as described in Section 2 and also described in detail elsewhere [19,20,25]. Briefly, the THz pulse is generated by focussing synchronous, optical pulses from a femtosecond fiber laser (IMRA femtolite, $\lambda=780$ nm, $P_{av}=20$ mW, pulse width of ~90 fs, repetition rate of 50 MHz) onto a biased photoconductive GaAs dipole antenna and detected by use of electro-optic sampling in a ZnTe crystal. A silicon Dove prism is placed at an intermediate focal plane of the THz beam [19]. The principles of generation and detection of pulsed THz radiation as well as the principles of THz-TDS are described, for instance, in [26]. Distilled water (Wako Pure Chemical Industries, Ltd.) and ethanol (Nacalai Tesque, Inc., 99.5% purity) was used without further purification. Water-cooled Peltier elements were used to keep a constant temperature of 25 °C±0.5 °C of the liquid.

The Fresnel reflection coefficients were obtained from the Fourier transformed temporal waveforms with and without a sample, respectively, and these coefficients were used to calculate the complex dielectric function of ethanol–water mixtures at 25 °C for ten different fractions of ethanol, $X_{\mathrm{EtOH}}=0.00$ (H_2O), 0.04, 0.08, 0.11, 0.18, 0.30, 0.50, 0.70, 0.90, and 1.00 (C_2H_5OH).

Figures 3(a) and 3(b) show the real and imaginary part of the complex dielectric function, $\hat{\epsilon}=\epsilon'+i\epsilon''$, of different

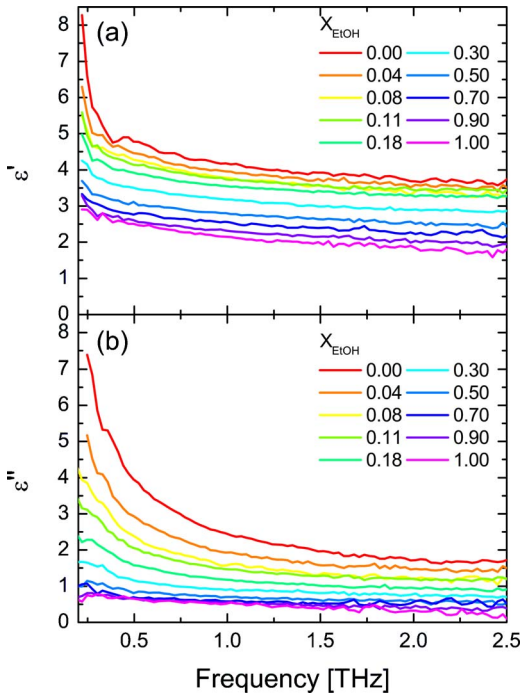

Fig. 3. (Color online) (a) Real and (b) imaginary part of the complex dielectric function of 10 different ethanol–water mixtures at 298 K (25 °C).

mixtures of ethanol (C_2H_5OH) and water (H_2O) as a function of frequency in the region 0.2–2.5 THz.

The measurements presented here are in good agreement with the substantial number of investigations of liquid water in the THz range [12,18,25,27–31], on liquid ethanol [18,28,29], and on mixtures of ethanol and water [18,29].

Since slow relaxation processes in the microwave region contribute substantially to the complex dielectric function, it is necessary to take these into account. Sato and Buchner have previously measured the complex dielectric functions of samples identical to the ones used in this work in the frequency range 0.1–89 GHz using TDR and waveguide interferometry [24]. We have included the measurements of Sato and Buchner in our analysis, and thereby we can cover more than four decades of frequency, from 10^{-4}–2.5 THz. As examples, Fig. 4 shows the complex dielectric function of (a) 18% and (b) 50% ethanol–water mixtures. One can clearly see that, in order to describe all the relaxation processes in ethanol–water mixtures, it is necessary to include data from the microwave region as well as the THz region.

We use a nonlinear fitting procedure based on the Levenberg–Marquardt algorithm to estimate the dielectric parameters by simultaneous fitting to the real and imaginary part of the complex dielectric function, and find that the complex dielectric function of ethanol–water mixtures can be decomposed into three relaxation components and a vibrational term, i.e., we use Eq. (14) with $N=3$ and $M=1$.

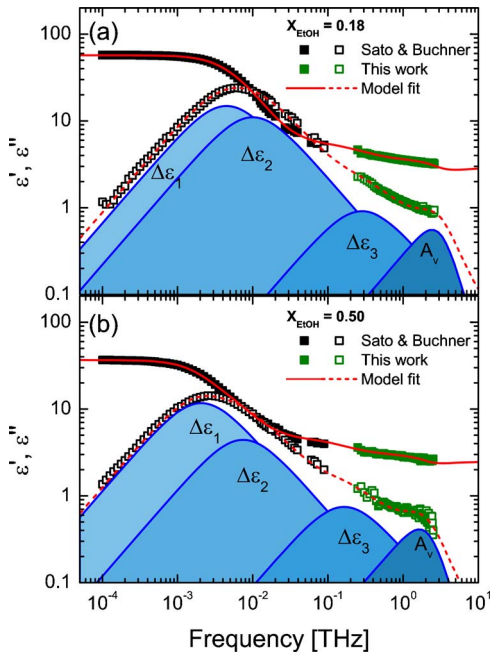

Fig. 4. (Color online) Real (solid symbols) and imaginary (open symbols) part of the complex dielectric function of (a) 11% and (b) 50% ethanol–water mixtures at 298 K (25°). Data recorded in the present work are shown with gray squares (green online), and data from Sato and Buchner [24] are shown in black squares. The fitted dielectric function is shown by solid (real part) and dashed (imaginary part) curves, respectively. The contributions to ϵ'' from the three relaxation processes and the vibrational term are shown in shades of gray (blue online).

Thus our fitting parameters are ϵ_s, $\Delta\epsilon_1$, $\Delta\epsilon_2$, $\Delta\epsilon_3$, and ϵ_∞ and τ_1, τ_2, and τ_3, and finally the vibrational amplitude A_V, angular frequency ω_V, and damping γ_V. It should be pointed out that several of the constants are linked with each other as can be seen by considering the total dielectric strength,

$$\epsilon_s - \epsilon_\infty = \Delta\epsilon_1 + \Delta\epsilon_2 + \Delta\epsilon_3 + \frac{A_V}{\omega_V^2}$$
$$= (\epsilon_s - \epsilon_1) + (\epsilon_1 - \epsilon_2) + \left(\epsilon_2 - \frac{A_V}{\omega_V^2} - \epsilon_\infty\right) + \frac{A_V}{\omega_V^2}, \quad (15)$$

where ϵ_1 and ϵ_2 are the low frequency limits of the intermediate and fast Debye relaxation components, respectively. Liquid water and the 4% mixture are best described by the use of only two Debye terms and one vibration term, i.e., $\Delta\epsilon_2=0$ for these mixtures, and our measurement of liquid ethanol show no sign of an intermolecular stretching vibration, i.e., $A_V=0$ for pure ethanol.

Yada *et al.* recently measured the temperature dependence of the complex dielectric function of water and heavy water with ATR THz spectroscopy [25] up to 3.5 THz and combined their data with microwave data [32,33] and far-infrared data [12]. They found that the complex dielectric function of liquid water at room temperature can be decomposed into four components: a slow relaxation mode at $\tau_1=9.4$ ps, a fast relaxation mode at $\tau_2=0.25$ ps, an intermolecular stretching vibration mode at ~5 THz, and an intermolecular libration mode at ~15 THz. The effect of isotopic substitution on the intermolecular stretch vibration was recently studied, also by Yada *et al.*, where the frequency range of their ATR technique was pushed to 7 THz [34]. Because of the bandwidth limitation (<2.5 THz) in the present work we have not included the intermolecular libration mode in our model.

In Table 1 we compare our fitting results for water with results from the literature. Although variations are seen between the various results, there is a good consistency between the fitted parameters.

In Table 2 our fitting parameters for liquid ethanol are shown together with previous results from Kindt *et al.* [28] and Sato *et al.* [24]. Both groups have used a triple Debye model to describe the relaxation processes of ethanol. Our data is consistent with the work of Kindt *et al.*, while Sato *et al.* report higher values of the high-frequency components (τ_3 and ϵ_∞), which also leads to a shift of the intermediate component (τ_2), most probably due to the lack of high-frequency data in their fitting procedure.

Our fits to the experimental data using Eq. (14) give nearly flat residuals close to zero and a reduced chi-squared $\chi^2 \leq 6\times10^{-3}$ in the entire measurable frequency range for all mixtures.

An overview of the fitted dielectric functions of the different ethanol–water mixtures is presented in Fig. 5. In Figs. 6–11 we summarize all the fitting parameters based on Eq. (14) as function of the ethanol concentration X_{EtOH}.

Table 1. Comparison of Relaxation Parameters of Water

Water	ϵ_s	$\Delta\epsilon_1$	τ_1 [ps]	$\Delta\epsilon_3$	τ_3 [ps]	$A_V/(2\pi)^2$ [THz^2]	$\omega_V/2\pi$ [THz]	$\gamma_V/2\pi$ [THz]	ϵ_∞
This work	78.3	72.3	8.34	2.12	0.36	28.4	5.01	7.06	2.68
Rønne *et al.* [27][a]	80.6[b]	72.1	8.5	1.9	0.17	—	—	—	3.3
Sato *et al.* [24]	78.3	72.2	8.32	2.14	0.39	—	—	—	3.96
Yada *et al.* [25][c]	79.9[b]	74.9	9.43	1.63	0.25	31.5	5.30	5.35	2.50[d]

[a]Measured at 19 °C.

[b]Fixed.

[c]Measured at 20 °C.

[d]Including amplitude of intermolecular libration mode.

In Fig. 6 it is seen that the static dielectric constant ϵ_s decreases with increasing ethanol concentration as observed previously [24,29,35–37]. Also the high-frequency permittivity is seen to decrease monotonically with increasing alcohol concentration.

In Fig. 7 the relaxation amplitudes, normalized to the total contribution to the dielectric constant from the relaxation terms ($\epsilon_s - \epsilon_\infty$) are shown as functions of the ethanol concentration. It is seen that the slow relaxation process is the most prominent, contributing 45–96% to the total dielectric strength. The intermediate and fast process contributes 6.2–48% and 2.4–5.0% to the total dielectric strength, respectively. The slow component shows a minimum near an ethanol concentration of 30% where it contributes to only half of the dielectric strength, whereas for pure water and pure ethanol it contributes to almost all of the dielectric function. The intermediate process shows a similar sequence but with opposite sign and contributes to almost half of the dielectric function in a 30% ethanol–water mixture. This indicates that the slow and intermediate process are strongly correlated. We ensured that the opposite trends seen in the concentration dependencies of $\Delta\epsilon_1$ and $\Delta\epsilon_2$ was not due to simple mathematical interdependence of the variables.

The mixing of ethanol and water at room temperature is an exothermic process where energy is released as the two components are mixed. The amount of released energy per mole of added ethanol, also called the mixing enthalpy ΔH^M, depends on the ethanol concentration [38] and is thus an important indicator of the formation and breaking of intermolecular hydrogen bonds during the mixing process. Interestingly, there seems to be a strong correlation between $\Delta\epsilon_1$, $\Delta\epsilon_2$, and ΔH^M of the solution. This correlation is detailed in Fig. 8, which shows the concentration dependence of the mixing enthalpy ΔH^M for ethanol–water mixtures (red curve [39]) together with the relative strengths of the slow (black squares) and intermediate (blue circles) relaxation processes.

In Fig. 9 we show the concentration dependence of the three relaxation times in the model. Figure 9(a) shows that the slow relaxation time, τ_1, has a nearly linear dependence of the ethanol concentration, in agreement with previous studies. In general, previous studies in the low-frequency region firmly characterizes the slow relaxation process [24,35–37] due to the facts that (a) this process occurs within their spectral range and (b) that the slow relaxation process is the most dominant of all the relaxation processes.

Figures 9(b) and 9(c) show the concentration dependence of the intermediate (τ_2) and fast (τ_3) relaxation processes. In contrast to the behavior of τ_1, τ_2 (and to some extent also τ_3) displays a nonmonotonous behavior with ethanol concentration, with a maximum of τ_2 at $X_{\mathrm{EtOH}} \approx 0.3-0.4$.

Similar to the concentration dependence of the mixing enthalpy, the mixing volume (volume change per added ethanol) of ethanol–water mixtures display a nonmonotonous behavior. In Fig. 10 we plot the normalized mixing volume $\Delta V_{mix}/n_T$ (solid, red curve), where n_T is the total number of molecules in the mixture, as function of X_{EtOH}. In the same graph we show the normalized values of τ_2 (black squares). It is apparent that there is a strong correlation between the mixing volume and the time constants of the intermediate and fast relaxation processes.

The reduction of the volume during the mixing process indicates a closer packing of the molecules in the liquid. Although detailed numerical simulation of this process is required, we speculate that the correlation between $\Delta V_{mix}/n_T$ and τ_2 is consistent with a slowing down of the relaxation processes due to less space available for the re-

Table 2. Comparison of Relaxation Parameters of Ethanol

Ethanol	ϵ_s	$\Delta\epsilon_1$	τ_1 [ps]	$\Delta\epsilon_2$	τ_2 [ps]	$\Delta\epsilon_3$	τ_3 [ps]	ϵ_∞
This work	24.4	20.0	163	1.40	4.51	1.21	0.33	1.85
Kindt *et al.* [28][a]	24.4[b]	20.2	161	1.43	3.3	0.79	0.22	1.93
Sato *et al.* [24]	24.5	20.0	165	0.74	10.4	1.19	1.69	2.60

[a]Measured at room temperature.

[b]Fixed.

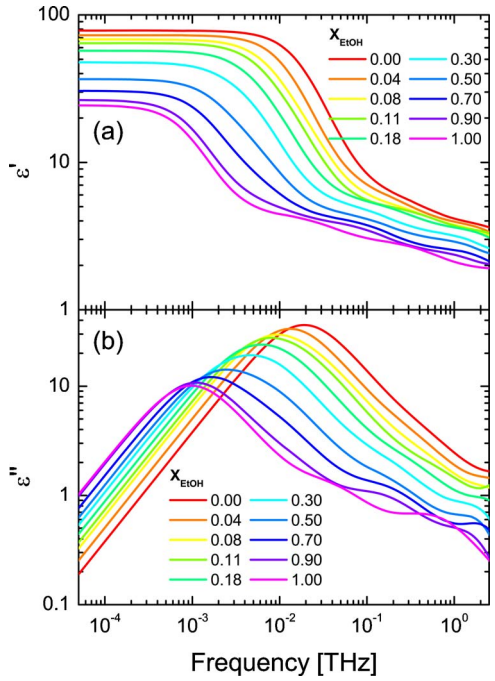

Fig. 5. (Color online) Fitted curves of (a) the real and (b) the imaginary part of the complex dielectric functions for different ethanol–water mixtures by using Eq. (14).

laxation processes. This would then indicate that the intermediate relaxation processes are of intermolecular nature.

This interpretation is further supported by MD simulations [40] and experimental data [41], which show that the mutual diffusion coefficients for ethanol–water mixtures are smallest in the region near $X_{\mathrm{EtOH}}=0.3$, and the self-diffusion coefficients of water in ethanol–water mixtures is smallest in the region near $X_{\mathrm{EtOH}}=0.4$.

The parameters for the intermolecular stretching vibration mode are plotted in Fig. 11. As previously mentioned, the vibration parameters of water are consistent with the findings of Yada *et al.*

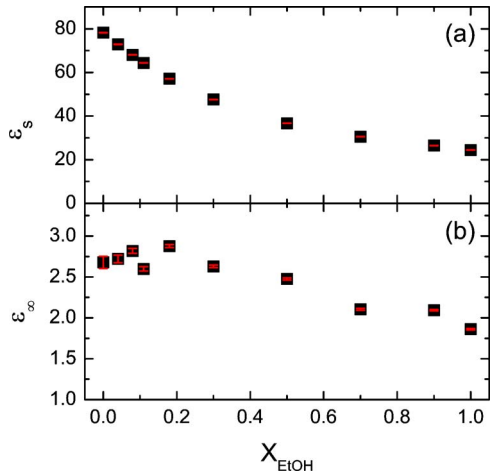

Fig. 6. (Color online) Fitted values and standard deviations of (a) the static dielectric constant, ϵ_s, and (b) the dielectric constant in the high frequency limit, ϵ_∞, of ethanol–water mixtures as a function of ethanol fraction X_{EtOH}.

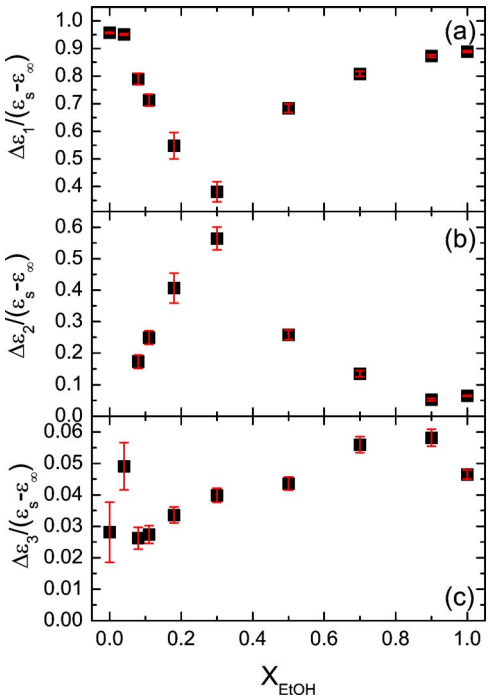

Fig. 7. (Color online) Debye relaxation strengths (a) $\Delta\epsilon_1$, (b) $\Delta\epsilon_2$, and $\Delta\epsilon_3$, normalized to the full dielectric strength $\epsilon_s-\epsilon_\infty$, of ethanol–water mixtures as functions of the ethanol concentration.

Since intermolecular vibrations occur in pure water, they are also bound to be present in ethanol–water mixtures to some extent. In the water-rich region the vibrational mode shifts to lower frequencies as the ethanol concentration increases, and it levels out above 30% to a frequency around 2.5 THz. One possible explanation of the frequency decrease could be that when ethanol is added to water some of the water molecules participating in the intermolecular vibrational motion will be substituted with heavier ethanol molecules resulting with an overall frequency drop. At this stage it is not clear why the resonance frequency remains fixed at higher ethanol concentrations. However, it is interesting to note that the resonance frequency remains fixed for concentrations above that of the minimum in the mixing enthalpy and

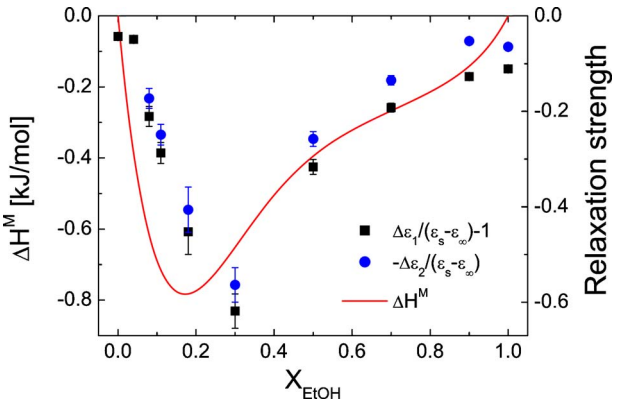

Fig. 8. (Color online) Mixing enthalpy of ethanol/water mixtures (red curve, from [39]) and the relaxation strengths of the slow Debye process (black points) as a function of ethanol concentration

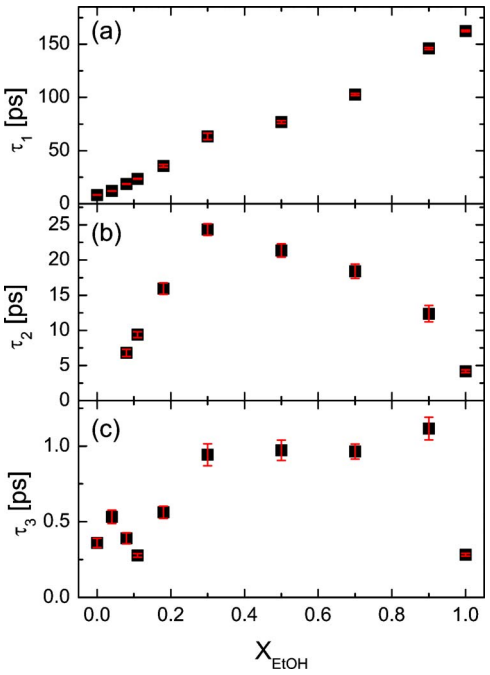

Fig. 9. (Color online) Debye relaxation times (a) τ_1, (b) τ_2, and (c) τ_3 of ethanol–water mixtures as a function of ethanol concentration.

approximately where the self-diffusion and mutual diffusion coefficients display their minima, as discussed above.

For pure ethanol our data indicate that the vibrational mode no longer contributes significantly to the dielectric function, indicating that water must be present in order to observe the effects of the mode.

5. INSPECTION OF LIQUIDS INSIDE BOTTLES

A wide range of glasses and polymers are transmissive to THz radiation. At the same time, typical surface quality of bottles for commercial liquids is sufficient for undisturbed transmission of THz radiation due to its long wavelength. Hence inspection of liquids inside bottles and other containers with THz radiation is possible. It has previously been demonstrated that it is possible to determine the alcohol content of a water–ethanol mixture inside polythylene teraphthalate (PET) and glass bottles [23]. In Fig. 12 the experimental configuration of the measurement on a bottle is shown. In this configuration the bottle wall itself is used as the interface to the liquid, thus lifting the requirement of removing the liquid from the bottle before the measurement.

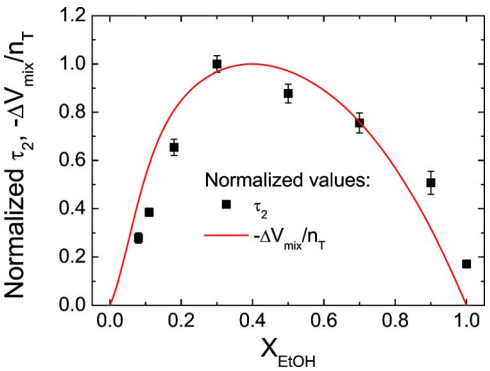

Fig. 10. (Color online) Mixing volume of ethanol–water mixtures (solid, red curve) and the time constants τ_2 (black squares).

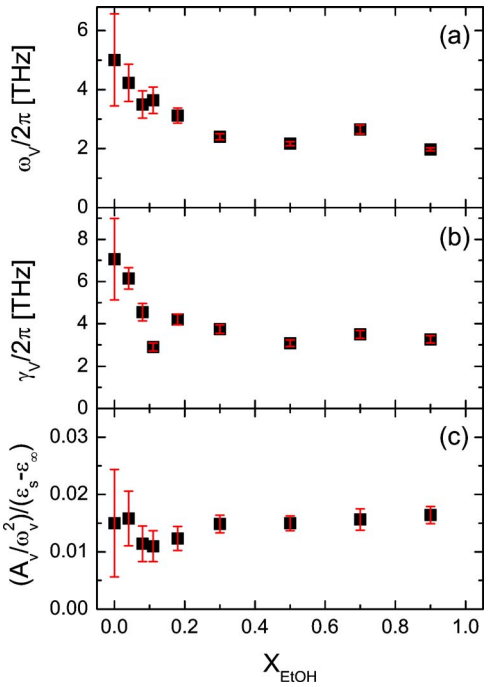

Fig. 11. (Color online) (a) Resonance frequency, (b) damping constant, and (c) vibration strength of the intermolecular stretching vibration of ethanol–water mixtures as a function of ethanol concentration.

The PET bottle wall has an index of refraction of approximately 1.75 in the 0.2–1.5 THz range [23]. While this index is significantly lower than that of water in the same range, the PET index is similar to that of certain other polar liquids, such as dioxan. In Fig. 13 we show the reflected THz signal from a PET bottle containing either water, ethanol, or dioxan. Each trace consists of two reflected portions of the same input signal, namely, the reflection from the outer surface of the bottle and, slightly delayed due to propagation through the bottle material, a second reflection from the interface between the bottle wall and the liquid.

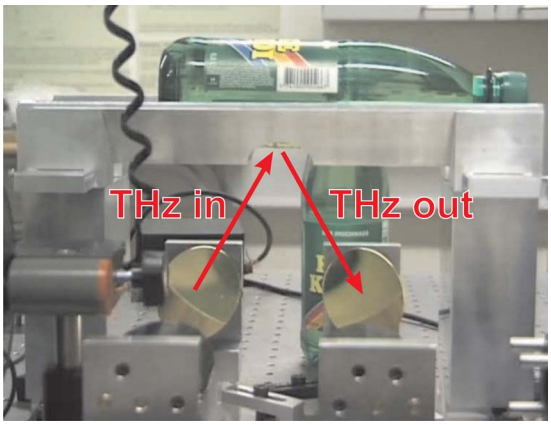

Fig. 12. (Color online) Self-referenced THz reflection spectroscopy of liquid inside a PET bottle.

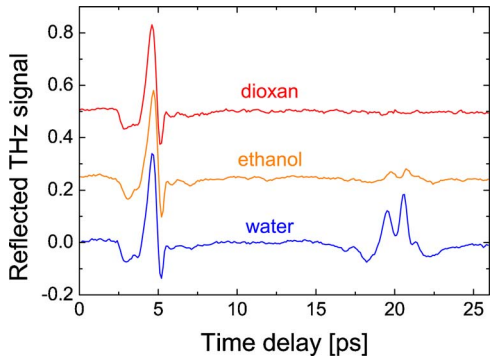

Fig. 13. (Color online) Reflected THz traces from a PET bottle containing water (lower trace), ethanol (middle trace), and dioxan (upper trace).

The reflected signal from the water-filled bottle shows a clear reflection from the PET–water interface. The corresponding reflection from the PET–ethanol interface in the ethanol-filled bottle shows a much weaker reflection amplitude due to the lower index of refraction of the liquid ethanol. When the bottle is filled with dioxan the second reflection virtually disappears, indicating very good index matching between PET and dioxan. Our observation of good index matching between PET ($n \approx 1.75$) and dioxan is not in complete agreement with previous determination of the index of refraction of pure dioxan [42] where the index of refraction was ported to decrease monotonically from 1.48–1.46 in the 0.5–2.5 THz range. We believe that this minor discrepancy is insignificant, and possibly due to impurities (such as water traces) in the dioxan used in our experiment, where no special precautions were taken to avoid water contamination.

The disappearance of the signal from the interface between the bottle wall and the liquid of course hinders any detailed analysis of the bottle content. However, the lack of a second reflection actually indicate that the PET bottle is filled with a liquid of relatively low refractive index, which on its own is useful information in some situations. Many volatile liquids, which at the same time are highly flammable, will have a low index of refraction, and thus THz reflection spectroscopy may be used for detection of flammable liquids in PET containers.

6. DIELECTRIC RELAXATION IN HYDROGEN PEROXIDE AND FUELS

Another class of hazardous liquids are oxidizers, which in connection with fuel components may form explosive mixtures. Thus there is a high demand for methods for standoff detection of liquids that may be used for the fabrication of liquid explosives. In this section we discuss reflection THz-TDS measurements of the dielectric properties of the oxidizer hydrogen peroxide as well as the fuel components nitromethane and nitroethane.

In Fig. 14(a) we show THz reflection traces from a PET bottle with a wall thickness of 0.65 mm, filled with water (blue trace) and a standard 30% (by weight) solution of hydrogen peroxide (red trace), a strong oxidizing and bleaching agent.

The reflected signal from the two liquids are virtually indistinguishable, immediately indicating that the dielectric properties of the hydrogen peroxide solution are very similar to those of pure water. This is further demonstrated in Fig. 14(b), where the real and imaginary part of the dielectric function of pure water (blue traces) are compared to those of the hydrogen peroxide solution (red traces). Within the signal-to-noise ratio of the experiment the two dielectric functions are identical. Previous reports showed little variation of the static dielectric constant of hydrogen peroxide solutions at room temperature [43–45], in agreement with the results published here.

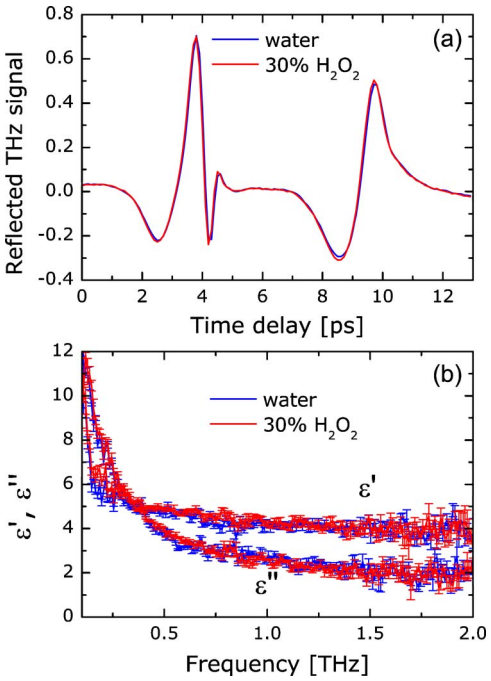

Fig. 14. (Color online) (a) Reflected THz traces from a PET surface in contact with water (blue trace) and a 30% hydrogen peroxide solution (red trace). (b) Real and imaginary part of the dielectric function of water (blue traces) and a 30% hydrogen peroxide solution (red traces). The error bars indicate the standard deviation between five consecutive scans.

One of the reasons for the striking similarity between liquid water and an aqueous solution of hydrogen peroxide is that the hydrogen peroxide molecule is isomorphous with the water molecule, i.e., it has a tetragonal electronic structure [45], and thus it can be incorporated into the intermolecular water structure with the same coordination number. Thus the intermolecular hydrogen bond network is left rather undisturbed by the addition of hydrogen peroxide, compared to the effect of solvating other molecules in water. At this point we dare to speculate that spectroscopy with higher spectral bandwidth may help to shed further light on the apparent similarity between liquid water and concentrated solutions of hydrogen peroxide.

Interestingly, the dielectric properties in the THz range of some non-hydrogen-bonded liquids are also well described by Debye-type relaxation processes, and thus in some aspects the dielectric properties of such liquids can be quite similar to those of liquid water. Here we consider the liquid fuels nitromethane (NM, molecular formula CH_3NO_2) and nitroethane (NE, molecular formula $CH_3CH_2NO_2$). The dominating attractive intermolecular forces in NM are dipole–dipole interactions [46], with

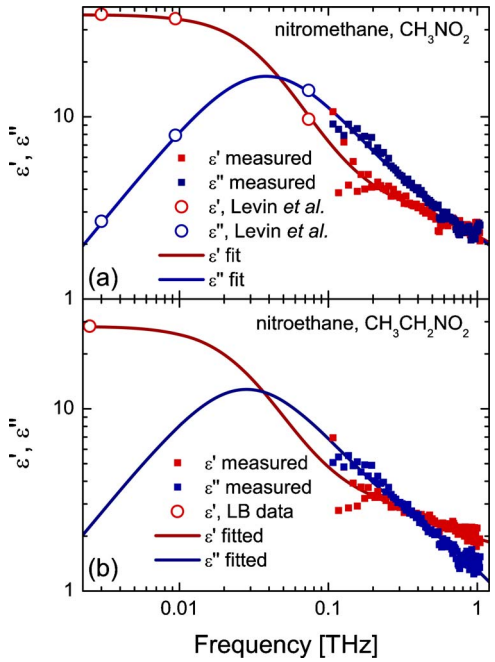

Fig. 15. (Color online) Complex permittivity of (a) nitromethane and and (b) nitroethane. Solid gray (red online) symbols and solid black (blue online) symbols represent our THz measurements, open symbols are literature values [48,49], solid lines are fits using the double Debye model to the available experimental data.

little or no intermolecular hydrogen bonding [47]. We assume similar intermolecular interactions in liquid NE, although very little information about the intermolecular interactions in liquid NE is available in the literature.

In Fig. 15(a) we show the complex dielectric function of NM, and in Fig. 15(b) the dielectric function of NE. The solid symbols represent our measurements in the 0.1–1.2 THz frequency range, and the open symbols are literature values. We use the few low-frequency values of the complex permittivity that are reported for NM [48], as well as the static permittivity of NE [49]. The combined experimental data are well fitted by a double Debye model, including two relaxation processes. The fitted curves of the real and imaginary parts of the permittivity of NM and NE are shown as solid lines in Figs. 15(a) and 15(b).

The best fitting parameters and their standard errors are given in Table 3. The characteristic relaxation times of 4.18 and 5.67 ps for NM and NE, respectively, are shorter than the slowest relaxation time of water (8.3 ps). This is consistent with a picture where the slowest relaxation process is related to intermolecular motion of the whole molecules. The weaker intermolecular bonds in NM and NE could then lead to a somewhat faster relaxation than is observed in bulk water. Further, the slightly slower relaxation process in NE than in NM is consistent with the larger dimensions of the NE molecules with respect to the NM molecules.

The slow relaxation process is much stronger than the faster relaxation process in both NM and NE, by the same ratio $\Delta\epsilon_1/\Delta\epsilon_2 \approx 18$, possibly again hinting at similar intermolecular dynamics in the two liquids. The corresponding ratio in liquid water is twice as large, indicating that the fast relaxation processes in NM and NE are more prominent than in water.

7. SUMMARY AND CONCLUSIONS

Water remains a liquid with many intriguing properties. The physical and optical properties of water and other polar liquids in the THz frequency range has been studied both by precise molecular dynamics simulations and by optical spectroscopy, with simulation results indicating that there is a connection between the microscopic dynamics and structure of the liquid and its thermodynamic properties. The link between optical experiments and the dynamics of the liquid is often to apply a phenomenological relaxation model to the dielectric spectrum of the liquid, and thus obtain information about the strength of the relaxation processes and their characteristic time constants. The most prominent modeling tool for this purpose is the Debye model, often with the inclusion of several relaxation processes which are then assumed to take place in a parallel fashion. This approach has given the possibility of identifying several relaxation processes in water and ethanol–water mixtures.

Broadband spectroscopy that includes information about the lowest-frequency intermolecular vibrational modes of the liquid has made it possible to combine data from DC measurements, the microwave regime, and the low and high THz regime, to obtain complete coverage of the frequency range that contains all the relaxation processes.

In our paper we have used such an approach to combine already published microwave data with our measurements of the dielectric function of water, ethanol–water mixtures, ethanol, aqueous solutions of hydrogen peroxide, and the fuels nitromethane and nitroethane. All these liquids were found to be well described by the Debye relaxation model with two (water, hydrogen peroxide solution, nitromethane, nitroethane) or three (water–ethanol mixtures and ethanol) relaxation terms. In the case of water and water–ethanol mixtures, the presence of the lowest intermolecular vibrational mode influences our data, and this mode was included in the modeling.

We found that the characteristics of the relaxation processes (relaxation strength and relaxation time constants) are correlated with the macroscopic thermodynamic prop-

Table 3. Relaxation Parameters for Nitromethane and Nitroethane

	ϵ_s	$\Delta\epsilon_1$	$\Delta\epsilon_2$	ϵ_∞	τ_1 [ps]	τ_2 [ps]
Nitromethane	36.4±0.7	33.3±0.7	1.89±0.20	1.26±0.17	4.18±0.12	0.16±0.02
Nitroethane	28.4[a]	25.4±0.1	1.39±0.12	1.60±0.06	5.67±0.14	0.29±0.03

[a]Kept fixed during fitting, value from [49]

erties of the liquid. Specifically it seems like there is a strong correlation between the mixing volume of ethanol–water mixtures and the intermediate and fast relaxation times—the smaller the mixing volume, the slower these relaxation times appear to be. Similarly, the largest enthalpy of mixing of ethanol–water mixtures appear at an ethanol concentration where the strength of the slow relaxation process is smallest and the strength of the intermediate relaxation process is highest.

We also found that the slow and intermediate relaxation times in the dipole–dipole correlated fuels nitromethane and nitroethane are approximately twice as fast as the corresponding times in water. Furthermore, the relative strength of the intermediate process with respect to the slow process is twice as large as the corresponding ratio in water. This we interpret as an indication of the smaller intermolecular forces in liquid nitromethane and nitroethane compared to the hydrogen-bonded water.

We suggest that THz-TDS measurements may be a useful tool for the distinction between benign liquids such as water and less concentrated ethanol–water solutions and hazardous liquids such as fuels and organic solvents. Some hazardous liquids, such as hydrogen peroxide, seem indistinguishable from pure water by their THz dielectric properties. However, increased spectral coverage to higher frequencies may shed further light on any differences in the relaxation dynamics of hydrogen peroxide and water.

The frequency coverage of the THz-TDS system is an important factor for the interpretation of the results. Based on the results presented here it is obvious that it is not possible to rely solely on data in the low THz region, since the faster processes are not covered by such experiments. We therefore believe that the ongoing progress on the improvement of bandwidth of THz-TDS systems, for instance by ultrabroadband photoconductive emitters and detectors or novel nonlinear crystals for ultrabroadband THz generation, and detection by electrooptic processes, will be very important for the progress of the experimental verification of numerical results. Furthermore, the low-frequency range, up to 0.1 THz, which is well-covered by microwave dielectric spectroscopy, plays a major role. Thus, spectroscopic studies that include both microwave techniques and the broadband THz techniques are important in order to obtain a complete picture of the extremely broadband relaxation processes in polar liquids.

ACKNOWLEDGMENTS

We thank Richard Buchner and Takaaki Sato for making their original spectroscopic data on water-ethanol mixtures available to us. We acknowledge the EU project TeraNova and the H. C. Ørsted Foundation for partial financial support. One of the authors (K.T.) acknowledges support from The Ministry of Education, Culture, Sports, Science and Technology (MEXT) of Japan (Grant-in-Aid for Creative Scientific Research program, 18GS0208).

REFERENCES

1. D. J. Segelstein, "The complex refractive index of water," M.S. thesis (Univ. of Missouri-Kansas City, 1981). Data can be found at http://www.philiplaven.com/p20.html.
2. T. Arikawa, M. Nagai, and K. Tanaka, "Characterizing hydration state in solution using terahertz time-domain attenuated total reflection spectroscopy," Chem. Phys. Lett. **457**, 12–17 (2008).
3. U. Heugen, G. Schwaab, E. Bründermann, M. Heyden, X. Yu, D. M. Leitner, and M. Havenith, "Solute-induced retardation of water dynamics probed directly by terahertz spectroscopy," Proc. Natl. Acad. Sci. U.S.A. **103**, 12301–12306 (2006).
4. M. Heyden, E. Bründermann, U. Heugen, G. Niehues, D. M. Leitner, and M. Havenith, "Long-range influence of carbohydrates on the solvation dynamics of water—Answers from terahertz absorption measurements and molecular modeling simulations," J. Am. Chem. Soc. **130**, 5773–5779 (2008).
5. D. M. Mittleman, M. C. Nuss, and V. L. Colvin, "Terahertz spectroscopy of water in inverse micelles," Chem. Phys. Lett. **275**, 332–338 (1997).
6. J. E. Boyd, A. Briskman, V. L. Colvin, and D. M. Mittleman, "Direct observation of terahertz surface modes in nanometer-sized liquid water pools," Phys. Rev. Lett. **87**, 147401 (2001).
7. J. E. Boyd, A. Briskman, C. M. Sayes, D. Mittleman, and V. Colvin, "Terahertz vibrational modes of inverse micelles," J. Phys. Chem. B **106**, 6346–6353 (2002).
8. J. Zhang and D. Grischkowsky, "Waveguide terahertz time-domain spectroscopy of nanometer water layers," Opt. Lett. **29**, 1617–1619 (2004).
9. J. Zhang and D. Grischkowsky, "Terahertz time-domain spectroscopy of submonolayer water adsorption in hydrophilic silica aerogel," Opt. Lett. **29**, 1031–1033 (2004).
10. P. Uhd Jepsen and B. M. Fischer, "Dynamic range in terahertz time-domain transmission and reflection spectroscopy," Opt. Lett. **30**, 29–31 (2005).
11. T. J. Parker, "Dispersive Fourier transform spectroscopy," Contemp. Phys. **31**, 335–353 (1990).
12. M. N. Afsar and J. B. Hasted, "Measurements of the optical constants of liquid H_2O and D_2O between 6 and 450 cm^{-1}," J. Opt. Soc. Am. **67**, 902–904 (1977).
13. D. Grischkowsky, S. Keiding, M. van Exter, and Ch. Fattinger, "Far-infrared time-domain spectroscopy with terahertz beams of dielectrics and semiconductors," J. Opt. Soc. Am. B **7**, 2006–2015 (1990).
14. M. van Exter, Ch. Fattinger, and D. Grischkowsky, "Terahertz time-domain spectroscopy of water vapor," Opt. Lett. **14**, 1128–1130 (1989).
15. P. Uhd Jepsen, R. H. Jacobsen, and S. R. Keiding, "Generation and detection of terahertz pulses from biased semiconductor antennas," J. Opt. Soc. Am. B **13**, 2424–2436 (1996).
16. A. Nahata, A. S. Weling, and T. F. Heinz, "A wideband coherent terahertz spectroscopy system using optical rectification and electro-optic sampling," Appl. Phys. Lett. **69**, 2321–2323 (1996).
17. L. Thrane, R. H. Jacobsen, P. Uhd Jepsen, and S. R. Keiding, "THz reflection spectroscopy of liquid water," Chem. Phys. Lett. **240**, 330–333 (1995).
18. P. Uhd Jepsen, U. Møller, and H. Merbold, "Investigation of aqueous alcohol and sugar solutions with reflection terahertz time-domain spectroscopy," Opt. Express **15**, 717–737 (2007).
19. M. Nagai, H. Yada, T. Arikawa, and K. Tanaka, "Terahertz time-domain attenuated total reflection spectroscopy in water and biological solution," Int. J. Infrared Millim. Waves **27**, 505–515 (2006).
20. H. Hirori, M. Nagai, and K. Tanaka, "Destructive interference effect on surface plasmon resonance in terahertz attenuated total reflection," Opt. Express **13**, 10801–10814 (2005).
21. N. E. Hill, W. E. Vaughan, A. H. Price, and M. Davis,

Dielectric Properties and Molecular Behaviour (Van Nostrand Reinhold Company, 1969).
22. R. M. Hill and L. A. Dissado, "Debye and non-Debye relaxation," J. Phys. C **18**, 3829–3836 (1985).
23. P. Uhd Jepsen, J. K. Nielsen, and U. Møller, "Characterization of aqueous alcohol solutions in bottles with THz reflection spectroscopy," Opt. Express **16**, 9318–9331 (2008).
24. T. Sato and R. Buchner, "Dielectric relaxation processes in ethanol/water mixtures," J. Phys. Chem. A **108**, 5007–5015 (2004).
25. H. Yada, M. Nagai, and K. Tanaka, "Origin of the fast relaxation component of water and heavy water revealed by terahertz time-domain attenuated total reflection spectroscopy," Chem. Phys. Lett. **464**, 166–170 (2008).
26. *Terahertz Spectroscopy: Principles and Applications* S. Dexheimer, ed. (CRC Press, 2007).
27. C. Rønne, L. Thrane, P.-O. Astrand, A. Wallqvist, K. V. Mikkelsen, and S. R. Keiding, "Investigation of the temperature dependence of dielectric relaxation in liquid water by THz reflection spectroscopy and molecular dynamics simulation," J. Chem. Phys. **107**, 5319–5331 (1997).
28. J. T. Kindt and C. A. Schmuttenmaer, "Far-Infrared dielectric properties of polar liquids probed by femtosecond terahertz pulse spectroscopy," J. Phys. Chem. **100**, 373–379 (1996).
29. H. Kitahara, T. Yagi, K. Mano, M. W. Takeda, S. Kojima, and S. Nishizawa, "Dielectric characteristics of water solutions of ethanol in the terahertz region," J. Korean Phys. Soc. **46**, 82–85 (2005).
30. J. B. Hasted, S. K. Husain, F. A. M. Frescura, and J. R. Birch, "The temperature variation of the near millimetre wavelength optical constants of water," Infrared Phys. **27**, 11–15 (1987).
31. J. Barthel, K. Bachhuber, R. Buchner, and H. Hetzenauer, "Dielectric spectra of some common solvents in the microwave region. Water and lower alcohols," Chem. Phys. Lett. **165**, 369–373 (1990).
32. U. Kaatze, "Complex permittivity of water as a function of frequency and temperature," J. Chem. Eng. Data **34**, 371–374 (1989).
33. J. M. Alison and R. J. Sheppard, "A precision waveguide system for the measurement of complex permittivity of lossy liquids and solid tissues in the frequency range 29 GHz to 90 GHz—III. The liquid system for 57 to 82 GHz: an investigation into water and formamide," Meas. Sci. Technol. **2**, 975–979 (1991).
34. H. Yada, M. Nagai, and K. Tanaka, "The intermolecular stretching vibration mode in water isotopes investigated with broadband terahertz time-domain spectroscopy," Chem. Phys. Lett. **473**, 279–283 (2009).
35. S. Mashimo, S. Kuwabara, S. Yagihara, and K. Higasi, "The dielectric relaxation of mixtures of water and primary alcohol," J. Chem. Phys. **90**, 3292–3294 (1989).
36. T. Sato, A. Chiba, and R. Nozaki, "Dynamical aspects of mixing schemes in ethanol-water mixtures in terms of the excess partial molar activation free energy, enthalpy, and entropy of the dielectric relaxation process," J. Chem. Phys. **110**, 2508–2521 (1999).
37. P. Petong, R. Pottel, and U. Kaatze, "Water-ethanol mixtures at different compositions and temperatures. A dieletric relaxation study," J. Phys. Chem. A **104**, 7420–7428 (2000).
38. R. Chang, *Physical Chemistry for the Chemical and Biological Sciences*, 3rd ed. (University Science Books, 2000).
39. J. A. Boyne and A. G. Williamson, "Enthalpies of mixture of ethanol and water at 25 °C," J. Chem. Eng. Data **12**, 318 (1967).
40. C. Zhang and X. Yang, "Molecular dynamics simulation of ethanol/water mixtures for structure and diffusion properties," Fluid Phase Equilib. **231**, 1–10 (2005).
41. M. T. Tyn and W. F. Calus, "Temperature and concentration dependence of mutual diffusion coefficients of some binary liquid systems," J. Chem. Eng. Data **20**, 310–316 (1975).
42. S. Schrödle, B. Fischer, H. Helm, and R. Buchner, "Picosecond dynamics and microheterogenity of water +dioxane mixtures," J. Phys. Chem. A **111**, 2043–2046 (2007).
43. P. M. Gross, Jr. and R. C. Taylor, "The dielectric constants of water, hydrogen peroxide, and hydrogen peroxide-water mixtures," J. Am. Chem. Soc. **72**, 2075–2080 (1950).
44. A. K. Lyaschenko, V. S. Goncharov, and P. S. Yastremskii, "Structure and dielectric properties of aqueous solutions of hydrogen peroxide," J. Struct. Chem. **17**, 871–876 (1976).
45. A. A. Potapov and I. Yu. Parkhomenko, "Dielectric properties of solutions isomorphous with water," Russian J. Gen. Chem. **75**, 34–39 (2005).
46. D. C. Sorescu, B. M. Rice, and D. L. Thompson, "Molecular dynamics simulations of liquid nitromethane," J. Phys. Chem. A **105**, 9336–9346 (2001).
47. H. E. Alper, F. Abu-Awwad, and P. Politzer, "Molecular dynamics simulations of liquid nitromethane," J. Phys. Chem. B **103**, 9738–9742 (1999).
48. V. V. Levin, E. A. Ovsoyan, and V. I. Ovchinnikov, "Dispersion of the dielectric constant of nitromethane," Russian J. Phys. Chem. **45**, 1333–1334 (1971).
49. O. Madelung, ed. *Numerical Data and Functional Relationships in Science and Technology*, Vol. 6 of Static Dielectric Constants of Pure Liquids and Binary Liquid Mixtures (Springer, 1991).